2024

Non-Catalytic Regulators Of The Secretory Pathway

Peyton VanWinkle
University of Alabama at Birmingham

NON-CATALYTIC REGULATORS OF THE SECRETORY PATHWAY

by

PEYTON E. VANWINKLE

ELIZABETH SZTUL, COMMITTEE CHAIR
SUSAN BELLIS
CHENBEI CHANG
AMJAD JAVED
JOHN M. PARANT
ROSA SERRA

A DISSERTATION

Submitted to the graduate faculty of the University of Alabama at Birmingham,
in partial fulfillment of the requirements for the degree of
Doctor of Philosophy

BIRMINGHAM, ALABAMA

2024

NON-CATALYTIC REGULATORS OF THE SECRETORY PATHWAY

PEYTON E VANWINKLE

CELL, DEVELOPMENTAL, AND INTEGRATIVE BIOLOGY

ABSTRACT

This thesis focuses on two key questions: 1) how are bone development and regeneration regulated by the CREB3L1 transcription factor; and 2) what is the mechanism of action of the endoplasmic reticulum resident protein JAGN1, which when dysregulated, causes severe congenital neutropenia (SCN)?

CREB3L1 regulates bone development and regeneration in mammalian models by facilitating the expression of *COL1A1* and components of the secretory pathway required for collagen secretion. We generated two zebrafish models of Creb3l1 dysfunction (*creb3l1*$^{\Delta bZIP/\Delta bZIP}$ and *creb3l1*$^{TA+/TA+}$). Both models showed that Creb3l1 functions in regulating *col1a1a* transcription and overall regenerate size are conserved in zebrafish. However, we also uncovered that Creb3l1 regulates patterning during development and regeneration by intersecting with the Sonic Hedgehog signaling pathway. This novel finding in zebrafish provides a foundation for future studies to explore CREB3L1 effects on Hedgehog signaling during healing of bone fractures in mammalian models.

JAGN1 mutations cause Severe Congenital Neutropenia (SCN) in patients and knocking-out JAGN1 leads to embryonic lethality in mice. JAGN1 has domains that suggest an “escort” function in transport of cargo proteins at the ER-Golgi interface. Unlike mammals, zebrafish have two jagn1 (*jagn1a* and *jagn1b)* genes. To determine the effects of their dysfunction, we separately knocked out each jagn1. The *jagn1a*$^{-/-}$ fish

survived to become healthy adults but exhibited defects in brain activity. In contrast, the *jagn1b*$^{-/-}$ fish died between 10- and 14-days post fertilization, recapitulating the lethality seen in mammals. Our zebrafish models will be key in future analyses of tissue-specific roles for jagn1.

To probe cellular function(s) of JAGN1, we used CRISPR/Cas9 to generate mouse embryonic fibroblasts expressing different forms of dysfunctional JAGN1. Interestingly, *Jagn1* mutant cells exhibited dramatic delay in spreading and adhesion, a novel role for JAGN1 in an ubiquitous cellular process. The molecular underpinnings of the spreading defect remain to be determined, but preliminary Bio-ID analyses suggest that JAGN1 may impact trafficking of adhesion molecules and/or affect actin cytoskeleton dynamics.

Based on the findings presented in this thesis, we propose a novel role for CREB3L1 in patterning during bone regeneration, and a novel function for JAGN1 in cell adhesion. Our findings broaden the knowledge of bone regeneration and inform on the possible molecular lesion responsible for JAGN1-linked neutropenia.

Keywords: CREB3L1, JAGN1, endoplasmic reticulum, bone, zebrafish, regeneration

DEDICATION

I dedicate this thesis to those who have always chosen to believe in me: my family, my friends, and my husband, who serves both roles with gusto.

ACKNOWLEDGEMENTS

I would like to begin by thanking Dr. Elizabeth Sztul for welcoming me into her lab in 2018, and trusting me to take control of a new project in her lab, which is being presented here. Your faith in me has given me the opportunity to explore new areas of research and learn so much about both science and life. I would also like to thank my laboratory members for their support of my research, from help with experiments to listening to my new ideas and providing camaraderie in the laboratory environment.

Next, I would like to thank my committee members, Dr. Chenbei Chang, Dr. Rosa Serra, Dr. Susan Bellis, Dr. John Parant, and Dr. Amjad Javed. Their support during my PhD has provided me with expertise and novel perspectives on my project, which have been invaluable towards the progress of my project. Thank you for agreeing to be on my committee and for supporting my journey as a scientist.

I am also fortunate to have a large friend support group, some of whom I have found through GBS. Allyson and Alexandria have both provided me with immense support through the last five years, and I am truly thankful for them. I am also thankful for the friends I made during my undergraduate work, Elizabeth and Carissa, for constantly listening to me talk about grad school- whether it was my research or just me complaining. Last but not least, I would like to thank my oldest friend, Alexandra, for believing in me even when I was a stupid teenager. I am so proud of where we have

ended up. For brevity, I will just say to all of my other wonderful friends, thank you for the love and joy you bring to my life, I am so lucky to have all of you.

I would of course, also like to thank my family- my mom and dad for always believing in me, and my siblings for being my friends, keeping me humble, and always surrounding me with love. And finally, thank you to my husband, who has weathered all of the storms of graduate school with me. I could not do it without you, Riley.

I feel like the luckiest woman alive to have had such a great support system to get me through graduate school, and I will be eternally thankful for everyone involved in getting me to this point. Thank you, thank you, thank you!

TABLE OF CONTENTS

Page

LIST OF TABLES

Table *Page*

LIST OF FIGURES

Figure *Page*

INTRODUCTION

DISRUPTION OF THE *CREB3L1* GENE CAUSES DEFECTS IN CAUDAL FIN REGENERATION AND PATTERNING IN ZEBRAFISH *DANIO RERIO*

LACK OF NUCLEAR LOCALIZATION OF THE CREB3L1 TRANSCRIPTION FACTOR CAUSES DEFECTS IN CAUDAL FIN BIFURCATION IN ZEBRAFISH DANIO RERIO

JAGN1, TETRASPANINS, AND ERV PROTEINS: IS COMMON TOPOLOGY INDICATIVE OF COMMON FUNCTION IN CARGO SORTING?

A NOVEL ROLE FOR JAGN1 IN REGULATING CELL-SUBSTRATE ADHESION

LIST OF ABBREVIATIONS

ATB	Adjacent to bZIP
ATF	Activating Transcription Factor
bZIP	Basic Leucine Zipper
COL1A1	Collagen Type I Alpha 1 Chain
COPI	Coat Protein I
COPII	Coat Protein II
CREB3L1	CAMP Responsive Element Binding Protein 3 Like 1
CRISPR	Clustered Regularly Interspaced Short Palindromic Repeats
DIG	Digoxigenin
dpa	Days Post Amputation
dpf	Days Post Fertilization
eGFP	Enhanced Green Fluorescent Protein
ER	Endoplasmic Reticulum
ERAD	Endoplasmic Reticulum Associated Degradation
ERK	Extracellular Signal-related Kinases
GRP	Glucose Regulated Protein
GTP	Guanosine Triphosphate
HB	Hybridization Buffer
HEK	Human Embryonic Kidney

JAGN1	Jagunal homolog 1
KO	Knockout
MEF	Mouse Embryonic Fibroblasts
Mpf	Months Post Fertilization
MSX	Muscle Segment Homeobox
NIS	Sodium Iodide Symporter
OASIS	Old Astrocyte Specific Induced Substance
OI	Osteogenesis Imperfecta
PFA	Paraformaldehyde
PH3	Phosphohistone 3
PTCH	Patched
RIP	Regulated Intramembrane Proteolysis
RT	Room temperature
S1P	Site 1 Protease
S2P	Site 2 Protease
SCN	Severe Congenital Neutropenia
SHH	Sonic Hedgehog
SMO	Smoothened
SNARE	SNAP Receptors
SSC	Saline Sodium Citrate
SURF, SFT	Surfeit
TA	Transcriptionally Active
Tg	Transgenic

TGN	Trans Golgi Network
TM	Transmembrane
TSPAN	Tetraspanin
UTR	Untranslated Region
XBP1	X-box binding protein 1

INTRODUCTION

The Secretory Pathway

The trafficking of proteins through the secretory pathway is a highly conserved biological process. It is responsible for the appropriate synthesis, modification, and localization of approximately 1/3 of the yeast proteome [1], and over 500 genes have been proposed to participate in this process [2]. This pathway includes a number of organellar compartments; beginning with the ER, passing through the Golgi apparatus, and eventually being transported to different compartments of the cell, or secreted extracellularly. [3] The secretory pathway begins when an RNA-loaded ribosome is docked into the endoplasmic reticulum. This occurs when a signal peptide is recognized by a signal-recognition particle (SRP), which then binds to the SRP receptor localized in the ER membrane. Upon docking, the peptide is co-translationally transferred through a channel known as a translocon (Figure 1, 1). The signal peptide is either cleaved to generate type I transmembrane and soluble proteins, or is uncleaved and generates type II transmembrane proteins [1]. As the protein is translated and enters the endoplasmic reticulum, it undergoes appropriate folding, facilitated by a group of proteins called chaperones [4]. During translocation through the ER membrane, many proteins undergo core glycosylation through the addition of a complex oligosaccharide precursor to an asparagine residue [1, 5].

The ER is best described as a milieu of activity; numerous modifications and quality control steps are performed before a protein can exit the ER (Figure 1, 2) [1]. Improperly folded proteins can cause ER stress and are selected for ER-associated degradation (ERAD), a process carried out by the proteasome, a large complex of proteases that degrades misfolded proteins (Figure 1, 3). To ensure proper glycosylation,

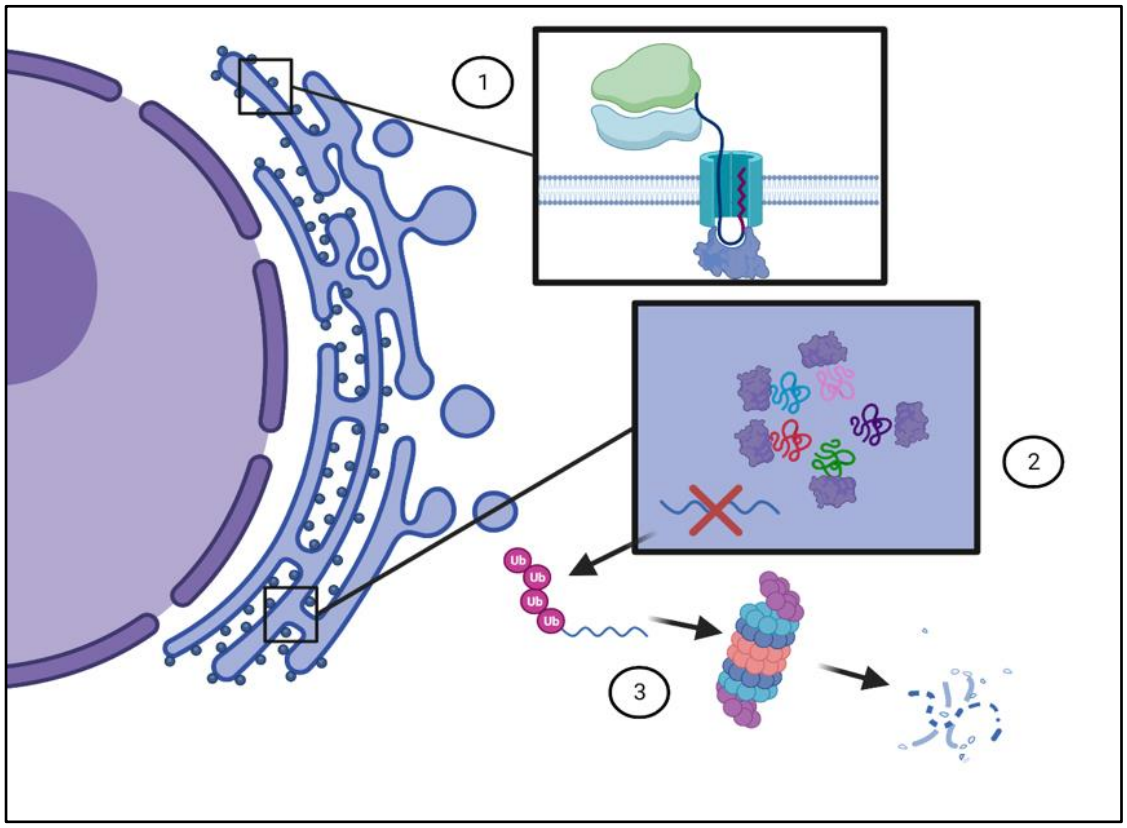

Figure 1: Illustration of early secretory pathway events in the endoplasmic reticulum. 1) Translation into the ER begins when a ribosome carrying a nascent peptide is docked into the endoplasmic reticulum, where it undergoes co-translational folding and glycosylation. 2) Proteins must be correctly folded to exit the ER. 3) Proteins that do not meet this quality control are degraded by ERAD.

proteins must bind to calnexin and calreticulin in order to exit the endoplasmic reticulum- accumulation of these protein leads to activation of ERAD [3, 6]. In cells where ERAD cannot ameliorate ER stress, an apoptotic program will be initiated, underscoring the importance of a functional early secretory pathway in cellular homeostasis [7].

Once modified and appropriately folded, cargo proteins are transported via COPII vesicles coated with heptameric coatamer complexes (Figure 2, 1, dark blue vesicle). In brief, the COPII coatamer is assembled on the membrane, a small GTPase, Sar1p, which subsequently cleaves GTP to GDP to facilitate the budding of membrane vesicles containing the cargo proteins off the endoplasmic reticulum. COPII vesicles rapidly uncoat to expose membrane proteins such as SNAREs that mediate the docking of the vesicle to SNAREs present on the cis-Golgi membrane. The SNAREs undergo a conformation change which mediates the fusion of the vesicle with the Golgi. Escaped ER resident proteins are then recycled from the Golgi to the ER via COPI-coated vesicles through a process analogous to that of COPII vesicle budding; COPI coatamer complexes are recruited by the small GTPase Arf1 in place of Sar1p (Figure 2, 1, dark green vesicle) [1, 8]. In the Golgi, cargo proteins mature by being processed via discreet enzymes in each cisterna (Figure 2, 2), undergoing posttranslational modifications such as glycosylation and sulfation. The modified proteins exit the Golgi through the trans-Golgi network (TGN) (Figure 2, 3,) and are trafficked to their respective compartments, such as lysosomes or the cell membrane. At the cell membrane, vesicles fuse via a process known as exocytosis, which can be constitutive or regulated [3, 9].

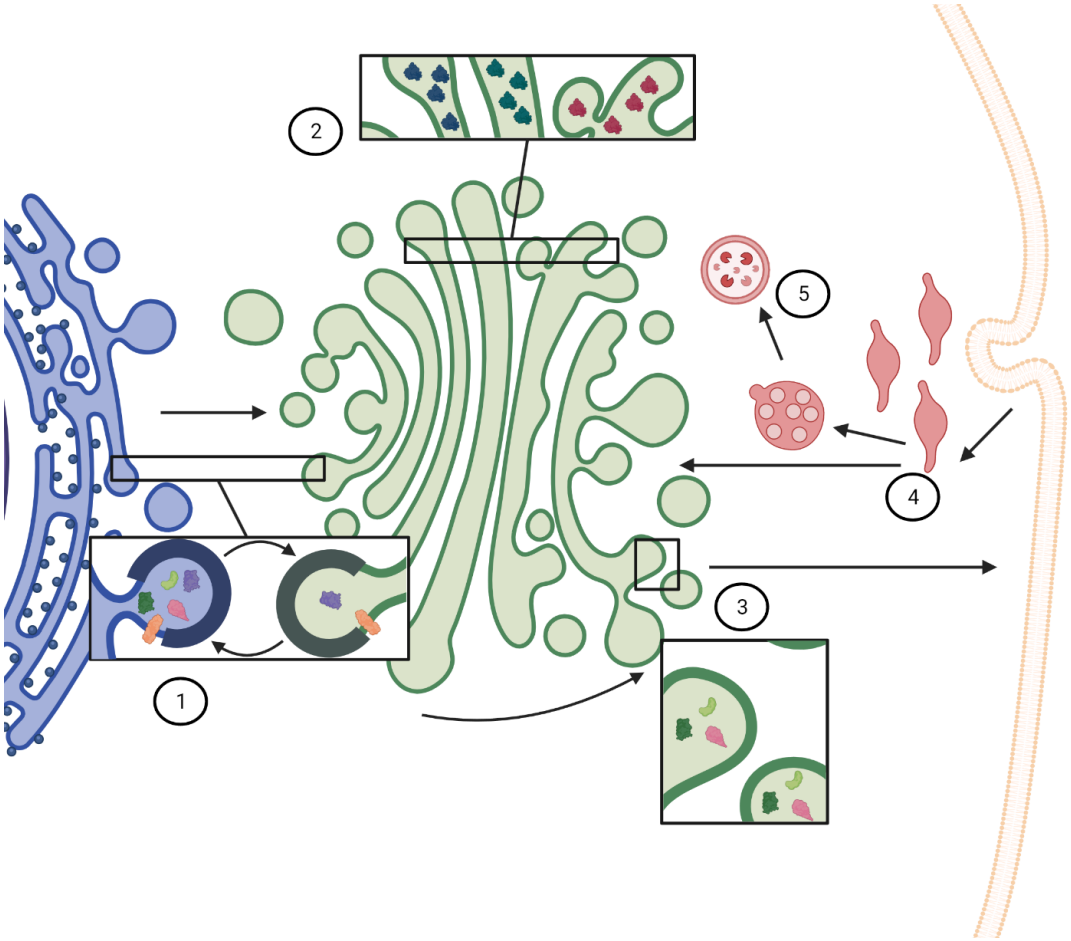

Figure 2: Illustration of early secretory pathway events transporting cargo through the golgi apparatus to the cell membrane . 1) Cargo is transported from the ER to the Golgi via COPII vesicles (blue) while COPI vesicles (green) recycle sorting and resident ER proteins. 2) The Golgi cisternae contain discrete sets of modifying enzymes responsible for maturation of proteins as they move through the golgi. 3) Fully mature proteins are transported to the plasma membrane. 4) Endocytosing membranes enter the sorting endosome and are returned to the plasma membrane or to 5) lysosomes for degradation.

Once on the cell membrane, proteins such as transmembrane receptors can be recycled via endocytosis, which is the process of budding cell membrane vesicles back into the cell. Endocytosis is mediated by clathrin adaptor and clathrin proteins in a manner similar to the COPI and COPII processes (Figure 2,4) [10, 11]. These endocytosed membranes and their cargo form a sorting, or early endosome, which then generates recycling endosomes, or sends the cargo to the lysosome for degradation

(Figure 2, 5) [10, 11]. Proteins in early endosomes can exit the endosomal cycle and be sent to the TGN (Figure 2, 4) [10].

Within the last fifty years, the established paradigms of the secretory pathway have been focused on ubiquitous biochemical processes that occur in a generalized "cell". Such common processes appear essential, as mutations in components facilitating them cause embryonical lethality [12-14]. However, recent work has begun to focus on tissue-specific functions of proteins previously studied in a non-tissue-specific context [2, 15-17]. This is especially relevant to diseases of the secretory pathway, which often cause phenotypes limited to one or two tissues. Characteristically, such diseases affect highly secretory tissues, and can be due to defects in the trafficking of structural proteins, plasma membrane receptors, components of intracellular organelles, hormones, or small molecules.

The transport of cargo proteins through the secretory pathway can be regulated on many different levels [18-20]. One of those is transcriptional control of genes encoding proteins that regulate the efficiency of trafficking. One of the transcription factors shown to influence the efficacy of the secretory pathway is the Creb3l1 transcription factor, and the first part of this thesis explores the function of this protein in bone development in zebrafish. Another way that trafficking of proteins is regulated is through the function of specific "escort" proteins that ferry cargo proteins between the compartments of the secretory pathway. The second part of my thesis explores the function of the JAGN1, a protein proposed to "escort" proteins from the ER to the Golgi in zebrafish development and in mammalian cells.

Regulation of the secretory pathway at a transcriptional level

While the structure, cellular localization, and catalytic activities of numerous enzymes regulating secretory traffic have been the focus of research for many decades, more recent work gives insights to the dynamic transcriptional regulation of these ubiquitous proteins [2, 21-23]. Much of this work focuses on the bZIP transcription factors such as the CREB/ATF family, and XBP1 [21, 24-26]. Within this group, the proteins ATF6 and ATF4, as well as XBP1, are key regulators of transcription of ER chaperones, as well as inducing metabolic changes, such as lipid biogenesis, to facilitate expansion of the secretory pathway [6, 7].

In contrast, the CREB3 family and their homologs in other species have been shown to facilitate the expansion of the secretory pathway [21, 22, 27]. All members of the CREB3 family are orthologous to the *Drosophila* gene *CrebA*, also known as box B-binding factor-2 (*BBF-2*), a gene important in regulating the expression of numerous components of the secretory pathway in response to increased secretory demand [22, 28]. Mammals have five orthologues of this gene (CREB3, CREB3L1, CREB3L2, CREB3L3, and CREB3L4), all of which (similarly to ATF6) are synthesized as transmembrane resident ER proteins. Under ER stress or specific developmental or physiological signaling events, CREBs are trafficked to the Golgi to undergo proteolytic cleavage. The proteolytic cleavage releases a transcription activating fragment (TA) that subsequently enters the nucleus where it can activate transcription [21, 22]. CREB3L1, which is the focus of work presented in this thesis, is best characterized as a regulator of secretory capacity as well as physiological development of astrocytes, bone, and thyroid [29-35]. CREB3L2 appears to have similar functions, but has been best characterized as an

important factor in regulating development of the nervous system, as well as chondrocyte development [36-40]. The functions of CREB3L3 and CREB3L4 have been mostly discussed in the context of physiological tissue development, and less in the regulation of membrane trafficking components [21, 27].

Bone development and repair

The skeleton is a rigid structure responsible for supporting and protecting the body's soft tissues. In order to form this structure, cells called osteoblasts must secrete an organic matrix composed of collagen, which is subsequently calcified to form mineralized bone. Osteoblast cells arise from mesenchymal stem cells, which differentiate into osteoblast progenitors, which subsequently differentiate into preosteoblasts expressing *RUNX2*, and finally into osteoblasts expressing *SP7*. These osteoblasts will mineralize upon a cartilaginous matrix, or directly from mechanism, generating endochondral or intramembranous bone formation, respectively. [41, 42]

When bone is injured, such as during fracture, the bone undergoes a multi-stage process to repair the broken bone. This involves the invasion of blood and inflammatory cells, the deposition of a cartilaginous callus, and replacement of this callus with a bony callus. This bony callus is then remodeled to establish compact bone, as well as an appropriate thickness and shape of the bone after repair [41, 43]. Both development and repair involve osteoblastic activity, which is the best characterized cell type in which CREB3L1 is expressed.

Role of CREB3L1 in bone development and repair

CREB3L1 was first characterized in 1999, as a gene specifically expressed in long-term cultured astrocytes and gliotic tissue. This gene, initially termed Old Astrocyte

Specifically Induced Substance (OASIS) was shown to be expressed at low levels in the brain, but highly expressed in cartilage and bone [28, 44, 45]. As is characteristic of members of the CREB/ATF family, CREB3L1 has an N-terminal transcription activating (TA) region containing a bZIP DNA binding domain, an ATB (adjacent to bZIP) domain exclusive to CREB3 family members, a transmembrane domain that anchors it in the ER and a C-terminal luminal domain [23, 30, 31]. CREB3L1 resides in the ER, but during ER stress, or developmental signals, CREB3L1 transits from the ER to the Golgi, where it undergoes proteolytic cleavage via intra-membrane proteolysis by the S1P serine protease of the subtilisin family, and then by the S2P zinc-metalloprotease. The S2P cleavage liberates the N-terminal transcription-activating "TA" fragment, which is then translocated to the nucleus, where it acts to regulate gene expression [31].

Tissue-specific targets of CREB3L1 have been identified in a variety of tissues. In murine glia, CREB3L1 increases the transcription of chondroitin-6-O-sulfotransferase 1 (*C6st1*), an enzyme responsible for sulfating the ECM molecule chondroitin, as well as unfolded protein response (UPR) genes such as *Grp78* and *Grp94* [33, 46, 47]. In rat pancreatic β-cells, a microarray analysis showed CREB3L1-dependent increase in the expression of genes related to extracellular matrix formation, such as 3'-Phosphoadenosine 5'-Phospho-sulfate Synthase 2 (*Papss2*), and related to protein secretion, such as *Copz2* and KDEL receptor 3 (*Kdelr3)* [48]. Overexpression of CREB3L1 in a rat thyroid cell model increased the size of the Golgi complex and induced the expression of Rab1b and GM130 components of the secretory pathway, suggesting an increase in secretory capacity [23]. Conversely, siRNA mediated

knockdown of CREB3L1 diminished Golgi complex volume and decreased the expression of Rab1 and GM130 proteins [23].

Previous studies of mouse development showed the strongest expression of *CREB3L1* in the preosteoblasts of the outer bony cortex of the ribs [44, 49]. Strong expression was also shown in alveolar bone and in the preodontoblast of tooth buds. This expression is transient, however, ranging from E12.5 to 18.5 with a peak at E14.5-16.5 [44]. CREB3L1$^{-/-}$ mice exhibit delayed mineralization of the skeleton, lower bone mineral density, and poorer fracture healing than their wild-type counterparts [32, 49]. This is likely due to CREB3L1 regulation of *Col1a1*¸an essential component of the bone organic matrix. CREB3L1$^{-/-}$ mice have lower expression of *Col1a1* mRNA, as well as lower levels of COL1A1 protein. Interestingly, the alterations in *Col1a1* expression are specific to bone [32, 44, 49].

Some aspects of the CREB3L1$^{-/-}$ mice phenotypes appear recapitulated in humans, with homozygous CREB3L1 mutations causing Osteogenesis Imperfecta 16 (OI16), a severe form of OI with perinatal fractures, poor mineralization of bones, and frequent perinatal lethality [50-54]. However, some individuals survive into adulthood, although they exhibit skeletal phenotypes, with bowed extremities and poor bone mineral density [51, 55]. Such severe phenotypes observed in mice and humans, underscore the essential role of CREB3L1 in bone formation and homeostasis. Beyond development, CREB3L1 is essential for appropriate fracture healing, with poor formation of the bony callus and poor expression of *Col1a1* at the fracture plane in CREB3L1$^{-/-}$ mice [32].

With life expectancy increasing every decade, a corresponding increase in fracture prevalence has been observed in the last 30 years [56]. Thus, it is more important

than ever to understand the mechanisms of bone development and healing, and the work presented in this thesis focuses on CREB3L1 as a novel research avenue on this subject. The research described in this thesis explores the role of CREB3L1 in bone development and regeneration.

Regulation of cargo sorting in the secretory pathway

Another layer of regulation in the secretory pathway involves the control of cargo sorting and specific protein sorting receptors. Proteins that serve this function facilitate cargo trafficking from the ER to the Golgi, from the Golgi to the ER, from the Golgi to endosomes, the lysosome or the plasma membrane [20, 57-62]. This escort function is a highly conserved process, with many escort proteins being evolutionary conserved from humans to yeast [62, 63]. One family of proteins, the Ervs (endoplasmic reticulum vesicle), are known for their roles in the selective sorting of cargo proteins within secretory pathway. Members of the Erv families are highly conserved and widely expressed throughout phylogeny, underscoring their importance in eukaryotic life. These selective regulators of protein traffic are characterized by a common membrane topology, with four membrane-spanning domains (tetraspanning), two extracellular/luminal loops and the N- and C-termini located within the cytosol.

Ervs were initially identified as factors required for selective protein sorting in the budding yeast *S. cerevisiae* (reviewed in [1, 64]). The Erv family is defined functionally, and only some of the members are tetraspanning, while others are single spanners [20]. Ervs are relatively small (<450 amino acids), and localize to the ER under steady state, but continuously cycle between the ER and the Golgi [20]. Herein, we discuss Erv29(SFT-4; SURF4) as a prototypical cargo sorter required to sort the yeast

carboxypeptidase for transport from the ER to the Golgi [65, 66]. The human ortholog of Erv29p, SURF4, also regulates ER export of cargo proteins, as RNAi depletion of SURF4 from the HepG2 hepatoma-derived cells inhibits the secretion of ApoB lipoprotein particles [67]. In a more general model of secretion, SURF4 also traffics proteins containing an "ER-ESCAPE" motif, which is a tripeptide motif at the amino terminus of a protein that increases its trafficking out of the ER [62]. In a murine model, SURF4 deletion leads to embryonic lethality at E9.5, while heterozygous mice exhibit an accumulation of SURF4 cargo (ApoB) in liver cells [68].

The molecular mechanism of Erv proteins action is well-described. Erv29p binds its cargo proteins through its lumenal large loop and couples them to the COPII coating machinery for exit from the ER [8, 31]. After transporting its cargo to the Golgi, Erv29p recycles to the ER via COPI coated vesicles. Ervs contain two C-terminal sorting motifs, a di-hydrophobic and/or di-acidic sorting motif that couples them to the COPII coating machinery for anterograde transport and a terminal di-lysine (-KKXX) motif that couples them to the COPI coating machinery for recycling back to the ER (reviewed in [2, 8, 30, 32, 34]). Overall, Erv29p is a representative protein sorter that mediates cargo exit out of the ER.

The Erv proteins share a number of key characteristics related to their cargo transport function: (1) they have a tetra-spanning membrane topology with two extracellular/lumenal loops and both N- and C-termini within the cytosol; (2) they are highly conserved and widely expressed; (3) they sort/traffic only selective "client" proteins without regulating overall secretion or endocytosis; (4) they sort/traffic cargoes present in many cell types, as well as cargoes present in only specialized cells; (5) they

bind their cargo through their larger extracellular/luminal domains; (6) they contain sorting motifs within their cytosolic termini for interaction with the cytosolic coating machinery. These shared characteristics are representative of cargo receptors in general and lay the groundwork for discussing other putative cargo sorters, such as JAGN1.

Structure And Functions Of Jagn1

JAGN1 (Jagunal) was first identified in the fruit fly *D. melanogaster* in a screen of lethal mutations on chromosome 3R [69]. Four alleles were described, three causing lethality at the first and second instar stages, and one semi-lethal. Phenotypic analysis showed that JAGN1 plays an important role in enriching the subcortex of the oocyte with ER proteins during stages 9 and 10 of oocyte development. A role for JAGN1 in protein trafficking was suggested by the finding that *jagn* mutations inhibit the transport of Yolkless (a transmembrane yolk receptor) to the lateral membrane of the oocyte. This function of JAGN1 was cargo-specific, as another transmembrane protein (Gurken) was transported normally. [69].

JAGN1 has no sequence similarity (as defined by BLAST searches) to any other protein and has been classified as its own family. JAGN1 amino acid sequences are highly conserved in model organisms, including the mouse (*M. musculus)*, the fruit fly (*D. melanogaster*), the frog (*X. tropicalis, X. laevis*), the zebrafish (*D. rerio*) and the nematode (*C. elegans*) (Figure 2A). The N- and C-termini of JAGN1 are especially highly conserved among species, suggesting that they represent important functional regions, perhaps interfaces for interactions with other proteins.

JAGN1 proteins in most species are relatively small (<200 amino acids) and are predicted to contain four trans-membrane domains, two extracellular/luminal loops and

both, the N- and the C-termini facing the cytoplasm (Figure 3). JAGN1 localizes to the ER under steady state [70], as do Erv cargo sorters [60, 62, 63, 65-67, 71-73]. The C-terminal -KKHK sequence of JAGN1 fits the consensus di-lysine motif present in proteins that cycle between the ER and the Golgi including the Erv cargo receptors [74, 75] (Figure 3). The di-lysine motif is recognized by the COPI recycling machinery, and interactions between JAGN1 and COPI subunits have been detected [70]. The C-terminus of JAGN1 also contains di-hydrophobic and di-acidic motifs, (Figure 3) which may link JAGN1 to the COPII coating machinery involved in anterograde ER to Golgi transport [19]. Thus, JAGN1 contains sorting motifs for incorporation into both, anterograde COPII vesicles and retrograde COPI vesicles, as might be expected for a protein moving cargoes between the ER and the Golgi.

JAGN1 shares key characteristics of tetraspaning Erv proteins: it has the same membrane topology; is highly conserved and widely expressed; may regulate the traffic of only select proteins; and contains sorting motifs within its C-terminus for interacting with coating machineries. These similarities are diagramed in Figure 3, and support our suggestion that JAGN1 traffics “client” proteins at the ER-Golgi interface, possibly in two directions. [18-20, 75-83].

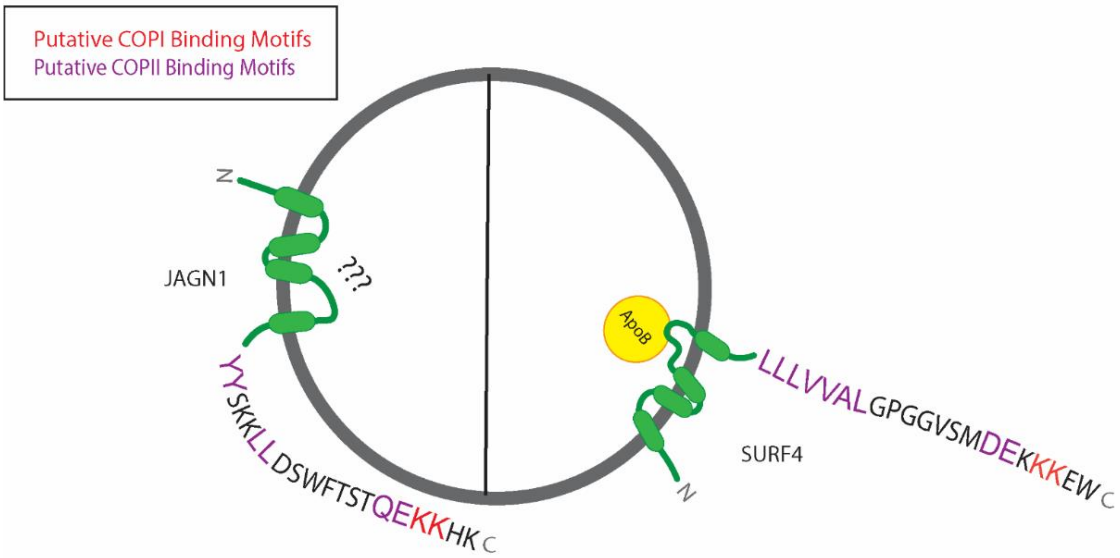

Figure 3: JAGN1 compared to other cargo sorting molecules JAGN1 may serve as a cargo-sorting molecule based on its similar topology as well as shared coatamer-binding motif properties. However, the cargo of JAGN1 remains to be elucidated.

Since its initial description in 2007, Jagn1 has received significant attention more recently, as it has been linked to severe congenital neutropenia (SCN). The first case of JAGN1-associated SCN (SCN6, OMIM # 616022) correlated with a homozygous mutation of the initiator methionine to isoleucine, possibly resulting in a translational null, or an alternative start site [70]. SCN6 patients present with recurrent infections caused by severe neutropenia (a count of less than 1500 neutrophils/µl of blood) due to impaired maturation of neutrophils. Neutrophils from SCN6 patients have decreased number of secretory granules and exhibit an enlarged ER. Dilation of the ER is often caused by defects in the exit of select cargo proteins, as extensively described in mouse chondrocytes and osteoblasts defective in collagen traffic (due to defects in COPII transport machinery) but not impaired in traffic of other proteins (for example [84]). This suggests that JAGN1 function might be required for trafficking of specific proteins out of the ER, as proposed above [70].

Mice with conditional *Jagn1* KO in hematopoietic cells develop normally, including their immune cell populations. However, their neutrophils are defective in pathogen clearance and show deficiencies in chemotaxis and granulopoiesis. Like neutrophils from SCN6 patients, neutrophils from mice silenced for JAGN1 expression show alterations in protein glycosylation, specifically, a reduction in sialylation [85]. Attempts to generate a *Jagn1* KO mouse proved unsuccessful due to lethality at stage E8.5 [85], indicating a requirement for JAGN1 during development. Importantly, lethality occured prior to the differentiation of blood cells, indicating a defect in the development of other tissues. The suggestion that Jagn1 functions in many if not all cells is supported by the extra-neutrophil phenotypes of SCN patients such as neurological delays and skeletal malformations. Moreover, Jagn1 evolutionary conservation throughout animal and plant phyla [86] strongly suggests that it functions in a basic ancient process. To explore this general role of Jagn1 in cell homeostasis, we probed the mechanism of Jagn1 action in both, an organism zebrafish and mammalian cells in culture.

Gaps in knowledge and objectives of the dissertation

The work presented herein is in effort to elucidate the functions of two very different secretory pathway regulators: the transcription factor CREB3L1 implicated in upregulating the capacity of the secretory pathway in response to secretory demand, and the putative cargo sorter JAGN1 proposed to control the trafficking of specific cargo proteins from the ER to the Golgi.

CREB3L1

CREB3L1 functions in bone development and repair have been characterized only in a murine model, with its role in fracture healing restricted only to the regulation of *COL1A1* expression. Mammalian models are suboptimal for studying bone repair, as mammals have extremely limited capacity to regenerate bone. In contrast, teleost fish such as the zebrafish readily regrow bony tissues such as fins after amputation, and represent an optimal system in which to probe the role of Creb3l1 in bone repair. My studies explored an under-studied niche in bone physiology and pathology. The results obtained provide novel insight into the role of Creb3l1 in the regulation of zebrafish development, as well as the requirement for Creb3l1 in a complex process of bone regeneration, including the patterning of bony tissues. My results have direct relevance to the increasingly important research area of fracture healing, as fracture prevalence has increased over the last 30 years [56].

JAGN1

The molecular mechanisms of JAGN1 action are unknown, and we posit that the similarity in membrane topology of JAGN1 to a well-characterized family of cargo sorting/transporting proteins, the Ervs, provides clues to the role of JAGN1 in organismal and cellular homeostasis. My studies explored the function of two Jagn1 orthologs in zebrafish development, as well as uncovered Jagn1 mode of action using mouse embryonic fibroblasts (MEFs) that have been modified through CRSPR/Cas9 to delete Jagn1. My results uncovered a previously unknown function of jagn1 in zebrafish brain development, and showcased the importance of only one of the Jagn1 orthologs in zebrafish survival. Moreover, using Jagn1 KO MEFs in culture, I uncovered defects in

cellular spreading, which correlated with decreased engagement of integrins and alterations in actin dynamics. My work affords the first ever insight into Jagn1 role in integrin distribution, and provides a model for how mutations in Jagn1 may cause SCN.

REFERENCES

1. Barlowe, C.K. and E.A. Miller, *Secretory protein biogenesis and traffic in the early secretory pathway.* Genetics, 2013. **193**(2): p. 383-410.
2. Feizi, A., et al., *Human protein secretory pathway genes are expressed in a tissue-specific pattern to match processing demands of the secretome.* npj Systems Biology and Applications, 2017. **3**(1): p. 22.
3. Shikano, S. and K.J. Colley, *Secretory Pathway*, in *Encyclopedia of Biological Chemistry (Second Edition)*, W.J. Lennarz and M.D. Lane, Editors. 2013, Academic Press: Waltham. p. 203-209.
4. Hartl, F.U. and M. Hayer-Hartl, *Molecular Chaperones in the Cytosol: from Nascent Chain to Folded Protein.* Science, 2002. **295**(5561): p. 1852-1858.
5. Reily, C., et al., *Glycosylation in health and disease.* Nature Reviews Nephrology, 2019. **15**(6): p. 346-366.
6. Almanza, A., et al., *Endoplasmic reticulum stress signalling – from basic mechanisms to clinical applications.* The FEBS Journal, 2019. **286**(2): p. 241-278.
7. Fribley, A., K. Zhang, and R.J. Kaufman, *Regulation of apoptosis by the unfolded protein response.* Methods Mol Biol, 2009. **559**: p. 191-204.
8. Lin, W.J. and S.R. Salton, *The regulated secretory pathway and human disease: insights from gene variants and single nucleotide polymorphisms.* Front Endocrinol (Lausanne), 2013. **4**: p. 96.
9. Lin, R.C. and R.H. Scheller, *Mechanisms of Synaptic Vesicle Exocytosis.* Annual Review of Cell and Developmental Biology, 2000. **16**(1): p. 19-49.
10. Donaldson, J.G., *Endocytosis*, in *Encyclopedia of Biological Chemistry (Second Edition)*, W.J. Lennarz and M.D. Lane, Editors. 2013, Academic Press: Waltham. p. 197-199.
11. Goldenring, J.R., *Recycling endosomes.* Curr Opin Cell Biol, 2015. **35**: p. 117-22.
12. Wang, S., et al., *GBF1 (Gartenzwerg)-dependent secretion is required for Drosophila tubulogenesis.* Journal of Cell Science, 2012. **125**(2): p. 461-472.
13. Sztul, E., et al., *ARF GTPases and their GEFs and GAPs: concepts and challenges.* Mol Biol Cell, 2019. **30**(11): p. 1249-1271.
14. Denecke, J., et al., *Secretory pathway research: the more experimental systems the better.* Plant Cell, 2012. **24**(4): p. 1316-26.
15. Sarmah, S., et al., *Sec24D-dependent transport of extracellular matrix proteins is required for zebrafish skeletal morphogenesis.* PLoS One, 2010. **5**(4): p. e10367.
16. Sheshachalam, A., et al., *Granule Protein Processing and Regulated Secretion in Neutrophils.* Frontiers in Immunology, 2014. **5**.
17. Wilson, D.G., et al., *Global defects in collagen secretion in a Mia3/TANGO1 knockout mouse.* J Cell Biol. **193**(5): p. 935-51.

18. Barlowe, C. and A. Helenius, *Cargo Capture and Bulk Flow in the Early Secretory Pathway.* Annual review of cell and developmental biology, 2016. **32**: p. 197-222.

19. Sato, K. and A. Nakano, *Mechanisms of COPII vesicle formation and protein sorting.* FEBS Letters, 2007. **581**(11): p. 2076-2082.

20. Dancourt, J. and C. Barlowe, *Protein sorting receptors in the early secretory pathway.* Annual review of biochemistry, 2010. **79**: p. 777-802.

21. Fox, R.M. and D.J. Andrew, *Transcriptional regulation of secretory capacity by bZip transcription factors.* Front Biol (Beijing), 2015. **10**(1): p. 28-51.

22. Fox, R.M., C.D. Hanlon, and D.J. Andrew, *The CrebA/Creb3-like transcription factors are major and direct regulators of secretory capacity.* J Cell Biol, 2010. **191**(3): p. 479-92.

23. García, I.A., et al., *CREB3L1-mediated functional and structural adaptation of the secretory pathway in hormone-stimulated thyroid cells.* Journal of cell science, 2017. **130**(24): p. 4155-4167.

24. Asada, R., et al., *The signalling from endoplasmic reticulum-resident bZIP transcription factors involved in diverse cellular physiology.* J Biochem, 2011. **149**(5): p. 507-18.

25. Paxman, R., et al., *Pharmacologic ATF6 activating compounds are metabolically activated to selectively modify endoplasmic reticulum proteins.* Elife, 2018. **7**.

26. Tanimura, A., et al., *Mitochondrial Activity and Unfolded Protein Response are Required for Neutrophil Differentiation.* Cellular Physiology and Biochemistry, 2018. **47**(5): p. 1936-1950.

27. Sampieri, L., P. Di Giusto, and C. Alvarez, *CREB3 Transcription Factors: ER-Golgi Stress Transducers as Hubs for Cellular Homeostasis.* Frontiers in Cell and Developmental Biology, 2019. **7**(123).

28. Honma, Y., et al., *Identification of a novel gene, OASIS, which encodes for a putative CREB/ATF family transcription factor in the long-term cultured astrocytes and gliotic tissue.* Brain Res Mol Brain Res, 1999. **69**(1): p. 93-103.

29. Nikaido, T., et al., *Expression of the novel transcription factor OASIS, which belongs to the CREB/ATF family, in mouse embryo with special reference to bone development.* Histochemistry and Cell Biology, 2001. **116**(2): p. 141-148.

30. Omori, Y., et al., *OASIS is a transcriptional activator of CREB/ATF family with a transmembrane domain.* Biochem Biophys Res Commun, 2002. **293**(1): p. 470-7.

31. Kondo, S., et al., *OASIS, a CREB/ATF-family member, modulates UPR signalling in astrocytes.* Nat Cell Biol, 2005. **7**(2): p. 186-94.

32. Funamoto, T., et al., *Roles of the endoplasmic reticulum stress transducer OASIS in fracture healing.* Bone, 2011. **49**(4): p. 724-32.

33. Iseki, K., et al., *Gliosis-specific transcription factor OASIS coincides with proteoglycan core protein genes in the glial scar and inhibits neurite outgrowth.* Biomed Res, 2012. **33**(6): p. 345-53.

34. García, I.A., et al., *CREB3L1-mediated functional and structural adaptation of the secretory pathway in hormone-stimulated thyroid cells.* J Cell Sci, 2017. **130**(24): p. 4155-4167.

35. Di Giusto, P., et al., *Transcription Factor CREB3L1 Regulates the Expression of the Sodium/Iodide Symporter (NIS) in Rat Thyroid Follicular Cells.* Cells, 2022. **11**(8).

36. Fox, R.M., C.D. Hanlon, and D.J. Andrew, *The CrebA/Creb3-like transcription factors are major and direct regulators of secretory capacity.* Journal of Cell Biology, 2010. **191**(3): p. 479-492.

37. Melville, D.B., et al., *The feelgood mutation in zebrafish dysregulates COPII-dependent secretion of select extracellular matrix proteins in skeletal morphogenesis.* Disease Models & Mechanisms, 2011. **4**(6): p. 763-776.

38. Saito, A., et al., *Chondrocyte proliferation regulated by secreted luminal domain of ER stress transducer BBF2H7/CREB3L2.* Mol Cell, 2014. **53**(1): p. 127-39.

39. McCurdy, E.P., et al., *Promotion of Axon Growth by the Secreted End of a Transcription Factor.* Cell Rep, 2019. **29**(2): p. 363-377.e5.

40. Chung, K.M., et al., *A systemic cell stress signal confers neuronal resilience toward oxidative stress in a Hedgehog-dependent manner.* Cell Rep, 2022. **41**(3): p. 111488.

41. Salhotra, A., et al., *Mechanisms of bone development and repair.* Nature Reviews Molecular Cell Biology, 2020. **21**(11): p. 696-711.

42. Langhans, M.T., P.G. Alexander, and R.S. Tuan, *Chapter 28 - Skeletal Development*, in *Principles of Developmental Genetics (Second Edition)*, S.A. Moody, Editor. 2015, Academic Press: Oxford. p. 505-530.

43. Pfeiffenberger, M., et al., *Fracture Healing Research—Shift towards In Vitro Modeling?* Biomedicines, 2021. **9**(7): p. 748.

44. Nikaido, T., et al., *Expression of the novel transcription factor OASIS, which belongs to the CREB/ATF family, in mouse embryo with special reference to bone development.* Histochem Cell Biol, 2001. **116**(2): p. 141-8.

45. Keller, R.B., et al., *Monoallelic and biallelic CREB3L1 variant causes mild and severe osteogenesis imperfecta, respectively.* Genetics in medicine : official journal of the American College of Medical Genetics, 2018. **20**(4): p. 411-419.

46. Okuda, H., et al., *OASIS regulates chondroitin 6-O-sulfotransferase 1 gene transcription in the injured adult mouse cerebral cortex.* Journal of Neurochemistry, 2014. **130**(5): p. 612-625.

47. Vellanki, R.N., L. Zhang, and A. Volchuk, *OASIS/CREB3L1 is induced by endoplasmic reticulum stress in human glioma cell lines and contributes to the*

unfolded protein response, extracellular matrix production and cell migration. PLoS One, 2013. **8**(1): p. e54060.

48. Vellanki, R.N., et al., *OASIS/CREB3L1 induces expression of genes involved in extracellular matrix production but not classical endoplasmic reticulum stress response genes in pancreatic beta-cells.* Endocrinology, 2010. **151**(9): p. 4146-57.

49. Murakami, T., et al., *Signalling mediated by the endoplasmic reticulum stress transducer OASIS is involved in bone formation.* Nat Cell Biol, 2009. **11**(10): p. 1205-11.

50. Symoens, S., et al., *Deficiency for the ER-stress transducer OASIS causes severe recessive osteogenesis imperfecta in humans.* Orphanet J Rare Dis, 2013. **8**: p. 154.

51. Lindahl, K., et al., *Homozygosity for CREB3L1 premature stop codon in first case of recessive osteogenesis imperfecta associated with OASIS-deficiency to survive infancy.* Bone, 2018. **114**: p. 268-277.

52. Guillemyn, B., et al., *A homozygous pathogenic missense variant broadens the phenotypic and mutational spectrum of CREB3L1-related osteogenesis imperfecta.* Hum Mol Genet, 2019. **28**(11): p. 1801-1809.

53. Andersson, K., et al., *Mutations in COL1A1/A2 and CREB3L1 are associated with oligodontia in osteogenesis imperfecta.* Orphanet J Rare Dis, 2020. **15**(1): p. 80.

54. Cui, M., et al., *OASIS modulates hypoxia pathway activity to regulate bone angiogenesis.* Sci Rep, 2015. **5**: p. 16455.

55. Cayami, F.K., et al., *The first family with adult osteogenesis imperfecta caused by a novel homozygous mutation in CREB3L1.* Mol Genet Genomic Med, 2019. **7**(8): p. e823.

56. Wu, A.-M., et al., *Global, regional, and national burden of bone fractures in 204 countries and territories, 1990–2019: a systematic analysis from the Global Burden of Disease Study 2019.* The Lancet Healthy Longevity, 2021. **2**(9): p. e580-e592.

57. Sterk, L.M., et al., *The tetraspan molecule CD151, a novel constituent of hemidesmosomes, associates with the integrin alpha6beta4 and may regulate the spatial organization of hemidesmosomes.* The Journal of cell biology, 2000. **149**(4): p. 969-982.

58. Sterk, L.M., et al., *Association of the tetraspanin CD151 with the laminin-binding integrins alpha3beta1, alpha6beta1, alpha6beta4 and alpha7beta1 in cells in culture and in vivo.* J Cell Sci, 2002. **115**(Pt 6): p. 1161-73.

59. Latysheva, N., et al., *Syntenin-1 Is a New Component of Tetraspanin-Enriched Microdomains: Mechanisms and Consequences of the Interaction of Syntenin-1 with CD63.* Molecular and Cellular Biology, 2006. **26**(20): p. 7707-7718.

60. Bue, C.A., C.M. Bentivoglio, and C. Barlowe, *Erv26p directs pro-alkaline phosphatase into endoplasmic reticulum-derived coat protein complex II transport vesicles.* Molecular biology of the cell, 2006. **17**(11): p. 4780-4789.

61. Emmer, B.T., et al., *The cargo receptor SURF4 promotes the efficient cellular secretion of PCSK9.* eLife, 2018. **7**: p. e38839.

62. Yin, Y., et al., *Surf4 (Erv29p) binds amino-terminal tripeptide motifs of soluble cargo proteins with different affinities, enabling prioritization of their exit from the endoplasmic reticulum.* PLoS biology, 2018. **16**(8): p. e2005140-e2005140.

63. Belden, W.J. and C. Barlowe, *Erv25p, a component of COPII-coated vesicles, forms a complex with Emp24p that is required for efficient endoplasmic reticulum to Golgi transport.* J Biol Chem, 1996. **271**(43): p. 26939-46.

64. Schekman, R. and L. Orci, *Coat proteins and vesicle budding.* Science, 1996. **271**(5255): p. 1526-33.

65. Foley, D.A., H.J. Sharpe, and S. Otte, *Membrane topology of the endoplasmic reticulum to Golgi transport factor Erv29p.* Mol Membr Biol, 2007. **24**(4): p. 259-68.

66. Belden, W.J. and C. Barlowe, *Role of Erv29p in collecting soluble secretory proteins into ER-derived transport vesicles.* Science (New York, N.Y.), 2001. **294**(5546): p. 1528-1531.

67. Saegusa, K., et al., *SFT-4/Surf4 control ER export of soluble cargo proteins and participate in ER exit site organization.* J Cell Biol, 2018. **217**(6): p. 2073-2085.

68. Emmer, B.T., et al., *Murine Surf4 is essential for early embryonic development.* PLOS ONE, 2020. **15**(1): p. e0227450.

69. Lee, S. and L. Cooley, *Jagunal is required for reorganizing the endoplasmic reticulum during Drosophila oogenesis.* The Journal of Cell Biology, 2007. **176**(7): p. 941-952.

70. Boztug, K., et al., *JAGN1 deficiency causes aberrant myeloid cell homeostasis and congenital neutropenia.* Nature genetics, 2014. **46**(9): p. 1021-1027.

71. Otte, S., et al., *Erv41p and Erv46p: new components of COPII vesicles involved in transport between the ER and Golgi complex.* J Cell Biol, 2001. **152**(3): p. 503-18.

72. Powers, J. and C. Barlowe, *Transport of axl2p depends on erv14p, an ER-vesicle protein related to the Drosophila cornichon gene product.* J Cell Biol, 1998. **142**(5): p. 1209-22.

73. Bue, C.A. and C. Barlowe, *Molecular dissection of Erv26p identifies separable cargo binding and coat protein sorting activities.* The Journal of biological chemistry, 2009. **284**(36): p. 24049-24060.

74. Arakel, E.C. and B. Schwappach, *Formation of COPI-coated vesicles at a glance.* J Cell Sci, 2018. **131**(5).

75. Béthune, J. and F.T. Wieland, *Assembly of COPI and COPII Vesicular Coat Proteins on Membranes.* Annual review of biophysics, 2018. **47**: p. 63-83.

76. D'Arcangelo, J.G., K.R. Stahmer, and E.A Miller, *Vesicle-mediated export from the ER: COPII coat function and regulation.* Biochim Biophys Acta, 2013. **11**(1833): p. 2464-2472.

77. Jackson, L.P., *Structure and mechanism of COPI vesicle biogenesis.* Current Opinion in Cell Biology, 2014(29): p. 67-73.

78. Lee, M.C. and E.A. Miller, *Molecular mechanisms of COPII vesicle formation.* Semin Cell Dev Biol, 2007. **18**(4): p. 424-34.

79. Lord, C., S. Ferro-Novick, and E.A. Miller, *The highly conserved COPII coat complex sorts cargo from the endoplasmic reticulum and targets it to the golgi.* Cold Spring Harbor perspectives in biology, 2013. **5**(2): p. a013367.

80. Szul, T. and E. Sztul, *COPII and COPI traffic at the ER-Golgi interface.* Physiology (Bethesda), 2011. **26**(5): p. 348-364.

81. Levy, S. and T. Shoham, *Protein-Protein Interactions in the Tetraspanin Web.* Physiology, 2005. **20**(4): p. 218-224.

82. Berditchevski, F. and E. Odintsova, *Tetraspanins as regulators of protein trafficking.* Traffic (Copenhagen, Denmark), 2007. **8**(2): p. 89-96.

83. Pols, M.S. and J. Klumperman, *Trafficking and function of the tetraspanin CD63.* Exp Cell Res, 2009. **315**(9): p. 1584-92.

84. Wilson, D.G., et al., *Global defects in collagen secretion in a Mia3/TANGO1 knockout mouse.* The Journal of cell biology, 2011. **193**(5): p. 935-951.

85. Wirnsberger, G., et al., *Jagunal homolog 1 is a critical regulator of neutrophil function in fungal host defense.* Nature genetics, 2014. **46**(9): p. 1028-1033.

86. VanWinkle, P.E., et al., *JAGN1, tetraspanins and Erv proteins: is common topology indicative of common function in cargo sorting?* American Journal of Physiology-Cell Physiology, 2020.

DISRUPTION OF THE *CREB3L1* GENE CAUSES DEFECTS IN CAUDAL FIN REGENERATION AND PATTERNING IN ZEBRAFISH *DANIO RERIO*

by

PEYTON E VANWINKLE, EUNJOO LEE, BRIDGE WYNN, TOMASZ J NAWARA, HOLLY THOMAS, JOHN PARANT, CECILIA ALVAREZ, ROSA SERRA AND ELIZABETH SZTUL

Under review at *Developmental Dynamics*, 2023

Format adapted for dissertation

ABSTRACT

Background: The gene cAMP-Responsive Element Binding protein 3-like-1 (*CREB3L1*) has been implicated in bone development in mice, with *CREB3L1* knock-out (KO) mice exhibiting fragile bones, and in humans with *CREB3L1* mutations associated with osteogenesis imperfecta. However, the mechanism through which Creb3l1 regulates bone development is not fully understood.

Results: To probe the role of Creb3l1 in organismal physiology, we used CRISPR-Cas9 genome editing to generate a Danio rerio (zebrafish) model of Creb3l1 deficiency. In contrast to the phenotypes observed in mammals, the Creb3l1 deficient fish do not display abnormalities in osteogenesis, except for a decrease in bifurcation of the caudal fin. Both, skeletal morphology and overall bone density appear normal in the mutant fish. However, the regeneration of caudal fin post-amputation is significantly affected, with a decrease in overall regenerate and mineralized bone area. Moreover, the mutant fish exhibit a severe patterning defect during regeneration, with a significant decrease in bifurcation complexity of the fin rays and distalization of the bifurcation sites. Analysis of genes implicated in bone development showed aberrant patterning of *shha* and *ptch2* in Creb3l1 deficient fish, linking Creb3l1 with Sonic Hedgehog signaling during fin regeneration.

Conclusions: Our results uncover a novel role for Creb3l1 in regulating tissue growth and patterning during regeneration.

INTRODUCTION

Although bone and skeleton may seem like relatively static tissues that support our bodies with their rigid mineralized structures, their growth and development during embryogenesis require dynamic expression of many interacting proteins. Together, these proteins facilitate a complex program of processes to regulate fate determination, patterning, and bone matrix deposition (reviewed in [1-3]). This program of events can be temporarily reactivated during bone repair and regeneration. Numerous factors involved in different aspects of bone development have been identified and interrogated. One such factor is the cAMP Responsive Element-Binding Protein 3 Like 1 (CREB3L1), also known as Old Astrocyte Specific Induced Substance (OASIS) [4].

Creb3l1 is a member of the ATF/CREB family of transmembrane transcription factors, which have a unique topology: an N-terminal cytoplasmic transcription activating (TA) region containing the DNA-binding basic-leucine zipper motif (bZIP) domain, a single transmembrane (TM) domain that tethers CREB3L1 in the membrane of the endoplasmic reticulum (ER), and a small C-terminal luminal domain (Figure 1A). This topology allows tight regulation of CREB3L1 activity, as it is transcriptionally inert while in the ER, and must be trafficked to the Golgi where it is cleaved by S1P and S2P proteases to release the TA fragment [5,6]. The ER to Golgi transport is initiated in response to ER stress or to a developmental or a physiological stimulus. After cleavage, the released TA fragment is able to enter the nucleus to regulate transcription of target genes, including genes related to bone development and secretory pathway expansion [5-9]. The best-understood function of CREB3L1 is its transcriptional regulation of *COL1A1*, a gene that encodes type 1 collagen, the major structural protein of bones. CREB3L1 regulates

COL1A1 gene expression by binding to an unfolded protein response element (UPRE) upstream of the *COL1A1* gene [10]. In addition, CREB3L1 has been shown to respond to a variety of stimuli in different cell types by increasing the transcription of components that regulate the efficiency of the secretory pathway [9-14]. This upregulation of secretory efficacy is especially important in the secretion of the bulky, rigid collagen cargo that makes up bones [6,8,10,15-17]. Thus, Creb3l1 involvement in both, collagen production and secretion makes CREB3L1 an essential factor in bone development [7,10,17-20].

The critical importance of CREB3L1 in bone formation is underscored by human patients with *CREB3L1* mutations that lead to severe osteogenesis imperfecta [12,18,21]. Such patients exhibit diminished expression of *COL1A1*, as well as reduced expression of components of the secretory pathway, including proteins involved in anterograde vesicle transport [20]. The critical role of CREB3L1 in bone development is also evident in *Creb3l1* KO mice, which are severely osteopenic [10]. These mice exhibit lower bone mineral density, spontaneous ankle fractures, and a lower rate of bone formation/bone surface. Importantly, *Creb3l1* is not expressed in osteoclasts[10], indicating that these defects are a result of poor bone deposition by osteoblasts, and not enhanced bone absorption by osteoclasts. In support, *Creb3l1*$^{-/-}$ osteoblasts have a lower expression of *Col1a1* and overall poorer mineralization capability [10].

In addition to its essential role in bone formation during development, Creb3l1 is required for bone regeneration. In a mouse femur fracture model, *Creb3l1* KO mice show defects in fracture healing, most likely due to reduced synthesis of collagen caused by a deficit in *Col1a1* transcription [11,17,22]. However, the mammalian model of bone regeneration has severe limitations, as mammalian bone has limited regenerative

capability. In contrast, *Danio rerio* zebrafish exhibit high capacity for bone regeneration, and this model has been widely used to discover and clarify key pathways involved in bone development and regeneration. A major benefit of the zebrafish is that they are able to fully regenerate numerous tissues, including complex structures containing bony tissue such as the caudal fin [23-30]. Bone regeneration is often studied after a partial amputation of the caudal fin, which within 21 days regenerates a tail of exact pre-amputation size and with pre-amputation patterning and tissue organization [24,31-33]. Further, the thin and translucent tail allows for straightforward visualization of the behavior of distinct cell types during successive stages of regeneration using cell type-specific fluorescent-labeled transgenic fish models or staining of fixed or live tissue [23,29,34,35].

Caudal fin regenerative outgrowth starts with the formation of a blastema, a mass of undifferentiated, proliferative cells, over each regenerating fin ray. The progenitor cells in the blastema differentiate to reform all the distinct tissues within the fin. Multiple pathways participate in regeneration, with FGF signaling required for blastema formation, Wnt signaling facilitating proliferation of progenitor cells, and Sonic hedgehog (Shh) signaling playing a major role in controlling differentiation into bone, as well as pattern establishment required for ray bifurcation [26,36-40]. One of the key events required to produce or reconstitute the normal architecture of the tail during development and regeneration is the establishment of the proximo-distal axis. The restoration of the axis is necessary to inform the characteristic bifurcation fin patterns that form when a single ray proximal to the amputation plane splits into two smaller rays [26,35,39,41,42]. The position of the bifurcation point is tightly regulated, and bifurcation is initiated within each ray at distinct lengths from the amputation plane, depending on the position of the

ray within the tail. The proximo-distal placement of the bifurcations in each ray (except the most lateral ones) is critical for overall fin architecture. Defects in the reformation of the proximodistal axis are easily scored by evaluating the bifurcation parameters of the regenerating fin [26,35,39,41,42]. Thus, the zebrafish caudal fin regeneration model allows a minimally invasive analysis of the role of Creb3l1 in caudal fin regeneration and patterning of the regenerating tissues, and may provide insights to its intersections with signaling pathways controlling regeneration and the establishment of the proximo-distal axis.

To probe the role of Creb3l1 in bone development and regeneration, we generated a zebrafish mutant expressing Creb3l1 lacking the majority of its coding sequence. The missing region of Creb3l1 includes the DNA-binding bZIP domain, rendering the mutant transcriptionally and functionally null (*creb3l1*$^{\Delta bZIP/\Delta bZIP}$). Analyses of the mutant fish indicate that their skeletal development is largely normal, in agreement with the phenotype of the *Creb3l1* KO mice[10]. However, while mammals lacking CREB3L1 or expressing mutant CREB3L1 exhibit low bone density and predisposition to bone fracture, *creb3l1*$^{\Delta bZIP/\Delta bZIP}$ zebrafish show normal bone density and lack spontaneous fractures. Yet, *creb3l1*$^{\Delta bZIP/\Delta bZIP}$ mutant fish exhibit decreased bifurcation complexity in the caudal fin, suggesting a developmental patterning defect. Moreover, we document that Creb3l1 activity is required for caudal fin regeneration, with *creb3l1*$^{\Delta bZIP/\Delta bZIP}$ zebrafish displaying a significantly decreased overall re-growth of the fin. This phenotype is linked to perturbations in cell proliferation due to the disruption in the cell cycle in *creb3l1*$^{\Delta bZIP/\Delta bZIP}$ regenerating caudal fins. Moreover, the *creb3l1*$^{\Delta bZIP/\Delta bZIP}$ zebrafish show strong defects in the patterning of the regenerated tissue. Specifically,

creb3l1$^{\Delta bZIP/\Delta bZIP}$ animals have significantly reduced number of bifurcations, as well as an increased distalization of the bifurcation point. Mechanistically, this may be caused by a perturbation in the Sonic Hedgehog signaling pathway, which we show by *in situ* hybridization to be spatially affected in the *creb3l1*$^{\Delta bZIP/\Delta bZIP}$ regenerating fin. Together, our results demonstrate a critical requirement for Creb3l1 function during regenerative bone growth, and identify Creb3l1 as a novel factor regulating the proximo-distal patterning of the caudal fin during regeneration.

RESULTS

1. Creb3l1 is a transmembrane transcription factor highly conserved between humans and zebrafish

Human and zebrafish Creb3l1 exhibit 58.9% overall amino acid sequence identity (Figure 1B). The highest sequence conservation is observed in the DNA-binding bZIP domain, with ~98% identity (indicated in red rectangle). The TM domain (indicated with an overlying orange line) is similarly conserved, with ~90% identity between the human and the fish sequences. The cleavage sites for the S1P and S2P proteases (indicated with green rectangles) are also highly conserved and are present within conserved motifs bracketing the cleavage sites. The C-terminal lumenal domain of human Creb3l1 shares only 28% identity with its zebrafish homolog. The high level of conservation within the DNA-binding domain and the TM region suggests a similar mechanism of Creb3l1 transcriptional action within the nucleus, as well as similar regulation of Creb3l1 activity through intramembranous cleavage in humans and in zebrafish.

Beyond the sequence similarity, human *CREB3L1* and zebrafish *creb3l1* also share high genomic synteny in their respective loci, with an overlap of 8 genes within

their respective neighboring megabases (adapted from Ensembl data [43]) (Figure 1C). The genomic synteny suggests that this group of genes, including human *CREB3L1* and zebrafish *creb3l1,* may form a gene cluster that undergoes simultaneous transcriptional regulation [44,45].

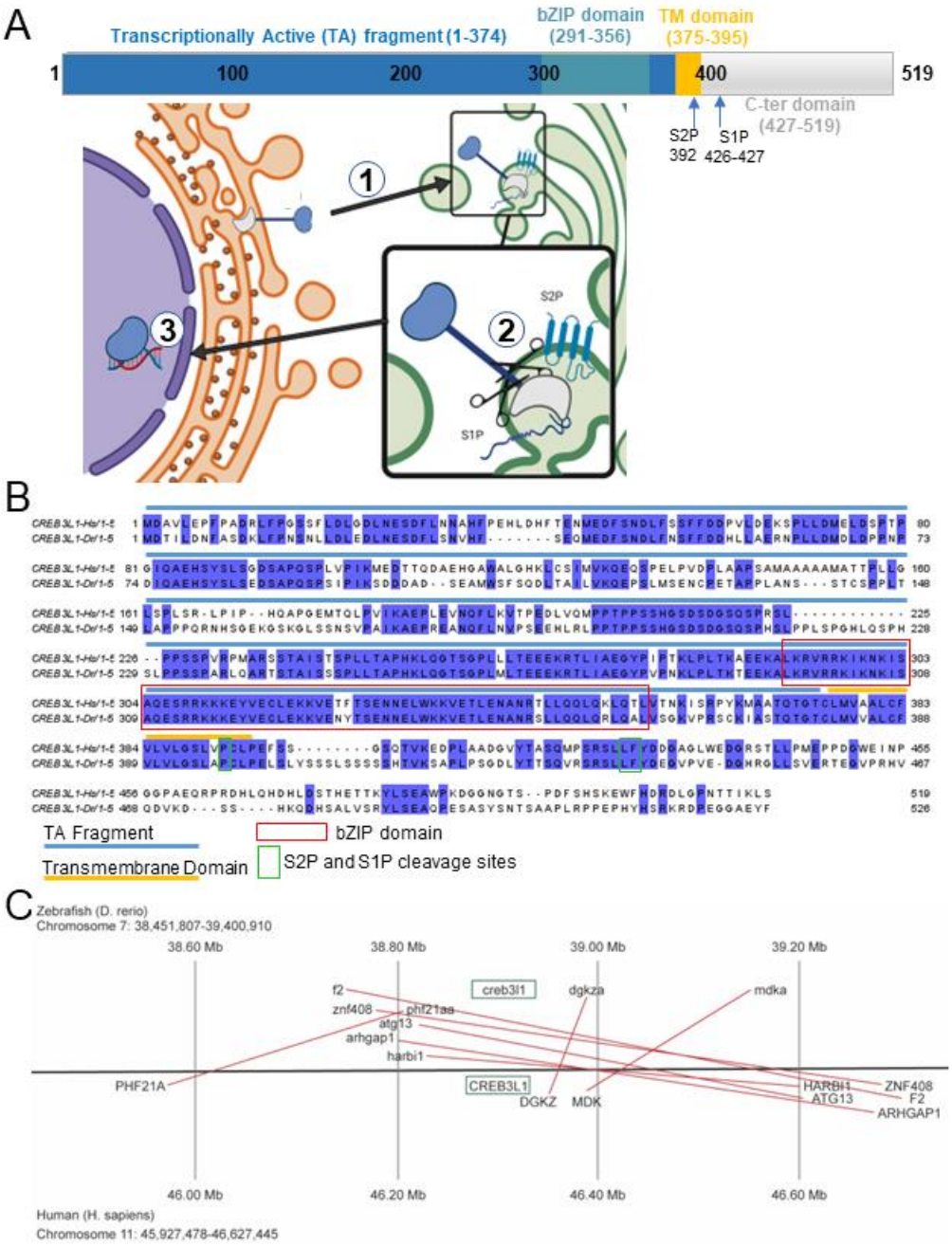

Figure 1: Creb3l1 is a transmembrane transcription factor highly conserved between humans and zebrafish

A) A schematic of Creb3l1 protein showing the N-terminal transcriptionally active (TA) region (amino acids 1-374) containing the DNA-binding bZIP domain (amino acids 291-356), followed by a single transmembrane (TM) domain (amino acids 375-395) and the C-terminal luminal domain (amino acids 427-519).

The sites cleaved by the S1P and S2P proteases are indicated by arrows. Creb3l1 resides in the endoplasmic reticulum and in response to stress is transported to the Golgi (step 1), where it is cleaved by S1P and S2P proteases (step 2). The released TA fragment then enters the nucleus to regulate transcription of target genes (step 3).

B) Alignment of human and zebrafish Creb3l1. The TA domain is indicated by a blue line and the TM domain is marked by an orange line. The DNA-binding bZIP domain is outlined in red. The sites cleaved by S1P and S2P are outlined in green. The highest level of amino acid conservation is in bZIP, the TM and regions of the TA immediately upstream from the bZIP. The S1P and S2P cleavage sites also reside within conserved domains. Identical residues are in blue.

C) The genetic loci of human and zebrafish Creb3l1 demonstrate high synteny, sharing 8 genes within the same ~1 megabase span in their respective genomes.

2. Creb3l1 mutant fish show overall normal skeletal development

The Creb3l1 loss-of-function allele (*creb3l1*$^{\Delta bZIP/\Delta bZIP}$) was generated by CRISPR/Cas9 – mediated genome editing using a guide targeting exon 2 (Figure 2A). The *creb3l1*$^{\Delta bZIP/\Delta bZIP}$ fish have a guide-induced insertion of 7 base pairs (boxed in green in Figure 2A) at 189 bp of the coding mRNA (green arrow). This leads to a mutation at amino acid 65 (change of D to P), followed by a frameshift resulting in the addition of 10 amino acids (in gray) not present in wild-type Creb3l1 before the TGA stop codon (in red).

To test for missense mediated decay of the mutant mRNA, we performed RT-PCR of *creb3l1* mRNA in wild-type and mutant larvae (primers are listed in Table 1). As shown in Figure 2B, transcription of *creb3l1* was upregulated ~3-fold in the *creb3l1*$^{\Delta bZIP/\Delta bZIP}$ fish, suggesting that the mutant mRNA is not degraded.

The mutant mRNA encodes a 75 amino acid peptide that includes only the N-terminal 64 amino acids of Creb3l1. Irrespective of whether this peptide is translated and stable in the *creb3l1*$^{\Delta bZIP/\Delta bZIP}$ fish, it lacks the majority of the *Creb3l1* sequence

including the DNA-binding bZIP domain, rendering it incapable of localizing to the ER and making it inactive as a transcription factor. The upregulation of *creb3l1* transcription may reflect a possible mechanism to compensate for the lack of functional Creb3l1 in the mutant fish.

The offspring of heterozygous *creb3l1*$^{+/\Delta bZIP}$ incrosses were genotyped at 7 days post fertilization (dpf) and show that zebrafish larvae are recovered at relatively normal Mendelian ratios (Figure 2C). This suggests that the lack of functional Creb3l1 is not lethal to larval survival. Moreover, mature fish were obtained from the incrosses (see below), consistent with results from the *Creb3l1* KO mice, which also survive to adulthood [10].

The *creb3l1*$^{\Delta bZIP/\Delta bZIP}$ fish grow to a size analogous to that of wild-type *creb3l1*$^{+/+}$ fish (Figure 2D), and show no obvious skeletal malformations (Figure 2E; larger images of the mCT scans are included in Supplemental Figure 1). Skeletal development appeared normal in both female and male *creb3l1*$^{\Delta bZIP/\Delta bZIP}$ fish, indicating lack of sexual dimorphism in the response to *creb3l1* mutation.

CREB3L1 has been shown to be required for normal bone density in mammals, as *Creb3l1* KO mice have porous fragile bones, a phenotype also observed in human patients with *CREB3L1* mutations [12,18,21,46-48]. In contrast, comparisons of mCT scans of *creb3l1*$^{+/+}$ and *creb3l1*$^{\Delta bZIP/\Delta bZIP}$ fish showed no significant difference in bone density as measured by the amount of hydroxyapatite (HA) in milligrams (mg), the mineral component of zebrafish bone, per cubic centimeter (cm^3) (Figure 2F). Thus, the lack of

Creb3l1 function is not deleterious to the growth of zebrafish, the development of their skeletons, or the density of their bones.

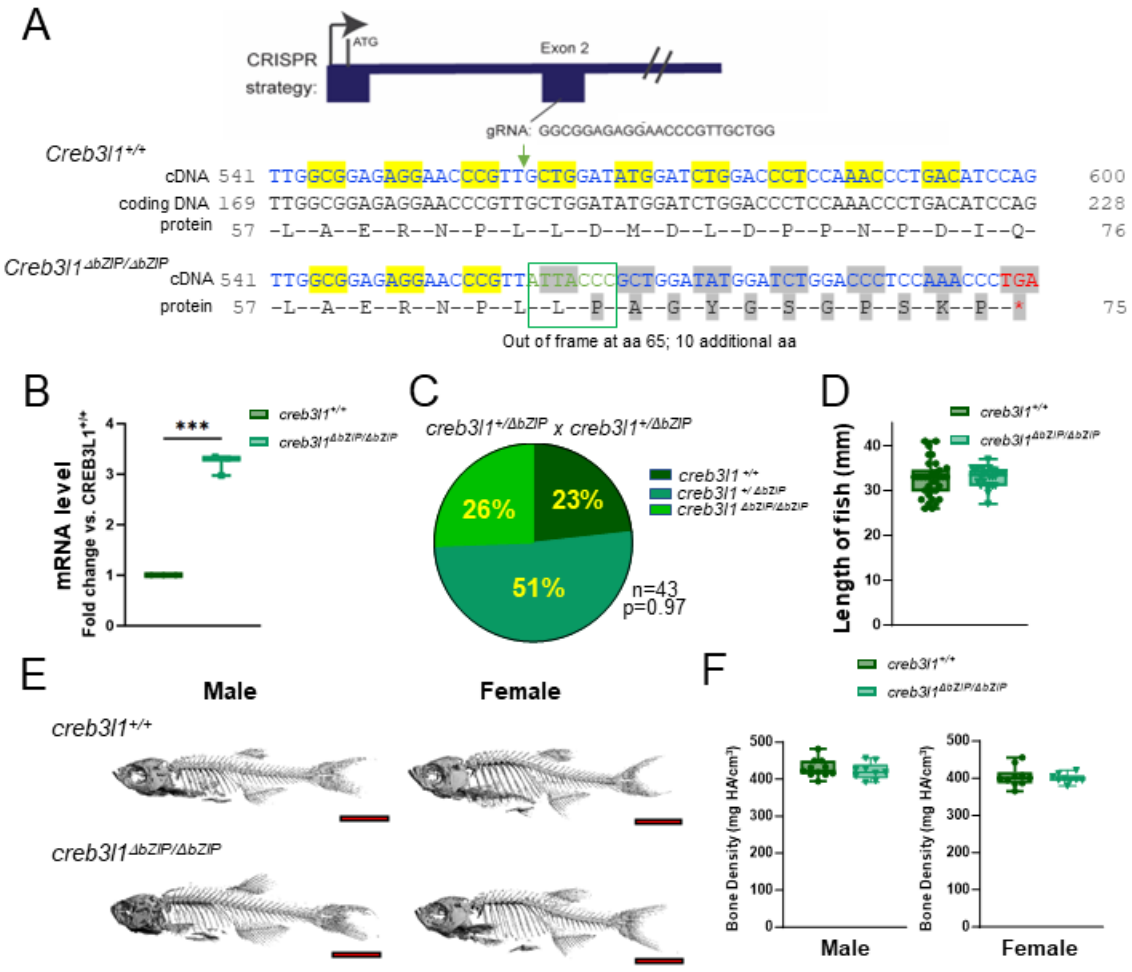

Figure 2: *creb3l1* mutant zebrafish are normal size and exhibit normal overall skeletal morphology and bone density

A) Exon 2 of the zebrafish *creb3l1* gene was targeted to generate *creb3l1*$^{\Delta bZIP/\Delta bZIP}$ fish with a +7 bp insertion (in green) that causes a frameshift mutation at amino acid 65. This mutation generates a Creb3l1 fragment encoding only the first N-terminal 65 amino acids of Creb3l1, followed by 10 additional amino acids not present in wild-type Creb3l1. Yellow highlights wild-type codons while gray highlights mutant codons and amino acids. TGA stop codon is in red. cDNA, consensus coding sequence and protein sequences are shown.

B) *creb3l1* mRNA levels were measured by RT-PCR in 7 dpf *creb3l1*$^{+/+}$ and *creb3l1*$^{\Delta bZIP/\Delta bZIP}$ larvae. Expression of *creb3l1* is significantly elevated in the *creb3l1*$^{\Delta bZIP/\Delta bZIP}$ larvae. n=3-4, ***p<0.001. Each data point represents a pool of ~30 larvae.

C) Larvae from heterozygous *creb3l1*$^{\Delta bZIP/+}$ incrosses were genotyped at 7 dpf and show the expected Mendelian ratios. n and p values are indicated.

D) The length of age-matched 6 mpf *creb3l1*$^{+/+}$ and *creb3l1*$^{\Delta bZIP/\Delta bZIP}$ fish was measured from the snout to the posterior-most point of the tail. There was no significant difference in length between the wild-type and the *creb3l1* mutant fish. n= 27-34. Each data point represents an individual fish.

E) Age-matched 3 mpf *creb3l1*$^{+/+}$ and *creb3l1*$^{\Delta bZIP/\Delta bZIP}$ fish were analyzed by μCT and representative scans of male and female animals are shown. The *creb3l1*$^{\Delta bZIP/\Delta bZIP}$ fish exhibit overall normal skeletal morphology. Scale bar=5mm.

F) Bone density (mgHA/cm^3) of the entire skeleton of male and female *creb3l1*$^{+/+}$ and *creb3l1*$^{\Delta bZIP/\Delta bZIP}$ fish was determined from the μCT scans. n=9-11. Each data point represents an individual fish.

3. Creb3l1 mutant fish show decreased fin ray bifurcations

To provide a baseline for subsequent caudal fin regeneration studies, we performed analyses of intact fins in wild-type and *creb3l1* mutant zebrafish. To visualize the behavior of osteoblasts, we crossed *creb3l1*$^{+/+}$ and *creb3l1*$^{\Delta bZIP/\Delta bZIP}$ fish to a transgenic fish line expressing eGFP under the promoter for the osteoblast-specific Sp7 transcription factor (Tg(Ola.Sp7:EGFP-CAAX)pd51; ZIRC line pd51Tg [28], referred to in this text as *Tg*(*Sp7::eGFP*)). We observed robust expression of *sp7::eGFP* in intact caudal fins of *creb3l1*$^{+/+,Tg(Sp7::eGFP/+)}$ and *creb3l1*$^{\Delta bZIP/\Delta bZIP,Tg(Sp7::eGFP/+)}$ fish that marks osteoblast distribution within individual rays and showcases the characteristic bifurcations of each ray (Figure 3A). Analysis of tail length (measured from the base of the caudal peduncle to the distal tip of the ray (orange lines in Figure 3A) in adult 6 mpf wild-type and *creb3l1* mutant zebrafish shows them to be analogous (Figure 3B). Similarly, the distance from the base of the caudal peduncle to the point of first

bifurcation (blue lines in Figure 3A) of 2nd and 3rd rays in both lobes of each fin is not significantly altered in the *creb3l1*$^{\Delta bZIP/\Delta bZIP}$ zebrafish (Figure 3C).

However, the complexity of bifurcation is altered in *creb3l1* mutant zebrafish tails, which show significantly fewer secondary bifurcations (Figure 3D, secondary bifurcations of each lepidotrichium are marked with arrows). Specifically, while in wild-type zebrafish tails, the 3rd, 4th and 5th rays show secondary bifurcation of both lepidotrichia (Figure 3D, two yellow, sienna and orange arrows, respectively), in the *creb3l1* mutant zebrafish tails, the analogous rays show only a single secondary bifurcation on the lateral lepidotrichium of each ray (one yellow, sienna and orange arrows). Similarly, the 6th and 7th ray in wild-type zebrafish tails show secondary bifurcation of the lateral lepidotrichia (Figure 3D, blue arrows), but in *creb3l1* mutant zebrafish tails, the same rays have no secondary bifurcations. Quantification of this phenotype, as assayed by the number of total bifurcations per fin, shows a significant decrease in the *creb3l1* mutant zebrafish (Figure 3E). This phenotype is the result of a significant decrease in secondary bifurcation number in the *creb3l1* mutant fins (Figure 3F).

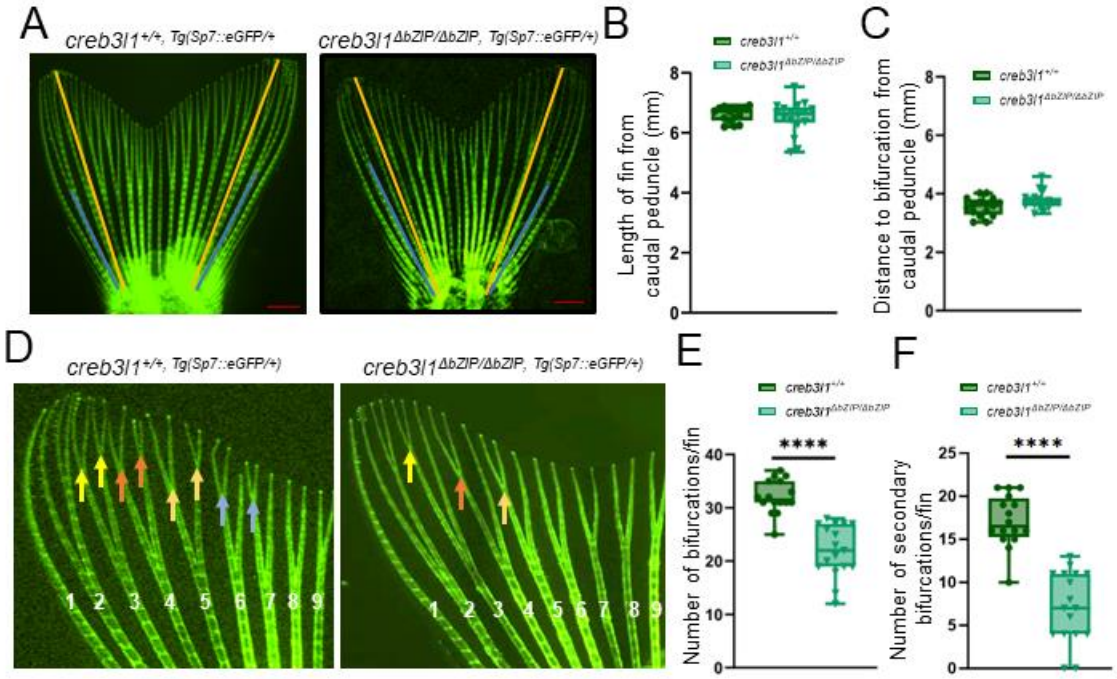

Figure 3: *creb3l1* mutant zebrafish exhibit perturbations in caudal fin patterning

A) Tails of age-matched 6 mpf *creb3l1*$^{+/+}$,Tg(Sp7::eGFP/+) and *creb3l1*$^{\Delta bZIP/\Delta bZIP}$,Tg(Sp7::eGFP/+) fish were imaged by fluorescence and representative images are shown. Orange lines from the caudal peduncle to the tip of 3rd rays mark distance measured as fin length. Blue lines mark the distance of the most proximal bifurcation point from the caudal peduncle of 2nd rays. Scale bar=1mm.

B) Images analogous to those in A were used to measure the length of 2nd and 3rd ray on both sides of the fin, and the average length/fin is shown. Each data point represents an individual fish. No difference in tail length was detected. n=15-17

C) Images analogous to those in A were used to measure the distance between the primary proximal bifurcation and the caudal peduncle of the 2nd and 3rd ray on both sides of the fin. The average distance was calculated and is shown. Each data point represents an individual fish. No difference in the proximo-distal position of the bifurcation point was detected. n=16-17

D) Higher magnification of images analogous to those in A (representative images are shown; the images were "stretched" along the x horizontal axis to more clearly visualize the distinct bifurcations). Secondary bifurcations of the 3rd ray are indicated by yellow arrows, of the 4th ray by sienna arrows, of the 5th ray by orange arrows and of the 6th and 7th ray by blue arrows.

E-F) Images analogous to those in A were used to measure the total number of bifurcations per fin (E) or the number of secondary bifurcations per fin (F). The complexity of bifurcations is lower in the *creb3l1* mutant fins, with fewer secondary bifurcations per fin than in wild-type *creb3l1* fins.

3. Regeneration of caudal fins is compromised in *creb3l1* mutant fish

Although there are no notable changes in skeletal size or bone density during *creb3l1*$^{\Delta bZIP/\Delta bZIP}$ fish development, the observed defect in bifurcation patterning prompted us to test whether changes in the levels of functional Creb3l1 may affect acute bone regeneration. We used the caudal fin amputation model in which ~50% of the tail fin is removed, causing an injury that is repaired in wild-type zebrafish within a few weeks [24]. We first examined the expression of *creb3l1* in wild-type fish at different days post amputation to define the most likely time frame for the possible action of Creb3l1 during regeneration. Expression of *creb3l1* has been shown to be upregulated in the regenerating blastema [42], suggesting a possible role in regeneration. As shown in Figure 4A, *creb3l1* mRNA was weakly expressed at 1 dpa and was more easily detectable in distinct domains at 3 and 5 dpa, with a more diffuse expression at 7 dpa. The signal in the 3 dpa regenerate was in a single "cap"-like structure over as yet unbranched fin rays or was present as two independent domains in rays that had already bifurcated (blue arrowhead). In the 5 and 7 dpa regenerates, the *creb3l1* signal was detected in each sister lepidotrichium of each regenerating ray, but appeared more diffuse. Additionally, at the later time points, *creb3l1* mRNA signal was detected within the inter-ray spaces populated by mesenchymal cells (Figure 4A, white arrow).

Because *creb3l1* expression in the regenerating tail appeared most robust at 3 dpa, we assessed the expression of a Creb3l1 target gene, the zebrafish *col1a1a* (a homolog to mammalian *COL1A1*) by *in situ* hybridization at 3 dpa. In wild-type zebrafish, *col1a1a* was expressed in a cap-like structure over each regenerating ray (Figure 4B, blue arrows),

as well as on the tips of the bony fin rays right below the amputation plane (Figure 4B, white arrows). In contrast, in *creb3l1* mutant zebrafish, *col1a1a* signal appeared fainter over the regenerating rays (Figure 4B, blue arrows), and was almost absent at the amputation plane (Figure 4B, white arrows).

To assess the role of Creb3l1 in caudal fin regeneration, age-matched 6 mpf *creb3l1*$^{+/+,Tg(Sp7::eGFP/+)}$ and *creb3l1*$^{\Delta bZIP/\Delta bZIP,Tg(Sp7::eGFP/+)}$ fish were subjected to 50% caudal fin amputation and regeneration was examined at 3, 7, 9 and 14 dpa by fluorescence (Figure 4C). The length of the regenerated rays at each time point after amputation was estimated from the length of $Sp7^+$ osteoblast-containing structures within the 2nd and 3rd rays on each side of the tail when measured from the amputation plane manually in FIJI [49] (Figure 4D, blue lines). As shown in Figure 4E, *creb3l1*$^{\Delta bZIP/\Delta bZIP,Tg(Sp7::eGFP/+)}$ fish exhibit a significant decrease in ray length of the regenerate at 3, 7, and 9 dpa.

Even more extensive differences between *creb3l1*$^{+/+,Tg(Sp7::eGFP/+)}$ and *creb3l1*$^{\Delta bZIP/\Delta bZIP,Tg(Sp7::eGFP/+)}$ fish were observed when the area containing differentiated osteoblasts within the regenerate was measured. The fluorescent images of the regenerates at each time post amputation were thresholded, and the area of the resulting binary image (Figure 4D) was then measured to define the total $Sp7^+$ area per regenerate. This value was then divided by the average ray width of all rays proximal to the amputation plane (width of two rays is indicated with orange lines in Figure 4D) to obtain

Sp7^{+} area per ray. As shown in Figure 4F, *creb3l1*$^{\Delta bZIP/\Delta bZIP,Tg(Sp7::eGFP/+)}$ fish exhibit a significantly decreased Sp7^{+} osteoblast area at all timepoints after amputation.

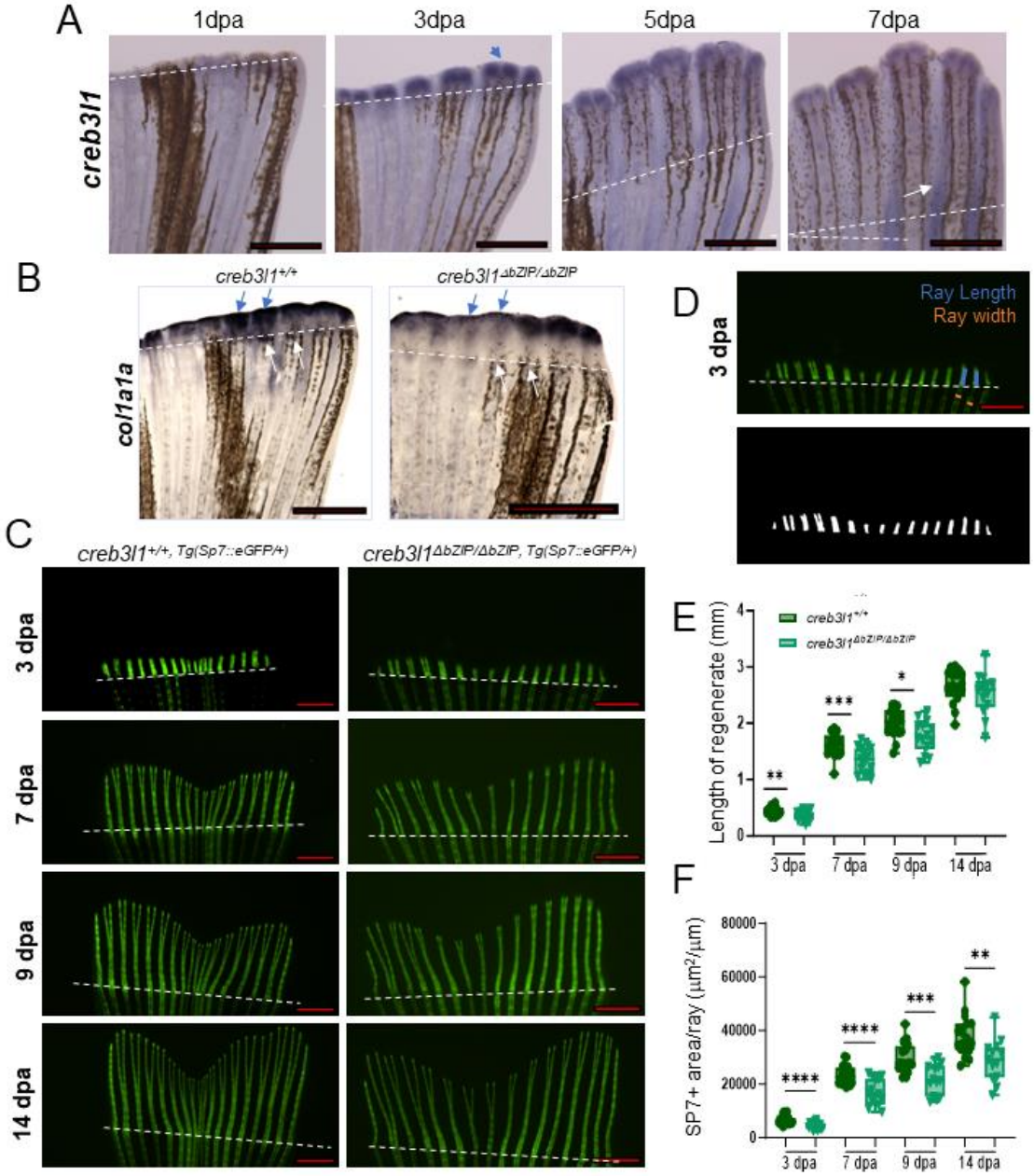

Figure 4: *creb3l1* mutant zebrafish show defects in the regeneration of the caudal fin

A) Approximately 50% of the caudal fin was amputated from 6 mpf wild-type fish, and *creb3l1* expression was monitored by *in situ* hybridization at the indicated dpa. *creb3l1* signal is predominantly detected at the distal tip of each regenerating ray and appears strongest at 3 dpa (blue arrow). Representative images are shown. n=3. Amputation planes are indicated with dashed line. Scale bar=1mm.

B) Approximately 50% of the caudal fin was amputated from 6 mpf *creb3l1*$^{+/+}$ and *creb3l1*$^{\Delta bZIP/\Delta bZIP}$ fish. Regenerates at 3 dpa were analyzed by *in situ* hybridization to assess the expression patterns of *col1a1a*. In wild-type fins, robust *col1a1* signal is detected over each regenerating ray (blue arrows), as well as immediately below the amputation plane (white arrows). In *creb3l1* mutant fins, *col1a1* signal is less apparent over the regenerating rays (blue arrows), and is undetectable at the amputation plane (white arrows). n=3. Scale bar=1mm.

C-F) Approximately 50% of the caudal fin was amputated from age-matched 6 mpf *creb3l1*$^{+/+,Tg(Sp7::eGFP/+)}$ and *creb3l1*$^{\Delta bZIP/\Delta bZIP,Tg(Sp7::eGFP/+)}$ fish, and regeneration was measured by fluorescence imaging at the indicated dpa. Amputation planes are indicated with dashed line. Scale bar=1mm.

C) Representative images at each dpa.

D) To quantify regenerate length, lines from the amputation plane to the tip of the 2nd and 3rd lateral rays were drawn manually on both sides of the regenerate (blue lines) and measured. Average ray width was measured for all rays (representative orange lines). The Sp7^{+}-labeled fluorescent area was determined by thresholding the fluorescence signal in the regenerate (lower panel).

E) Images analogous to those in C were used to measure the lengths of the 2nd and 3rd most lateral rays on both sides of the fin as in D. Each data point represents an individual fish. The *creb3l1*$^{\Delta bZIP/\Delta bZIP,Tg(Sp7::eGFP/+)}$ fish show significantly shorter regenerates at 3, 7 and 9 dpa. n=13-23. *p≤0.05; **p≤0.01; ***p≤0.001.

F) Images analogous to those in C were used to calculate the area occupied by Sp7^{+} labeled osteoblasts, corrected for the average ray width (Sp7^{+} area/ray) as in D. Each data point represents an individual fish. The *creb3l1*$^{\Delta bZIP/\Delta bZIP,Tg(Sp7::eGFP/+)}$ fish show significantly decreased Sp7^{+} area/RAY at all timepoints. n=13-23. **p≤0.01; ***p≤0.001; ****p≤0.0001.

3. Regeneration of caudal fins is compromised in *creb3l1* mutant fish We wanted to assess whether the defects in regeneration observed in 6 mpf fish were age-dependent, as well as determine whether the lack of functional Creb3l1 might affect bone mineralization during regeneration. Thus, we performed 50% tail amputation on 3, 6 and 8 mpf *creb3l1*$^{+/+}$ and *creb3l1*$^{\Delta bZIP/\Delta bZIP}$ fish, and at 9 dpa stained them with the calcein fluorophore. Regenerates were then examined via brightfield imaging to assess the size of the regenerate and by fluorescence to measure the extend of new bone formation (Figure 5A). The regenerate outlines were traced by hand (representative shown by red line in Figure 5A, 3 mpf brightfield panel) and the amputation planes were represented with a

dashed line. The area delineated by the red line and the amputation plane was measured and represents the total regenerated area (REGEN). To correct for any differences in the size of the fins prior to amputation, the REGEN area was normalized to the total stump width (STU) (representative shown by a black line in Figure 5A, 3 mpf brightfield panel). As shown in Figure 5B, the REGEN/STU area of *creb3l1*$^{\Delta bZIP/\Delta bZIP}$ 6 mpf fish is lower than that of wild-type fish, consistent with the data shown above in Figure 4F. Moreover, a significant decrease in the size of the regenerate is also apparent in 3 mpf and 8 mpf *creb3l1*$^{\Delta bZIP/\Delta bZIP}$ fish (Figure 5B).

To assess whether lack of Creb3l1 affects bone mineralization during regeneration, calcein-stained regenerates were imaged, the fluorescent signal was thresholded and the area of the resulting binary image (representative image shown in Figure 5C) was then measured to define the real mineralization area (RMA). To correct for the size of the fins prior to amputation, total RMA was normalized to the average ray width (RAY) within the tail (representative rays are marked by orange lines in Figure 5A, 3 mpf fluorescence panel). As shown in Figure 5D, mineralized area was not significantly different, but was trending towards lower value in 3 mpf *creb3l1*$^{\Delta bZIP/\Delta bZIP}$ fish relative to *creb3l1*$^{+/+}$ fish. Mineralized area was significantly lower in the lepidotrichia of 6 mpf and 8 mpf *creb3l1*$^{\Delta bZIP/\Delta bZIP}$ fish relative to *creb3l1*$^{+/+}$ fish.

Taken together, these results indicate that the lack of functional Creb3l1 causes a decrease in the overall size of the regenerate in 3, 6 and 8 mpf fish, suggesting that this phenotype is not age-dependent. Moreover, *creb3l1*$^{\Delta bZIP/\Delta bZIP}$ fish also exhibit decreased mineralization of the regenerated bone, a phenotype trending in 3 mpf fish but more

evident in 6 and 8 mpf animals, suggesting that the effect on mineralization worsens with age.

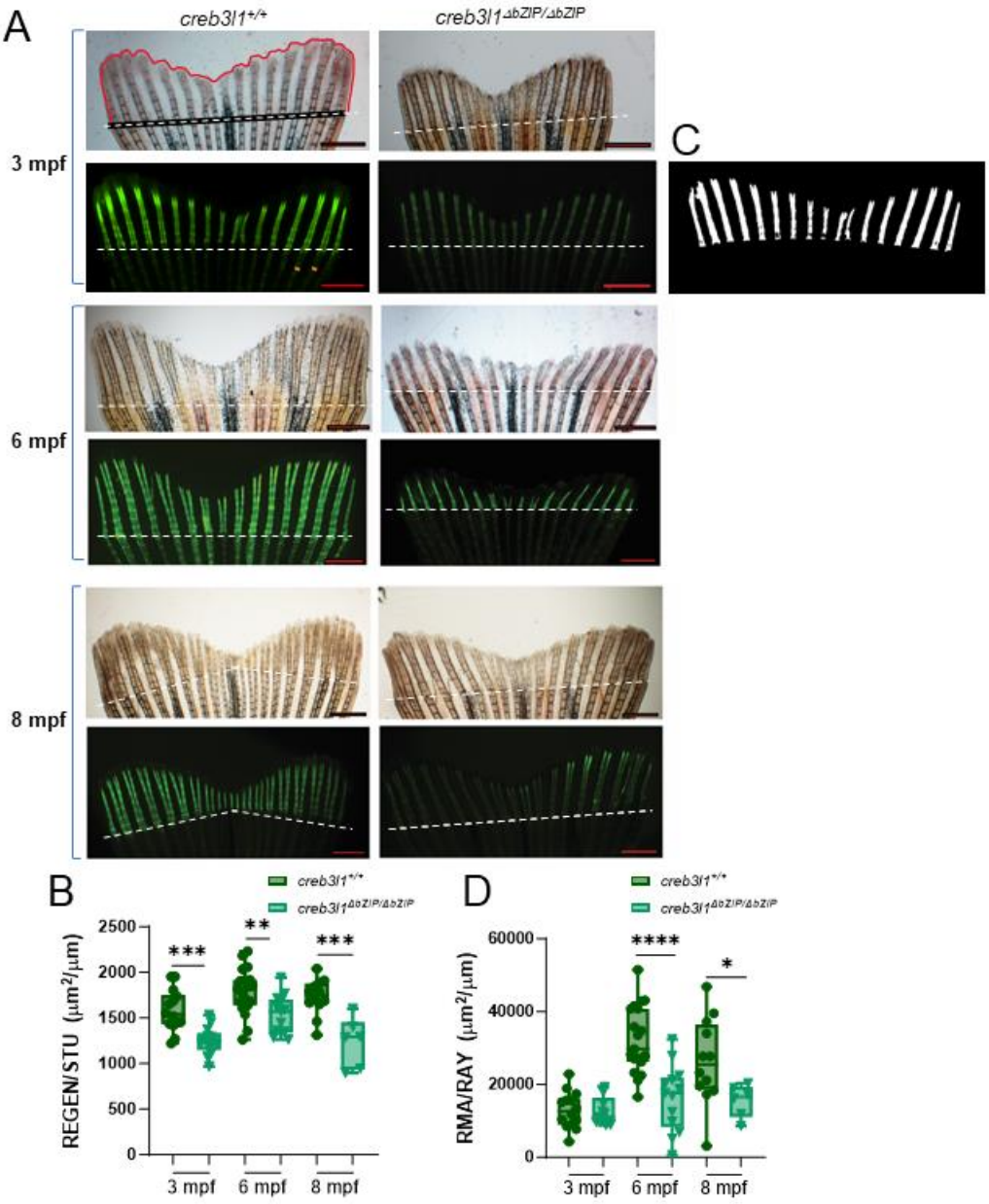

Figure 5: *creb3l1* mutant zebrafish show defects in the ossification of the regenerating caudal fin

A) Approximately 50% of the caudal fin was amputated from 3 mpf, 6 mpf and 8 mpf *creb3l1*$^{+/+}$ and *creb3l1*$^{\Delta bZIP/\Delta bZIP}$ fish. At 9 dpa, the tail regenerates were visualized in brightfield (upper panels) and after staining with calcein fluorophore to visualize mineralized tissue (green, lower panels). Representative images are shown. A representative brightfield image shows manually traced regenerate outline (red line) and the stump width (black line). A representative fluorescent image shows manually traced width of rays (orange lines mark two rays) within the fin. Amputation planes are indicated with dashed line. Scale bar=1mm.

B) Brightfield images analogous to those in A were used to calculate the regenerate area enclosed by the red and black lines (as in A) and corrected for the stump width (REGEN/STU). Each data point represents an individual fish. The *creb3l1* mutant fish show significantly smaller regenerates than the wild-type fish. n=6-19. ** $p \leq 0.01$; *** $p \leq 0.001$.

C) Representative threshold of calcein-stained regenerate used to analyze mineralized area.

D) Fluorescence images analogous to those in A were thresholded and used to calculate the area of mineralized bone corrected for the average width of the rays (RMA/RAY). Each data point represents an individual fish. The *creb3l1* mutant fish show significantly less mineralization than wild-type fish. n=6-19. * $p \leq 0.05$; **** $p \leq 0.0001$.

4. Decreased regeneration in *creb3l1* mutant fish correlates with defects in cell cycle

The observed decrease in the area of the regenerate (visualized by both, the presence of *sp7::eGFP*-containing osteoblasts and brightfield microscopy) prompted us to examine whether increased apoptosis and/or decreased cell proliferation may account for the decrease in size. *creb3l1*$^{+/+,Tg(Sp7::eGFP/+)}$ and age-matched *creb3l1*$^{\Delta bZIP/\Delta bZIP,Tg(Sp7::eGFP/+)}$ fish at 6 mpf were subjected to 50% caudal fin amputation and at 3 dpa processed for immunofluorescence with antibodies against the cleaved form of caspase-3, a marker of apoptotic cells [50], or against phosphohistone-H3 (PH3), a marker of mitotic cells [51]. The anti-PH3 antibody used recognizes the Ser10 phosphosite on PH3. As shown in Figure 6A, and quantified in Figure 6B, no significant difference in the number of cells containing cleaved caspase was seen in the *creb3l1* mutant fish relative to wild-type fish. Similarly, the number of proliferative cells marked by PH3 in the *creb3l1* mutant fish regenerates was not significantly different than in wild-type fish regenerates (Figure 6C and quantified in Figure 6D). This finding seemed surprising since the decrease in the regenerate area in *creb3l1* mutant fish suggested either increased apoptosis (that should be reflected by increased cleaved caspase staining) or decreased proliferation (that should be detected by decreased PH3 staining).

Since we observed neither, we explored whether the PH3 staining might be spurious in that the PH3 stained cells could exhibit cell cycle arrest. Serine 10 (Ser10) of Histone H3 is phosphorylated in association with mitotic chromatin condensation in late G2 and M phase of the cell cycle, but quickly dissipates after late anaphase [51,52]. Thus, robust PH3 staining would be visible in cells that are stalled in G2/M, and in mitotic cells during prophase, metaphase and early anaphase. To determine whether the PH3-positive cells in *creb3l1* mutant regenerates may exhibit cell cycle arrest, we examined the number of $PH3^{+}$ cells in metaphase or anaphase within the regenerates of *creb3l1*$^{+/+,Tg(Sp7::eGFP/+)}$ and *creb3l1*$^{\Delta bZIP/\Delta bZIP,Tg(Sp7::eGFP/+)}$ fish. We defined cells in metaphase as those having PH3-stained DNA condensed in an equatorial position, and cells in anaphase as those that had two clearly separated PH3-stained DNA structures (representative images are shown in Figure 6E). Analysis of analogous images detected a significant decrease in the number of metaphase (Figure 6F) and anaphase (Figure 6G) cells in the *creb3l1*$^{\Delta bZIP/\Delta bZIP,Tg(Sp7::eGFP/+)}$ regenerate. A possible explanation for these results is that the PH3-positive cells in wild-type regenerates undergo mitosis to generate two daughter cells (Figure 6H). In contrast, many of the PH3-positive cells in *creb3l1*$^{\Delta bZIP/\Delta bZIP,Tg(Sp7::eGFP/+)}$ regenerates are at a stage of a cell cycle prior to metaphase (Figure 6H). Thus, it appears that the lack of functional Creb3l1 causes a mitotic arrest, hereby providing a likely explanation for the smaller size of regenerates in the *creb3l1*$^{\Delta bZIP/\Delta bZIP,Tg(Sp7::eGFP/+)}$ fish.

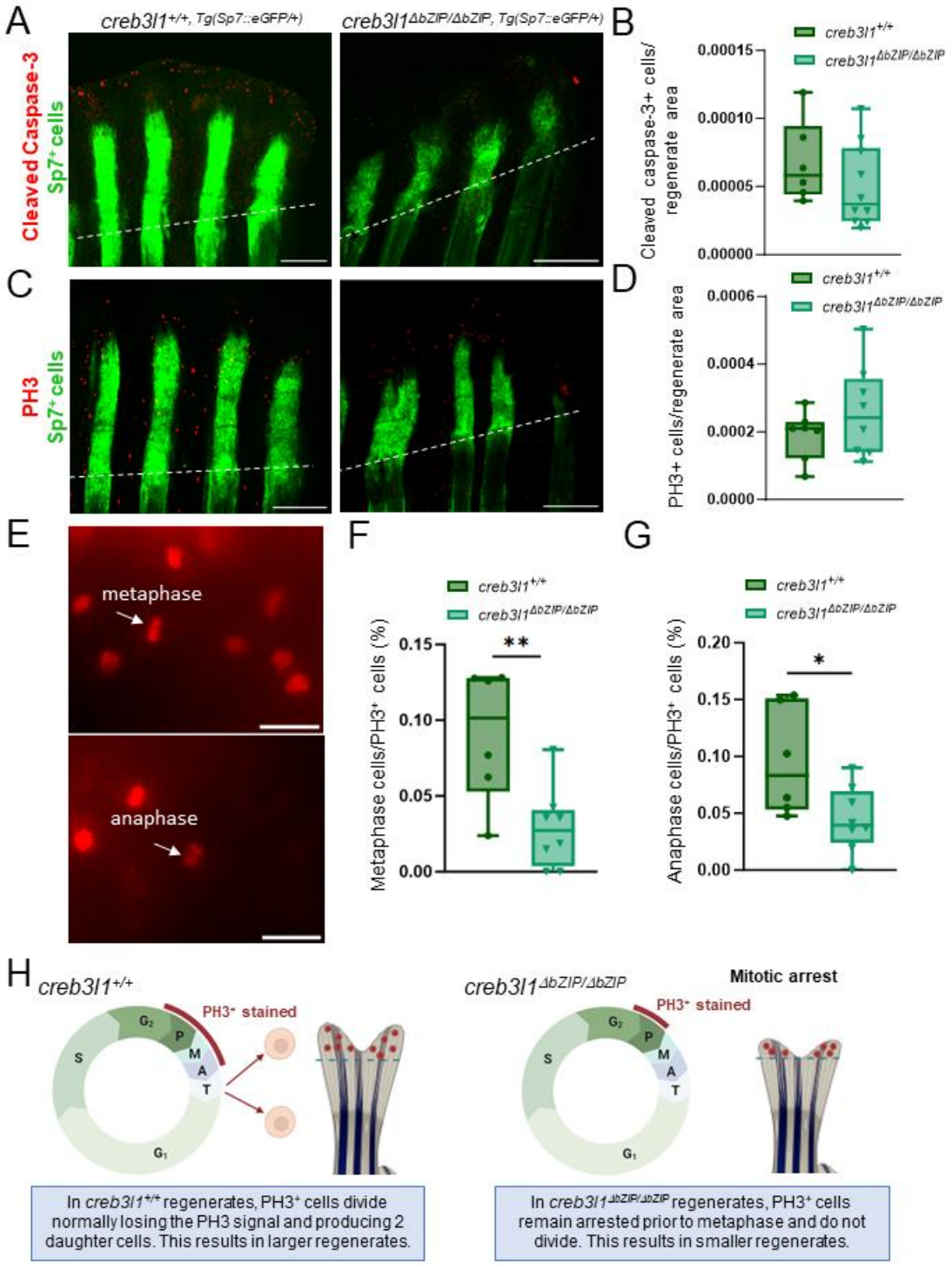

Figure 6: *creb3l1* mutant zebrafish show mitotic defects during regeneration

A-G) Approximately 50% of the caudal fin was amputated from age-matched 6 mpf *creb3l1*$^{+/+,Tg(Sp7::eGFP/+)}$ and *creb3l1*$^{\Delta bZIP/\Delta bZIP,Tg(Sp7::eGFP/+)}$ fish. At 3 dpa, the regenerating tails were processed with antibodies to cleaved caspase-3 or PH3, followed by secondary antibodies conjugated to Alexa-594 (red) fluorophore,

and then imaged by brightfield (not shown) and fluorescence (representative images of regenerates stained for cleaved caspase (A) or PH3 (C)). Amputation planes are indicated with dashed line. Scale bar=1mm.

B) Brightfield and fluorescent images analogous to those in A were used to measure total regenerate area (as in Figure 5A) and to count the number of cells positive for cleaved caspase-3 within the entire regenerate. The results are presented as the number of stained cells per whole regenerate area. Each data point represents an individual fish. n=6-10. No significant difference was seen between the wild-type and *creb3l1* mutant fish.

D) Brightfield and fluorescent images analogous to those in C were used to measure total regenerate area (as in Figure 5A) and to count the number of cells positive for PH3 in the entire regenerate. The results are presented as the number of stained cells per whole regenerate area. Each data point represents an individual fish. n=6-10. No significant difference was seen between the wild-type and *creb3l1* mutant fish.

E) Regenerates stained for PH3 were imaged at higher magnification to identify metaphase and anaphase cells (white arrows). Representative images are shown. Metaphase cells were defined as cells with an elongated, non-circular nuclear signal (the metaphase plate). Anaphase cells were defined as cells with chromosomes appearing to be pulled to opposite poles of the cell. Scale bar= 20μm.

F and G) Fluorescent images of regenerates stained for PH3 were used to count cells in metaphase (F) and anaphase (G) and are presented as a ratio to total $PH3^+$ cells counted within the imaged regenerate. $creb3l1^{\Delta bZIP/\Delta bZIP}$,Tg(Sp7::eGFP/+) fish have significantly fewer cells in metaphase and anaphase. n=6-8. *p≤0.05, **p≤0.01.

H) Diagram illustrating the proposed mechanism to reconcile similar PH3 staining with decreased regenerate size in $creb3l1^{\Delta bZIP/\Delta bZIP}$ fish relative to $creb3l1^{+/+}$ fish. In wild-type fish, $PH3^+$ cells complete mitosis to generate two daughter cells, and rapidly loose the PH3 signal in late anaphase. In contrast, in *creb3l1* mutant fish, $PH3^+$ cells remain arrested at lateG2/early mitosis M, and continue to be stained with PH3, but do not complete cell division. This cell cycle arrest would lead to overall smaller regenerates in *creb3l1* mutant fish.

5. *creb3l1* mutant fish show aberrant patterning of the regenerating caudal fin

As shown above in Figure 3, we detected a decrease in the characteristic bifurcations that form within each bony ray in intact tails of $creb3l1^{\Delta bZIP/\Delta bZIP}$ fish. To determine whether a patterning defect also occurs during fin regeneration, we measured the number of ray bifurcations in regenerates in age-matched $creb3l1^{+/+,Tg(Sp7::eGFP/+)}$ and $creb3l1^{\Delta bZIP/\Delta bZIP,Tg(Sp7::eGFP/+)}$ fish by fluorescence imaging at 7, 9 and 14 dpa. As shown in Figure 7A (representative images at 7 dpa) and quantified in Figure 7C, significantly

fewer bifurcations were present in the *creb3l1*$^{\Delta bZIP/\Delta bZIP,Tg(Sp7::eGFP/+)}$ fish regenerates relative to wild-type fish regenerates at all examined time points after amputation. The decrease was largely due to the absence of secondary bifurcations: while wild-type fish showed secondary bifurcations on a number of rays (white arrows in Figure 7A mark representative secondary bifurcations), the *creb3l1*$^{\Delta bZIP/\Delta bZIP}$ mutant fish had a significant decrease in secondary bifurcations (gray arrows in Figure 7A mark lepidotrichia without secondary bifurcations; quantified in Figure 7D).

We also examined the relative position of the most proximal bifurcation point by measuring the distance between the amputation plane and the first bifurcation within the second and third ray of each regenerate of age-matched *creb3l1*$^{+/+,Tg(Sp7::eGFP/+)}$ and *creb3l1*$^{\Delta bZIP/\Delta bZIP,Tg(Sp7::eGFP/+)}$ fish at 7, 9 and 14 dpa. Lines from the bifurcation point to the amputation plane were drawn manually on 2nd and 3rd ray (white lines in Figure 7A) and their length measured. As shown in Figure 7E, a significant increase in the distance between the amputation site and the first bifurcation was observed in the *creb3l1*$^{\Delta bZIP/\Delta bZIP,Tg(Sp7::eGFP/+)}$ mutant fish at all points post amputation.

We also measured the number of bifurcations and the position of bifurcations in age-matched 6mpf wild-type and *creb3l1*$^{\Delta bZIP/\Delta bZIP}$ mutant fish regenerates stained with calcein 9 dpa. As shown in Figure 7B and quantified in Figure 7F, significantly fewer bifurcations were present in the *creb3l1*$^{\Delta bZIP/\Delta bZIP}$ mutant regenerates relative to wild-type regenerates. The decrease was predominantly in secondary bifurcations, with wild-type fish showing secondary bifurcations on a number of rays (white arrows in Figure 7B), while the *creb3l1*$^{\Delta bZIP/\Delta bZIP}$ mutant fish had no secondary bifurcations (gray arrows in Figure 7B). Moreover, the position of the most proximal bifurcation point relative to the

amputation point (marked by white lines in Figure 7B) was increased in the *creb3l1*$^{\Delta bZIP/\Delta bZIP}$ mutant regenerates relative to wild-type regenerates (Figure 7G). Thus, using the *sp7::eGFP* to visualize osteoblasts, or calcein staining to visualize newly formed mineralized tissue, we observed a significant decrease in number of bifurcations, as well as the distalization of the proximal branching point in the *creb3l1* mutant fish.

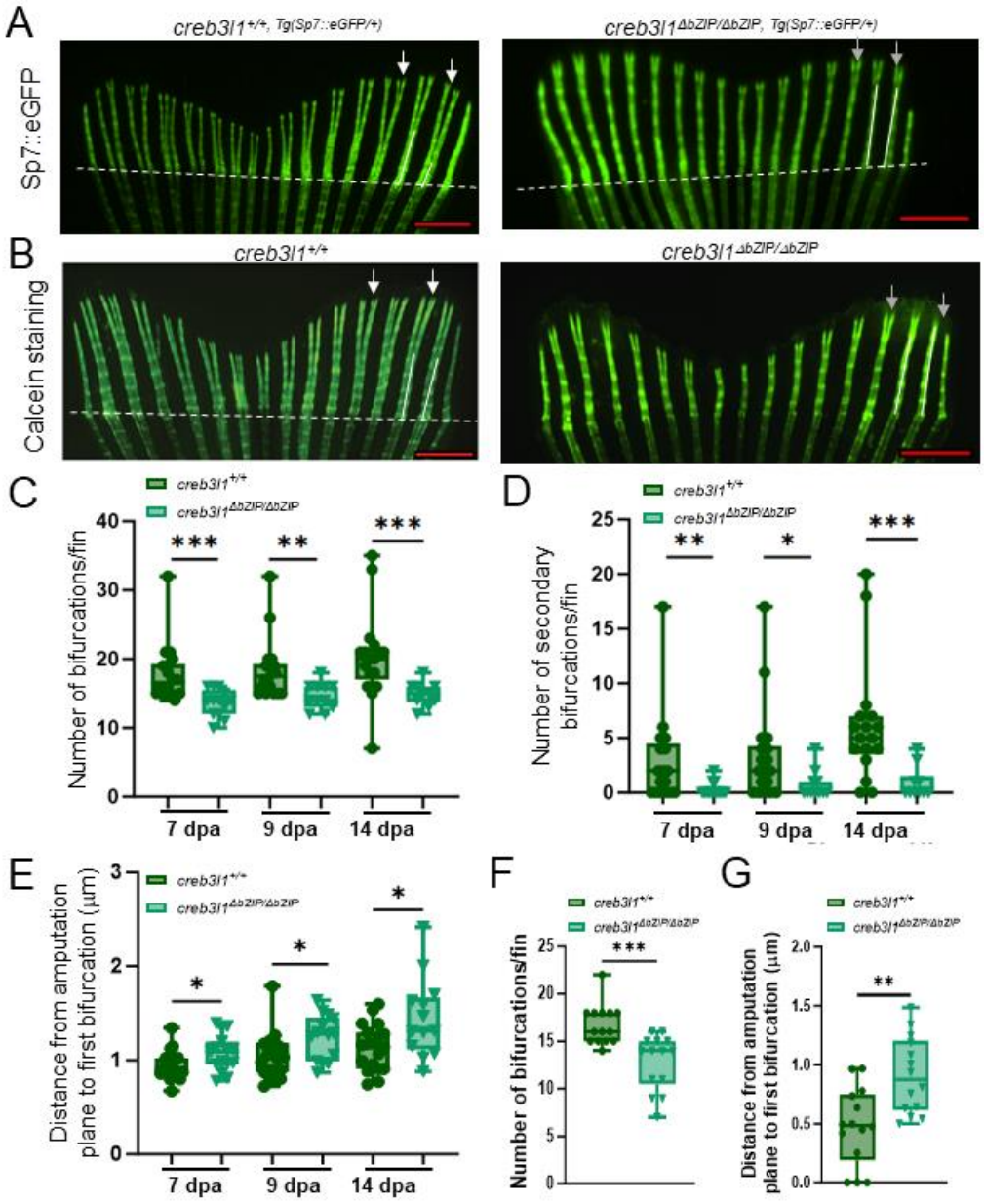

Figure 7: *creb3l1* mutant zebrafish exhibit bifurcation defects during regeneration of the caudal fin

A) Approximately 50% of the caudal fin was amputated from 6 mpf *creb3l1*$^{+/+}$,Tg(Sp7::eGFP/+) and *creb3l1*$^{\Delta bZIP/\Delta bZIP}$,Tg(Sp7::eGFP/+) fish. At different dpa, the tails were imaged directly by fluorescence. Representative images of 7 dpa regenerates are shown. Amputation planes are indicated with dashed line. The distance between the primary proximal bifurcation point and the amputation plane in the 2nd and 3rd ray is marked with white lines. Secondary bifurcations are indicated by white arrows. Lack of secondary bifurcation is marked with gray arrows. Scale bar=1mm.

B) Approximately 50% of the caudal fin was amputated from 6 mpf *creb3l1*$^{+/+}$ and *creb3l1*$^{\Delta bZIP/\Delta bZIP}$ fish. At 9 dpa, the tails were stained with calcein fluorophore and imaged by fluorescence. Representative images of regenerates are shown. Amputation planes are indicated with dashed lines. The distance between the primary proximal bifurcation point and the amputation plane in the 2nd and 3rd ray is marked with white lines. Secondary bifurcations are indicated by white arrowheads. Lack of secondary bifurcation is marked with gray arrows. Scale bar=1mm.

C) Images analogous to those in A were used to quantitate the number of total bifurcations in a 7, 9 and 14 dpa regenerate. Each data point represents an individual fish. n=10-18. **p≤0.01; ***p≤0.001.

D) Images analogous to those in A were used to quantitate the number of secondary bifurcations in a 7, 9 and 14 dpa regenerate. Each data point represents an individual fish. n=10-18. *p≤0.05; **p≤0.01; ***p≤0.001.

E) Images analogous to those in A were used measure the distance from the amputation plane to first bifurcation in the 2nd and 3rd distal ray in the regenerate. Each data point represents an individual fish. Significant increase in distance is observed in *creb3l1*$^{\Delta bZIP/\Delta bZIP}$,Tg(Sp7::eGFP/+) fish at all dpa. n=12-20. *p≤0.05.

F) Images analogous to those in B were used to quantitate the number of bifurcations in the regenerating fin at 9 dpa. Each data point represents an individual fish. n=14. ***p≤0.001.

G) Images analogous to those in B were used measure the distance from the amputation plane to first bifurcation in the 2nd and 3rd distal ray in the regenerate. Significant increase in distance is observed in *creb3l1*$^{\Delta bZIP/\Delta bZIP}$ mutant fish at 9 dpa. n=14. **p≤0.01

6. *creb3l1* mutant fish show aberrant expression of *shha* and *ptch2*

Bifurcation defects are often indicative of aberrant establishment of the proximo-distal axis, an important patterning event in limb development [41,42]. Our results document significant bifurcation changes in fish lacking functional Creb3l1, and suggest that Creb3l1 participates in the establishment of the proximo-distal axis during fin regeneration. A key pathway controlling fin regeneration is the Sonic Hedgehog pathway, which functions in the basal epidermis to regulate bifurcation of the regenerating fin [23]. Current models postulate that Hedgehog signaling promotes the physical coupling of preosteoblasts to distally migrating basal epithelial cells, and that the tightly regulated

expression of *shha* and its downstream target *ptch2* leads to the characteristic branching configurations [23,26].

Thus, we examined the expression pattern of *shha* and *ptch2* in the regenerates of age-matched 6 mpf *creb3l1*$^{+/+}$ and *creb3l1*$^{\Delta bZIP/\Delta bZIP}$ fish at 3 dpa and 7 dpa. As shown in Figure 8A, the expression of *shha* in 3 dpa regenerating fins of wild-type zebrafish is restricted to the distal tip of the regenerating ray, with the *shha* signal present in two distinct domains capping a branching ray (black arrows), in agreement with previous reports [31]. In contrast, in the *creb3l1*$^{\Delta bZIP/\Delta bZIP}$ 3 dpa regenerate, *shha* expression was detected in a single diffuse domain atop an amputated ray (Figure 8A, blue arrow). This defect in *shha* patterning in *creb3l1*$^{\Delta bZIP/\Delta bZIP}$ fish persisted at 7 dpa: while in the wild-type *creb3l1*$^{+/+}$ regenerate, the *shha* signal was clearly separated into two concentrated foci, each on top of a bifurcated lobe of the regenerating lepidotrichia (Figure 8B, black arrows), in the *creb3l1*$^{\Delta bZIP/\Delta bZIP}$ regenerate, the *shha* signal was less tightly segregated within two points, and some rays still contained only a single *shha* domain on top of as yet unbranched ray (Figure 8B, blue arrow).

A difference also was observed in the expression pattern of *patch2*. In 3 dpa wild-type regenerate, the *ptch2* signal was restricted in a cap-like structure centered over each regenerating ray, with minimal expression between the rays (Figure 8A, white arrow marks the boundary between concentrated foci of *patch2* expression). In contrast, in the *creb3l1*$^{\Delta bZIP/\Delta bZIP}$ 3 dpa regenerates, the *patch2* signal was less organized, more punctate, and appeared to be diffusely present within the spaces between the rays (Figure 8B, white arrow). The defect in *patch2* patterning in the *creb3l1*$^{\Delta bZIP/\Delta bZIP}$ regenerates also was observed at 7 dpa: while in wild-type fish, two clearly separate *ptch2* “caps” decorated

each bifurcated lobe of the regenerating lepidotrichia (Figure 8B, white arrows), in the *creb3l1*$^{\Delta bZIP/\Delta bZIP}$ regenerate, the *ptch2* signal appeared within a single larger ”cap” positioned over the regenerating ray (Figure 8B, white arrows). Together, these results indicate that a lack of functional Creb3l1 correlates with a perturbation in the Shh signaling pathway by either directly controlling events that regulate *shha* positioning or by regulating bifurcation events that subsequently may lead to irregularities in *shha* patterning as a downstream event.

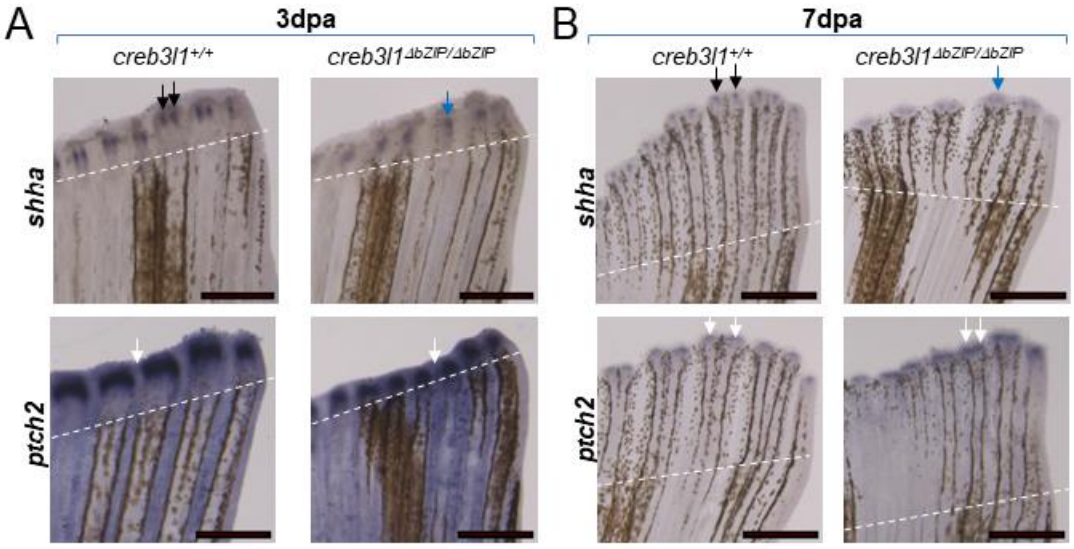

and *creb3l1*$^{\Delta bZIP/\Delta bZIP}$ fish. Regenerates at 3 dpa (A) and 7 dpa (B) were analyzed by *in situ* hybridization to assess the expression patterns of *shha* and *ptch2*. Amputation planes are indicated with dashed line. Scale bar=1mm.

A) The *shha* signal in wild-type *creb3l1*$^{+/+}$ fish exhibits the characteristic two-point staining (black arrows). In contrast, in *creb3l1* mutant fish, *shha* signal is largely in a single domain over the regenerating ray (blue arrow). The *ptch2* signal in wild-type *creb3l1*$^{+/+}$ regenerate is segregated into defined caps over regenerating rays with unstained areas between the caps (white arrow). In contrast, *patch2* expression is more diffuse in *creb3l1*$^{\Delta bZIP/\Delta bZIP}$ regenerate (white arrow).

B) In wild-type *creb3l1* fish, the *shha* signal appears in two clearly separated foci over each bifurcated ray (black arrows). In contrast, *shha* signal more diffuse in *creb3l1* mutant regenerates (blue arrow). The *ptch2* signal in wild-type *creb3l1*$^{+/+}$ fish segregates into two domains as the ray bifurcates (white arrows). In contrast, in *creb3l1*$^{\Delta bZIP/\Delta bZIP}$ mutant regenerate, *ptch2* signal predominantly remains within a single diffuse domain (white arrows). n=3-7.

DISCUSSION

This work characterizes a novel zebrafish model in which to assess the role of the Creb3l1 transcription factor function in organismal development and physiology. Our *creb3l1* mutant fish express Creb3l1 lacking the majority of its coding region and missing the essential DNA-binding bZIP domain, the trans-membrane domain and the luminal domain, thus preventing the Creb3l1 fragment from binding to DNA and acting as a transcription factor or localizing to the ER. Utilizing this new *creb3l1*$^{\Delta bZIP/\Delta bZIP}$ zebrafish model, we aimed to understand the role of Creb3l1 in bone development and during the regeneration of the caudal fin as a paradigm for complex tissue regeneration.

Our analyses show that relative to wild-type animals, the *creb3l1*$^{\Delta bZIP/\Delta bZIP}$ fish do not exhibit significant changes in growth, skeletal morphology and bone density, but show a lower complexity of bifurcation in the caudal fin rays. Ray bifurcation patterns are characteristic in different fish species [53]. While in adult wild-type zebrafish, we observed the characteristic secondary branching of the rays, the number of secondary bifurcations was significantly decreased in the *creb3l1*$^{\Delta bZIP/\Delta bZIP}$ zebrafish.

The relatively mild phenotypes in zebrafish contrast with the serious defects in mammalian bone development caused by the lack of CREB3L1 or *CREB3L1* mutations. *Creb3l1* KO mice are significantly smaller than their littermates and despite having normal skeletal development, and exhibit poor bone mineralization and frequent fractures [11,17]. Humans with *CREB3L1* mutations have severe osteogenesis imperfecta and even perinatal lethality [12,13,18,20,46]. These differences highlight some of the limitations of the zebrafish model, as uterine development of humans and mice places more strain on the developing bones, as well as the force placed on bones when humans and mice begin to

ambulate. Furthermore, zebrafish possess significantly more intramembranous bone compared to the endochondral bones affected by lack of functional Creb3l1 in humans and mice. Moreover, *creb3l1* homologs *creb3l2* and *creb3l3l* are broadly expressed in zebrafish [54,55], and their expression overlaps with *creb3l1* expression in a cell cluster containing osteogenic markers, suggesting a possible compensatory mechanism during bone development [55,56]. Zebrafish *creb3l2* (an ortholog of human *CREB3L2* which regulates chondrogenesis[57]) and *creb3l3l* (an ortholog of human *CREB3L3* gene enriched in the liver and regulating triglyceride metabolism therein[58,59]) are broadly expressed in the regenerating fin [54], possibly providing a compensatory mechanism during Creb3l1 deficiency. The occurrence of partial functional redundancy between Creb3l1 homologs is evident from experiments on Creb3l1 and Creb3l2 in endometrial stromal cells, with phenotypes becoming most severe when both *CREB3L1* and *CREB3L2* are knocked down [60]. Thus, expression of *creb3l2 and/or creb3l3l* may provide a compensatory mechanism during the development of *creb3l1*$^{\Delta bZIP/\Delta bZIP}$ fish.

We used our *creb3l1*$^{\Delta bZIP/\Delta bZIP}$ fish as a model to explore the role of Creb3l1 in the regeneration of complex bony tissues. Utilizing the *sp7::eGFP-CAAX* transgene (pd51Tg) [28] to generate wild-type *creb3l1*$^{+/+}$ and *creb3l1*$^{\Delta bZIP/\Delta bZIP}$ fish expressing eGFP in osteoblasts, and the robust system of the regenerating caudal fin, we observed a significantly decreased post-amputation regeneration in the *creb3l1* mutant fish. The *creb3l1*$^{\Delta bZIP/\Delta bZIP}$ fish tail regenerates were shorter in length and had a significantly reduced total area. Moreover, by utilizing calcein staining of mineralized tissue, we uncovered defects in the mineralized area of bone in the *creb3l1*$^{\Delta bZIP/\Delta bZIP}$ fish. This is consistent with a delay in the healing of bone fractures in *Creb3l1* KO mice, which

exhibit slower mineralization of the bony callus [17]. Thus, our data suggest that the need for Creb3l1 function during bone regeneration is at least partially conserved between zebrafish and mammals.

The decreased regenerate size in the *creb3l1*$^{\Delta bZIP/\Delta bZIP}$ fish prompted us to compare the levels of apoptosis and proliferation in wild-type and *creb3l1* mutant fish. Surprisingly, there were no significant changes in the number of cells with cleaved caspase 3 (a marker for cells undergoing apoptosis) or stained for PH3 (a marker for dividing cells) in wild-type and *creb3l1*$^{\Delta bZIP/\Delta bZIP}$ fish, implying analogous levels of cell apoptosis and division in wild-type and mutant fish. Such results appeared contradictory to the smaller regenerates in the *creb3l1*$^{\Delta bZIP/\Delta bZIP}$ fish, and suggested a possible mitotic arrest. Indeed, quantification of the number of PH3-positive cells that have entered metaphase and anaphase showed that *creb3l1*$^{\Delta bZIP/\Delta bZIP}$ fish regenerates have significantly fewer mitotic cells. PH3 associates with condensed chromatin in late G2 phase, and remains bound during mitosis from prophase to late anaphase, but rapidly dissociates from chromatin in late anaphase/early telophase [51,52]. Thus, a possible explanation for the difference in regenerate size in wild-type and the *creb3l1*$^{\Delta bZIP/\Delta bZIP}$ fish is that in wild-type fish, cells divide continuously, with the PH3 pattern reflecting a snapshot in time, while in the *creb3l1*$^{\Delta bZIP/\Delta bZIP}$ fish, many cells do not progress through mitosis, with the PH3 pattern reflecting an accumulation of mitotically arrested cells. Such a mitotic deficiency could be the result of several factors, including ER stress shown previously to cause cell cycle arrest at the G2/M phase [61]. Creb3l1 has been reported as a transducer of ER stress [5,8,10,14-18,21,62,63], and it is likely that cells lacking functional Creb3l1 exhibit increased ER stress, leading to a possible increase in G2/M-arrested cells. Such a

scenario would result in normal numbers of $PH3^{+}$ cells, but reduced size of the regenerate. Why this effect of CREB3L1 deficiency is only visible during tail regeneration and doesn't affect fish growth during development remains to be explored.

Examination of the ray patterning of the regenerating fins indicates a significant defect in bifurcations in the *creb3l1*$^{\Delta bZIP/\Delta bZIP}$ fish at every examined point after amputation. The *creb3l1*$^{\Delta bZIP/\Delta bZIP}$ fish exhibit similar number of primary, amputation plane-proximal bifurcations as the wild-type fish, but they do not generate the secondary, more distal bifurcations, leading to a significant decrease in the total number of bifurcations. Equally important, the primary bifurcations in the *creb3l1*$^{\Delta bZIP/\Delta bZIP}$ fish are significantly more distal to the amputation plane than in wild-type fish. Such distalization phenotype is highly indicative of defects in the development of the proximo-distal axis, a highly conserved process required for zebrafish and human limb development [64]. The establishment of the axis in the regenerating caudal fin is regulated by several pathways, including FGF, Wnt, Retinoic Acid, and Sonic Hedgehog [42]. Of particular interest to this study was Sonic Hedgehog, due to its role in caudal fin bifurcation [26,31] . Additionally, recent findings in mice demonstrate that Shh signaling is selectively activated during the regeneration of severely damaged bone, while it is dispensable during healing of small fractures[65]. This is exceptionally relevant when considering the complex environment of caudal fin regeneration. When assayed via *in situ* hybridization, we found a change in the distribution of *shha* expression in the *creb3l1*$^{\Delta bZIP/\Delta bZIP}$ regenerating fins: while *shha* expression in wild-type regenerates is detected in distinct twin puncta at the distal tip, *shha* expression in the *creb3l1*$^{\Delta bZIP/\Delta bZIP}$ regenerate exhibits a more diffuse staining, with the two puncta connecting in some fin rays to create a single point of signaling.

Furthermore, at 7 dpa, *ptch2,* an effector of Sonic Hedgehog signaling, is expressed in wild-type regenerate as distinct domains over the bifurcating ray, but in *creb3l1*$^{\Delta bZIP/\Delta bZIP}$ regenerate, *ptch2* is localized in a single domain at the tip of the regenerating ray. These results suggest that functional Creb3l1 is required to establish a restricted pattern of *shha* expression and signaling that informs morphogenic branching.

The exact mechanism through which Creb3l1 may be influencing Shh signaling remains to be determined. Within the developing caudal fin, as well as the local environment of the regenerate, it is possible that Creb3l1 affects the localization of *shha* signaling via a direct mechanism. It is also possible that Creb3l1 intersects with the Retinoic Acid (RA) pathway, as alterations in retinoic acid homeostasis also shift bifurcation distally [66]. Another way Creb3l1 may affect the localization of *shha* signaling is via an effect on the thyroid hormone (TH) signaling pathway. TH has been shown to be a regulator of branchpoint positioning in the regenerating tail, and reduction in TH levels causes marked reduction in the number of bifurcations and a significant distalization of branchpoints, without notable effects on the overall size of the fish, a phenotype similar to our *creb3l1*$^{\Delta bZIP/\Delta bZIP}$ fish [41]. Notably, in the absence of TH, *shha* domains fail to separate into distinct points [41], a phenotype observed in our *creb3l1*$^{\Delta bZIP/\Delta bZIP}$ fish during regeneration. How could Creb3l1 control the TH pathway? TH formation by thyroid follicular cells requires the Sodium/Iodide Symporter (NIS) that mediates active iodide accumulation required for the synthesis of all iodide-containing thyroid hormones [67]. Importantly, NIS expression has been shown to be modulated by CREB3L1 in rat thyroid follicular cells, with overexpression and inhibition of CREB3L1 inducing an increase and decrease in NIS protein, respectively [68]. This raises the possibility that the lack of

functional Creb3l1 within the zebrafish thyrocytes decreases the production of NIS, which causes a decrease in NIS-mediated iodide uptake and decreased TH production. The reduced TH levels then cause defects in *shha* pathway signaling, leading to defects in bifurcation during development and regeneration. As such, we suggest that the alterations in bifurcation in *creb3l1*$^{\Delta bZIP/\Delta bZIP}$ fish could be attributed to remote defects in TH production that nevertheless affect signaling locally within the caudal fin.

Together, our findings demonstrate that Creb3l1 plays a key role in the development and regeneration of the zebrafish caudal fin, by showcasing a novel functions for this protein in tissue patterning. Specifically, we show that Creb3l1 participates in re-establishing the proximo-distal axis during fin regeneration by impacting the *shha* signaling pathway. Recent findings on the essential role of Sonic Hedgehog's in the healing of severe bone injury in mammals [65] suggest that the intersection of *shha* signaling with Creb3l1 may have implications for therapeutic approaches to fracture healing in mammals. This is a novel finding, and may provide a foundation for future research on complex tissue regeneration. Our results significantly expand the current understanding of Creb3l1 function(s) by uncovering a previously unknown role for this protein in tissue patterning and potential modulation of Shh signaling.

EXPERIMENTAL PROCEDURES

Zebrafish husbandry

Zebrafish (*Danio rerio*) were maintained in accordance with the University of Alabama at Birmingham's Institutional Animal Care and Use Committee, according to the Zebrafish Research Facility and the vertebrate animal welfare protocol (APN 21787).

Adult fish were housed on an Aquaneering circulating water system, on a 14:10 light:dark cycle at 28ºC. Fish were fed Gemma Micro 300 twice daily with one live *Artemia* feeding. Fish were bred using the standard system water and two-piece tank system to prevent oophagy. Eggs were harvested, sorted for healthy eggs, and raised in E3[69] until placed on the system or utilized for experiments. Fish from ages 3 to 6 months were used and age-matched for experiments.

Generation of creb3l1 mutant fish and SP7-GFP transgenes

Alt-R crRNA target sites were designed with Integrated DNA Technologies Alt-R CRISPR HDR Design Tool (https://www.idtdna.com/pages/tools/alt-r-crispr-hdr-design-tool). Alt-R CRISPR-Cas9 crRNA, tracrRNA (Integrated DNA Technologies) and Alt-R S.p. Cas9 Nuclease V3 (Integrated DNA Technologies)) was prepared following manufacturer instructions. 3 µM sgRNA (Guide sequence: GGCGGAGAGGAACCCGTTGC) were obtained through diluting 100 µM crRNA and 100 µM tracrRNA into Nuclease-Free Duplex Buffer (Integrated DNA Technologies), heating at 98ºC for 5 min, then cooling to room temperature. 0.5 µL Cas9 protein was diluted with Cas9 working buffer (20 mM HEPES; 150 mM KCl, pH7.5) to yield a working concentration of 0.5 µg/µL. The diluted Cas9 protein working solution was mixed 1:1 with 3 µM sgRNA solution and then incubated at 37 ºC for 10 min to obtain RNP complex. RNP complex was freshly prepared and left on ice until microinjection. Microinjection was performed by injecting ~1 nL of RNP complex into yolk of 1-cell stage wild-type (AB) embryos.

F0 adults generated from this injection were crossed to AB fish to generate heterozygous offspring. Heterozygous offspring were then sequenced via Sanger

Sequencing (primers: F: 5'-TTTGTGGTCTCTCTCCAGCA-3', R: 5'-GGATGGATGGCAGGAAAGTA-3') to determine sequences of CRISPR indels. Sequenced heterozygous fish were crossed to generate homozygous offspring. These offspring were sequenced once more to verify homozygosity for the mutant allele.

For analysis of fin rays in vivo, *creb3l1* mutant fish were outcrossed to AB Ola.Sp7:EGFP-CAAX [28] fish, henceforth referred to as Sp7::eGFP, or *creb3l1*$^{Tg(Sp7::eGFP/+)}$ fish. Resultant heterozygotes were then incrossed with homozygous CREB3L1 mutants to generate fish homozygous for their respective mutations, and heterozygous for the Sp7::eGFP transgene. Fish were screened at 3-5 dpf for fluorescence in the craniofacial bones and raised according to standard husbandry protocols.

Genotyping by High Resolution Melt Analysis in Zebrafish

To isolate genomic DNA, adult fish were anaesthetized in 250mg/L Tricaine until opercular motion slowed. Tail clippings were collected from fish and incubated at 98°C for 20 min in 40 µl 25 mM NaOH in a 96-well plate; then neutralized with 40 µl of 40 mM Tris-HCl. For genotyping of whole embryos or larvae, the incubation time at 98°C was shortened to 10 minutes. PCR reactions contained 1 µl of LC Green Plus Melting Dye (Biofire Defense), 1 µl of 10x enzyme buffer, 0.2 µl of dNTP Mixture (10 mM each), 0.3 µl of 15 mM $MgCl_2$, 0.3 µl of each primer (F: 5'-GATCATCTGTTGGCGGAGAG -3', R: 5'- TTGGAGGGTCCAGATCCATA -3') (10 µM), 1 µl of genomic DNA, 0.05 µl of Taq DNA Polymerase (Genscript), and DNA/RNAse free water up to 10 µl. The PCR reaction protocol was 98ºC for 30 sec, then 45 cycles of 98ºC for 10 sec, 59ºC for 20 sec, and 72ºC for 15 sec, followed by 95ºC for

30 sec and then rapid cooling to 4ºC. Following PCR, melting curves were generated and analyzed using the LightScanner instrument (Idaho Technology) over a 65-95°C range.

RT-PCR

7dpf larvae were anaesthetized with 250mg/L tricaine and collected in a 1.5mL Eppendorf tube (~30 fish/pool). Excess embryo media was removed and 350uL of Trizol was added. Pooled larvae were homogenized by pestle in Trizol and purified using a Direct-zol RNA Miniprep Plus Kit from Zymo Research, including gDNA removal. The concentration of the RNA was measured using a NanoDrop ND-1000. RNA with a 260/280 of ~2.0 was used for further analyses. Up to 2µg of RNA was utilized to synthesize cDNA in the High-Capacity cDNA Reverse Transcription Kit (Applied Biosystems) with RNaseOUT™ Recombinant Ribonuclease Inhibitor (Invitrogen). Prepared cDNA was used for RT-PCR, using a SYBR Green Power UP (Applied Biosystems) master mix, with 0.8 mM Primer concentration (all primers are listed in Table 1). A 10 µL final volume reaction was prepared, with 1 µL of cDNA. This was run using the standard cycling time/temperatures for SYBR Green Power UP with 0.8 mM Primer concentration (all primers are listed in Table 1). Fold change was calculated via the $2^{-\Delta\Delta Ct}$ method [70]. ΔCt values were utilized for statistics and were compared via t-test or Mann-Whitney test, as described below.

Gene	Primers	Use
creb3l1	F: GCAGAGCCCTCTCCTCAC R: GCACCCGTTTGAGTGCTTT	RT-PCR
elfa (housekeeping gene)	F: TACCCTCCTCTTGGTCGC R: TTGGAACGGTGTGATTGAG	RT-PCR
col1a1a	F: CGATGGCTTCCAGTTCGAGT R: TAATACGACTCACTATAGGGCCAGGGGGATTTTACACGCT	Generation of in situ probe
creb3l1	F: GATGCGGCCGCCTGTGTTTTGTGTTGGT R: GATCGTCGACGAAATATTCAGCTCCTCC	Generation of plasmid for in situ probe template

Table 1: Details of primers utilized to perform RT-PCR, generate in situ probes, or clone from zebrafish cDNA.

Micro Computed Tomography (mCT)

Age-matched fish were fixed in 4% PFA (paraformaldehyde) in phosphate buffered saline (PBS, pH 7.4) with 0.5% Triton X-100 overnight at 4°C. Fixed zebrafish were scanned using the Scanco µCT40 desktop cone-beam micro-CT scanner (Scanco Medical AG, Brüttisellen, Switzerland) using µCT Tomography v6.4-2 (Scanco Medical AG, Brüttisellen, Switzerland). Scans were automatically reconstructed into 2-D slices and slices were analyzed using the µCT Evaluation Program (v.6.5-2, Scanco Medical). The zebrafish were placed in a 36mm diameter scanning holder and scanned at the following settings: 18µm voxel size, 70kVp, 114µA, 1000 projections/180 degrees with an integration time of 200ms. The region of interest was drawn around the fish and the analysis was performed on all slices that any part of the fish appeared in. Bone was thresholded at 140.3 mgHA/ccm and the 3-D analysis performed. Data were obtained on

bone volume and density. 3D images were obtained from the 3D evaluation software (μCT Ray v.4.2, Scanco Medical).

Measurement of uninjured fish

The length of fish at 6 months post fertilization (mpf) was measured with a ruler and recorded. Tails of both wild-type and mutant fish carrying the sp7::eGFP transgene were imaged on a Nikon AZ100 dissection microscope with fluorescence filters to visualize gross morphology of the caudal fin. Photos were analyzed in FIJI ImageJ 1.54f) [71] to measure the indicated parameters.

Caudal fin amputation model of regeneration and visualization of mineralized regenerate

Age-matched fish were anaesthetized in a 250 mg/L tricaine until opercular motion was slowed and fish were no longer responsive to touch. Fish underwent 50% tailfin amputation via transection with a scalpel blade. Tails were photographed after amputation. Fish were then recovered in system water and allowed to regenerate for the indicated times. At the indicated day post amputation (dpa), the fish were immersed in a 0.2% calcein solution (pH 7.5) [34,72,73] for 20 minutes, briefly rinsed, and then de-stained in fresh system water for 20 minutes. The stained fish were imaged on a Nikon AZ100 dissection microscope in both brightfield and fluorescent filters to visualize gross morphology and mineralization of the regenerate. Photos were analyzed in FIJI ImageJ 1.54f) [71] to measure the indicated parameters.

The size and patterning of the mineralized regenerate was evaluated by a protocol adapted from Cardiera et. al [27]. Briefly, utilizing FIJI (ImageJ 1.53f51) [71], the total area of

the regenerate (REG) of the amputated tail was measured using the FIJI Measure function, then normalized to the width of the stump at the amputation plane (STU). To measure the real mineralized area (RMA), the polygon tool was utilized to outline the fluorescently labelled bones with the distal tip of each lepidotrichia and the base of the regenerated area marking the boundary of the estimated mineralized area. Using this selected region, the threshold tool was utilized to isolate pixels of fluorescently-stained bone based on individual image intensity histograms (16 bit image binning). The total area of these particles was then analyzed via the Analyze Particles function in FIJI. In addition, the distance from the amputation plane to bifurcation in both, calcein stained and transgenic fish was measured from the amputation plane to the base of the bifurcation on the 2nd and 3rd most lateral fin rays on the tail, using the line segment tool. Rays with bifurcation points proximal to the amputation plane were excluded from the analysis.

Visualization of Sp7^{+} cell populations during regeneration

For dynamic analyses of caudal fin regeneration, wild-type and CREB3L1 mutant fish expressing Sp7::eGFP underwent amputation as described above. Fish were returned to system water, and imaged using a Nikon AZ100 dissection microscope at 3, 7, 9 and 14 dpa, under tricaine anesthetic. The images were evaluated for the length of the regenerate and the area of Sp7^{+} cells, using the same methods used to quantify and normalize RMA (see above). In addition, the bifurcation depth in both calcein stained and transgenic fish was measured as described above.

Detection of apoptotic and proliferating cells

Fins were amputated as described above. 3 dpa fins were collected and fixed in 2% PFA in PBS (pH 7.4) overnight at 4°C. Fixed tails were processed as described

(König et al., 2018). Briefly, fixed fins were washed in PBS, blocked in 5% goat serum in PBS with 0.3% Triton-X (PBSTX) for 1 hr, and stained overnight with primary either anti-Cleaved Caspase 3 (BD Biosciences, diluted 1:500) or anti-phospho-histone H3 (Ser10) (Cell Signaling Technology, diluted 1:1000). Tails were washed in PBSTX twice (once for 5 min, and once for 1 hr), and stained with goat-anti-rabbit IgG-Alexa Fluor Plus 594 (Thermo Scientific, diluted 1:500) in blocking solution for 2 hours at room temperature. Stained tails were washed as above and mounted with glass coverslips on glass slides in 90% glycerol with 0.5% propyl gallate. Representative images were captured with a Nikon A1R-HD25 Confocal microscope, with a 10x objective and processed with FIJI. To quantify the number of stained cells, tails were imaged on the Nikon Ti2 widefield microscope at 10x or 20x objective, and the images analyzed via FIJI [71].

Probe preparation for in situ hybridization

Probes were generated as described by in vitro transcription with digoxigenin-labelled UTP (Roche) of PCR products engineered to have a T7 site (primers in Table 2) or linearized plasmids (details in Table 3)

Gene	Linearizing enzyme (Promega)	Polymerase
creb3l1	*Not*I	T3 (New England Biolabs)
msxb	*Sal*I	T7 (Fisher Scientific)
ptch2	*Xba*I	T3
shha	*Hind*III	T7

Table 2: Details of plasmid preparation to generate in situ probes.

In situ hybridization

3 and 7 dpa fins were amputated via scalpel and fixed overnight at 4°C in 4% PFA in PBS (pH 7.4). The tails were treated as previously described [74], with slight modifications. Briefly, fins were washed in PBS, and dehydrated in 100% methanol for at least 2 hours at -20°C. Dehydrated fins were rehydrated stepwise with 5 min washes in ethanol (75% EtOH/25% PBST, 50% EtOH/50% PBST, 25% EtOH/75% PBST), and washed in PBS with 0.1% Tween 20 (PBST) before 1 hr of prehybridization and subsequent overnight hybridization with 0.5mg/mL digoxigenin-conjugated probes in hybridization buffer (HB) containing 50% Formamide, 5xSSC saline sodium citrate, 1mg/mL Torula RNA (Sigma-Aldrich), 100 μg/mL heparin, 1x Denhart's, 0.1% Tween 20, 5 mM EDTA) [75] in a 65°C water bath. Hybridized tails were washed for 10 min at 65°C in stepwise HB/2xSSC solutions (75% HB/25% 2xSSC, 50% HB/50% 2xSSC, 25% HB/75% SSC) followed by a series of 0.2xSSC/PBS 5 min washes with (75% 0.2xSSC/25% PBST, 50% 0.2xSSC/50% PBST, 25% 0.2xSSC/75% PBST). Washed tails were blocked in 2mg/mL BSA in PBST for one hour at RT, and then incubated with tail pre-adsorbed anti-DIG antibody fragments (Roche, Sigma-Aldrich, diluted 1:2000) for two hours at RT. Tails were then washed 3x with a staining solution (100 mM Tris-HCl (pH 9.5), 50 mM $MgCl_2$, 100 mM NaCl, 0.1% Tween 20, 1 mM levamisole) and incubated in BM Purple (Roche, Sigma-Aldrich) until developed (overnight at RT or 4ºC to reduce background.) Stained tails were washed in multiple PBST washes and fixed with 4% PFA overnight at 4ºC. and washed again multiple times. Prepared tails were

mounted in a 12 well culture plate in PBST and imaged using a Leica M205 FCA dissection microscope.

Statistical analyses

All experiments were performed in duplicate or greater. Data were collected and analyzed with Graphpad Prism - Version 10. Mendelian ratio data (Figure 2B) was analyzed using a chi-square analysis of observed vs. expected values. All other data comparing *creb3l1* wild-type vs. mutant fish were first analyzed for normality of the data and descriptive statistics. Based on these analyses, the appropriate analyses of non-paired data were chosen; for normal data, unpaired t-tests were utilized, with or without Welch's correction for differences in standard deviation. For data that was not normally distributed, the non-parametric Mann-Whitney test was utilized. Significance was determined as a $p<0.05$ threshold. (* $p\leq0.05$; ** $p\leq0.01$; *** $p\leq0.001$, **** ≤0.0001).

ACKNOWLEDGEMENTS

We are grateful to Drs. Appel (University of Colorado SOM), Grunwald (University of Utah), DeLaurier (University of South Carolina at Aiken) and Chang (University of Alabama at Birmingham) for sharing their in situ probes, reagents, and expertise. We thank members of the Sztul and Serra lab for helpful comments on the project and the manuscript. We also thank UAB's Zebrafish Research Facility and High Resolution Imaging Facility for providing technical resources and advice. Figures 1 and 6 include graphics generated on BioRender.com. This work was supported by awards from the National Institute of General Medical Sciences (R01GM122802 to ES) and the National Institute of Dental and Craniofacial Research (5T90DE022736-09 to PEV).

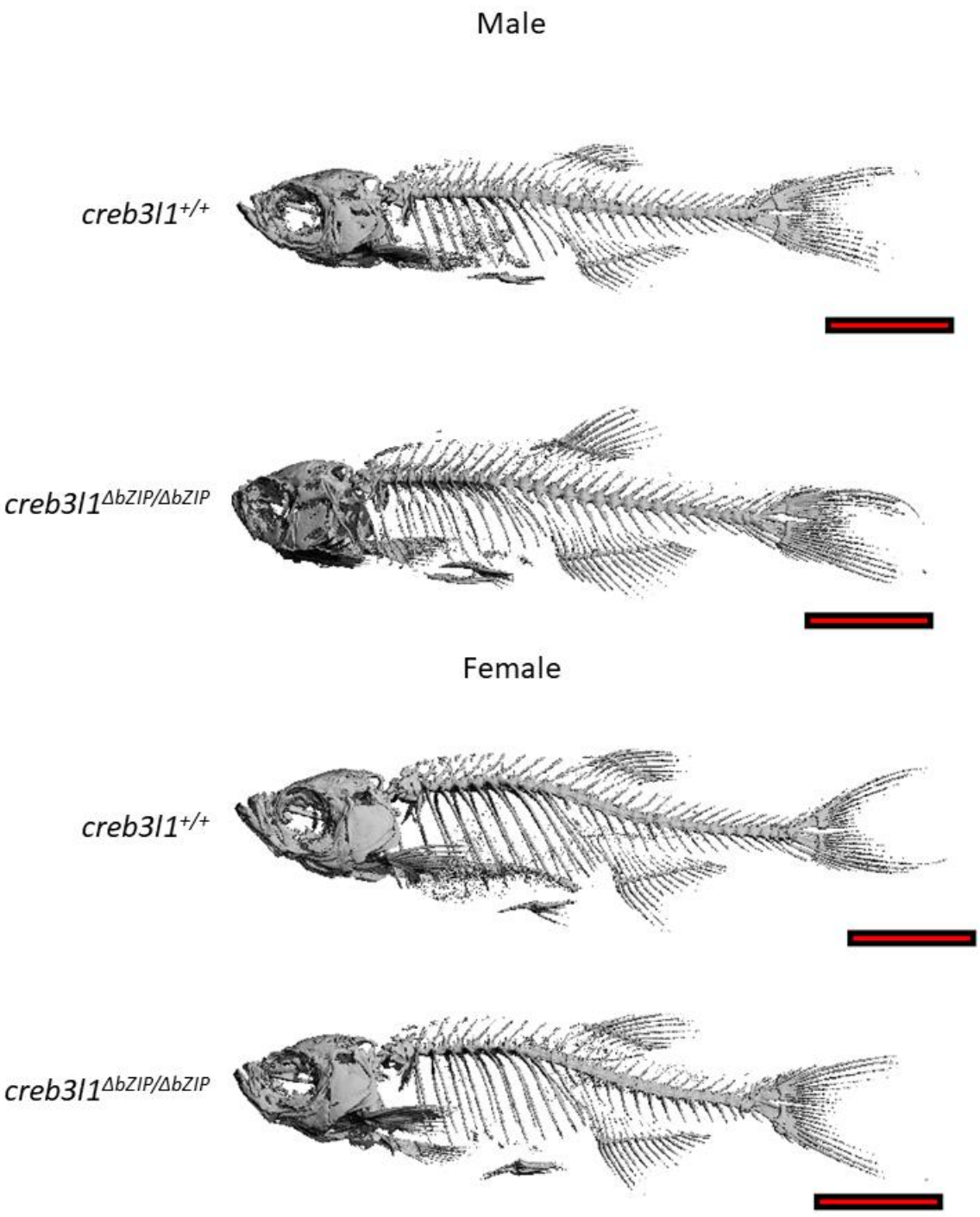

Supplemental Figure 1. *creb3l1* mutant zebrafish have normal overall skeletal morphology

Age-matched 3 mpf *creb3l1*$^{+/+}$ and *creb3l1*$^{\Delta bZIP/\Delta bZIP}$ fish were analyzed by μCT and representative scans of male and female animals are shown. The *creb3l1*$^{\Delta bZIP/\Delta bZIP}$ fish exhibit overall normal skeletal morphology.

REFERENCES

1. Langhans MT, Alexander PG, Tuan RS. Chapter 28 - Skeletal Development. In: Moody SA, ed. *Principles of Developmental Genetics (Second Edition)*. Oxford: Academic Press; 2015:505-530.
2. Marks SC, Gartland A, Odgren PR. Skeletal Development. In: Martini L, ed. *Encyclopedia of Endocrine Diseases*. New York: Elsevier; 2004:261-272.
3. Rutkovskiy A, Stensløkken KO, Vaage IJ. Osteoblast Differentiation at a Glance. *Med Sci Monit Basic Res*. Sep 26 2016;22:95-106. https://doi.org10.12659/msmbr.901142.
4. Honma Y, Kanazawa K, Mori T, et al. Identification of a novel gene, OASIS, which encodes for a putative CREB/ATF family transcription factor in the long-term cultured astrocytes and gliotic tissue. *Brain Res Mol Brain Res*. May 21 1999;69(1):93-103. https://doi.org10.1016/s0169-328x(99)00102-3.
5. Murakami T, Kondo S, Ogata M, et al. Cleavage of the membrane-bound transcription factor OASIS in response to endoplasmic reticulum stress. *Journal of Neurochemistry*. 2006;96(4):1090-1100. https://doi.orghttps://doi.org/10.1111/j.1471-4159.2005.03596.x.
6. Omori Y, Imai J, Suzuki Y, Watanabe S, Tanigami A, Sugano S. OASIS is a transcriptional activator of CREB/ATF family with a transmembrane domain. *Biochem Biophys Res Commun*. Apr 26 2002;293(1):470-7. https://doi.org10.1016/s0006-291x(02)00253-x.
7. Schubert SW, Abendroth A, Kilian K, et al. bZIP-Type transcription factors CREB and OASIS bind and stimulate the promoter of the mammalian transcription factor GCMa/Gcm1 in trophoblast cells. *Nucleic acids research*. Jun 2008;36(11):3834-46. https://doi.org10.1093/nar/gkn306.
8. Kondo S, Murakami T, Tatsumi K, et al. OASIS, a CREB/ATF-family member, modulates UPR signalling in astrocytes. *Nat Cell Biol*. Feb 2005;7(2):186-94. https://doi.org10.1038/ncb1213.
9. García IA, Torres Demichelis V, Viale DL, et al. CREB3L1-mediated functional and structural adaptation of the secretory pathway in hormone-stimulated thyroid cells. *Journal of cell science*. 2017;130(24):4155-4167. https://doi.org10.1242/jcs.211102.
10. Murakami T, Saito A, Hino S, et al. Signalling mediated by the endoplasmic reticulum stress transducer OASIS is involved in bone formation. *Nat Cell Biol*. Oct 2009;11(10):1205-11. https://doi.org10.1038/ncb1963.
11. Murakami T, Hino S, Nishimura R, Yoneda T, Wanaka A, Imaizumi K. Distinct mechanisms are responsible for osteopenia and growth retardation in OASIS-deficient mice. *Bone*. Mar 1 2011;48(3):514-23. https://doi.org10.1016/j.bone.2010.10.176.

12. Lindahl K, Åström E, Dragomir A, et al. Homozygosity for CREB3L1 premature stop codon in first case of recessive osteogenesis imperfecta associated with OASIS-deficiency to survive infancy. *Bone*. Sep 2018;114:268-277. https://doi.org10.1016/j.bone.2018.06.019.

13. Keller RB, Tran TT, Pyott SM, et al. Monoallelic and biallelic CREB3L1 variant causes mild and severe osteogenesis imperfecta, respectively. *Genet Med*. Apr 2018;20(4):411-419. https://doi.org10.1038/gim.2017.115.

14. Asada R, Saito A, Kawasaki N, et al. The endoplasmic reticulum stress transducer OASIS is involved in the terminal differentiation of goblet cells in the large intestine. *J Biol Chem*. Mar 9 2012;287(11):8144-53. https://doi.org10.1074/jbc.M111.332593.

15. Miyagi H, Kanemoto S, Saito A, et al. Transcriptional regulation of VEGFA by the endoplasmic reticulum stress transducer OASIS in ARPE-19 cells. *PLoS One*. 2013;8(1):e55155. https://doi.org10.1371/journal.pone.0055155.

16. Vellanki RN, Zhang L, Volchuk A. OASIS/CREB3L1 is induced by endoplasmic reticulum stress in human glioma cell lines and contributes to the unfolded protein response, extracellular matrix production and cell migration. *PLoS One*. 2013;8(1):e54060. https://doi.org10.1371/journal.pone.0054060.

17. Funamoto T, Sekimoto T, Murakami T, Kurogi S, Imaizumi K, Chosa E. Roles of the endoplasmic reticulum stress transducer OASIS in fracture healing. *Bone*. Oct 2011;49(4):724-32. https://doi.org10.1016/j.bone.2011.06.012.

18. Symoens S, Malfait F, D'Hondt S, et al. Deficiency for the ER-stress transducer OASIS causes severe recessive osteogenesis imperfecta in humans. *Orphanet journal of rare diseases*. Sep 30 2013;8:154. https://doi.org10.1186/1750-1172-8-154.

19. Iseki K, Hagino S, Nikaido T, et al. Gliosis-specific transcription factor OASIS coincides with proteoglycan core protein genes in the glial scar and inhibits neurite outgrowth. *Biomedical research (Tokyo, Japan)*. Dec 2012;33(6):345-53. https://doi.org10.2220/biomedres.33.345.

20. Guillemyn B, Kayserili H, Demuynck L, et al. A homozygous pathogenic missense variant broadens the phenotypic and mutational spectrum of CREB3L1-related osteogenesis imperfecta. *Human molecular genetics*. Jun 1 2019;28(11):1801-1809. https://doi.org10.1093/hmg/ddz017.

21. Keller RB, Tran TT, Pyott SM, et al. Monoallelic and biallelic CREB3L1 variant causes mild and severe osteogenesis imperfecta, respectively. *Genetics in medicine : official journal of the American College of Medical Genetics*. 2018;20(4):411-419. https://doi.org10.1038/gim.2017.115.

22. Nikaido T, Yokoya S, Mori T, et al. Expression of the novel transcription factor OASIS, which belongs to the CREB/ATF family, in mouse embryo with special reference to bone development. *Histochemistry and Cell Biology*. 2001/08/01 2001;116(2):141-148. https://doi.org10.1007/s004180100279.

23. Braunstein JA, Robbins AE, Stewart S, Stankunas K. Basal epidermis collective migration and local Sonic hedgehog signaling promote skeletal branching morphogenesis in zebrafish fins. *Developmental Biology*. 2021/09/01/ 2021;477:177-190. https://doi.orghttps://doi.org/10.1016/j.ydbio.2021.04.010.

24. Sehring IM, Weidinger G. Recent advancements in understanding fin regeneration in zebrafish. *WIREs Developmental Biology*. 2020;9(1):e367. https://doi.orghttps://doi.org/10.1002/wdev.367.

25. Thompson JD, Ou J, Lee N, et al. Identification and requirements of enhancers that direct gene expression during zebrafish fin regeneration. *Development*. 2020;147(14). https://doi.org10.1242/dev.191262.

26. Armstrong BE, Henner A, Stewart S, Stankunas K. Shh promotes direct interactions between epidermal cells and osteoblast progenitors to shape regenerated zebrafish bone. *Development*. 2017;144(7):1165-1176. https://doi.org10.1242/dev.143792.

27. Cardeira J, Gavaia PJ, Fernández I, et al. Quantitative assessment of the regenerative and mineralogenic performances of the zebrafish caudal fin. *Scientific reports*. 2016/12/19 2016;6(1):39191. https://doi.org10.1038/srep39191.

28. Nachtrab G, Kikuchi K, Tornini VA, Poss KD. Transcriptional components of anteroposterior positional information during zebrafish fin regeneration. *Development*. Sep 2013;140(18):3754-64. https://doi.org10.1242/dev.098798.

29. Knopf F, Hammond C, Chekuru A, et al. Bone Regenerates via Dedifferentiation of Osteoblasts in the Zebrafish Fin. *Developmental Cell*. 2011/05/17/ 2011;20(5):713-724. https://doi.orghttps://doi.org/10.1016/j.devcel.2011.04.014.

30. Bayliss PE, Bellavance KL, Whitehead GG, et al. Chemical modulation of receptor signaling inhibits regenerative angiogenesis in adult zebrafish. *Nat Chem Biol*. 2006;2(5):265-273. https://doi.org10.1038/nchembio778.

31. Laforest L, Brown CW, Poleo G, et al. Involvement of the sonic hedgehog, patched 1 and bmp2 genes in patterning of the zebrafish dermal fin rays. *Development*. Nov 1998;125(21):4175-84. https://doi.org10.1242/dev.125.21.4175.

32. Stewart S, Gomez AW, Armstrong BE, Henner A, Stankunas K. Sequential and opposing activities of Wnt and BMP coordinate zebrafish bone regeneration. *Cell Rep*. Feb 13 2014;6(3):482-98. https://doi.org10.1016/j.celrep.2014.01.010.

33. Ouyang X, Panetta NJ, Talbott MD, et al. Hyaluronic acid synthesis is required for zebrafish tail fin regeneration. *PLoS One*. 2017;12(2):e0171898. https://doi.org10.1371/journal.pone.0171898.

34. Recidoro AM, Roof AC, Schmitt M, et al. Botulinum Toxin Induces Muscle Paralysis and Inhibits Bone Regeneration in Zebrafish. *Journal of Bone and Mineral Research*. 2014;29(11):2346-2356. https://doi.orghttps://doi.org/10.1002/jbmr.2274.

35. Blum N, Begemann G. Retinoic acid signaling spatially restricts osteoblasts and controls ray-interray organization during zebrafish fin regeneration. *Development*. 2015;142(17):2888-2893. https://doi.org10.1242/dev.120212.

36. Whitehead GG, Makino S, Lien CL, Keating MT. fgf20 is essential for initiating zebrafish fin regeneration. *Science*. Dec 23 2005;310(5756):1957-60. https://doi.org10.1126/science.1117637.

37. Stoick-Cooper CL, Weidinger G, Riehle KJ, et al. Distinct Wnt signaling pathways have opposing roles in appendage regeneration. *Development*. Feb 2007;134(3):479-89. https://doi.org10.1242/dev.001123.

38. Braunstein JA, Robbins AE, Stewart S, Stankunas K. Basal epidermis collective migration and local Sonic hedgehog signaling promote skeletal branching morphogenesis in zebrafish fins. *Dev Biol*. Sep 2021;477:177-190. https://doi.org10.1016/j.ydbio.2021.04.010.

39. Zhang J, Jeradi S, Strähle U, Akimenko M-A. Laser ablation of the sonic hedgehog-a-expressing cells during fin regeneration affects ray branching morphogenesis. *Developmental Biology*. 2012/05/15/ 2012;365(2):424-433. https://doi.orghttps://doi.org/10.1016/j.ydbio.2012.03.008.

40. Quint E, Smith A, Avaron F, et al. Bone patterning is altered in the regenerating zebrafish caudal fin after ectopic expression of sonic hedgehog and bmp2b or exposure to cyclopamine. *Proceedings of the National Academy of Sciences*. 2002;99(13):8713-8718. https://doi.orgdoi:10.1073/pnas.122571799.

41. Harper M, Hu Y, Donahue J, et al. Thyroid hormone regulates proximodistal patterning in fin rays. *Proceedings of the National Academy of Sciences*. 2023;120(21):e2219770120. https://doi.orgdoi:10.1073/pnas.2219770120.

42. Rabinowitz JS, Robitaille AM, Wang Y, et al. Transcriptomic, proteomic, and metabolomic landscape of positional memory in the caudal fin of zebrafish. *Proc Natl Acad Sci U S A*. Jan 31 2017;114(5):E717-e726. https://doi.org10.1073/pnas.1620755114.

43. Cunningham F, Allen JE, Allen J, et al. Ensembl 2022. *Nucleic acids research*. 2021;50(D1):D988-D995. https://doi.org10.1093/nar/gkab1049.

44. Amores A, Force A, Yan Y-L, et al. Zebrafish hox Clusters and Vertebrate Genome Evolution. *Science*. 1998;282(5394):1711-1714. https://doi.orgdoi:10.1126/science.282.5394.1711.

45. Elizondo LI, Jafar-Nejad P, Clewing JM, Boerkoel CF. Gene clusters, molecular evolution and disease: a speculation. *Curr Genomics*. Mar 2009;10(1):64-75. https://doi.org10.2174/138920209787581271.

46. Cayami FK, Maugeri A, Treurniet S, et al. The first family with adult osteogenesis imperfecta caused by a novel homozygous mutation in CREB3L1. *Mol Genet Genomic Med*. Aug 2019;7(8):e823. https://doi.org10.1002/mgg3.823.

47. Andersson K, Malmgren B, Åström E, Nordgren A, Taylan F, Dahllöf G. Mutations in COL1A1/A2 and CREB3L1 are associated with oligodontia in

osteogenesis imperfecta. *Orphanet journal of rare diseases*. Mar 31 2020;15(1):80. https://doi.org10.1186/s13023-020-01361-4.

48. Lindsay SE, Nicol LE, Gamayo AC, Raney EM. An Unusual Presentation of Osteogenesis Imperfecta: A Case Report. *JBJS Case Connect*. Nov 22 2021;11(4). https://doi.org10.2106/jbjs.Cc.21.00480.

49. Schindelin J, Arganda-Carreras I, Frise E, et al. Fiji: an open-source platform for biological-image analysis. *Nature Methods*. 2012/07/01 2012;9(7):676-682. https://doi.org10.1038/nmeth.2019.

50. Stennicke HR, Salvesen GS. Properties of the caspases. *Biochimica et Biophysica Acta (BBA) - Protein Structure and Molecular Enzymology*. 1998/09/08/ 1998;1387(1):17-31. https://doi.orghttps://doi.org/10.1016/S0167-4838(98)00133-2.

51. Prigent C, Dimitrov S. Phosphorylation of serine 10 in histone H3, what for? *Journal of Cell Science*. 2003;116(18):3677-3685. https://doi.org10.1242/jcs.00735.

52. Hendzel MJ, Wei Y, Mancini MA, et al. Mitosis-specific phosphorylation of histone H3 initiates primarily within pericentromeric heterochromatin during G2 and spreads in an ordered fashion coincident with mitotic chromosome condensation. *Chromosoma*. 1997/11/01 1997;106(6):348-360. https://doi.org10.1007/s004120050256.

53. König D, Page L, Chassot B, Jaźwińska A. Dynamics of actinotrichia regeneration in the adult zebrafish fin. *Developmental Biology*. 2018/01/15/ 2018;433(2):416-432. https://doi.orghttps://doi.org/10.1016/j.ydbio.2017.07.024.

54. Hou Y, Lee HJ, Chen Y, et al. Cellular diversity of the regenerating caudal fin. *Science Advances*. 2020;6(33):eaba2084. https://doi.orgdoi:10.1126/sciadv.aba2084.

55. Farnsworth DR, Saunders LM, Miller AC. A single-cell transcriptome atlas for zebrafish development. *Developmental Biology*. 2020/03/15/ 2020;459(2):100-108. https://doi.orghttps://doi.org/10.1016/j.ydbio.2019.11.008.

56. Fox RM, Hanlon CD, Andrew DJ. The CrebA/Creb3-like transcription factors are major and direct regulators of secretory capacity. *Journal of Cell Biology*. 2010;191(3):479-492. https://doi.org10.1083/jcb.201004062.

57. Saito A, Kanemoto S, Zhang Y, Asada R, Hino K, Imaizumi K. Chondrocyte Proliferation Regulated by Secreted Luminal Domain of ER Stress Transducer BBF2H7/CREB3L2. *Molecular Cell*. 2014/01/09/ 2014;53(1):127-139. https://doi.orghttps://doi.org/10.1016/j.molcel.2013.11.008.

58. Nakagawa Y, Shimano H. CREBH Regulates Systemic Glucose and Lipid Metabolism. *Int J Mol Sci*. May 8 2018;19(5). https://doi.org10.3390/ijms19051396.

59. Luebke-Wheeler J, Zhang K, Battle M, et al. Hepatocyte nuclear factor 4alpha is implicated in endoplasmic reticulum stress-induced acute phase response by

regulating expression of cyclic adenosine monophosphate responsive element binding protein H. *Hepatology*. Oct 2008;48(4):1242-50. https://doi.org10.1002/hep.22439.

60. Pittari D, Dalla Torre M, Borini E, et al. CREB3L1 and CREB3L2 control Golgi remodelling during decidualization of endometrial stromal cells. *Front Cell Dev Biol*. 2022;10:986997. https://doi.org10.3389/fcell.2022.986997.

61. Lee D, Hokinson D, Park S, et al. ER Stress Induces Cell Cycle Arrest at the G2/M Phase Through eIF2α Phosphorylation and GADD45α. *International Journal of Molecular Sciences*. 2019;20(24). https://doi.org/10.3390/ijms20246309.

62. Kondo S, Hino SI, Saito A, et al. Activation of OASIS family, ER stress transducers, is dependent on its stabilization. *Cell Death Differ*. Dec 2012;19(12):1939-49. https://doi.org10.1038/cdd.2012.77.

63. Asada R, Kanemoto S, Kondo S, Saito A, Imaizumi K. The signalling from endoplasmic reticulum-resident bZIP transcription factors involved in diverse cellular physiology. *J Biochem*. May 2011;149(5):507-18. https://doi.org10.1093/jb/mvr041.

64. Towers M, Wolpert L, Tickle C. Gradients of signalling in the developing limb. *Current Opinion in Cell Biology*. 2012/04/01/ 2012;24(2):181-187. https://doi.orghttps://doi.org/10.1016/j.ceb.2011.11.005.

65. Serowoky MA, Kuwahara ST, Liu S, Vakhshori V, Lieberman JR, Mariani FV. A murine model of large-scale bone regeneration reveals a selective requirement for Sonic Hedgehog. *npj Regenerative Medicine*. 2022/05/17 2022;7(1):30. https://doi.org10.1038/s41536-022-00225-8.

66. Cunningham TJ, Duester G. Mechanisms of retinoic acid signalling and its roles in organ and limb development. *Nat Rev Mol Cell Biol*. Feb 2015;16(2):110-23. https://doi.org10.1038/nrm3932.

67. Martín M, Geysels RC, Peyret V, Bernal Barquero CE, Masini-Repiso AM, Nicola JP. Implications of Na(+)/I(-) Symporter Transport to the Plasma Membrane for Thyroid Hormonogenesis and Radioiodide Therapy. *J Endocr Soc*. Jan 1 2019;3(1):222-234. https://doi.org10.1210/js.2018-00100.

68. Di Giusto P, Martín M, Funes Chabán M, Sampieri L, Nicola JP, Alvarez C. Transcription Factor CREB3L1 Regulates the Expression of the Sodium/Iodide Symporter (NIS) in Rat Thyroid Follicular Cells. *Cells*. Apr 13 2022;11(8). https://doi.org10.3390/cells11081314.

69. Westerfield M. *The Zebrafish Book: A Guide for the Laboratory Use of Zebrafish (Danio Rerio)*. University of Oregon Press; 2007.

70. Livak KJ, Schmittgen TD. Analysis of Relative Gene Expression Data Using Real-Time Quantitative PCR and the 2−ΔΔCT Method. *Methods*. 2001/12/01/ 2001;25(4):402-408. https://doi.orghttps://doi.org/10.1006/meth.2001.1262.

71. Schindelin J, Rueden CT, Hiner MC, Eliceiri KW. The ImageJ ecosystem: An open platform for biomedical image analysis. *Molecular Reproduction and Development*. 2015;82(7-8):518-529. https://doi.orghttps://doi.org/10.1002/mrd.22489.

72. Du SJ, Frenkel V, Kindschi G, Zohar Y. Visualizing Normal and Defective Bone Development in Zebrafish Embryos Using the Fluorescent Chromophore Calcein. *Developmental Biology*. 2001/10/15/ 2001;238(2):239-246. https://doi.orghttps://doi.org/10.1006/dbio.2001.0390.

73. Geurtzen K, Vernet A, Freidin A, et al. Immune Suppressive and Bone Inhibitory Effects of Prednisolone in Growing and Regenerating Zebrafish Tissues. *Journal of bone and mineral research : the official journal of the American Society for Bone and Mineral Research*. Dec 2017;32(12):2476-2488. https://doi.org10.1002/jbmr.3231.

74. Poss KD, Shen J, Nechiporuk A, et al. Roles for Fgf signaling during zebrafish fin regeneration. *Dev Biol*. Jun 15 2000;222(2):347-58. https://doi.org10.1006/dbio.2000.9722.

75. Saint-Jeannet J-P. Whole-Mount In Situ Hybridization of Xenopus Embryos. *Cold Spring Harbor protocols*. December 1, 2017 2017;2017(12):pdb.prot097287. https://doi.org10.1101/pdb.prot097287.

LACK OF NUCLEAR LOCALIZATION OF THE CREB3L1 TRANSCRIPTION FACTOR CAUSES DEFECTS IN CAUDAL FIN BIFURCATION IN ZEBRAFISH *DANIO RERIO*

by

PEYTON E VANWINKLE, BRIDGE WYNN, EUNJOO LEE, TOMASZ J NAWARA, HOLLY THOMAS, CECILIA ALVAREZ, JOHN PARANT, ROSA SERRA AND ELIZABETH SZTUL

Under review at *Cells, Tissues, Organs*, 2023

Format adapted for dissertation.

ABSTRACT

The formation of normal bone and bone healing require the cAMP-responsive element binding protein 3-like-1 (Creb3l1) transmembrane transcription factor, as deletion of the murine *CREB3L1* results in osteopenic animals with limited capacity to repair bone after fracture. Creb3l1 undergoes regulated intra-membrane proteolysis (RIP) to release the N-terminal transcription activating (TA) fragment that enters the nucleus and regulates the expression of target genes. To expand our understanding of Creb3l1 role in skeletal development and skeletal patterning, we aimed to generate animals expressing only the TA fragment of Creb3l1 lacking the transmembrane domain and thereby not regulated through RIP. However, the CRISPR/Cas9-mediated genome editing in zebrafish *D. rerio* caused a frame-shift mutation that added 56 random amino acids at the C-terminus of the TA fragment (TA+), making it unable to enter the nucleus. Thus, TA+ doesn't regulate transcription, and the *creb3l1*$^{TA+/TA+}$ fish animals are *creb3l1* transcriptional nulls. We document that the *creb3l1*$^{TA+/TA+}$ fish exhibit defects in the patterning of caudal fin lepidotrichia, with significantly distalized points of proximal bifurcation and decreased secondary bifurcations. Moreover, using the caudal fin amputation model, we show that *creb3l1*$^{TA+/TA+}$ fish have decreased capacity for regeneration, and that their regenerates replicate the distalization and bifurcation defects observed in intact fins of *creb3l1*$^{TA+/TA+}$ animals. These defects correlate with altered expression of the *shha* and *ptch2* components of the Sonic Hedgehog signaling pathway

in *creb3l1*$^{TA+/TA+}$ regenerates. Together, our results uncover a previously unknown intersection between Creb3l1 and the Sonic Hedgehog pathway, and document a novel role of Creb3l1 in tissue patterning.

INTRODUCTION

Factors that regulate skeletal development have been extensively studied in mammalian and other vertebrate model organisms [Marks et al., 2004;Langhans et al., 2015;Rutkovskiy et al., 2016]. Key among them are transcription factors that control the growth, differentiation and function of cells and tissues that contribute to bone formation, homeostasis and repair. One of the transcription factors linked to bone formation and repair is Creb3l1, as patients with *CREB3L1* mutations exhibit osteopenia, severe bone fractures and major bone malformations [Symoens et al., 2013;Keller et al., 2018;Lindahl et al., 2018;Cayami et al., 2019;Guillemyn et al., 2019]. Further proof of Creb3l1 importance in bone formation is provided by *CREB3L1*$^{-/-}$ mice, which exhibit significantly decreased bone density and extensive spontaneous bone fractures, despite having morphologically normal skeletons [Murakami et al., 2009]. Moreover, *CREB3L1*$^{-/-}$ mice do not form normal bony calluses after femur fracture, suggesting a role for Creb3l1 in bone reformation [Funamoto et al., 2011]. The murine system is limited in the study of bone regeneration, as mammals have low capacity for skeletal regrowth after fracture. Thus, to extend our understanding of Creb3l1 function in bone regeneration, we chose the zebrafish *D. rerio* model, which undergoes a well-characterized regeneration of bony tissue after amputation (reviewed in [Sehring and Weidinger, 2020;Dietrich et al., 2021]).

Creb3l1 a member of the ATF/CREB family of transcription factors [Asada et al., 2011;Fox and Andrew, 2015]. Unlike most transcription factors, which are synthesized as soluble cytosolic proteins, Creb3l1 is synthesized as a transmembrane protein of the ER with several domains; a transcriptionally activating (TA) cytosolic N-terminus containing the DNA-binding bZIP domain, a single trans-membrane spanning domain and a luminal tail (Figure 1A). While in the ER, Creb3l1 is inactive since its TA domain lacks access to the nuclear DNA. To become transcriptionally functional, Creb3l1 must be transported from the ER to the Golgi, where it is cleaved through regulated intramembrane proteolysis (RIP) to release the N-terminal TA fragment into the cytosol. The TA fragment contains a nuclear localization signal that mediates its transport into the nucleus, where it binds cAMP response element (CRE) and CRE-like sites to regulate transcription of target genes [Kondo et al., 2005;Saito et al., 2012;Greenwood et al., 2014;Di Giusto et al., 2022]. Importantly, the traffic of Creb3l1 from the ER to the Golgi is tightly controlled and only occurs in response to developmental and physiological cues. Thus, Creb3l1 transcriptional activity is normally repressed, and Creb3l1 requires regulated transport to the Golgi and processing therein to act as a transcription factor.

Previous studies document the skeletal phenotypes when Creb3l1 function is compromised through *CREB3L1* mutations or *CREB3L1* deletion, but there have been no reports on the effects of unregulated activity of Creb3l1. We aimed to explore this by creating a zebrafish that expresses the N-terminal fragment of Creb3l1 that lacks the transmembrane domain, and is therefore capable of bypassing the need for regulated traffic and RIP. We used CRISPR/Cas9-mediated gene editing to target exon 9 of *creb3l1* and isolated an allele that encodes only the first 376 amino acids of Creb3l1 and lacks the

transmembrane and luminal domains. However, the CRISPR/Cas9 RNA guide also caused the addition of 56 amino acids not normally found in Creb3l1 to the C-terminus of the TA fragment to generate *creb3l1*$^{TA+/TA+}$ animals. Unexpectedly, the C-terminal extension prevents the TA+ fragment from entering the nucleus, thereby making the *creb3l1*$^{TA+/TA+}$ allele a transcriptional null.

Herein, we document that the *creb3l1*$^{TA+/TA+}$ fish develop into adults of a size analogous to wild-type fish and without obvious morphological skeletal defects. However, adult *creb3l1*$^{TA+/TA+}$ fish exhibit defects in the patterning of their caudal fins, with a significant distalization of bifurcation points and significantly decreased number of secondary bifurcations on sister rays. We used the caudal fin amputation model to show that the *creb3l1*$^{TA+/TA+}$ fish exhibit defects in caudal fin regeneration, with a significant decrease in the overall size of the regenerate and reduced mineralization of the regenerated lepidotrichia. Moreover, the same defects in the distalization of bifurcation points and limited secondary bifurcations observed during development were also present in the regenerating rays. The positional patterning of the caudal fin is controlled through multiple signaling pathways, including the Sonic Hedgehog pathway [Laforest et al., 1998;Wehner et al., 2014;Armstrong et al., 2017;Sehring and Weidinger, 2020]. We document that the patterning defects observed in the *creb3l1*$^{TA+/TA+}$ regenerates correlate with abnormal transcription of the *shha* and *ptch2* genes. Specifically, in situ hybridization shows that both, *shha* and *ptch2* transcripts fail to fully separate into distinct foci during the regeneration of individual lepidotrichia, and instead remain diffusely distributed above the regenerating rays.

Taken together, our results document that functional Creb3l1 is required for normal caudal fin development and regeneration. Specifically, we uncover a novel role for Creb3l1 in regulating the spatial positioning and the complexity of lepidotrichial bifurcation in caudal fin. Creb3l1 controls these processes during both, caudal fin bone development and during bone regeneration after amputation. This new function of Creb3l1 appears to intersects with the Sonic Hedgehog pathway to facilitate the characteristic ray patterns of *D. rerio* caudal fins, suggesting a novel intersection of two important developmental factors.

MATERIALS AND METHODS

Zebrafish husbandry

Zebrafish (*Danio rerio*) were maintained in accordance with the University of Alabama at Birmingham's Institutional Animal Care and Use Committee, according to the Zebrafish Research Facility and the vertebrate animal welfare protocol (APN 21787). Fish were housed on a circulating water system, on a 14:10 light:dark cycle. Fish were fed Gemma Micro 300 twice daily with one live artemia feeding. Fish were bred using the standard system water and two-piece tank system to prevent oophagy. Eggs were harvested, sorted for healthy eggs, and raised in E3 [Westerfield, 2007] until placed on the system or utilized for experiments.

Generation of creb3l1 mutant fish and SP7-GFP transgenes

Alt-R crRNA target sites were designed with Integrated DNA Technologies Alt-R CRISPR HDR Design Tool (https://www.idtdna.com/pages/tools/alt-r-crispr-hdr-design-tool). Alt-R CRISPR-Cas9 crRNA, tracrRNA (IDT #1072532) and Alt-R S.p. Cas9

Nuclease V3 (IDT #1081058) was prepared following manufacturer instructions. 3 µM sgRNA (Table 1) were obtained through diluting 100 µM crRNA and 100 µM tracrRNA into Nuclease-Free Duplex Buffer (IDT #11-05-01-03), heating at 98ºC for 5 min, then cooling to room temperature. 0.5 µL Cas9 protein was diluted with Cas9 working buffer (20 mM HEPES; 150 mM KCl, pH7.5) to yield a working concentration of 0.5 µg/µL. The diluted Cas9 protein working solution was mixed 1:1 with 3 µM sgRNA solution and then incubated at 37 ºC for 10 min to obtain RNP complex. RNP complex was freshly prepared and left on ice until microinjection. Microinjection was performed by injecting ~1 nL of RNP complex into yolk of 1-cell stage wild-type (AB) embryos.

F0 adults generated from this injection were crossed to AB fish to generate heterozygous offspring. Heterozygous offspring were then sequenced via Sanger Sequencing to determine sequences of CRISPR indels. Sequenced heterozygous fish were crossed to generate homozygous offspring. These offspring were sequenced once more to verify homozygosity for the mutant allele.

Allele	Guide
creb3l1$^{TA+/TA+}$	AAGATCGCCTCAACACAGAC
Sequencing primers:	F: TTTGTGGTCTCTCTCCAGCA R: GGATGGATGGCAGGAAAGTA
Genotyping primers:	F: GATCATCTGTTGGCGGAGAG R: TTGGAGGGTCCAGATCCATA

Table 1: gRNA and primers utilized to generate and characterize *creb3l1*$^{TA+/TA+}$ mutant.

Genotyping by High Resolution Melt Analysis in Zebrafish

To isolate genomic DNA, adult fish were anaesthetized in 250mg/L Tricaine until opercular motion stopped. Tail clippings were collected from fish and incubated at 98°C

for 20 min in 40 µl 25 mM NaOH in a 96-well plate; then neutralized with 40 µl of 40 mM Tris-HCl. For genotyping of whole embryos or larvae, the incubation time at 98°C was shortened to 10 minutes. PCR reactions contained 1 µl of LC Green Plus Melting Dye (Biofire Defense, BCHM-ASY-0005), 1 µl of 10x enzyme buffer, 0.2 µl of dNTP Mixture (10 mM each), 0.3 µl of $MgCl_2$, 0.3 µl of each primer (10 µM), 1 µl of genomic DNA, 0.05 µl of Taq (Genscript #E00101), and water up to 10 µl. Primers are detailed in Table 1. The PCR reaction protocol was 98ºC for 30 sec, then 45 cycles of 98ºC for 10 sec, 59ºC for 20 sec, and 72ºC for 15 sec, followed by 95ºC for 30 sec and then rapid cooling to 4ºC. Following PCR, melting curves were generated and analyzed using the LightScanner instrument (Idaho Technology) over a 65-95°C range.

RT-PCR

7dpf larvae were anaesthetized with tricaine and collected (~30 fish/pool). Pooled larvae were homogenized by pestle in Trizol and purified using a Direct-zol RNA Miniprep Plus Kit from Zymo Research (Cat. # R R1058), including gDNA removal. The concentration of the RNA was measured using a NanoDrop ND-1000. RNA with a 260/280 of ~2.0 was used for further analyses. Up to 2µg of RNA was utilized to synthesize cDNA in the High-Capacity cDNA Reverse Transcription Kit (Applied Biosystems, Cat. # 4368814) with RNAse inhibitor (Invitrogen, Cat. # 10777019). Prepared cDNA was used for RT-PCR, using a SYBR Green Power UP (Applied Biosystems, Cat. A25742) master mix, with 0.8 mM Primer concentration (all primers are listed in Table S3). A 10 µL final volume reaction was prepared, with 1 µL of cDNA. This was run using the standard cycling time/temperatures for SYBR Green Power UP.

mCT

Adult fish were fixed in 4% PFA (paraformaldehyde) in phosphate buffered saline (PBS, pH 7.4) with 0.5% Triton X-100 overnight at 4°C. Fixed zebrafish were scanned using the Scanco µCT40 desktop cone-beam micro-CT scanner (Scanco Medical AG, Brüttisellen, Switzerland) using µCT Tomography v6.4-2 (Scanco Medical AG, Brüttisellen, Switzerland). Scans were automatically reconstructed into 2-D slices and slices were analyzed using the µCT Evaluation Program (v.6.5-2, Scanco Medical). The zebrafish were placed in a 36mm diameter scanning holder and scanned at the following settings: 18µm voxel size, 70kVp, 114µA, 1000 projections/180 degrees with an integration time of 200ms. The region of interest was drawn around the fish and the analysis was performed on all slices that any part of the fish appeared in. Bone was thresholded at 140.3 mgHA/ccm and the 3-D analysis performed. Data were obtained on bone volume and density. 3D images were obtained from the 3D evaluation software (µCT Ray v.4.2, Scanco Medical).

Measurement of uninjured fish

The length of fish at 6 mpf was measured with a ruler and recorded. Tails of both wild-type and mutant fish carrying the sp7::eGFP transgene were imaged on a Nikon AZ100 dissection microscope with fluorescent filters to visualize gross morphology of the caudal fin. Photos were analyzed in FIJI ImageJ 1.54f) [Schindelin et al., 2015] to measure the indicated parameters.

Caudal fin amputation model of regeneration and visualization of mineralized regenerate

Fish at indicated age were anaesthetized in a 250 mg/L tricaine until opercular motion was slowed and fish were no longer responsive to touch. Fish underwent 50%

tailfin amputation via transection with a #10 scalpel blade. Tails were photographed after amputation. Fish were then recovered in system water and allowed to regenerate for the indicated times.

The size and patterning of the mineralized regenerate was evaluated by a protocol adapted from Cardiera et. al (Cardeira et al., 2016). Briefly, utilizing FIJI (ImageJ 1.53f51)(Schindelin et al., 2015), the total area of the regenerate (REG) of the amputated tail was measured using the FIJI Measure function, then normalized to the width of the stump at the amputation plane (STU). To measure the real mineralized area (RMA), the polygon tool was utilized to outline the fluorescently labelled bones with the distal tip of each lepidotrichia and the base of the regenerated area marking the boundary of the estimated mineralized area. Using this selected region, the threshold tool was utilized to isolate pixels of fluorescently-stained bone based on individual image intensity histograms (16 bit image binning). The total area of these particles was then analyzed via the Analyze Particles function in FIJI. In addition, the distance of bifurcation from the amputation plane in both calcein stained and transgenic fish was measured on the 2nd and 3rd most lateral fin rays on the tail, using the line segment tool.

Visualization of Sp7^{+} cell populations during regeneration

For analysis of tail regeneration over time, *creb3l1* mutant fish were outcrossed to AB Ola.Sp7:EGFP-CAAX [Nachtrab et al., 2013] fish, henceforth referred to as Sp7::eGFP, or *creb3l1*$^{sp7::eGFP/+}$ fish. Resultant heterozygotes were then incrossed with homozygous CREB3L1 mutants to generate fish homozygous for their respective mutations, and heterozygous for the Sp7::eGFP transgene. Fish were screened at 3-5 dpf

for fluorescence in the craniofacial bones and raised according to standard husbandry protocols.

For dynamic analyses of caudal fin regeneration, wild-type and CREB3L1 mutant fish expressing Sp7::eGFP underwent amputation as described above. Fish were returned to system water, and imaged using a Nikon AZ100 dissection microscope at 3, 7, 9 and 14 dpa, under tricaine anesthetic. The images were evaluated for the length of the regenerate and the area of $Sp7^{+}$ cells, using the same methods used to quantify and normalize RMA (see above). In addition, distance from the amputation plane to the first bifurcation point was measured in both calcein stained and transgenic fish on the 2nd and 3rd most lateral fin rays on the tail, using the line segment tool.

In situ hybridization

3 and 7 dpa fins were amputated via surgical scissors and fixed overnight at 4°C in 4% PFA in PBS (pH 7.4). The tails were treated as previously described [Poss et al., 2000], with slight modifications. Briefly, fins were washed in PBS, and dehydrated in 100% methanol for at least 2 hours at -20°C. Dehydrated fins were rehydrated stepwise with 5 min washes in ethanol (75% EtOH/25% PBST, 50% EtOH/50% PBST, 25% EtOH/75% PBST), and washed in PBS with 0.1% Tween 20 (PBST) before 1 hr of prehybridization and subsequent overnight hybridization with 0.5mg/mL digoxigenin-conjugated probes in hybridization buffer (HB) containing 50% Formamide, 5xSSC saline sodium citrate, 1mg/mL Torula RNA (Sigma-Aldrich Cat.#R6625), 100 µg/mL heparin, 1x Denhart's, 0.1% Tween 20, 5 mM EDTA) [Saint-Jeannet, 2017] in a 65°C water bath. Hybridized tails were washed for 10 min at 65°C in stepwise HB/2xSSC solutions (75% HB/25% 2xSSC, 50% HB/50% 2xSSC, 25% HB/75% SSC) followed by

a series of 0.2xSSC/PBS 5 min washes with (75% 0.2xSSC/25% PBST, 50% 0.2xSSC/50% PBST, 25% 0.2xSSC/75% PBST). Washed tails were blocked in 2mg/mL BSA in PBST for one hour at RT, and then incubated with tail pre-adsorbed anti-DIG antibody fragments (Roche, Sigma-Aldrich Ca. #11093274910, diluted 1:2000) for two hours at RT. Tails were then washed 3x with a staining solution (100 mM Tris-HCl (pH 9.5), 50 mM $MgCl_2$, 100 mM NaCl, 0.1% Tween 20, 1 mM levamisole) and incubated in BM Purple (Roche, Sigma-Aldrich Ca. #11442074001) until developed (overnight at RT or 4ºC to reduce background.) Stained tails were washed in multiple PBST washes and fixed with 4% PFA overnight at 4ºC. and washed again multiple times. Prepared tails were mounted in a 12 well culture plate in PBST and imaged using a Leica M205 FCA dissection microscope.

Gene	Linearizing enzyme	Polymerase
creb3l1	Not1	T3
ptch2	XbaI	T3
shha	HindIII	T7

Table 2: Details of plasmid preparation to generate in situ probes.

Gene	Primers	Use
creb3l1	F: GCAGAGCCCTCTCCTCAC R: GCACCCGTTTGAGTGCTTT	RT-PCR
Elfa (housekeeping gene)	F: TACCCTCCTCTTGGTCGC R: TTGGAACGGTGTGATTGAG	RT-PCR
creb3l1	F: GAT GCGGCCGCCTGTGTTTTGTGTTGGT R: GATCGTCGACGAAATATTCAGCTCCTCC	Generation of plasmid for in situ probe template

Table 3: Details of primers utilized to clone from zebrafish cDNA.

Immunofluorescence

Cells were processed as in [Omori et al., 2002;Kondo et al., 2005;Murakami et al., 2006;Schubert et al., 2008;García et al., 2017]. Cells were fixed in 3% paraformaldehyde in PBS for 15 min, and quenched with 10 mM ammonium chloride in PBS for another 10 min. Subsequently, cells were permeabilized in 0.1% Triton X-100 in PBS for 10 min. Coverslips were then washed in PBS, blocked in PBS containing 2.5% goat serum and 0.2% Tween 20 for 5 min, and in PBS, 0.4% fish skin gelatin and 0.2% Tween-20 for another 5 min. Cells were incubated with primary antibody (anti-HA, BioLegend Ca.# 901501. Anti-GM130, Proteintech Group Ca.# 11308-1-AP) diluted in 0.4% fish skin gelatin for 1 h at room temperature, washed in PBS–0.2% Tween 20, and blocked as described above. Cells were then incubated with secondary antibodies (Goat-anti-rabbit IgG-Alexa Fluor Plus 594, Thermo Scientific Ca.# A32740. Goat anti Mouse IgG-Alexa Fluor 488, Thermo Scientific Ca.# A-11001)diluted in 2.5% goat serum for 1 hr at room temperature. Nuclei were stained using DAPI (Thermo Scientific™ Ca. #62248) for 3 minutes. Coverslips were then washed 5x with PBS–0.2% Tween 20 and mounted on slides in ProLong Gold antifade reagent (Invitrogen P36980). Cells were visualized with a Nikon Ti2 widefield microscope, with a 20x objective, and images were processed utilizing the Nikon Acquisition software and FIJI [Schindelin et al., 2012].

Western blot analysis

Cells were lysed in RIPA buffer(10), and mixed with 4x Laemmli Sample buffer (BioRad Ca. #1610747). Samples were loaded into 8% Tris-Glycine gels (Fisher Scientific Ca. # XP00085BOX) with the Precision Plus (Bio-Rad Ca. #1610374) and ran

using a Novex mini gel tank (Thermo Fisher Ca. #NW2000). The gels were then blotted on nitrocellulose membranes and blocked for using 5% dry powdered milk. Blocked membranes were stained with appropriate antibodies (anti-HA, BioLegend Ca.# 901501Anti-BIG2, EMD Millipore Ca.# MABS1246) for one hour to overnight at RT or 4ºC. Membranes were washed 3x for 5 minutes in Tris-buffered Saline (TBST) and incubated in appropriate HRP-Conjugated secondary antibodies (Goat-anti-mouse IgG-HRP, Southern Biotech, Ca. #1030-05) Membranes were washed 3x in TBST before imaging with SuperSignal™ Chemiluminescent substrate (Thermo Fisher™ Ca. #34578X4) on an Bio-Rad ChemiDoc™ MP Imaging System. Resultant images were processed in FIJI [Schindelin et al., 2012]

Statistical analyses

All experiments were performed in duplicate or greater. Data were collected and analyzed with Graphpad Prism - Version 10. Mendelian ratio data (Figure 2B) was analyzed using a chi-square analysis of observed vs. expected values. All other data comparing *creb3l1* wild-type vs. mutant fish were first analyzed for normality of the data and descriptive statistics. Based on these analyses, the appropriate analyses of non-paired data were chosen; for normal data, unpaired t-tests were utilized, with or without Welch's correction for differences instandard deviation. For data that was not normally distributed, the non-parametric Mann-Whitney test was utilized. Significance was determined as a $p<0.05$ threshold. (* $p\leq0.05$; ** $p\leq0.01$; *** $p\leq0.001$, **** ≤0.0001).

RESULTS

1. Generation of *creb3l1*$^{TA+/TA+}$ fish

To further our understanding of Creb3l1 function in bone development, we aimed to generate a *creb3l1* allele that expresses only the N-terminal fragment of Creb3l1 (amino acids 1-379) lacking the transmembrane and luminal domains (Figure 1A, 1-379). This fragment would make the transcriptional activity of Creb3l1 independent of developmental or physiological stimuli, as the nuclear entry of the N-terminal fragment would not require the trafficking and RIP processing of full-length Creb3l1. However, CRISPR/Cas9-mediated genome editing using a guide RNA targeting exon 9 (Figure 1B) induced a net insertion of +4 base pairs (removed 5 base pairs and inserted 9 base pairs) at 1118 bp of the coding mRNA (Figure 1B, black arrow), leading to a mutation at amino acid 375 (a change of T to I), followed by a frameshift resulting in the addition of 56 amino acids (Figure 1B, residues in green) not present in wild-type Creb3l1, before the frameshift-induced TGA stop codon.

To test for missense mediated decay of the mutant mRNA, *creb3l1* mRNA levels were assessed by RT-PCR in wild-type and *creb3l1*$^{TA+/TA+}$ larvae (primers are listed in Table 3). As shown in Figure 1C, transcription of *creb3l1* was upregulated ~1.5-fold in *creb3l1*$^{TA+/TA+}$ fish, indicating that the mutant mRNA is not degraded and could be translated into a TA+ fragment.

To assess whether the mutant mRNA is translated into a protein and if so, whether the produced peptide can enter the nucleus, we used a heterologous system. We used a mammalian expression vector to generate three constructs: 1) vector containing the coding sequence of the *D. rerio* wild-type *creb3l1*$^{+/+}$; 2) vector containing the coding

sequence of the *creb3l1*$^{TA+/TA+}$ allele; and 3) vector containing the coding sequence of amino acids 1-379 of Creb3l1, the true TA without additional amino acids (as in Figure 1A). Each protein was tagged at its C-terminus with an HA (YPYDVPDYA) tag. The three constructs were transfected into HEK (human embryonic kidney) or HeLa cells, and the expression and the localization of the proteins were assessed by Western immunoblotting and immunofluorescence. The behavior of the TA+ fragment was compared to that of wild-type Creb3l1 and the 1-379 amino acid-long true TA fragment.

Western blotting with anti-HA of cell lysates detects proteins of the expected molecular weight in the relevant lanes, with a band of ~70 kDa for full-length Creb3l1 (Figure 1D, FL lane), a size reported before that most likely represents the phosphorylated or otherwise post-translationally modified ~59 kDa peptide [Chen et al., 2014;Kamikawa et al., 2021]. We detected a band of ~55 kDa for the TA+ fragment (TA+ lane), and a slightly smaller band of ~54 kDa for the 1-379 fragment (lane 1-379). The sizes of both fragments are slightly larger than those calculated based on the number of amino acids (~48 kDa for TA+ and ~43 kDa for 1-397), most likely reflecting phosphorylation of both peptides. The lack of bands in not transfected cells (NT lane) or cells transfected with an empty vector (EV lane) documents the specificity of the immunoblot. The lower recovery of the TA+ fragment is due to aggregation (see below), suggesting that although the protein is stably expressed, it forms aggresomes that are known to be resistant to lysis [García-Mata et al., 1999;Lamark and Johansen, 2012].

Immunofluorescence analysis using anti-HA to detect the Creb3l1 constructs and anti-GM130 to visualize the Golgi shows full-length Creb3l1 localized in an ER pattern, as evidenced by a clearly defined nuclear “ring” (Figure 1E, arrows) and a reticular

network of tubules seen in cell periphery (Figure 1E, right panel). This ER localization is consistent with previous reports [Omori et al., 2002;Kamikawa et al., 2021]. In contrast, the TA+ fragment is not detected in the expected nuclear pattern, and instead appears in amorphous foci within the cytosol (Figure 1F, arrows). Even in cells expressing high levels of the TA+ fragment, the protein is not seen in the nucleus, but appears coalesced into aggregates within the cytoplasm (Figure 1F, right panel, arrows). The TA+ localization is in stark contrast to the distribution of the 1-379 true TA fragment, which shows the expected nuclear localization Figure 1F.

Together, these results suggest that the 56 random amino acids added to the C-terminus of the TA fragment cause aggregation and inhibit the translocation of TA+ into the nucleus, thereby precluding TA+ from binding DNA to regulate transcription of target genes. Thus, our results imply that the *creb3l1*$^{TA+/TA+}$ allele doesn't generate a constitutively transcription activating TA fragment, but instead represents a *creb3l1* transcriptional null.

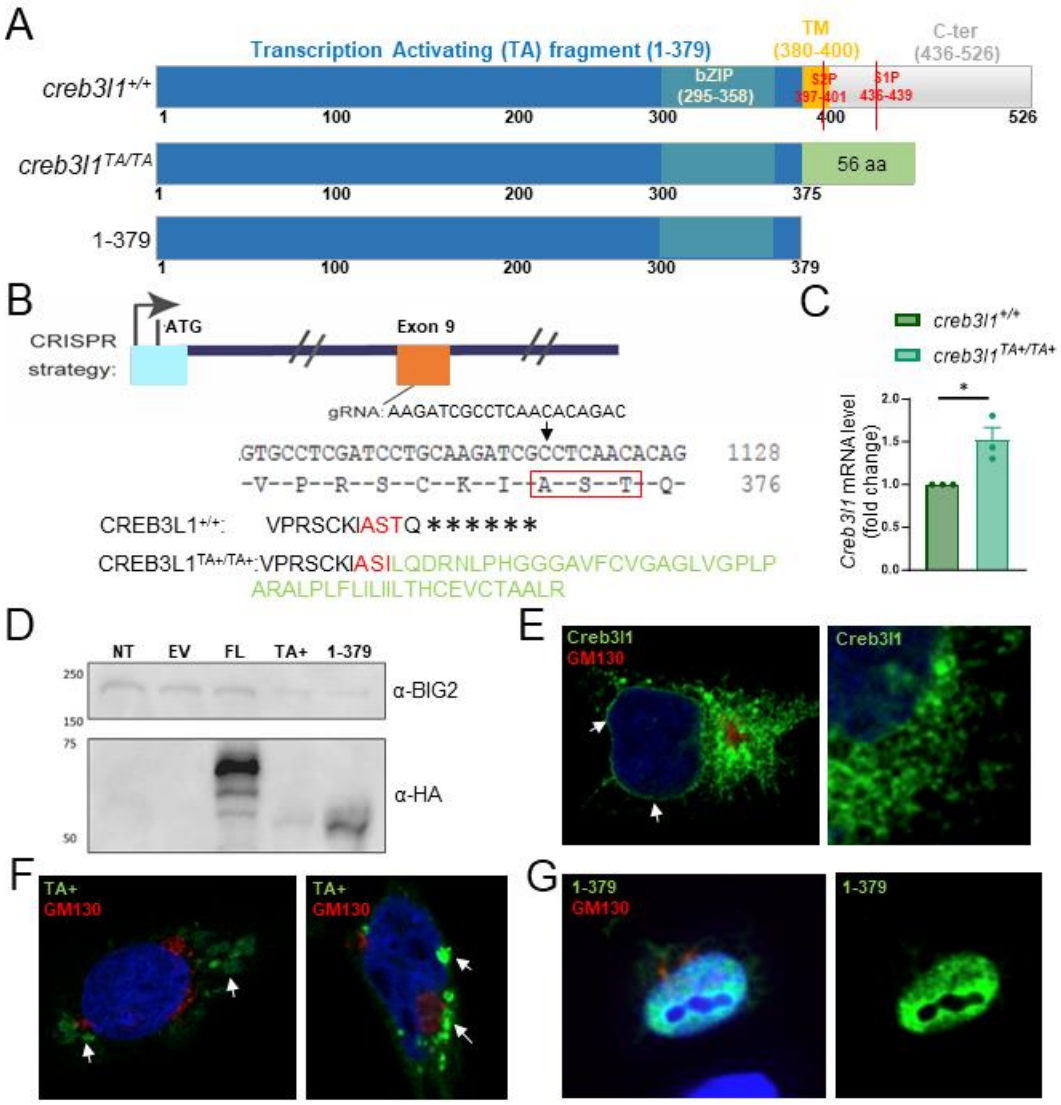

Figure 1. Generating *creb3l1* mutant zebrafish

A) Schematic representation of constructs expressing full length zebrafish Creb3l (creb3l1$^{+/+}$), the CRISPR/Cas9-generated TA fragment (*creb3l1*$^{TA+/TA+}$), and a fragment encoding amino acids 1-379 (1-379) that is generated *in vivo* by S2P cleavage. The domains are represented by different colors and the sites cleaved by S1P and S2P are indicated. The 56 amino acids added to the C-terminus of the TA fragment are in green.

B) Exon 9 of the zebrafish *creb3l1* gene was targeted to generate *creb3l1*$^{TA+/TA+}$ fish with a +4 bp insertion (5 bp deletion and 9 bp insertion) that causes a frameshift mutation at amino acid 375 (T to I in the AST sequence, in red). The *creb3l1*$^{TA+/TA+}$ allele encodes a fragment of *creb3l1* that contains the TA domain followed by 56 amino acids (in green) not found in Creb3l1.

C) *creb3l1* mRNA levels were assessed in *creb3l1*$^{+/+}$ and *creb3l1*$^{TA+/TA+}$ 7dpf larvae. The *creb3l1*$^{TA+/TA+}$ larvae show elevated levels of *creb3l1* transcript. n=3-4, ***p<0.001. Each data point represents a pool of ~30 larvae.

D) HEK cells were mock transfected, or transfected with empty vector, vector encoding either creb3l1$^{+/+}$, *creb3l1*$^{TA+/TA+}$, or the 1-397 construct shown in A (each tagged with HA at C-terminus), and after 24 hours, cells were lysed and the lysates analyzed by SDS-PAGE and Western blotting with anti-HA and anti-BIG1 (loading control). Bands of the appropriate MW were detected in the relevant lanes, but not in lanes containing untransfected cells or cells transfected with empty vector, showcasing the specificity of the immunoblot.

E-G) HeLa cell were transfected with creb3l1$^{+/+}$, *creb3l1*$^{TA+/TA+}$, or the 1-397 construct shown in A (each tagged with HA at C-terminus), and after 24 hours, cells were processed for double immune-fluorescence with anti-HA and anti-GM130 (Golgi marker) and stained with DAPI. E) full-length creb3l1$^{+/+}$ localizes to ER, as indicated by its presence in ER continuous with the nuclear membrane (left panel, white arrows) and in anastomosing ER tubules in cell periphery (right panel). F) The *creb3l1*$^{TA+/TA+}$ fragment is detected in amorphous cytoplasmic foci (left panel, white arrows). In cells expressing higher levels of *creb3l1*$^{TA+/TA+}$, the protein is sequestered in cytoplasmic aggregates (right panel, white arrows). G) The 1-397 fragment is concentrated in the nucleus (left panel), indicating efficient nuclear import. The right panel shows only the 1-397 signal.

2. *creb3l1*$^{TA+/TA+}$ fish do not exhibit defects in size, overall skeletal development, or bone density

Heterozygous *creb3l1*$^{+/TA+}$ fish were crossed, and their offsprings genotyped at 7 days post fertilization (dpf) to determine the effect of lack of Creb3l1 function on viability. As shown in Figure 2A, larvae from *creb3l1*$^{+/TA+}$ pairings are recovered at relatively normal Mendelian ratios, and no statistically significant change was seen when the observed versus the expected results were compared via a chi-square analysis. However, a consistent slightly lower recovery of the *creb3l1*$^{TA+/TA+}$ larvae was observed, suggesting a possible decrease in fitness. Overall, it appears that the lack of functional Creb3l1 is not lethal or significantly detrimental to larval survival. Moreover, mature, fertile *creb3l1*$^{TA+/TA+}$ fish were obtained from the incrosses, and their overall growth, measured as length at 6 months post fertilization (mpf), was not significantly different from *creb3l1*$^{+/+}$ fish (Figure 2B).

Skeletal development of wild-type and *creb3l1*$^{TA+/TA+}$ fish at 3 and 8 mpf was assessed by mCT scans. As shown in Figure 2C, no obvious skeletal malformations were observed in *creb3l1*$^{TA+/TA+}$ fish relative to wild-type fish. This phenotype is in agreement with the lack of skeletal deformation in the *Creb3l1* KO mice [Murakami et al., 2009]. Skeletal development appeared normal in both female and male *creb3l1*$^{TA+/TA+}$ fish (data not shown), indicating lack of sexual dimorphism in the response to loss of Creb3l1 function.

CREB3L1 has been shown to be required for normal bone density in mammals, as *CREB3L1* KO mice show porous fragile bones, a phenotype also observed in human patients with *CREB3L1* mutations [Symoens et al., 2013;Lindahl et al., 2018;Cayami et al., 2019;Andersson et al., 2020;Lindsay et al., 2021]. In contrast, mCT analysis of *creb3l1*$^{+/+}$ and *creb3l1*$^{TA+/TA+}$ fish at 3 and 8 mpf showed no significant difference in bone density as measured by the amount of hydroxyapatite (HA) in milligrams (mg) per cubic centimeter (ccm) (Figure 2D). Thus, lack of Creb3l1 function has no major deleterious effects on zebrafish skeletal development.

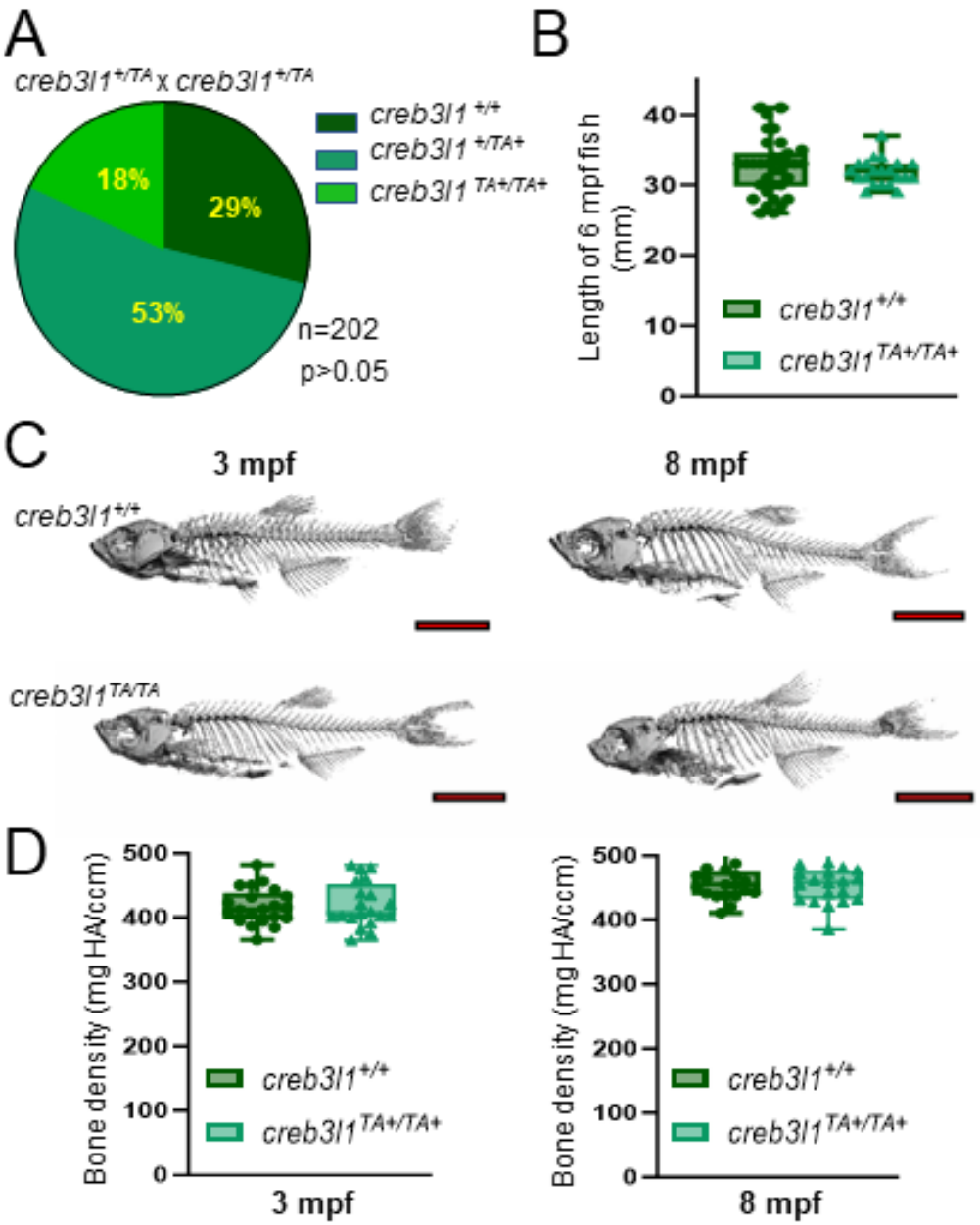

Figure 2: *creb3l1*$^{TA+/TA+}$ fish exhibit no significant changes in size, skeletal morphology or bone density

A) Larvae from heterozygous *creb3l1*$^{TA+/+}$ incrosses were genotyped at 7 dpf and the recovery ratios are presented. Nearly Mendelian ratios were obtained, with a slight decrease in the recovery of *creb3l1*$^{TA+/TA+}$ animals. n and p values are indicated.

B) Body length of 6 mpf *creb3l1*$^{+/+}$ and *creb3l1*$^{TA+/TA+}$ fish was measured. No significant difference in size was apparent. n=21-34. Each data point represents an individual fish.

C) Representative mCT scans of *creb3l1*$^{+/+}$ and *creb3l1*$^{TA+/TA+}$ male fish at 3 and 8 mpf. No obvious defects in skeletal morphology was seen when visualized by 3D projections of the mCT scans. n=9-11

E) Bone density (mgHA/ccm) was measured by mCT scans in *creb3l1*$^{+/+}$ and *creb3l1*$^{TA+/TA+}$ fish at 3 and 8 mpf. Values for male fish are presented (analogous values were obtained for female fish, data not shown). No significant differences in bone density was detected. n=9-11. Each data point represents an individual fish.

3. Caudal fins of *creb3l1*$^{TA+/TA+}$ fish exhibit defects in bifurcation of lepidotrichia

To easily follow bone development events, we crossed our *creb3l1*$^{+/+}$ and *creb3l1*$^{TA+/TA+}$ fish to a transgenic fish line expressing eGFP under the regulatory region of the osteoblast-specific transcription factor SP7 (*Sp7::eGFP* (ZFIN: pd51Tg) [Nachtrab et al., 2013]). As shown in Figure 3A, both, the *creb3l1*$^{+/+,Sp7::eGFP/+}$ and the *creb3l1*$^{TA+/TA+,Sp7::eGFP/+}$ fish express *sp7::eGFP* in their caudal fins, thereby allowing the analysis of bony structures within the tail. The length of the tail was determined after averaging the lengths of the 2nd and 3rd fin ray in each lobe from the caudal peduncle to the end of the fin (Figure 3A, light blue lines). As shown in the quantification in Figure 3C, no significant difference ($p>0.9$) in fin length was observed between *creb3l1*$^{+/+,Sp7::eGFP/+}$ and *creb3l1*$^{TA+/TA+,Sp7::eGFP/+}$ fish. This is consistent with the analogous body length of *creb3l1*$^{+/+}$ and *creb3l1*$^{TA+/TA+}$ fish shown above, as fish tail growth is isometric to body growth.

We next measured the area occupied by Sp7^{+} osteoblasts, as a reflection of ray bone development. During growth, osteoblasts line the inside and the outside of each semi-circular hemi-ray of each lepidotrichium, and thus outline the newly formed bone. The entire fluorescent area from the tips of the scales (Figure 3A, orange lines) to the tips

of the rays was measured. To correct for variation in tail size of individual fish, the total fluorescent area was divided by tail width to generate $Sp7^{+}$ area/tail. As shown in Figure 3D, no significant difference in $Sp7^{+}$ area/tail was observed between *creb3l1*$^{+/+,Sp7::eGFP/+}$ and *creb3l1*$^{TA+/TA+,Sp7::eGFP/+}$ fish.

In mature zebrafish, caudal fins are supported by 16-18 lepidotrichia, all of which except the most ventral and dorsal one are split into two sister rays. The point at which the sister rays bifurcate (bifurcation depth) varies between rays, but the overall pattern is consistent from animal to animal. In addition, some sister rays form secondary, more distal bifurcations to generate an overall ray pattern specific to a particular species of fish. Changes in bifurcation depth and/or in secondary bifurcations occur in response to defects in multiple developmentally regulated signaling pathways and are easily scored.

To assess the effect of loss of Creb3l1 function on the bifurcation depth of sister rays, we measured the distance between the caudal peduncle and the first bifurcation point of the 2nd and 3rd lepidotrichia in each lobe of *creb3l1*$^{+/+}$ and *creb3l1*$^{TA+/TA+}$ fish (Figure 3A, pink lines). When the averages of such measurements were analyzed, a significant decrease in the bifurcation depth was observed in *creb3l1*$^{TA+/TA+}$ fish relative to *creb3l1*$^{+/+}$ fish (Figure 3E). This indicates a substantial distalization of the bifurcation point of sister rays and implies an alteration in the proximo-distal axis in the *creb3l1*$^{TA+/TA+}$ animals.

We next assessed the bifurcation complexity in tails of *creb3l1*$^{+/+}$ and *creb3l1*$^{TA+/TA+}$ fish by counting the number of rays present at the very distal end of the tail. As shown in Figure 3F, the *creb3l1*$^{TA+/TA+}$ fish have significantly fewer bifurcations. This overall decrease is due to a significant reduction in secondary bifurcations of sister

lepidotrichium bifurcates (Figure 3B, red arrows), but in *creb3l1*$^{TA+/TA+}$ fish, only one of the sister rays bifurcates (Figure 3B, red arrow). Similarly, in *creb3l1*$^{+/+}$ fish, one of the sister rays of the 5th lepidotrichium bifurcates (Figure 3B, blue arrow), but the corresponding sister ray in *creb3l1*$^{TA+/TA+}$ fish doesn't bifurcate (Figure 3B, blue arrow). These results suggest that loss of Creb3l1 function causes the distalization of both, the initial separation of lepidotrichia into sister rays and the secondary bifurcation of the sister rays. Moreover, it appears that the distalization of some sister rays is so severe as to preclude secondary bifurcations.

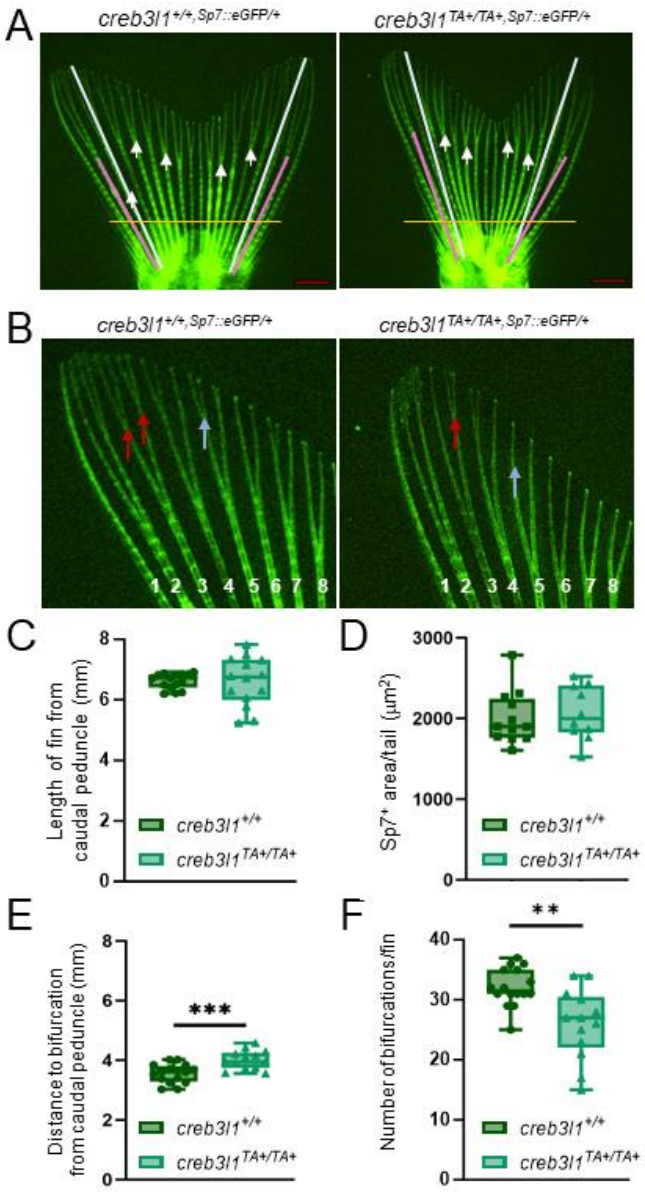

Figure 3: *creb3l1*$^{TA+/TA+}$ zebrafish exhibit defects in caudal fin ray bifurcation

A) Fins of 6 mpf *creb3l1*$^{+/+,Sp7::eGFP/+}$ and *creb3l1*$^{TA+/TA+,Sp7::eGFP/+}$ fish were examined by direct fluorescence. The length of fins was measured from the caudal peduncle to the tip of the 3rd ray in both lobes (white lines). Bifurcation depth of the 2nd and 3rd ray was measured from the caudal peduncle to the bifurcation point in both lobes (pink lines) and averaged. Secondary bifurcations are marked with white arrows. Orange line demarcates the region used to quantitate $Sp7^+$ area (all area distal to the orange lane). Scale bar = 1 mm.

B) Higher magnification of representative images of caudal fins from *creb3l1*$^{+/+,Sp7::eGFP/+}$ and *creb3l1*$^{TA+/TA+,Sp7::eGFP/+}$ fish. Red arrows point to secondary bifurcations of 3rd sister rays, while blue arrows points to a secondary bifurcation of 5th sister ray.

C) The lengths of tails are not significantly different between *creb3l1*$^{+/+,Sp7::eGFP/+}$ and *creb3l1*$^{TA+/TA+,Sp7::eGFP/+}$ fish. n=14-15. Each data point represents an individual fish.

D) The Sp7^{+} area/tail is not significantly different between *creb3l1*$^{+/+,Sp7::eGFP/+}$ and *creb3l1*$^{TA+/TA+,Sp7::eGFP/+}$ fish. n=13-23. Each data point represents an individual fish.

E) The distance from caudal peduncle to the first point of bifurcation is significantly increased in *creb3l1*$^{TA+/TA+,Sp7::eGFP/+}$ fins relative to *creb3l1*$^{+/+,Sp7::eGFP/+}$ fish. n=13-16. Each data point represents an individual fish. ***p≤0.001

F) The total number of bifurcations per fin were assessed and show that *creb3l1*$^{TA+/TA+,Sp7::eGFP/+}$ fins have significantly fewer bifurcations/fin relative to *creb3l1*$^{+/+,Sp7::eGFP/+}$ fins. n=13-16. Each data point represents an individual fish. **p≤0.01

4. Regeneration of caudal fins is compromised in *creb3l1*$^{TA+/TA+}$ fish

Despite the lack of notable skeletal defects during *creb3l1*$^{TA+/TA+}$ fish development, but in light of the caudal fin patterning defect, we sought to test whether the loss of functional Creb3l1 may affect bone regeneration. In order to do this, a caudal fin amputation model was utilized. In this model, ~50% of the tail fin is removed, causing an injury that is repaired in wild-type zebrafish within a few weeks [Sehring and Weidinger, 2020;Uemoto et al., 2020]. The model was used to visualize bone regeneration in 6 mpf *creb3l1*$^{+/+,Sp7::eGFP/+}$ and *creb3l1*$^{TA+/TA+,Sp7::eGFP/+}$ fish [Sehring and Weidinger, 2020]. Tails were examined at 7, 9 and 14 days post amputation (dpa) by fluorescence, and the length of the regenerate was determined after averaging the lengths of the 2nd and 3rd fin ray in each lobe from the caudal peduncle to the end of the fin (Figure 4A, light blue lines). As shown in Figure 4B, no significant difference (p>0.9) in regenerate length was observed between *creb3l1*$^{+/+,Sp7::eGFP/+}$ and *creb3l1*$^{TA+/TA+,Sp7::eGFP/+}$

fish at any of the time points. This parallels the lack of difference in body and tail length of adult *creb3l1*$^{+/+}$ and *creb3l1*$^{TA+/TA+}$ fish.

We next measured the area occupied by Sp7^{+} osteoblasts, as a reflection of newly formed bone during regeneration. The entire fluorescent area distal to the amputation plane was measured. To correct for possible variation in tail size prior to amputation, we measured the width of all lepidotrichia in each lobe below the amputation plane (Figure 4A, sienna lines), and the total fluorescent area was divided by the average ray width to generate the Sp7^{+} area/ray value. As shown in Figure 4C, *creb3l1*$^{TA+/TA+,Sp7::eGFP/+}$ fish exhibit a significantly decreased osteoblast area at every time point post amputation. This decrease occurs despite the normal length of the regenerate, and indeed the rays in the *creb3l1*$^{TA+/TA+,Sp7::eGFP/+}$ regenerate are thinner and spindly.

To assess the positional memory of of the *creb3l1*$^{TA+/TA+,Sp7::eGFP/+}$ fish regenerates, distance from the amputation plane to the first point of bifurcation was measured in the 2nd and 3rd lepidotrichia of each lobe in the regenerates at each time point after amputation (Figure 4A, 14 dpa panels, pink lines). As shown in Figure 4D, the average distance between the caudal peduncle and the bifurcation point was significantly increased in the *creb3l1*$^{TA+/TA+,Sp7::eGFP/+}$ fish, with distalization of the bifurcation point already evident at 7 dpa. Although there was no statistically significant difference at 9 dpa, this is due to increased variability of this cohort, and the *creb3l1*$^{TA+/TA+,Sp7::eGFP/+}$ fish trended towards increased bifurcation depth. A highly significant distalization of the bifurcation point was evident in the 14 dpa *creb3l1*$^{TA+/TA+,Sp7::eGFP/+}$ regenerates.

The *creb3l1*$^{TA+/TA+,Sp7::eGFP/+}$ regenerates also exhibit less complex bifurcation, with a significant decrease in the total number of bifurcations per fin at every analyzed

dpa (Figure 4E). As in the uninjured fin of adult *creb3l1*$^{TA+/TA+,Sp7::eGFP/+}$ fish, the decrease was predominantly due to deficits in secondary bifurcations of sister rays. While secondary bifurcations were already evident in 7 dpa *creb3l1*$^{+/+,Sp7::eGFP/+}$ regenerates (Figure 4A, 7 dpa, red arrows), *creb3l1*$^{TA+/TA+,Sp7::eGFP/+}$ regenerates lacked secondary bifurcations even at 14 dpa. Thus, in addition to defects in regenerating osteoblastic tissue, the *creb3l1*$^{TA+/TA+,Sp7::eGFP/+}$ fish demonstrate deficits in spatial patterning of bony structures.

The reduced area occupied by Sp7^{+} osteoblasts in *creb3l1*$^{TA+/TA+,Sp7::eGFP/+}$ regenerates prompted us to determine whether the mineralization of the regenerating bone also might be affected. We performed 50% tail amputation on 6 mpf *creb3l1*$^{+/+}$ and *creb3l1*$^{TA+/TA+}$ fish, and stained 9 dpa regenerates with calcein (Figure 5A, the tails were also imaged by brightfield). Calcein is a green fluorophore that chelates calcium and binds to mineralized bone, thereby visualizing newly reformed bone. Regenerates stained with calcein fluorophore were imaged by fluorescence and the fluorescent area of the entire regenerate was measured to identify the real mineralization area (RMA). To correct for different fin size in different fish, total RMA was normalized to the average ray width (ray) within the tail (as described above). As shown in Figure 5B, mineralized area was significantly lower in the lepidotrichia of *creb3l1*$^{TA+/TA+}$ fish relative to *creb3l1*$^{+/+}$ fish.

These results indicate that loss of Creb3l1 function in *creb3l1*$^{TA+/TA+}$ animals results in decreased bone re-formation.

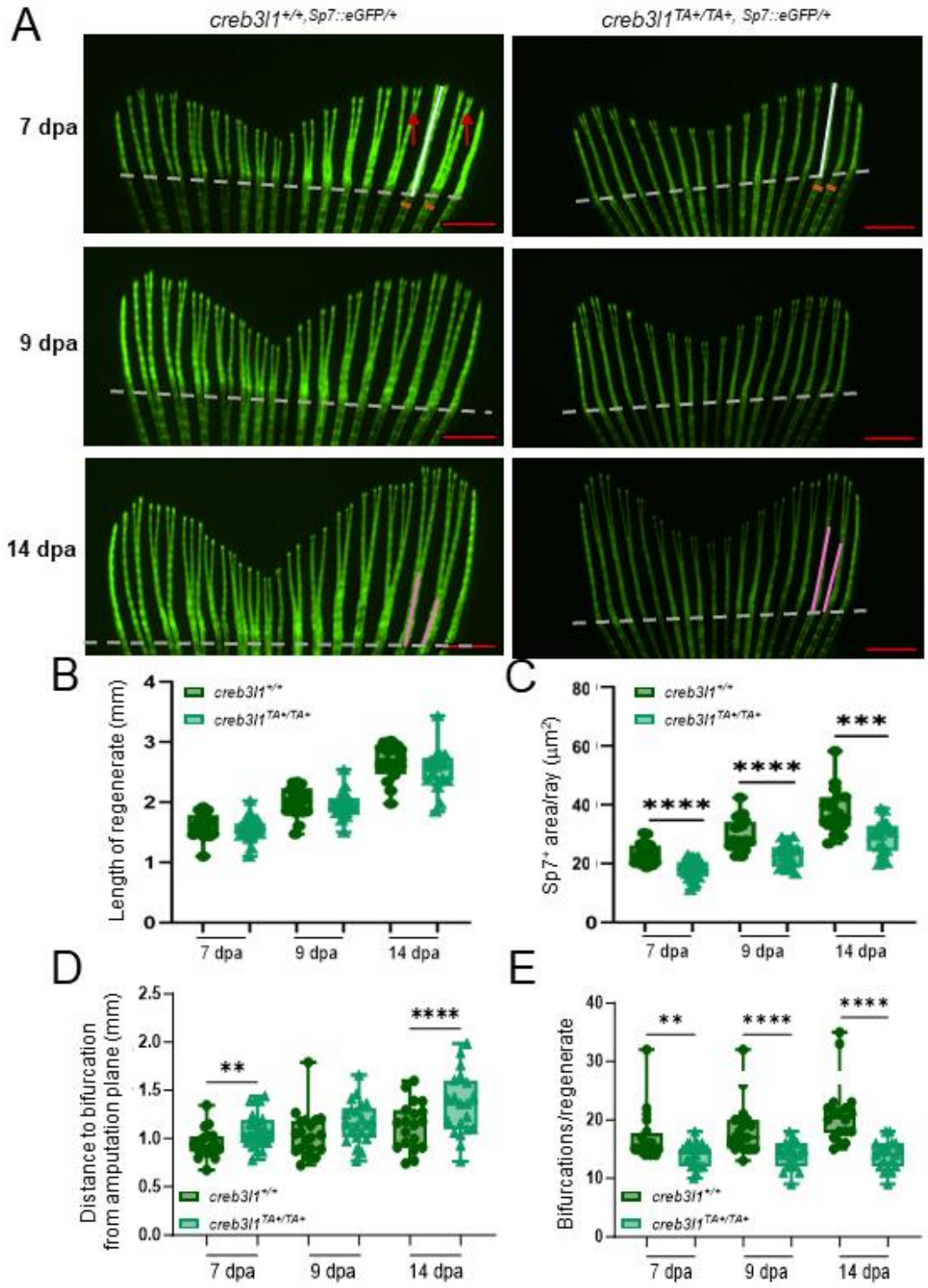

Figure 4: *creb3l1*$^{TA+/TA+}$ zebrafish show decreased regenerative capacity of the caudal fin

A) Approximately 50% of the caudal fin was amputated from 6 mpf *creb3l1*$^{+/+,Sp7::eGFP/+}$ and *creb3l1*$^{TA+/TA+,Sp7::eGFP/+}$ fish. At the indicated dpa, tails were imaged by fluorescence. Representative images are shown. Amputation planes are indicated with dashed line in all panels. 7 dpa panels: white lines indicate the length of the regenerate, red arrows point to secondary bifurcations of sister rays, sienna lines mark the width of the 2nd ray below the amputation plane. 14 dpa panels: pink lines indicate the bifurcation depth of the 2nd and 3rd ray. Scale bar = 1 mm.

B) Fluorescence images analogous to those in A were used to measure the lengths of the 2nd and 3rd ray in both lobes and averaged. Regenerate lengths are not significantly different between *creb3l1*$^{+/+,Sp7::eGFP/+}$ and *creb3l1*$^{TA+/TA+,Sp7::eGFP/+}$ fish at all assayed dpa. n=14-15. Each data point represents an individual fish.

C) Fluorescence images analogous to those in A were used to calculate the area occupied by fluorescent $Sp7^+$ osteoblasts (area distal to amputation plane), corrected for the average width of all rays in each lobe ($Sp7^+$ area/ray). The *creb3l1*$^{TA+/TA+,Sp7::eGFP/+}$ fish show significantly decreased $Sp7^+$ area/ray at all timepoints. n=13-23. Each data point represents an individual fish. ***p≤0.001; ****≤0.0001.

D) Fluorescence images analogous to those in A were used to measure the distance from the amputation plane to first bifurcation in the 2nd and 3rd ray in both lobes, and averaged. Significant increase in bifurcation depth is observed in *creb3l1*$^{TA+/TA+,Sp7::eGFP/+}$ fish at 7 and 14 dpa. n=18-25. **p≤0.01; ****≤0.0001.

E) Fluorescence images analogous to those in A were used to count the total number of bifurcations in a regenerate. The *creb3l1*$^{TA+/TA+,Sp7::eGFP/+}$ fish have significantly fewer bifurcations/regenerate relative to *creb3l1*$^{+/+,Sp7::eGFP/+}$ fish. Each data point represents an individual fish. n=18-24. **p≤0.01; ****≤0.0001.

5. The *creb3l1*$^{TA+/TA+}$ fish show aberrant expression of Sonic Hedgehog pathway genes during caudal fin regeneration

The bifurcations of regenerating lepidotrichia in the caudal fin are controlled by multiple signaling pathways, including the Sonic Hedgehog pathway. Specifically, *shha* is expressed in a tight "cap" overlaying each regenerating ray early in regeneration and rapidly redistributes into two distinct points, each overlaying the future site of ray bifurcation [Laforest et al., 1998;Armstrong et al., 2017;Braunstein et al., 2021]. In agreement, in *creb3l1*$^{+/+}$ 3 dpa regenerates, *shha* was expressed either in a cap-like structure positioned over a ray (Figure 5C, blue arrow) or already separated into two

distinct points (Figure 5C, red arrow). In contrast, the *creb3l1*$^{TA+/TA+}$ 3 dpa regenerates exhibited only single diffuse regions of *shha* expression (Figure 5C, green arrow), and no separated *shha* foci were detected. At 7 dpa, in *creb3l1*$^{+/+}$ regenerates, all *shha* expression was restricted to two clearly separate points, each within an already bifurcated regenerating lepidotrichia (Figure 5D, red arrows). In contrast, in the *creb3l1*$^{TA+/TA+}$ regenerate, the *shha* signal was detected in a diffuse cap over each lepidotrichium (Figure 5D, green arrows).

S*hha* signaling controls the expression of *ptch2*, and we also observed differences in the expression patterns of this gene, with differences between the *creb3l1*$^{+/+}$ and *creb3l1*$^{TA+/TA+}$ regenerates more evident at later times during regeneration. In *creb3l1*$^{+/+}$ 3 dpa regenerates, *ptch2* expression was detected in a single cap over each lepidotrichium (Figure 5C, blue arrow), and an analogous expression pattern of *ptch2* was observed in the *creb3l1*$^{TA+/TA+}$ 3 dpa regenerate (Figure 5C, green arrow). The pattern of *ptch2* expression changed over time, and in *Creb3l1*$^{+/+}$ 7 dpa regenerate, *ptch2* segregated into two separate points overlaying each of the bifurcated regenerating ray (Figure 5D, red arrows). In contrast, in the *creb3l1*$^{TA+/TA+}$ 7 dpa regenerate, the *ptch2* signal appeared diffuse and without clear separation into distinct points over the majority of the regenerating rays (Figure 5D, green arrows). In those rays that showed initiation of bifurcation at 7 dpa, *ptch2* expression was segregated into two points, but diffuse staining was still detectable between the two concentrated foci (Figure 5D, black arrow).

Together, these results suggest that loss of Creb3l1 activity causes a defect in establishing the normal *shha* signaling pattern required for correct ray bifurcation.

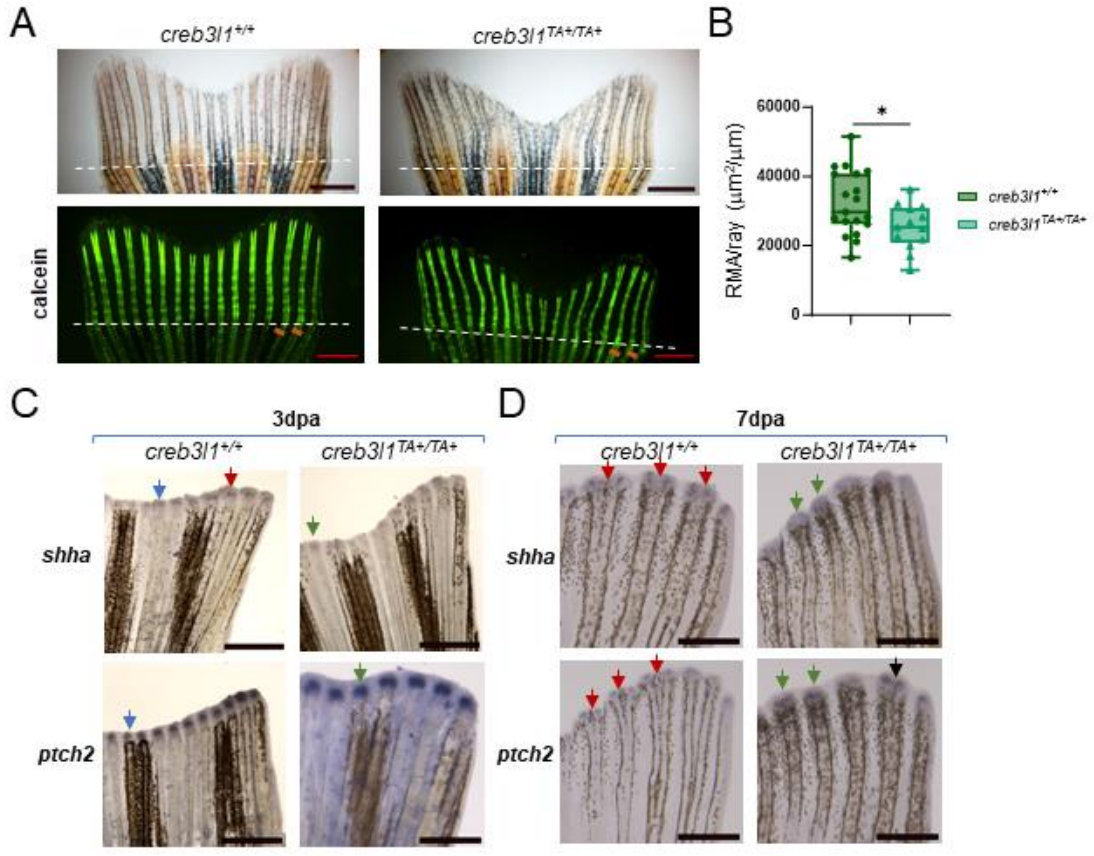

Figure 5: *creb3l1*$^{TA+/TA+}$ zebrafish show decreased mineralization and have alterations in expression patterns of Sonic Hedgehog pathway components

A) Approximately 50% of the caudal fin was amputated from 6 mpf *creb3l1*$^{+/+}$ and *creb3l1*$^{TA+/TA+}$ fish. At 9 dpa, the tails were stained with calcein and imaged via brightfield and fluorescence. Representative images are shown. Amputation planes are indicated with dashed lines. Sienna lines in calcein panels mark the width of the 2nd and 3rd rays below the amputation plane. Scale bar = 1 mm.

B) Fluorescence images analogous to those in A were used to measure the fluorescent mineralized area (RMA: total fluorescence distal to amputation plane), which was normalized to the average width of all fin rays below the amputation plane. The *creb3l1*$^{TA+/TA+}$ fish exhibit significantly decreased mineralization of the regenerated bone. n=13-19. Each data point represents an individual fish. *p≤0.05

C-D) Approximately 50% of the caudal fin was amputated from 6 mpf *creb3l1*$^{+/+}$ and *creb3l1*$^{TA+/TA+}$ fish. At 3 dpa (C) and 7 dpa (D), tails were processed for *in situ* hybridization to detect expression of *shha* and *ptch2* components of the Sonic Hedgehog pathway. Representative images are shown. C) *shha* signal in *creb3l1*$^{+/+}$ regenerates is either in a single cap over a regenerating ray (blue arrow) or is already separated into two foci (red arrow).

In contrast, in *creb3l1*$^{TA+/TA+}$ regenerates, all *shha* signal is in a single cap over regenerating rays. *ptch2* signal is in a single cap in both, *creb3l1*$^{+/+}$ and *creb3l1*$^{TA+/TA+}$ regenerates (blue and green arrow, respectively). D) all *shha* signal in *creb3l1*$^{+/+}$ regenerates is separated into two foci (red arrows), but is still within a single cap in *creb3l1*$^{TA+/TA+}$ regenerates (green arrows). *ptch2* signal in *creb3l1*$^{+/+}$ regenerates is separated into two distinct foci (red arrows), but is mostly present in a single diffuse domain in *creb3l1*$^{TA+/TA+}$ regenerates (green arrows). Separation of the patch2 signal can be seen in some *creb3l1*$^{TA+/TA+}$ regenerates (black arrow). n=3-7.

DISCUSSION

The mechanisms that regulate the patterning of vertebrate skeletal appendages, such as limbs in mammals and fins in teleost fish, have been extensively studied using multiple model organisms [Marks et al., 2004;Nachtrab et al., 2013;Cunningham and Duester, 2015;Langhans et al., 2015;Tickle and Towers, 2017;Braunstein et al., 2021]. The *Danio rerio* zebrafish are a widely utilized model, with well characterized and easily analyzed patterns of skeletal structures. Zebrafish have the advantage of relative ease of genetic manipulations and the existence of transgenic lines that fluorescently label cells to allow static and dynamic imaging of specific cells and tissues. Further and of specific importance to this study is the high regenerative potential of zebrafish fins, which in combination with the previously stated considerations, provides significant advantages over other model organisms [Sehring and Weidinger, 2020;Uemoto et al., 2020].

A characteristic feature of zebrafish caudal fins is a fan-like arrangement of 16-18 bony rays composed of bony segments formed by two opposed hemi-rays that connect to other segments by joints. Ray segments are added distally during fin growth or

regeneration [Christou et al., 2018;König et al., 2018]. The inner and outer surface of the rays are lined by osteoblasts and the inner space of each lepidotrichium is filled with intra-ray tissue, mainly composed of mesenchymal cells. Between the rays is an inter-ray mesenchymal tissue that is vascularized, innervated, and pigmented. The rays are organized in a species-specific pattern, and they branch to generate a complex pattern of bifurcations, with primary bifurcations forming around 30 dpf, followed by secondary and sometimes tertiary branches. Bifurcations are added terminally during development or regeneration [Azevedo et al., 2012;Blum and Begemann, 2015;Uemoto et al., 2020].

Unlike mammals, zebrafish fully regenerate fins with appropriate patterning and tissue diversity after amputation within weeks of injury. This makes zebrafish optimal for studying regeneration and probe mechanisms that regulate skeletal patterning. Regeneration proceeds through a highly conserved program of events that includes wound healing, followed by blastema formation, and then regenerative outgrowth [Schebesta et al., 2006;Knopf et al., 2011;Sehring and Weidinger, 2020]. Regeneration of bone structures within rays involves the dedifferentiation of osteoblasts, followed by their proliferation, and subsequent redifferentiation [Knopf et al., 2011;Stewart et al., 2014]. Importantly, caudal fin regeneration not only involves tissue regrowth, but also requires positional memory in which the correct branching pattern of rays is re-established along the proximo-distal axis [Rabinowitz et al., 2017]. Bifurcations are strong indicators of proximo-distal patterning, and changes in the number or position of branch points are an excellent read-out of patterning defects [Harper et al., 2023]. Regenerating lepidotrichia initiate bifurcation via Shh signalling as early as 4 dpa, and almost all of the previously bifurcated rays have at least one bifurcation at 9-10 dpa [Laforest et al., 1998].

Herein, we used zebrafish caudal fin development and an amputation-regeneration system to assess the role of the Creb3l1 transcription factor in the formation and patterning of bony structures. Using CRISP/Cas9-mediated gene editing, we generated a fish line (*creb3l1*$^{TA+/TA+}$) that expresses a TA+ fragment of Creb3l1 containing the transcription activating TA domain in tandem with 56 additional amino acids not found in Creb3l1. Importantly, this TA+ fragment is unable to enter the nucleus, and hence doesn't bind DNA or activate target genes. Thus, *creb3l1*$^{TA+/TA+}$ fish are in fact null for Creb3l1 transcription regulating activity.

Comparisons between wild-type and *creb3l1*$^{TA+/TA+}$ fish show that despite the lack of functional Creb3l1, *creb3l1*$^{TA+/TA+}$ larvae show relatively normal survival rates, while adult *creb3l1*$^{TA+/TA+}$ fish have normal body and tail lengths, as well as normal overall skeletal development and bone density. Yet, upon closer examination, the *creb3l1*$^{TA+/TA+}$ fish do exhibit defects in skeletal development, with a major distalization of bifurcation points in caudal fin rays and significant reduction in branching complexity. The latter is due to significantly fewer secondary bifurcations. Thus, we document that transcriptionally active Creb3l1 is required to facilitate the correct patterning of skeletal structures during fin development. Patterning defects were not observed in the *CREB3L1* KO mice [Murakami et al., 2009] , but it is likely that the exquisitely sensitive zebrafish model allowed this insight, not possible in a mammalian system. Thus, it might be beneficial to utilize multiple model systems to probe regulatory mechanisms of bone development and patterning.

We also probed the effects of loss of functional Creb3l1 on bone regeneration by comparing caudal fin regrowth after amputation in wild-type and *creb3l1*$^{TA+/TA+}$ fish. We

document a significant decrease in $Sp7^{+}$ area, as well as distalization of branch points in *creb3l1*$^{TA+/TA+}$ fish at all examined time points after amputation. The bifurcation frequency was also reduced, and the decrease was due to almost complete lack of secondary bifurcations in the *creb3l1*$^{TA+/TA+}$ regenerate. The similarity in the developmental and regenerative phenotypes is consistent with the current model of fin regeneration re-activating a developmental program [Knopf et al., 2011;Stewart et al., 2014]. Our results suggest that positional memory is retained in the *creb3l1*$^{TA+/TA+}$ fish, since ray distalization and decreased secondary branching observed in caudal fins of adult fish is faithfully recapitulated during post-amputation regeneration.

Previous studies have shown that the same regulatory mechanisms appear to function during caudal fin development and regeneration, and identified components of the Wnt, Bmp, Fgf, retinoic acid, and Hh signaling pathways as key regulators of skeletal growth and differentiation, positional memory, and spatio-temporal pattern establishment that govern the sites and frequency of ray branching [!!! INVALID CITATION !!! 90,91,99-102,107,108,111-113,116,136,145,150,156,160]. Formation of bifurcations requires precise Shh signaling through its Smoothened (Smo) effector [Braunstein et al., 2021]. Smo-dependent Shh signaling appears largely dedicated to ray branching, as inhibiting this pathway minimally disrupts fin outgrowth, or skeletal differentiation during caudal fin development or regeneration. During regeneration, *shha* is expressed only by basal epidermal cells overlying preosteoblasts at the distal aspect of the outgrowing ray. Subsequently, each *shha*-expressing epidermal domain splits laterally and is followed by the segregation of pre-osteoblast into two pools over each regenerating ray [Laforest et al., 1998;Zhang et al., 2012;Armstrong et al., 2017]. More

recent studies demonstrated that the highly localized Shh/Smo activity guides the pre-osteoblasts to gradually follow the separating Shha signal. After separating, the divided pools of osteoblasts give rise to each of the two sister rays. However, despite numerous studies exploring the genes and pathways required for branch pattern establishment, our understanding of this process is still incomplete, with a limited understanding of the regulators that intersect with the Shh pathway.

Previous studies documented that defects in Shh signaling cause distalization and lack of bifurcation during regeneration in animals in which *shha*-expressing basal epidermal cells fail to separate into distinct pools [Harper et al., 2023]. A similar phenotype of our *creb3l1*$^{TA+/TA+}$ fish suggested possible defects in Shh signaling. In support, our *in situ* analysis of *shha* and its downstream effector *ptch2* expression patterns in *creb3l1*$^{TA+/TA+}$ fish showed a failure of the *shha* and *ptch2* signals to separate into two entities, suggesting an underlaying defect in the sorting of the basal epidermal cells into two populations. Thus, transcription activating function of Creb3l1 appears to be required for patterning events during regeneration through intersecting with the Shh signaling pathway. This previously unexplored role for Creb3l1 in bone patterning expand our understanding of factors that impact the regulation of Shh signaling.

The molecular mechanism through which lack of Creb3l1-mediated transcription impacts regenerative bone formation and patterning remains to be defined, as Creb3l1 activity could be required within the regenerating tail (*creb3l1* expression is upregulated in a 3 dpa regenerate, data not shown), or in a remote tissue. Within the regenerating tail, Creb3l1 could be key for upregulating *col1a1* expression, as Creb3l1 has been shown to facilitate *col1a1* transcription in a mouse model of bone fracture [Funamoto et al., 2011].

Additionally, Creb3l1 could act locally to increase the transcription of transport factors such as Sec24d, GM130 and Rab1b [García et al., 2017;Keller et al., 2018] that increase the efficacy of the secretory pathway to handle the increased production of collagen. Alternatively, Creb3l1-mediated gene expression in remote tissues could impact patterning of bony rays. For example, Creb3l1 has been shown to regulate the transcription of the sodium-iodide symporter (NIS) in thyroid cells [Di Giusto et al., 2022], and NIS is required for iodide uptake into cells, the first step in the biosynthesis of thyroid hormone (TH) [Hingorani et al., 2010]. Importantly, lack of TH production has been shown to cause dramatic distalization of bifurcations and decrease in bifurcation frequency in developing and regenerating caudal fin [Harper et al., 2023]. This effect of TH is mediated through Shh, since insufficient levels of TH lead to lack of separation of *shha* transcripts into two distinct puncta [Harper et al., 2023], the exact phenotype observed in our *creb3l1*$^{TA+/TA+}$ fish. It is also possible that lack of Creb3l1 transcriptional function in both, the local tissue and a distant endocrine organ might be responsible for the defects seen in the caudal fin of *creb3l1*$^{TA+/TA+}$ fish.

ACKNOWLEDGEMENTS

We are grateful to Drs. Appel (University of Colorado SOM) and Chang (University of Alabama at Birmingham) for sharing their *in situ* probes, reagents, and expertise. We thank members of the Sztul and Serra labs for helpful comments on the project and the manuscript. We also thank UAB's Zebrafish Research Facility and High Resolution Imaging Facility for providing technical resources and advice.

STATEMENT OF ETHICS

Study approval statement: The use of animals in this study was approved by the University of Alabama at Birmingham's Institutional Animal Care and Use Committee (IACUC). This approval is for the vertebrate animal welfare protocol APN 21787. The remainder of the study did not require ethics approval.

CONFLICT OF INTEREST STATEMENT

Authors have no conflicts of interest to disclose.

FUNDING SOURCES

This work was supported by awards from the National Institute of General Medical Sciences (R01GM122802 to ES) and the National Institute of Dental and Craniofacial Research (5T90DE022736-09 to PEV). The funder had no role in the design, data collection, data analysis, and reporting of this study.

AUTHOR CONTRIBUTIONS

The authors of this paper contributed as such:

Experimentation, development of reagents (plasmids, etc.): PEV, BW, EL, TJN, HT.

Writing, editing, and conceptualization: PEV, JP, CA, RS, ES.

DATA AVAILABILITY STATEMENT

All data are available from the corresponding author upon request.

REFERENCES

Andersson K, Malmgren B, Åström E, Nordgren A, Taylan F, Dahllöf G. Mutations in COL1A1/A2 and CREB3L1 are associated with oligodontia in osteogenesis imperfecta. Orphanet journal of rare diseases. 2020 Mar 31;15(1):80.

Armstrong BE, Henner A, Stewart S, Stankunas K. Shh promotes direct interactions between epidermal cells and osteoblast progenitors to shape regenerated zebrafish bone. Development. 2017 Apr 1;144(7):1165-76.

Asada R, Kanemoto S, Kondo S, Saito A, Imaizumi K. The signalling from endoplasmic reticulum-resident bZIP transcription factors involved in diverse cellular physiology. J Biochem. 2011 May;149(5):507-18.

Azevedo AS, Sousa S, Jacinto A, Saúde L. An amputation resets positional information to a proximal identity in the regenerating zebrafish caudal fin. BMC Developmental Biology. 2012 2012/08/25;12(1):24.

Blum N, Begemann G. Retinoic acid signaling spatially restricts osteoblasts and controls ray-interray organization during zebrafish fin regeneration. Development. 2015;142(17):2888-93.

Braunstein JA, Robbins AE, Stewart S, Stankunas K. Basal epidermis collective migration and local Sonic hedgehog signaling promote skeletal branching morphogenesis in zebrafish fins. Developmental Biology. 2021 2021/09/01/;477:177-90.

Cayami FK, Maugeri A, Treurniet S, Setijowati ED, Teunissen BP, Eekhoff EMW, et al. The first family with adult osteogenesis imperfecta caused by a novel homozygous mutation in CREB3L1. Mol Genet Genomic Med. 2019 Aug;7(8):e823.

Chen Q, Lee CE, Denard B, Ye J. Sustained induction of collagen synthesis by TGF-β requires regulated intramembrane proteolysis of CREB3L1. PLoS One. 2014;9(10):e108528.

Christou M, Iliopoulou M, Witten PE, Koumoundouros G. Segmentation pattern of zebrafish caudal fin is affected by developmental temperature and defined by multiple fusions between segments. Journal of Experimental Zoology Part B: Molecular and Developmental Evolution. 2018;330(6-7):330-40.

Cunningham TJ, Duester G. Mechanisms of retinoic acid signalling and its roles in organ and limb development. Nat Rev Mol Cell Biol. 2015 Feb;16(2):110-23.

Di Giusto P, Martín M, Funes Chabán M, Sampieri L, Nicola JP, Alvarez C. Transcription Factor CREB3L1 Regulates the Expression of the Sodium/Iodide Symporter (NIS) in Rat Thyroid Follicular Cells. Cells. 2022 Apr 13;11(8).

Dietrich K, Fiedler IA, Kurzyukova A, López-Delgado AC, McGowan LM, Geurtzen K, et al. Skeletal Biology and Disease Modeling in Zebrafish. Journal of Bone and Mineral Research. 2021;36(3):436-58.

Fox RM, Andrew DJ. Transcriptional regulation of secretory capacity by bZip transcription factors. Front Biol (Beijing). 2015 Feb 1;10(1):28-51.

Funamoto T, Sekimoto T, Murakami T, Kurogi S, Imaizumi K, Chosa E. Roles of the endoplasmic reticulum stress transducer OASIS in fracture healing. Bone. 2011 Oct;49(4):724-32.

García-Mata R, Bebök Z, Sorscher EJ, Sztul ES. Characterization and dynamics of aggresome formation by a cytosolic GFP-chimera. J Cell Biol. 1999 Sep 20;146(6):1239-54.

García IA, Torres Demichelis V, Viale DL, Di Giusto P, Ezhova Y, Polishchuk RS, et al. CREB3L1-mediated functional and structural adaptation of the secretory pathway in hormone-stimulated thyroid cells. Journal of cell science. 2017;130(24):4155-67.

Greenwood M, Bordieri L, Greenwood MP, Rosso Melo M, Colombari DS, Colombari E, et al. Transcription factor CREB3L1 regulates vasopressin gene expression in the rat hypothalamus. J Neurosci. 2014 Mar 12;34(11):3810-20.

Guillemyn B, Kayserili H, Demuynck L, Sips P, De Paepe A, Syx D, et al. A homozygous pathogenic missense variant broadens the phenotypic and mutational spectrum of CREB3L1-related osteogenesis imperfecta. Human molecular genetics. 2019 Jun 1;28(11):1801-09.

Harper M, Hu Y, Donahue J, Acosta B, Dievenich Braes F, Nguyen S, et al. Thyroid hormone regulates proximodistal patterning in fin rays. Proceedings of the National Academy of Sciences. 2023;120(21):e2219770120.

Hingorani M, Spitzweg C, Vassaux G, Newbold K, Melcher A, Pandha H, et al. The biology of the sodium iodide symporter and its potential for targeted gene delivery. Curr Cancer Drug Targets. 2010 Mar;10(2):242-67.

Kamikawa Y, Saito A, Matsuhisa K, Kaneko M, Asada R, Horikoshi Y, et al. OASIS/CREB3L1 is a factor that responds to nuclear envelope stress. Cell Death Discov. 2021 Jun 29;7(1):152.

Keller RB, Tran TT, Pyott SM, Pepin MG, Savarirayan R, McGillivray G, et al. Monoallelic and biallelic CREB3L1 variant causes mild and severe osteogenesis imperfecta, respectively. Genetics in medicine : official journal of the American College of Medical Genetics. 2018;20(4):411-19.

Knopf F, Hammond C, Chekuru A, Kurth T, Hans S, Weber Christopher W, et al. Bone Regenerates via Dedifferentiation of Osteoblasts in the Zebrafish Fin. Developmental Cell. 2011 2011/05/17/;20(5):713-24.

Kondo S, Murakami T, Tatsumi K, Ogata M, Kanemoto S, Otori K, et al. OASIS, a CREB/ATF-family member, modulates UPR signalling in astrocytes. Nat Cell Biol. 2005 Feb;7(2):186-94.

König D, Page L, Chassot B, Jaźwińska A. Dynamics of actinotrichia regeneration in the adult zebrafish fin. Developmental Biology. 2018 2018/01/15/;433(2):416-32.

Laforest L, Brown CW, Poleo G, Géraudie J, Tada M, Ekker M, et al. Involvement of the sonic hedgehog, patched 1 and bmp2 genes in patterning of the zebrafish dermal fin rays. Development. 1998 Nov;125(21):4175-84.

Lamark T, Johansen T. Aggrephagy: selective disposal of protein aggregates by macroautophagy. Int J Cell Biol. 2012;2012:736905.

Langhans MT, Alexander PG, Tuan RS. Chapter 28 - Skeletal Development. In: Moody SA, editor. Principles of Developmental Genetics (Second Edition). Oxford: Academic Press; 2015. p. 505-30.

Lindahl K, Åström E, Dragomir A, Symoens S, Coucke P, Larsson S, et al. Homozygosity for CREB3L1 premature stop codon in first case of recessive osteogenesis imperfecta associated with OASIS-deficiency to survive infancy. Bone. 2018 Sep;114:268-77.

Lindsay SE, Nicol LE, Gamayo AC, Raney EM. An Unusual Presentation of Osteogenesis Imperfecta: A Case Report. JBJS Case Connect. 2021 Nov 22;11(4).

Marks SC, Gartland A, Odgren PR. Skeletal Development. In: Martini L, editor. Encyclopedia of Endocrine Diseases. New York: Elsevier; 2004. p. 261-72.

Murakami T, Kondo S, Ogata M, Kanemoto S, Saito A, Wanaka A, et al. Cleavage of the membrane-bound transcription factor OASIS in response to endoplasmic reticulum stress. Journal of Neurochemistry. 2006;96(4):1090-100.

Murakami T, Saito A, Hino S, Kondo S, Kanemoto S, Chihara K, et al. Signalling mediated by the endoplasmic reticulum stress transducer OASIS is involved in bone formation. Nat Cell Biol. 2009 Oct;11(10):1205-11.

Nachtrab G, Kikuchi K, Tornini VA, Poss KD. Transcriptional components of anteroposterior positional information during zebrafish fin regeneration. Development. 2013 Sep;140(18):3754-64.

Omori Y, Imai J, Suzuki Y, Watanabe S, Tanigami A, Sugano S. OASIS is a transcriptional activator of CREB/ATF family with a transmembrane domain. Biochem Biophys Res Commun. 2002 Apr 26;293(1):470-7.

Poss KD, Shen J, Nechiporuk A, McMahon G, Thisse B, Thisse C, et al. Roles for Fgf signaling during zebrafish fin regeneration. Dev Biol. 2000 Jun 15;222(2):347-58.

Rabinowitz JS, Robitaille AM, Wang Y, Ray CA, Thummel R, Gu H, et al. Transcriptomic, proteomic, and metabolomic landscape of positional memory in the caudal fin of zebrafish. Proc Natl Acad Sci U S A. 2017 Jan 31;114(5):E717-e26.

Rutkovskiy A, Stensløkken KO, Vaage IJ. Osteoblast Differentiation at a Glance. Med Sci Monit Basic Res. 2016 Sep 26;22:95-106.

Saint-Jeannet J-P. Whole-Mount In Situ Hybridization of Xenopus Embryos. Cold Spring Harbor protocols. 2017 December 1, 2017;2017(12):pdb.prot097287.

Saito A, Kanemoto S, Kawasaki N, Asada R, Iwamoto H, Oki M, et al. Unfolded protein response, activated by OASIS family transcription factors, promotes astrocyte differentiation. Nature Communications. 2012 2012/07/24;3(1):967.

Schebesta M, Lien C-L, Engel FB, Keating MT. Transcriptional Profiling of Caudal Fin Regeneration in Zebrafish. TheScientificWorldJOURNAL. 2006 1900/01/01;6:947207.

Schindelin J, Arganda-Carreras I, Frise E, Kaynig V, Longair M, Pietzsch T, et al. Fiji: an open-source platform for biological-image analysis. Nature Methods. 2012 2012/07/01;9(7):676-82.

Schindelin J, Rueden CT, Hiner MC, Eliceiri KW. The ImageJ ecosystem: An open platform for biomedical image analysis. Molecular Reproduction and Development. 2015;82(7-8):518-29.

Schubert SW, Abendroth A, Kilian K, Vogler T, Mayr B, Knerr I, et al. bZIP-Type transcription factors CREB and OASIS bind and stimulate the promoter of the mammalian transcription factor GCMa/Gcm1 in trophoblast cells. Nucleic acids research. 2008 Jun;36(11):3834-46.

Sehring IM, Weidinger G. Recent advancements in understanding fin regeneration in zebrafish. WIREs Developmental Biology. 2020;9(1):e367.

Stewart S, Gomez AW, Armstrong BE, Henner A, Stankunas K. Sequential and opposing activities of Wnt and BMP coordinate zebrafish bone regeneration. Cell Rep. 2014 Feb 13;6(3):482-98.

Symoens S, Malfait F, D'Hondt S, Callewaert B, Dheedene A, Steyaert W, et al. Deficiency for the ER-stress transducer OASIS causes severe recessive osteogenesis imperfecta in humans. Orphanet journal of rare diseases. 2013 Sep 30;8:154.

Tickle C, Towers M. Sonic Hedgehog Signaling in Limb Development. Front Cell Dev Biol. 2017;5:14.

Uemoto T, Abe G, Tamura K. Regrowth of zebrafish caudal fin regeneration is determined by the amputated length. Scientific reports. 2020 2020/01/20;10(1):649.

Wehner D, Cizelsky W, Vasudevaro Mohankrishna D, Özhan G, Haase C, Kagermeier-Schenk B, et al. Wnt/β-Catenin Signaling Defines Organizing Centers that Orchestrate Growth and Differentiation of the Regenerating Zebrafish Caudal Fin. Cell Reports. 2014 2014/02/13/;6(3):467-81.

Westerfield M. The Zebrafish Book: A Guide for the Laboratory Use of Zebrafish (Danio Rerio). University of Oregon Press; 2007.

Zhang J, Jeradi S, Strähle U, Akimenko M-A. Laser ablation of the sonic hedgehog-a-expressing cells during fin regeneration affects ray branching morphogenesis. Developmental Biology. 2012 2012/05/15/;365(2):424-33.

JAGN1, TETRASPANINS, AND ERV PROTEINS: IS COMMON TOPOLOGY INDICATIVE OF COMMON FUNCTION IN CARGO SORTING?

by

PEYTON E. VANWINKLE, FELICIA PARISH, YVONNE J.K. EDWARDS AND ELIZABETH SZTUL

American Journal of Physiology: Cell Physiology, Volume 319, Issue 4, Pages C667-C674

Format adapted and errata corrected for dissertation

ABSTRACT

The endoplasmic reticulum protein Jagunal (JAGN1) was first identified as a requirement for *Drosophila melanogaster* oocyte development. Subsequent studies in human patients linked mutations in JAGN1 to severe congenital neutropenia, as well as a broad range of additional symptoms, suggesting that JAGN1 function is required in many tissues. Moreover, JAGN1 orthologs are found throughout animal and plant phylogeny, suggesting that JAGN1 supports fundamental cellular processes not restricted to egg development or neutrophil function. JAGN1 lacks sequence similarity or recognizable domains other than a coatomer protein complex I-binding motif, and its cellular function is currently unknown. JAGN1 shares a tetraspanning membrane topology with two families of known cargo transporters: the tetraspanins and the endoplasmic reticulum vesicle (Erv) proteins. Herein, we discuss the similarities between JAGN1, tetraspanins, and Ervs and, based on those, suggest a role for JAGN1 in facilitating the traffic of cell-restricted and ubiquitously expressed proteins at the endoplasmic reticulum-Golgi interface.

INTRODUCTION

Protein traffic between the compartments of the secretory and endocytic pathways is essential for all aspects of eukaryotic cell life. Proteins are transported to their ultimate cellular destinations by selective sorting and packaging into carrier vesicles that bud from one compartment, travel some distance within the cell, and then fuse with the next compartment to deposit their cargo. Two families of proteins, the tetraspanins and the

endoplasmic reticulum vesicles (Ervs), are known for their roles in the selective sorting of cargo proteins within the endocytic and secretory pathways, respectively. Members of the tetraspanin and the Erv families are highly conserved and widely expressed throughout phylogeny, underscoring their importance in eukaryotic life. These selective regulators of protein traffic are characterized by a common membrane topology, with four membrane-spanning domains, two extracellular/luminal loops, and the NH_2- and COOH-termini located within the cytosol.

The Jagunal homolog 1 (JAGN1) protein exhibits analogous tetra-spanning topology, and the disruption of JAGN1 function in invertebrate and mammalian organisms appears to cause defects in the traffic of specific proteins. JAGN1 is highly conserved and widely expressed throughout phylogeny, suggesting that it regulates a process common to many eukaryotic cells. Yet, the molecular mechanisms of JAGN1 action remain uncharacterized. In this perspective, we first describe the current understanding of JAGN1 function, then discuss how tetraspanins and Erv proteins act in protein sorting/traffic and the commonality of their mechanisms of action, and finally use the tetraspanin/Erv paradigm to postulate a possible mode of action for JAGN1 in cargo sorting and traffic.

ORGANISMAL AND CELLULAR EFFECTS OF JAGN1 MUTATIONS OR DELETION

Discovery of JAGN1

JAGN1 (Jagunal: small egg in Korean) was first identified in the fruit fly *Drosophila melanogaster* in a screen of lethal mutations on chromosome 3R (30).

Four alleles were described, three causing lethality at the first and second instar stages and one semilethal. Phenotypic analysis showed that JAGN1 plays an important role in enriching the subcortex of the oocyte with endoplasmic reticulum (ER) proteins during stages 9 and 10 of oocyte development. A role for JAGN1 in protein trafficking was suggested by the finding that *jagn* mutations inhibit the transport of Yolkless (a transmembrane yolk receptor) to the lateral membrane of the oocyte (30). This function of JAGN1 was cargo specific, since another transmembrane protein (Gurken) was transported normally.

Homology and Predicted Structure of JAGN1

JAGN1 orthologs are found across the animal and plant kingdoms (Fig. 1*A*). Within Animalia, JAGN1 orthologs are present in the nine major multicellular phyla: in the Porifera [sponges, which are the most primitive of metazoans (46), e.g., *Amphimedon queenslandica* and choanoflagellates, small single-celled protists, e.g., *Monosiga brevicollis*, *Salpingoeca rosetta*]; Cnidaria (e.g., *Nematostella vectensis*, *Hydra vulgaris*, *Stylophora pistillata*); Platyhelminthes (e.g., *Schistosoma hematobium*, *Pocillopora damicornis*); Annelida (e.g., *Helobdella robusta*, *Capitella teleta*); Nematoda (e.g., *Caenorhabditis elegans*); Mollusca (e.g., *Crassostrea gigas*); Arthropoda (e.g., *D. melanogaster*, *Anopheles gambiae);* Echinodermata (e.g., *Strongylocentrotus purpuratus*); and Chordata, which includes vertebrates such as amphibians (e.g., *Xenopus laevis*), reptiles (e.g., *Crotalus adamanteus*), birds (e.g., *Gallus gallus*), fishes (e.g., *Danio rerio*), and mammals (e.g., *Homo sapiens*). UniProt identifiers of proteins used for phylogenetic analyses are found in Supplemental Table S1 (see https://doi.org/10.6084/m9.figshare.12654047) (49a, 49b, 49c).

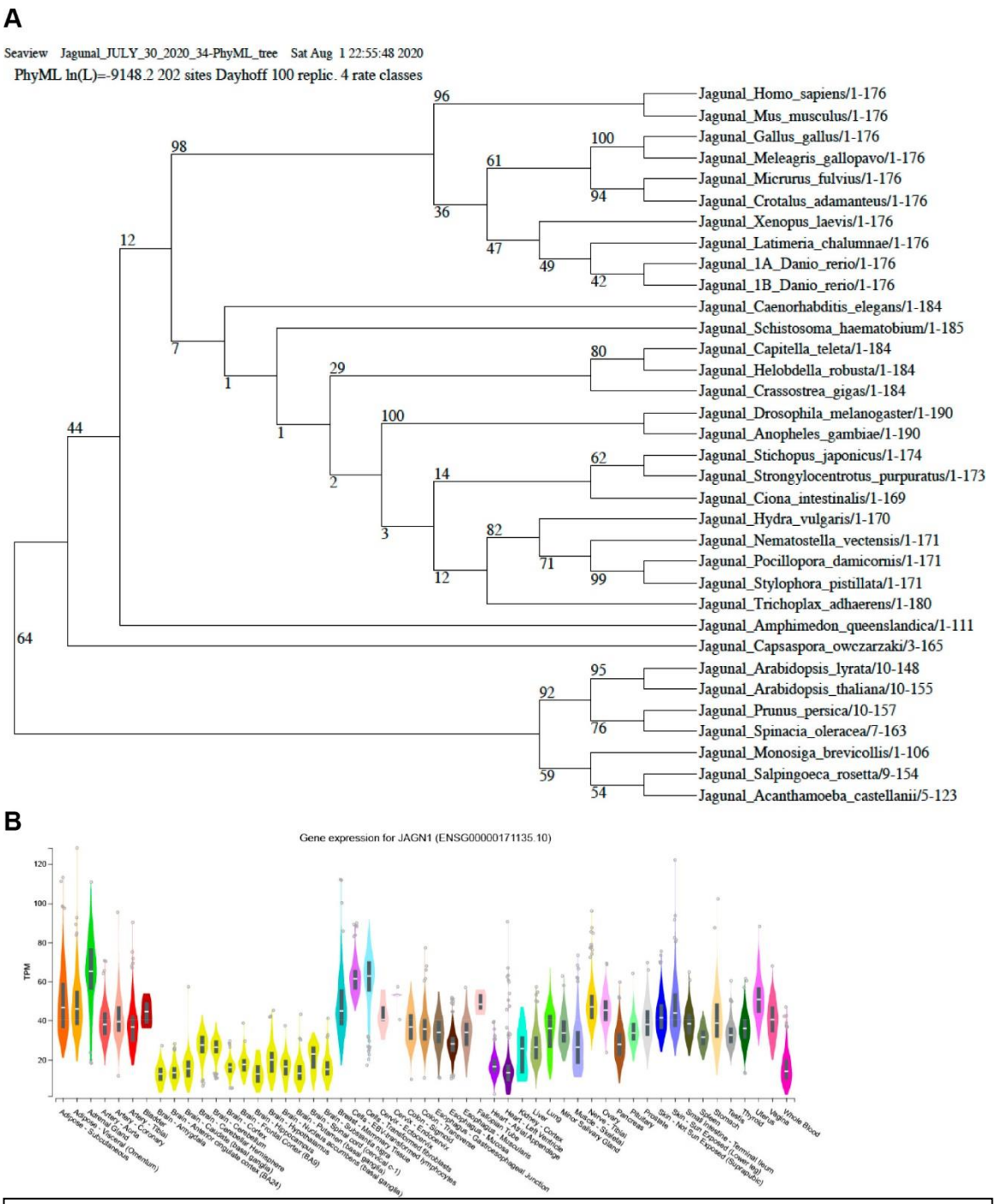

Fig. 1. Phylogeny and tissue distribution of Jagunal homolog 1 (JAGN1). *A*: phylogenetic analysis of Jagunal shows wide distribution throughout kingdoms and phyla and high order of conservation between orthologs. Jagunal protein sequences have been biocurated in UniProt (49a, 49b, 49c) and Pfam (19, 22). The methods for biocuration and biocuration cross referencing between UniProt (49a, 49b, 49c) and Pfam (19, 22) have been described.

In Pfam (version 33.1), the Jagunal protein family comprises 540 members spanning 411 species. Thirty-four members of the Pfam Jagunal protein family (Pfam accession: PF07086) (19, 22) were selected from representative and diverse taxonomic ranks and phyla. The thirty-four representative Jagunal protein sequences were downloaded from UniProt (release 2020_03) (49a, 49b, 49c) using keyword searches. The keyword searches were constructed using a search term for the protein name together with the representative species name (e.g., "*Jagunal Homo sapiens*"). To generate an alignment of the 34 representative Jagunal protein sequences, hmmsearch from the HMMER package (version 3.1b2) was run with the default parameters (http://hmmer.org) and the raw Hidden Markov Model (HMM) for the Pfam Jagunal protein family (https://pfam.xfam.org/family/PF07086/hmm). Based on the HMM-aligned representative Jagunal protein sequences, a phylogenetic tree was generated using the software Seaview (version 4.7) (24). The phylogenetic tree was generated with the PhyML method (25), selecting the model DAYHOFF matrix with 100 bootstrap replicates. The nos. indicated on the phylogenetic tree are the support values for bootstrap. The UniProt unique entry identifier and the UniProt mnemonic identifier for each of the protein names used in the phylogenetic tree are provided (Supplemental Table S1; see https://doi.org/10.6084/m9.figshare.12654047). *B*: JAGN1 expression in human tissues from the GTEx Portal (accessed on 8/9/2019) shows wide distribution in analyzed tissues. Tissues in the same colors indicate common developmental type.

Within Plantae, JAGN1 orthologs can be found three of its four phyla: in Angiospermophyta (flowering plants, e.g., *Arabidopsis thaliana*); Coniferophyta (conifers, e.g., *Picea sitchensis*); and Bryophyta (mosses, e.g., *Physcomitrella patens*). The JAGN1 orthologs in Angiospermophyta are most similar to animal JAGN orthologs in the NH_2-terminal sequences but diverge in the COOH-terminal amino acid sequences. JAGN1 in conifers and mosses are highly diverged from JAGN1 in flowering plants, and could be better described as "JAGN1-like" rather than JAGN1. Interestingly, our searches did not identify JAGN1 orthologs in the fungi kingdom, nor in the Filicinophyta (fern phylum) within the plant kingdom. Although it remains possible that those organisms lack JAGN1, it is perhaps more likely that fewer genomes have been sequenced and well annotated and that limited sequence similarity makes it difficult to detect bona fide JAGN orthologs.

In support of JAGN1 performing a basic cellular function in animal and plant cells, JAGN1 is ubiquitously expressed in human tissues (Fig. 1*B*), and this is probably also true for other multicellular species.

JAGN1 has no sequence similarity (as defined by BLAST searches) to any other protein and has been classified as its own family. JAGN1 amino acid sequences are highly conserved in model organisms, including the mouse (*Mus musculus*), the fruit fly (*D. melanogaster*), the frog (*X. laevis*), the zebrafish (*D. rerio*), and the nematode (*C. elegans*) (Fig. 2*A*). The NH_2- and COOH-termini of JAGN1 are especially highly conserved among species, suggesting that they represent important functional regions, perhaps interfaces for interactions with other proteins.

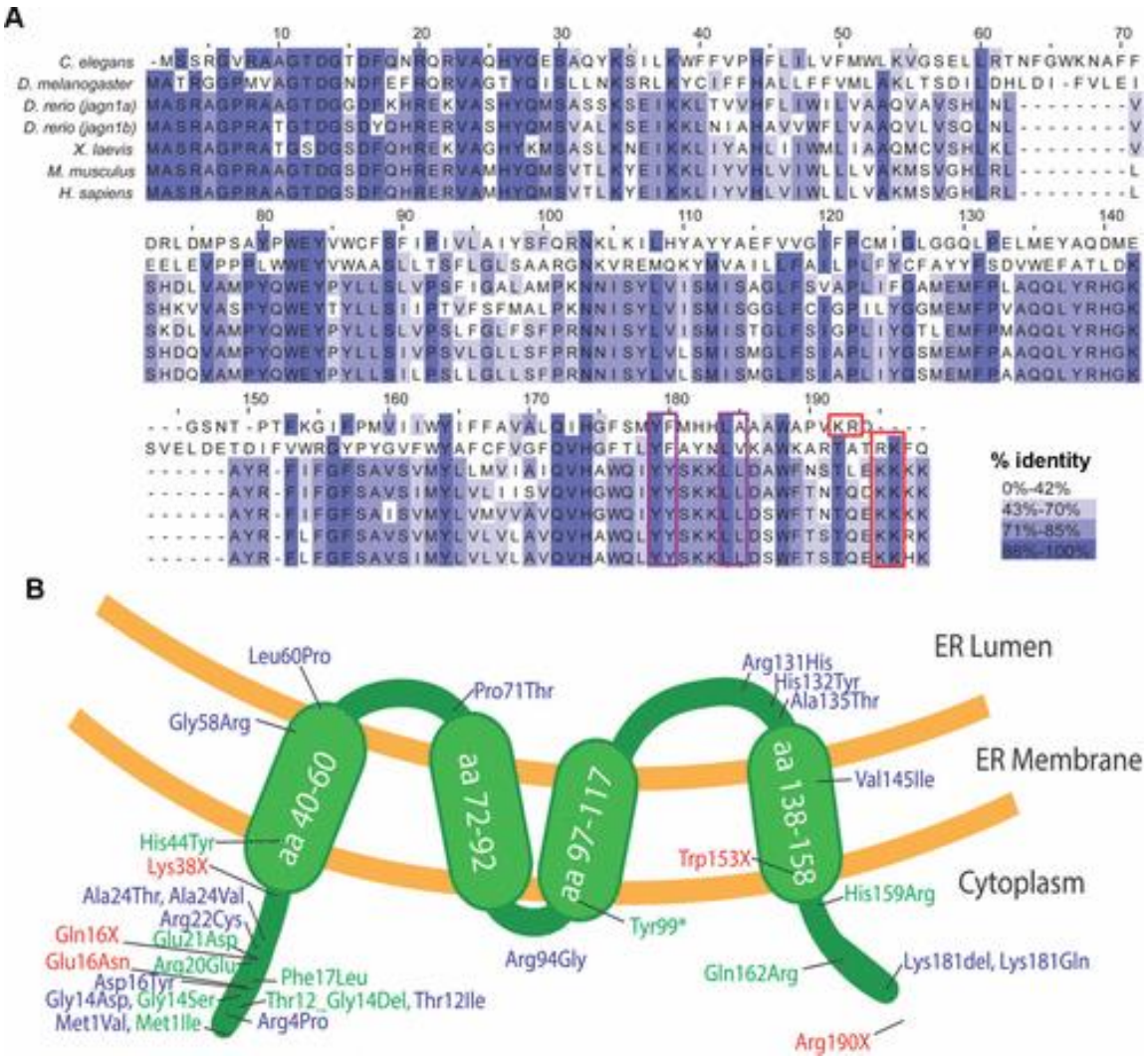

Fig. 2. Sequence conservation, membrane topology, and pathogenic mutations in Jagunal homolog 1 (JAGN1). *A*: an alignment of JAGN1 orthologs in the nematode (*Caenorhabditis elegans*), fruit fly (*Drosophila melanogaster*), zebrafish (*Danio rerio*; zebrafish contains two genes), frog (*Xenopus laevis*), and mouse (*Mus musculus*) relative to human sequence shows extensive sequence conservation. Transmembrane domains are marked by lines above the sequence. The intensity of color reflects the level of identity between JAGN1 orthologs. The highly conserved coatomer protein complex I (COPI)-sorting motifs are boxed in red. Possible coatomer protein complex II (COPII)-sorting motifs are boxed in purple. Alignments were performed via ClustalW with default parameters, as configured (36). *B*: schematic of JAGN1 membrane topology showing 4 transmembrane domains and cytoplasmic NH_2- and COOH-termini. Human mutations associated with severe congenital neutropenia and identified in literature are in green while those reported in ClinVar are in blue. Mutations identified in *D. melanogaster* are in red.

JAGN1 proteins in most species are relatively small (<200 amino acids) and are predicted to contain four transmembrane domains, two extracellular/luminal loops and both the NH_2- and the COOH-termini facing the cytoplasm (Fig. 2*B*). JAGN1 localizes to the ER under steady state (13), as do Erv cargo sorters (9, 10, 14, 15, 23, 37, 39, 41, 53). The COOH-terminal -KKHK sequence of JAGN1 fits the consensus dilysine motif present in proteins that cycle between the ER and the Golgi, including the Erv cargo receptors (reviewed in Refs. 2, 12) (Fig. 2*A*). The dilysine motif is recognized by the coatomer protein complex I (COPI) recycling machinery, and interactions between JAGN1 and COPI subunits have been detected (13). The COOH-terminus of JAGN1 also contains dihydrophobic and diacidic motifs (Fig. 2*A*) that may link JAGN1 to the coatomer protein complex II (COPII)-coating machinery involved in anterograde ER-to-Golgi transport (44). Thus, JAGN1 contains sorting motifs for incorporation into both anterograde COPII vesicles and retrograde COPI vesicles, as might be expected for a protein moving cargoes between the ER and the Golgi. Detailed reviews of ER-Golgi traffic mediated by COPII and COPI vesicles have been published (4, 12, 17, 18, 26, 29, 35, 44, 48).

JAGN1 and Severe Congenital Neutropenia

The first case of JAGN1-associated severe congenital neutropenia (SCN) (SCN6, OMIM no. 616022) correlated with a homozygous mutation of the initiator methionine to isoleucine, possibly resulting in a translational null (13) (Fig. 2*B*). Subsequent analysis of 74 patients with SCN identified nine additional mutations in JAGN1 [8 homozygous and 1 heterozygous complemented mutation; 8 were missense, and 1 was nonsense (1, 13) (Fig. 2*B*)]. Mutations reported in ClinVar are also included in Fig. 2*B*. Interestingly, the

majority of mutations cluster in the highly conserved NH_2-terminus and within the second extracellular loop, implicating these regions in JAGN1 functionality.

SCN6 patients present with recurrent infections caused by severe neutropenia (a count of <1,500 neutrophils/μL of blood) resulting from impaired maturation of neutrophils. Neutrophils from SCN6 patients have decreased number of secretory granules and exhibit an enlarged ER. Dilation of the ER is often caused by defects in the exit of select cargo proteins, as extensively described in mouse chondrocytes and osteoblasts defective in collagen traffic (due to defects in COPII transport machinery) but not impaired in traffic of other proteins (50). This suggests that JAGN1 function might be required for trafficking of specific proteins out of the ER. Neutrophils from SCN6 patients also exhibit an altered *N*-glycome, with a decrease in fucosylation of numerous proteins (discussed in detail below) (13).

Mouse Models of JAGN1 Deletion

Attempts to generate a *Jagn1* knockout (KO) mouse proved unsuccessful because of lethality at embryonic day 8.5 (E8.5) (51), indicating a requirement for JAGN1 during development before blood cell differentiation. Mice with conditional *Jagn1* KO in hematopoietic cells develop normally, including their immune cell populations (51). However, their neutrophils are defective in pathogen clearance and show deficiencies in chemotaxis and granulopoiesis. Like neutrophils from SCN6 patients, neutrophils from mice silenced for JAGN1 expression show alterations in protein glycosylation, specifically, a reduction in sialylation. Glycosylation was aberrant on proteins involved in neutrophil migration and killing efficacy such as integrins, collagenase, lactoferrin, and neutrophilic granule proteins, perhaps underlying the defective response to infections.

Extra-Hematopoietic Symptoms

SCN6 patients often exhibit short stature, scoliosis, dental deformations, pancreatic insufficiency, bone abnormalities, and neurodevelopmental delay, suggesting that JAGN1 function is required organism-wide and not only in neutrophils (3, 13, 16). This suggests that if JAGN1 is involved in protein sorting/trafficking, the protein "clients" it traffics are present in many (if not all) cells of an SCN patient.

ROLES OF TETRASPANINS AND ERV PROTEINS IN PROTEIN SORTING

The molecular mechanisms of JAGN1 action are unknown, and we posit that the similarity in membrane topology of JAGN1 to two well-characterized families of 4-transmembrane-spanning cargo sorting/transporting proteins, the tetraspanins and the Ervs, might provide clues to the role of JAGN1 in cellular and organismal homeostasis. Below we discuss key parameters of tetraspanin and Erv function in cargo sorting, and then draw on the similarities between those proteins and JAGN1 to propose a role for JAGN1 in transporting cell-specific proteins, as well as a ubiquitously expressed subset of Golgi glycosyltransferases.

Tetraspanins

Tetraspanins are a large family of relatively small (<350 amino acids) proteins characterized by a tetraspanning membrane topology and a function in the traffic of cargo proteins through the secretory and endosomal pathways (reviewed in Refs. 31, 42, 49, 52, 57). Herein, we chose CD151 and CD63 as paradigms for comparisons with JAGN1.

CD151 localizes to the plasma membrane, as well as lysosomes and endosomes (34), and regulates the endocytosis of a variety of integrins, including $\alpha_3\beta_1$, $\alpha_5\beta_1$, $\alpha_6\beta_1$, $\alpha_6\beta_4$, and $\alpha_7\beta_1$ (34, 47, 55), which control the signaling function of these cell-surface proteins (34). CD63 (tetraspanin-30) localizes to late endosomes and lysosomes but cycles between those compartments and the cell surface (38) to facilitate traffic of ubiquitous proteins such as integrins, as well as cell-specific cargos, including the C-X-C chemokine receptor type 4 (CXCR4), neutrophil elastase, the β-subunit of the gastric H^+-K^+-ATPase, membrane-type 1-matrix metalloproteinase (MT1-MMP), and TIMP metallopeptidase inhibitor 1 (TIMP-1) (27, 38, 54). CD63 is widely expressed in phylogeny (Supplemental Fig. S1; all supplemental material is available at https://doi.org/10.6084/m9.figshare.12654047).

The molecular mechanism by which CD151 sorts/traffics cargoes has been elucidated, and CD151 binding to its integrin clients requires the large extracellular/luminal loop (34, 47, 55). The domains of CD63-cargo interactions are not as well established, but its interaction with the proneutrophil elastase also requires the large extracellular/luminal loop (27).

Both, CD151 and CD63 interact with the adaptor/clathrin-coating machinery through COOH-terminal tyrosine-based internalization motifs (11). CD151 interacts with the adaptor protein-2 (AP-2) complex at the plasma membrane, allowing for clathrin-mediated endocytosis of CD151 carrying its client proteins (11). CD63 and bound cargoes also are endocytosed from the cell surface through interactions with the AP-2 adaptor complex, but the internalized CD63 and associated cargoes are then sorted within

endosomes and targeted for lysosomes via interaction with the AP-3 adaptor complex (38).

Erv Proteins

Erv proteins were identified as factors required for selective protein sorting in the budding yeast *S. cerevisiae* (reviewed in Refs. 5, 45). The Erv family is defined functionally, and only some of the members belong to the tetraspanning family while others are single spanners (18). Ervs are relatively small (<450 amino acids), and localize to the ER under steady state, but continuously cycle between the ER and the Golgi (18). Herein, we discuss Erv26(TEX261) and Erv29[surfeit locus protein 4 homolog (SFT-4); SURF4].

Erv26p(TEX261) is required for the ER export of the secretory pro-alkaline phosphatase (ALP), a hydrolytic enzyme destined to the yeast vacuole (14, 15). Depletion or mutations in Erv26p cause accumulation of pro-ALP in the ER but do not affect the maturation and traffic of another vacuolar enzyme, carboxypeptidase Y, underscoring Erv26p selectivity for its clients. Erv26p also is required to traffic the Ktr3p mannosyltransferase, a Golgi-localized type II transmembrane protein. Ktr3p exit from the ER is decreased in cells lacking functional Erv26p, while another transmembrane protein, Erv41, is transported irrespective of Erv26p functionality. The role of Erv26p in the transport of a Golgi-localized glycosylation enzyme in yeast is reminiscent of the glycosylation defects (lack of fucosylation and sialylation) observed in cells lacking JAGN1 or containing mutant JAGN1 in mammalian cells. Consistent with its role in the traffic of ubiquitous glycosyltransferases, Erv26 is widely expressed and highly

conserved throughout phylogeny (Supplemental Fig. S2; see https://doi.org/10.6084/m9.figshare.12654047).

Erv29p(SFT-4; SURF4) is required to sort the yeast pro-α-factor and carboxypeptidase for transport from the ER to the Golgi (10, 23). Like Erv26p, Erv29p is selective for its cargo, and defects in Erv29p do not affect constitutive secretion. The *C. elegans* ortholog of Erv29, SFT-4, is required for the export of the vitellogenin-2 yolk protein from the ER (41). Loss of SFT-4 causes the accumulation of lipoprotein yolk particles within a distended ER lumen, a morphological characteristic of defects in ER exit of other proteins, such as fibrillar collagens (50). SFT-4 localizes to the ER at steady state but cycles between the ER and the Golgi (18, 41). The human ortholog of Erv29p, SURF4, also regulates ER export of cargo proteins: RNAi depletion of SURF4 from the HepG2 hepatoma-derived cells inhibits the secretion of apolipoprotein B (ApoB) lipoprotein particles (41). In a murine model, SURF4 deletion leads to embryonic lethality at E9.5, while heterozygous mice exhibit an accumulation of SURF4 cargo (ApoB) in liver cells (21). Importantly, overall secretion from HEK293 cells depleted of SURF4 was normal, implying that SURF4 facilitates the traffic of a limited and specific set of "client" proteins (21).

The molecular mechanism of these Erv proteins' action is well described, and, like the tetraspanins, the Erv proteins bind their cargo through their extracellular/luminal large loops (10, 14).

Ervs sort cargo proteins for exit from the ER by coupling them to the COPII-coating machinery (10, 18). After transporting their cargo to the Golgi, Ervs recycle via COPI-coated vesicles to mediate reiterative cycles of transport. Ervs contain two COOH-

terminal sorting motifs, a dihydrophobic and/or diacidic sorting motif that couples them to the COPII-coating machinery for anterograde transport and a terminal dilysine (-KKXX) motif that couples them to the COPI-coating machinery for recycling back to the ER (reviewed in Refs. 5, 18, 20, 23, 41).

In summary, the tetraspanins and the Erv proteins share a number of key characteristics related to their cargo transport function: *1*) they have a tetraspanning membrane topology with two extracellular/luminal loops and both NH_2- and COOH-termini within the cytosol; *2*) they are highly conserved and widely expressed; *3*) they sort/traffic only selective client proteins without regulating overall secretion or endocytosis; *4*) they sort/traffic cargoes present in many cell types (integrins for tetraspanins, glycosyltransferase for Erv26), as well as cargoes present in only specialized cells (neutrophil elastase for CD63 in neutrophils, lipoprotein particles for SURF4 in hepatocytes); *5*) they bind their cargo through their larger extracellular/luminal domains; and *6*) they contain sorting motifs within their cytosolic termini for interaction with the cytosolic-coating machinery (AP/clathrin coats for the tetraspanins and COPII and COPI coats for the Ervs). These shared characteristics of tetraspanins and Erv proteins form the foundation for modeling the possible role of JAGN1 in sorting specific client proteins at the ER-Golgi interface.

MODEL OF JAGN1 FUNCTION BASED ON SIMILARITIES TO TETRASPANINS AND ERV PROTEINS

JAGN1 shares key characteristics of tetraspanins and Erv proteins: it has the same membrane topology; is highly conserved and widely expressed; regulates the traffic of only select proteins; and contains sorting motifs within its COOH-terminus for

interacting with coating machineries. These similarities are diagramed in Fig. 3 and support our suggestion that JAGN1 traffics client proteins at the ER-Golgi interface, possibly in two directions:

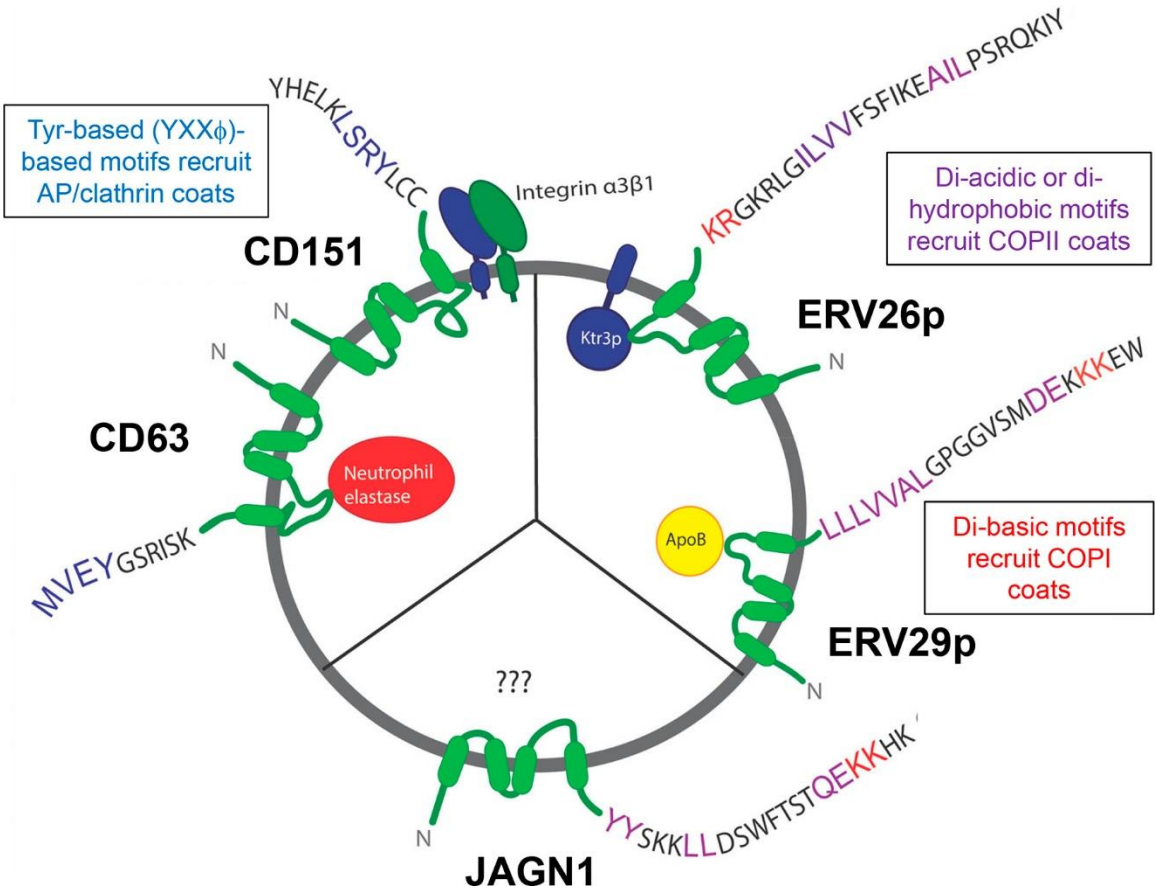

Fig. 3. Similarities between Jagunal homolog 1 (JAGN1), tetraspanins, and endoplasmic reticulum vesicle proteins (Ervs). Two members of the tetraspanin family (CD63 and CD151), two members of the Erv family (Erv26p and Erv29p), and JAGN1 show analogous 4-transmembrane-spanning topology, with NH_2- and COOH-termini in the cytosol. Tetraspanins and Ervs bind their cargo proteins via the large luminal loop, but whether and how JAGN1 may bind cargo proteins is unknown. The Tyr-based (Y-X-X-ϕ) sorting motifs that link tetraspanins to the adaptor protein (AP)/clathrin coating machinery are in blue. The known and putative diacidic or dihydrophobic sorting motifs that link Erv proteins and JAGN1 to the coatomer protein complex I (COPII)-coating machinery are in purple. The known and putative dibasic sorting motifs that link Erv proteins and JAGN1 to the coatomer protein complex I (COPI)-coating machinery are in red.

Direction 1

JAGN1 may facilitate the anterograde ER-to-Golgi traffic of proteins by sorting them into ER-derived COPII vesicles destined to the Golgi. Such client proteins may include cell-specific cargos exemplified by the yolk protein receptor in the oocytes of *D. melanogaster* (30) or any of the numerous neutrophil-specific cargoes (although the exact clients of JAGN1 in neutrophils remain to be elucidated) (13, 28, 51). Such cargoes likely are responsible for the most acute and cell- and/or tissue-specific phenotypes when JAGN1 function is compromised. Selective cell- and/or tissue-specific phenotypes are often observed when components of traffic machineries are compromised, as reported for skeletal defects in patients with mutations in the Sec24D component of the COPII coat (43, 56). JAGN1 also may traffic ubiquitously expressed glycosyltransferases from the ER to the Golgi, as suggested by the function of Erv26p in mediating the ER-to-Golgi transport of the Ktr3p Golgi glycosyltransferase (14).

Direction 2

JAGN1 may mediate the retrograde Golgi-to-ER traffic of some glycosyltransferases. Golgi-localized glycosylation enzymes are known to continuously cycle between the Golgi and the ER (40), implying that these proteins must be sorted in both the anterograde and the retrograde directions to achieve their correct steady-state localization. Indeed, many *cis*-Golgi-localized glycosyltransferases bind directly to COPI, presumably to be sorted into the retrograde pathway (33). However, JAGN1 deficiency appears to selectively affect fucosylation (observed in SCN6 patients) and sialylation (observed in mouse neutrophils deleted of JAGN1), two processes catalyzed by glycosyltransferases localized to the *trans*-Golgi. Importantly, fucosyltransferase and

sialyltransferase lack COPI-binding motifs and must use adaptor proteins to aid their incorporation into recycling COPI vesicles (33). It is possible that JAGN1 facilitates such recycling process.

Fucosylation and sialylation (and terminal glycosylation in general) are essential for mammalian development and physiological homeostasis (32). The proposed function of JAGN1 in the sorting/traffic of the fucosyl- and sialyltransferases can explain the many extra-hematopoietic phenotypes observed in SCN6 patients, since glycosylation is essential in all cells, albeit some might be less sensitive to glycosylation changes.

CONCLUSIONS AND FUTURE DIRECTIONS

Experimental evidence will be needed to assess JAGN1 function in the transport of cell-specific proteins, as well as ubiquitous glycosyltransferases. It will be essential to test whether JAGN1 cycles between the ER and the Golgi, and if JAGN1 traffics proteins in both anterograde and retrograde directions. Although the presence of the COPI-sorting motif in JAGN1 supports the cycling model, it remains to be determined if JAGN1 binds COPII components. It also will be important to uncover the identity of JAGN1 cargoes in different cell types and assess whether pathogenic mutations within JAGN1 affect the trafficking of all or only some proteins. Especially relevant will be to test the effects of mutations in the larger extracellular/luminal loop of JAGN1, since those seem involved in cargo binding in tetraspanins and Ervs. Only such experimental data will illuminate the possibility that JAGN1 represents a third member of a family of tetraspanning cargo sorters/traffickers.

GRANTS

This work was supported by National Institute of General Medical Sciences Grant R01GM122802 and by the National Science Foundation (MCB-1615607).

DISCLOSURES

No conflicts of interest, financial or otherwise, are declared by the authors.

AUTHOR CONTRIBUTIONS

P.E.V., Y.J.K.E., and E.S. prepared figures; P.E.V. and E.S. drafted manuscript; P.E.V., F.P., Y.J.K.E., and E.S. edited and revised manuscript; P.E.V., F.P., Y.J.K.E., and E.S. approved final version of manuscript.

REFERENCES

1. **Al-Herz W, Chou J, Delmonte OM, Massaad MJ, Bainter W, Cast- agnoli R, Klein C, Bryceson YT, Geha RS, Notarangelo LD.** Comprehensive genetic results for primary immunodeficiency disorders in a highly consanguineous population. *Front Immunol* 9: 3146, 2019. doi:10.3389/ fimmu.2018.03146.

2. **Arakel EC, Schwappach B.** Formation of COPI-coated vesicles at a glance. *J Cell Sci* 131: jcs209890, 2018 [Erratum in *J Cell Sci* 131: jcs218347, 2018]. doi:10.1242/jcs.209890.

3. **Baris S, Karakoc-Aydiner E, Ozen A, Delil K, Kiykim A, Ogulur I, Baris I, Barlan IB.** JAGN1 deficient severe congenital neutropenia: two cases from the same family. *J Clin Immunol* 35: 339 –343, 2015. doi:10. 1007/s10875-015-0156-2.

4. **Barlowe C, Helenius A.** Cargo capture and bulk flow in the early secretory pathway. *Annu Rev Cell Dev Biol* 32: 197–222, 2016. doi:10. 1146/annurev-cellbio-111315-125016.

5. **Barlowe CK, Miller EA.** Secretory protein biogenesis and traffic in the early secretory pathway. *Genetics* 193: 383–410, 2013. doi:10.1534/ genetics.112.142810.

9. **Belden WJ, Barlowe C.** Erv25p, a component of COPII-coated vesicles, forms a complex with Emp24p that is required for efficient endoplasmic reticulum to Golgi transport. *J Biol Chem* 271: 26939 –26946, 1996. doi:10.1074/jbc.271.43.26939.
10. **Belden WJ, Barlowe C.** Role of Erv29p in collecting soluble secretory proteins into ER-derived transport vesicles. *Science* 294: 1528 –1531,2001. doi:10.1126/science.1065224.

11. **Berditchevski F, Odintsova E.** Tetraspanins as regulators of protein trafficking. *Traffic* 8: 89–96, 2007. doi:10.1111/j.1600-0854.2006.00515.x.

12. **Béthune J, Wieland FT.** Assembly of COPI and COPII vesicular coat proteins on membranes. *Annu Rev Biophys* 47: 63–83, 2018. doi:10.1146/ annurev-biophys-070317-033259.

13. **Boztug K, Järvinen PM, Salzer E, Racek T, Mönch S, Garncarz W, Gertz EM, Schäffer AA, Antonopoulos A, Haslam SM, Schieck L, Puchałka J, Diestelhorst J, Appaswamy G, Lescoeur B, Giambruno R, Bigenzahn JW, Elling U, Pfeifer D, Conde CD, Albert MH, Welte K, Brandes G, Sherkat R, van der Werff Ten Bosch J, Rezaei N, Etzioni A, Bellanné-Chantelot C, Superti-Furga G, Penninger JM, Bennett KL, von Blume J, Dell A, Donadieu J, Klein C.** JAGN1 deficiency causes aberrant myeloid cell homeostasis and congenital neutropenia. *Nat Genet* 46: 1021–1027, 2014. doi:10.1038/ng.3069.

14. **Bue CA, Barlowe C.** Molecular dissection of Erv26p identifies separable cargo binding and coat protein sorting activities. *J Biol Chem* 284: 24049 –24060, 2009. doi:10.1074/jbc.M109.022590.

15. **Bue CA, Bentivoglio CM, Barlowe C.** Erv26p directs pro-alkaline phosphatase into endoplasmic reticulum-derived coat protein complex II transport vesicles. *Mol Biol Cell* 17: 4780 –4789, 2006. doi:10.1091/mbc. e06-05-0455.

16. **Cifaldi C, Serafinelli J, Petricone D, Brigida I, Di Cesare S, Di Matteo G, Chiriaco M, De Vito R, Palumbo G, Rossi P, Palma P, Cancrini C, Aiuti A, Finocchi A.** Next-generation sequencing reveals a JAGN1 mutation in a syndromic child with intermittent neutropenia. *J Pediatr Hematol Oncol* 41: e266 – e269, 2019. doi:10.1097/MPH. 0000000000001256.

17. **D'Arcangelo JG, Stahmer KR, Miller EA.** Vesicle-mediated export from the ER: COPII coat function and regulation. *Biochim Biophys Acta* 1833: 2464 –2472, 2013. doi:10.1016/j.bbamcr.2013.02.003.

18. **Dancourt J, Barlowe C.** Protein sorting receptors in the early secretory pathway. *Annu Rev Biochem* 79: 777–802, 2010. doi:10.1146/annurev- biochem-061608-091319.

19. **El-Gebali S, Mistry J, Bateman A, Eddy SR, Luciani A, Potter SC, Qureshi M, Richardson LJ, Salazar GA, Smart A, Sonnhammer ELL, Hirsh L, Paladin L, Piovesan D, Tosatto SCE, Finn RD.** The Pfam protein families database in 2019. *Nucleic Acids Res* 47: D427–D432, 2019. doi:10.1093/nar/gky995.

20. **Emmer BT, Hesketh GG, Kotnik E, Tang VT, Lascuna PJ, Xiang J, Gingras AC, Chen XW, Ginsburg D.** The cargo receptor SURF4 promotes the efficient cellular secretion of PCSK9. *eLife* 7: 7, 2018. doi:10.7554/eLife.38839.

21. **Emmer BT, Lascuna PJ, Tang VT, Kotnik EN, Saunders TL, Khori- aty R, Ginsburg D.** Murine Surf4 is essential for early embryonic development. *PLoS One* 15: e0227450, 2020. doi:10.1371/journal.pone. 0227450.

22. **Finn RD, Coggill P, Eberhardt RY, Eddy SR, Mistry J, Mitchell AL, Potter SC, Punta M, Qureshi M, Sangrador-Vegas A, Salazar GA, Tate J, Bateman A.** The Pfam protein families database: towards a more sustainable future. *Nucleic Acids Res* 44: D279 –D285, 2016. doi:10.1093/ nar/gkv1344.

23. **Foley DA, Sharpe HJ, Otte S.** Membrane topology of the endoplasmic reticulum to Golgi transport factor Erv29p. *Mol Membr Biol* 24: 259 –268, 2007. doi:10.1080/09687860601178518.

24. **Gouy M, Guindon S, Gascuel O.** SeaView version 4: a multiplatform graphical user interface for sequence alignment and phylogenetic tree building. *Mol Biol Evol* 27: 221–224, 2010. doi:10.1093/molbev/msp259.

25. **Guindon S, Dufayard JF, Lefort V, Anisimova M, Hordijk W, Gas- cuel O.** New algorithms and methods to estimate maximum-likelihood phylogenies: assessing the performance of PhyML 3.0. *Syst Biol* 59: 307–321, 2010. doi:10.1093/sysbio/syq010.

26. **Jackson LP.** Structure and mechanism of COPI vesicle biogenesis. *Curr Opin Cell Biol* 29: 67–73, 2014. doi:10.1016/j.ceb.2014.04.009.

27. **Källquist L, Hansson M, Persson A-M, Janssen H, Calafat J, Tapper H, Olsson I.** The tetraspanin CD63 is involved in granule targeting of neutrophil elastase. *Blood* 112: 3444–3454, 2008. doi:10.1182/blood-2007-10-116285.

28. **Khandagale A, Lazzaretto B, Carlsson G, Sundin M, Shafeeq S, Römling U, Fadeel B.** JAGN1 is required for fungal killing in neutrophil extracellular traps: Implications for severe congenital neutropenia. *J Leu- koc Biol* 104: 1199–1213, 2018. doi:10.1002/JLB.4A0118-030RR.

29. **Lee MC, Miller EA.** Molecular mechanisms of COPII vesicle formation. *Semin Cell Dev Biol* 18: 424–434, 2007. doi:10.1016/j.semcdb.2007.06.007.

30. **Lee S, Cooley L.** Jagunal is required for reorganizing the endoplasmic reticulum during *Drosophila* oogenesis. *J Cell Biol* 176: 941–952, 2007. doi:10.1083/jcb.200701048.

31. **Levy S, Shoham T.** The tetraspanin web modulates immune-signalling complexes. *Nat Rev Immunol* 5: 136–148, 2005. doi:10.1038/nri1548.

32. **Li J, Hsu H-C, Mountz JD, Allen JG.** Unmasking fucosylation: from cell adhesion to immune system regulation and diseases. *Cell Chem Biol* 25: 499–512, 2018. doi:10.1016/j.chembiol.2018.02.005.

33. **Liu L, Doray B, Kornfeld S.** Recycling of Golgi glycosyltransferases requires direct binding to coatomer. *Proc Natl Acad Sci USA* 115: 8984–8989, 2018. doi:10.1073/pnas.1810291115.

34. **Liu L, He B, Liu WM, Zhou D, Cox JV, Zhang XA.** Tetraspanin CD151 promotes cell migration by regulating integrin trafficking. *J Biol Chem* 282: 31631–31642, 2007. doi:10.1074/jbc.M701165200.

35. **Lord C, Ferro-Novick S, Miller EA.** The highly conserved COPII coat complex sorts cargo from the endoplasmic reticulum and targets it to the golgi. *Cold Spring Harb Perspect Biol* 5: a013367, 2013. doi:10.1101/ cshperspect.a013367.

36. **Madeira F, Park YM, Lee J, Buso N, Gur T, Madhusoodanan N, Basutkar P, Tivey ARN, Potter SC, Finn RD, Lopez R.** The EMBL- EBI search and sequence analysis tools APIs in 2019. *Nucleic Acids Res* 47: W636–W641, 2019. doi:10.1093/nar/gkz268.

37. **Otte S, Belden WJ, Heidtman M, Liu J, Jensen ON, Barlowe C.** Erv41p and Erv46p: new components of COPII vesicles involved in transport between the ER and Golgi complex. *J Cell Biol* 152: 503–518, 2001. doi:10.1083/jcb.152.3.503.

38. **Pols MS, Klumperman J.** Trafficking and function of the tetraspanin CD63. *Exp Cell Res* 315: 1584–1592, 2009. doi:10.1016/j.yexcr.2008.09.020.

39. **Powers J, Barlowe C.** Transport of axl2p depends on erv14p, an ER- vesicle protein related to the Drosophila cornichon gene product. *J Cell Biol* 142: 1209–1222, 1998. doi:10.1083/jcb.142.5.1209.

40. **Rhee SW, Starr T, Forsten-Williams K, Storrie B.** The steady-state distribution of glycosyltransferases between the Golgi apparatus and the endoplasmic reticulum is approximately 90:10. *Traffic* 6: 978–990, 2005. doi:10.1111/j.1600-0854.2005.00333.x.

41. **Saegusa K, Sato M, Morooka N, Hara T, Sato K.** SFT-4/Surf4 control ER export of soluble cargo proteins and participate in ER exit site organization. *J Cell Biol* 217: 2073–2085, 2018. doi:10.1083/jcb.201708115.

42. **Saiz ML, Rocha-Perugini V, Sánchez-Madrid F.** Tetraspanins as orga- nizers of antigen-presenting cell function. *Front Immunol* 9: 1074, 2018. doi:10.3389/fimmu.2018.01074.

43. **Sarmah S, Barrallo-Gimeno A, Melville DB, Topczewski J, Solnica- Krezel L, Knapik EW.** Sec24D-dependent transport of extracellular matrix proteins is required for zebrafish skeletal morphogenesis. *PLoS One* 5: e10367, 2010. doi:10.1371/journal.pone.0010367.

44. **Sato K, Nakano A.** Mechanisms of COPII vesicle formation and protein sorting. *FEBS Lett* 581: 2076–2082, 2007. doi:10.1016/j.febslet.2007.01.091.

45. **Schekman R, Orci L.** Coat proteins and vesicle budding. *Science* 271: 1526–1533, 1996. doi:10.1126/science.271.5255.1526.

46. **Srivastava M, Simakov O, Chapman J, Fahey B, Gauthier ME, Mitros T, Richards GS, Conaco C, Dacre M, Hellsten U, Larroux C, Putnam NH, Stanke M, Adamska M, Darling A, Degnan SM, Oakley TH, Plachetzki DC, Zhai Y, Adamski M, Calcino A, Cummins SF, Goodstein DM, Harris C, Jackson DJ, Leys SP, Shu S, Woodcroft BJ, Vervoort M, Kosik KS, Manning G, Degnan BM, Rokhsar DS.** The Amphimedon queenslandica genome and the evolution of animal com- plexity. *Nature* 466: 720–726, 2010. doi:10.1038/nature09201.

47. **Sterk LM, Geuijen CA, Oomen LC, Calafat J, Janssen H, Sonnenberg A.** The tetraspan molecule CD151, a novel constituent of hemidesmo- somes, associates with the integrin alpha6beta4 and may regulate the spatial organization of hemidesmosomes. *J Cell Biol* 149: 969–982, 2000. doi:10.1083/jcb.149.4.969.

48. **Szul T, Sztul E.** COPII and COPI traffic at the ER-Golgi interface. *Physiology (Bethesda)* 26: 348–364, 2011. doi:10.1152/physiol.00017.2011.

49. **Termini CM, Gillette JM.** Tetraspanins function as regulators of cellular signaling. *Front Cell Dev Biol* 5: 34, 2017. doi:10.3389/fcell.2017.00034.

49a. **UniProt Consortium.** Activities at the Universal Protein Resource (Uni- Prot). *Nucleic Acids Res* 42: D191–D198, 2014. doi:10.1093/nar/gkt1140.

49b. **UniProt Consortium.** UniProt: a worldwide hub of protein knowledge. *Nucleic Acids Res* 47: D506–D515, 2019. doi:10.1093/nar/gky1049.

49c. **The UniProt Consortium.** UniProt: the universal protein knowledgebase. *Nucleic Acids Res* 45: D158 –D169, 2017. doi:10.1093/nar/gkw1099.

50. **Wilson DG, Phamluong K, Li L, Sun M, Cao TC, Liu PS, Modrusan Z, Sandoval WN, Rangell L, Carano RAD, Peterson AS, Solloway MJ.** Global defects in collagen secretion in a Mia3/TANGO1 knockout mouse. *J Cell Biol* 193: 935–951, 2011. doi:10.1083/jcb.201007162.

51. **Wirnsberger G, Zwolanek F, Stadlmann J, Tortola L, Liu SW, Perlot T, Järvinen P, Dürnberger G, Kozieradzki I, Sarao R, De Martino A, Boztug K, Mechtler K, Kuchler K, Klein C, Elling U, Penninger JM.** Jagunal homolog 1 is a critical regulator of neutrophil function in fungal host defense. *Nat Genet* 46: 1028 – 1033, 2014. doi:10.1038/ng.3070.

52. **Yeung L, Hickey MJ, Wright MD.** The many and varied roles of tetraspanins in immune cell recruitment and migration. *Front Immunol* 9: 1644, 2018. doi:10.3389/fimmu.2018.01644.

53. **Yin Y, Garcia MR, Novak AJ, Saunders AM, Ank RS, Nam AS, Fisher LW.** Surf4 (Erv29p) binds amino-terminal tripeptide motifs of soluble cargo proteins with different affinities, enabling prioritization of their exit from the endoplasmic reticulum. *PLoS Biol* 16: e2005140 – e2005140, 2018. doi:10.1371/journal.pbio.2005140.

54. **Yoshida T, Ebina H, Koyanagi Y.** N-linked glycan-dependent interac- tion of CD63 with CXCR4 at the Golgi apparatus induces downregulation of CXCR4. *Microbiol Immunol* 53: 629 –635, 2009. doi:10.1111/j.1348- 0421.2009.00167.x.

55. **Zevian S, Winterwood NE, Stipp CS.** Structure-function analysis of tetraspanin CD151 reveals distinct requirements for tumor cell behaviors mediated by α3β1 versus α6β4 integrin. *J Biol Chem* 286: 7496 –7506, 2011. doi:10.1074/jbc.M110.173583.

56. **Zhang H, Yue H, Wang C, Gu J, He J, Fu W, Hu W, Zhang Z.** Novel mutations in the SEC24D gene in Chinese families with autosomal recessive osteogenesis imperfecta. *Osteoporos Int* 28: 1473–1480, 2017. doi:10.1007/s00198-016-3866-2.

57. **Zou F, Wang X, Han X, Rothschild G, Zheng SG, Basu U, Sun J.** Expression and function of tetraspanins and their interacting partners in B cells. *Front Immunol* 9: 1606, 2018. doi:10.3389/fimmu.2018.01606.

A NOVEL ROLE FOR JAGN1 IN REGULATING CELL-SUBSTRATE ADHESION

by

PEYTON E. VANWINKLE, BRIDGE WYNN, HADLEY ROSENGRANT, OLGIERD TALAROWSKI, EUNJOO LEE, HOLLY THOMAS, DEVI NARRA, CLAIRE CONKLIN, SUMMER THYME, JOHN PARANT, RICHARD KAHN, ELIZABETH SZTUL

In preparation, 2024

Format adapted for dissertation

ABSTRACT

JAGN1 protein function is essential, as shown by the early embryonic lethality of JAGN1 KO mice. JAGN1 is ubiquitously expressed in nearly all animal and plant phyla, suggesting that JAGN1 performs a basic cellular function, common to all eukaryotic cells. Yet, such a conserved function for JAGN1 remains to be elucidated.

Zebrafish are well suited to study JAGN1 because they express two orthologues (*jagn1a* mainly expressed in the brain at early larval stages, and *jagn1b* expressed in most other tissues), raising the possibility that single knockouts would prevent embryonic lethality. This proved to be the case for our *jagn1a*$^{-/-}$ fish, which lived to adulthood, but exhibited defects in brain activity. In contrast, our *jagn1b*$^{-/-}$ zebrafish died between 7 and 14 days post fertilization, partially recapitulating the phenotype of the murine KO. Importantly, our zebrafish models provide a unique system to study jagn1 function in adult and larval fish, with the added advantage of the jagn1 orthologs affecting tissue-specific events.

To probe cellular functions of JAGN1, we generated three mouse embryonic fibroblast (MEF) lines expressing distinct dysfunctional forms of JAGN1. These cell lines exhibited a prominent defect in spreading and adhering to substrate after plating. Phalloidin staining of the actin cytoskeleton showed that *Jagn1* KO cells spread more slowly and contain a more compact actin cytoskeleton. Further informing the adhesive

defect, these cells also exhibited a delayed deposition of focal adhesion proteins paxillin and integrin α5.

Preliminary analyses of proteins proximal to *Jagn1* by Bio-ID identified proteins known to facilitate ER-Golgi traffic, as well as numerous actin interactors. Together, these findings support the proposed role of JAGN1 in transporting cargo proteins (potentially adhesion proteins), but also raise the possibility of a more direct role in modulating actin dynamics.

Introduction

Jagunal (*JAGN1;* Jagunal1 (Jagn1): small egg in Korean) was first described in a screen of lethal mutations on chromosome 3R of the fruit fly *D. melanogaster* [2]. Three alleles were shown to cause lethality at the first and second instar stages, and one was semi-lethal. Analysis of the larvae showed a defect in the enrichment of the subcortex of the oocyte with ER proteins during stages 9 and 10 of oocyte development. Moreover, these Jagn1 mutations inhibited the transport of Yolkless (a transmembrane yolk receptor) to the lateral membrane of the oocyte, without affecting the transport of another transmembrane protein (Gurken), suggesting that JAGN1 may function in protein traffic and that such function may be cargo-specific.

Subsequent studies implicated JAGN1 as a critical factor in neutrophil-mediated immune response. Patients with *JAGN1* mutations exhibit SCN (Severe Congenital Neutropenia) with recurrent infections, a reduced number of circulating neutrophils and defects in neutrophil-mediated cytotoxicity [3-7]. Currently, 10 patient mutations have been reported in the literature [8], with the vast majority being point mutations, and only

one truncation (Figure 1A). Jagn1 protein is predicted to contain four trans-membrane domains, two ER lumenal loops and both, the N- and the C-termini in the cytoplasm, and the mutations preferentially occur within the cytosolic N- and C-termini (Figure 1A). Along with the characteristic neutropenia, SCN patients have a spectrum of syndromic symptoms (malformation of facial bones, skeletal malformations, epilepsy, developmental delays, and other less common symptoms [8, 9]), suggesting a requirement for Jagn1 function in multiple tissues. The molecular underpinning of these phenotypes are currently unknown, but SCN patients have aberrant glycosylation of neutrophil proteins. Moreover, neutrophils isolated from these patients have increased levels of BiP (a chaperone protein responsible for mediating ER stress), suggesting a possible role for Jagn1 in cellular stress response [8-10]. This function for Jagn1 is supported by results in cell culture models, which show increased levels of Jagn1 during chemically induced ER stress [11], and implicate Jagn1 in ameliorating ER stress to prevent apoptotic cell death [12].

Attempts to generate a *Jagn1* KO mouse via a flox-Cre system were futile due to embryonic lethality at stage E8.5, indicating a requirement for JAGN1 function during early development [13]. The inability to generate a *Jagn1* KO mice suggests that the SCN6 patients have at least some Jagn1 activity, and it is perhaps relevant that the majority of SCN6 mutations are missense rather than nonsense. Subsequently, mice with a conditional *Jagn1* KO in only hemopoietic cells showed normal development, and did not exhibit neutropenia [13]. However, their neutrophils were defective in pathogen clearance and the mice showed lower survival rates after systemic infection with *Candida albicans*, a commensal yeast in most healthy individuals, but which causes life-

threatening systemic infections in immunocompromised individuals [14, 15]. The mutant mice had increased fungal burden and increased hyphal growth associated with increased virulence and tissue damage (nephritis, splenitis and liver and lung damage) [6]. Moreover, they showed a significant decrease in the recruitment of neutrophils to the site of intraperitoneal injection with *Candida*, and neutrophils isolated from these mice were defective in chemotaxis when assayed in culture [13]. Furthermore, neutrophils isolated from these mutant mice exhibited decreased killing potency and a reduction in glycosylation (sialylation) on proteins involved in neutrophil migration and killing efficacy such as integrins, collagenase, lactoferrin, and neutrophilic granule proteins [13]. Recently generated mice with conditional KO of *Jagn1* only in the pro-B cell cells (*Jagn1*$^{\Delta B}$ mutants) exhibit normal development, but aberrant levels of bone marrow plasma cells, as well as elevated numbers of B cells in the spleen [16]. The mutant B cells exhibit increased ER stress, as shown by increased XBP1 splicing. Moreover, human patient B cells produced IgG1 with an aberrant glycoprofile, indicating a role for JAGN1 in protein glycosylation in B cells is addition to neutrophils [16].

JAGN1 orthologs are found across all the 9 major multicellular animal phyla and in 3 of the 4 plant phyla [17], suggesting that Jagn1 performs a basic cellular function shared by eukaryotic cells, and its cellular role is not restricted to neutrophil or egg development. Jagn1 orthologs have between 170 and 183 amino acids (Figure 1B), with no sequence similarity (as defined by BLAST searches) to other proteins, and Jagn1 constitutes its own family. The amino acid sequence similarity of Jagn1 orthologs is high throughout the entire protein, with the highest amino acid sequence conservation in the N-terminus. Remarkably, a stretch of 6 amino acids is conserved in organisms as diverse

as plants (*A. thaliana*), worms (*C. elegans*), flies (*D. melanogaster*) and mammals (*H. sapiens*), suggesting that it may represent a functional domain. In mammalian cells, JAGN1 has been localized to the ER [10] but its exact cellular function is currently unknown.

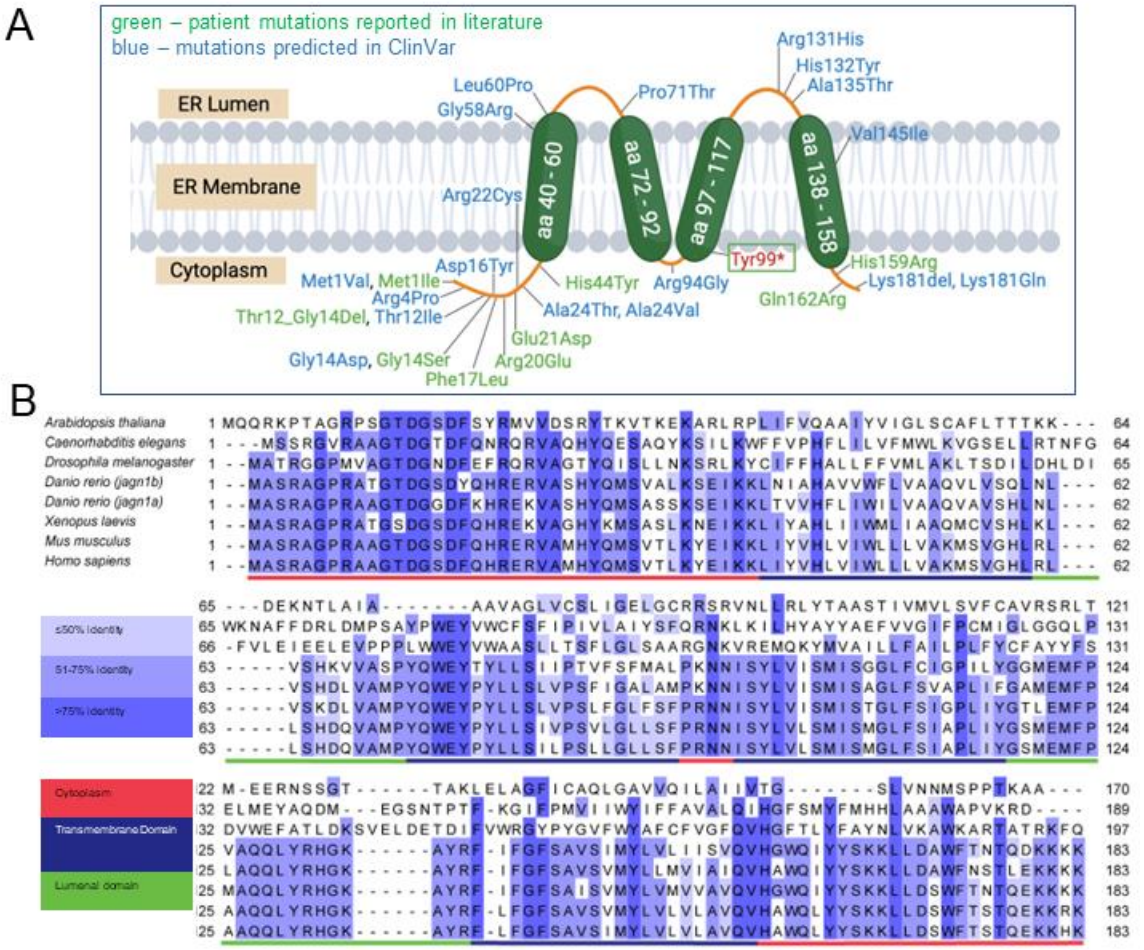

Figure 1. JAGN1 is a tetraspanning protein conserved across phyla.

A) JAGN1 is predicted to have 4 transmembrane domains, two luminal loops and a cytoplasmic N- and C-termini. Point mutations in Jagn1 reported to cause SCN6 are in green, with the single known nonsense mutation indicated in red. Mutations reported in ClinVar are indicated in green **B)** High sequence conservation between JAGN1 homologs in *A. Thaliana, C. elegans, D. melanogaster, D. rerio (jagn1a/b), X. laevis, M. musculus, and H. sapiens.*

JAGN1 is ubiquitously expressed in human tissues [17], and this is probably also true for other multicellular species, further suggesting that Jagn1 performs a basic cellular function. As such, research into more generic phenotypes of JAGN1 mutation(s) may provide insight into a conserved cellular process, in contrast to the highly specialized functions that have been elucidated in hematopoietic cells and developing oocytes. Thus, we developed a novel zebrafish *D. rerio* animal model that allows the analysis of organismal function of JAGN1. We chose the zebrafish because their genome encodes two *JAGN1* genes, *jagn1a* and *jagn1b*. The gene duplication present in the zebrafish (but not in mammalian models) could lead to functional redundancy or result in neo-functionalization so that the two genes may support the same function(s) of JAGN1 or one may assume a distinct function(s). Importantly, this may allow the generation of viable animals when only one of the genes is eliminated, a situation not possible in mammals with only a single *JAGN1* gene.

We used CRISPR/Cas9 to generate *jagn1a*$^{-/-}$ and *jagn1b*$^{-/-}$ zebrafish and analyzed the organismal function of each. We report that *jagn1a*$^{-/-}$ KO fish develop to adulthood and appear morphologically normal, but that the larvae exhibit defects in brain activity. In contrast, no adult fish were recovered from heterozygous crosses of *jagn1b*$^{+/-}$ fish, and all homozygous *jagn1b*$^{-/-}$ mutant larvae died by 14 days post fertilization (dpf). Our results suggest the evolutionary specialization of Jagn1a as a functional requirement in brain development and/or function, with Jagn1b supporting function(s) analogous to those mediated by the single *JAGN1* gene in other organisms.

To also explore the cellular functions of Jagn1, we generated three distinct lines of CRISPR/Cas9-modified mouse embryonic fibroblasts (MEFs) lacking a functional

Jagn1. Due to JAGN1's proposed role in ER-Golgi and Golgi-ER trafficking, we evaluated the morphology of the Golgi in the JAGN1 mutant cells. This revealed a change in Golgi size and architecture, consistent with defects in membrane traffic at the ER-Golgi interface. An additional striking phenotype in JAGN1 mutant cells was a significant defect in spreading and the formation of focal adhesions after plating.

Using Bio-ID to analyze the proteins proximal to JAGN1, we identified multiple proteins known to function in ER-Golgi and Golgi-ER trafficking, as well as a number of proteins involved in modulating actin function, or acting as actin scaffolds. This information supports the role of JAGN1 as a cargo protein "escort" required for transporting specific proteins at the ER-Golgi interface, but also raises the possibility that JAGN1 may directly regulate actin dynamics. Importantly, both of these processes are ubiquitous, consistent with the wide distribution and critical importance of JAGN1.

RESULTS

1. Zebrafish larvae deleted of *jagn1a* develop into morphologically normal adults, but exhibit decreased brain activity

The zebrafish *D. rerio* have two *jagn1* genes encoding Jagn1a and Jagn1b that show high level of amino acid conservation (Figure 2A). Interestingly, there is limited conservation in expression patterns. Single cell RNASeq of pooled 1, 2, and 5 dpf zebrafish larvae [1] documents an almost mutually exclusive distribution of the jagn1a and jagn1b transcripts, with Jagn1a almost exclusively expressed in the brain and Jagn1b expressed in all other tissues (Figure 2B).

We used CRISPR-Cas9 technology to target exon 3 of *jagn1a* gene. Outcrossing the initial generation (F0) to wild-type (AB) fish allowed us to isolate a single allele of *jagn1a* with a 17 bp deletion (Figure 2C). The 17 bp deletion causes the Jagn1 sequence to go out of frame at amino acid 69 and results in the addition of 126 amino acids not endogenous to jagn1a. The *jagn1a*$^{-/-}$ larvae are recovered at normal Mendelian ratios (Figure 2D), and morphologically normal fish grow to adulthood. This suggests that the zebrafish *jagn1a* is not a functional ortholog of the mammalian Jagn1, as KO of Jagn1 in mice causes embryonic lethality. This difference could be due to the largely brain-specific distribution of jagn1a. Importantly, the survival of the *jagn1a*$^{-/-}$animals allows a future inquiry into the brain-specific role of *jagn1a* to provide novel insight into neurological defects in SCN patients with *JAGN1* mutations, without deleterious (fatal) effects of Jagn1 deletion in other tissues.

An established multi-day analysis of distinct aspects of zebrafish behavior was used to show that the *jagn1a*$^{-/-}$ larvae exhibit mostly normal sleep and waking activity, as well as normal response to a tapping stimulus (Figure 2E). In contrast, probing brain activity of the *jagn1a*$^{-/-}$ larvae by assessing the phosphorylation of the extracellular signal-regulated kinase (ERK) shows decreased brain activity (Figure 2F). In the nervous system, ERK phosphorylation is induced by glutamate release and its subsequent binding to ionotropic and metabotropic receptors found throughout the brain and spinal cord in neurons and glia. Highest concentrations of glutamate are found in synaptic vesicles in nerve terminals from where it can be released by exocytosis. Thus, ERK phosphorylation reflects synaptic transmission and is a readout of neuronal activity. ERK phosphorylation was assessed in the *jagn1a*$^{-/-}$ larvae relative to *jagn1a*$^{+/-}$ and *jagn1a*$^{+/+}$ animals by staining

for phospho-ERK and ERK, and normalizing phospho-ERK to total ERK within each larva. As shown in Figure 2F, the *jagn1a*$^{-/-}$ larvae had lower brain activity (indicated by purple pseudocoloring) that represents lower activation of neurons [18]. Each panel represents the composite analysis from a replicate of brain activity quantification.

2. Deletion of zebrafish *jagn1b* causes larval lethality

CRISPR-Cas9-mediated targeting of exon 3 of *jagn1b* gene led to the isolation of a single mutant with an 11bp insertion (Figure 2G). The +11bp insertion causes the sequence of Jagn1b to go out of frame at amino acid 64 and causes the addition of 6 extra amino acids. The *jagn1b*$^{-/-}$ larvae are recovered at normal Mendelian ratios at 7 dpf, but their number decreases at 11 dpf, and *jagn1b*$^{-/-}$ larvae are not detected at 14 dpf (Figure 2H). It appears that that the majority of the *jagn1b*$^{-/-}$ larvae die between 11dpf and 14 dpf, and no viable adults have been recovered (data not shown). The relatively late lethality in zebrafish is in contrast to embryonic lethality at E8.5 in mice, suggesting that in zebrafish, *jagn1a* may compensate for *jagn1b* in younger larvae, or the function of Jagn1b is not required during zebrafish early development. Thus, Jagn1b is a closer functional ortholog of mammalian Jagn1 than Jagn1a, as Jagn1b (but not Jagn1a) is required for organismal survival.

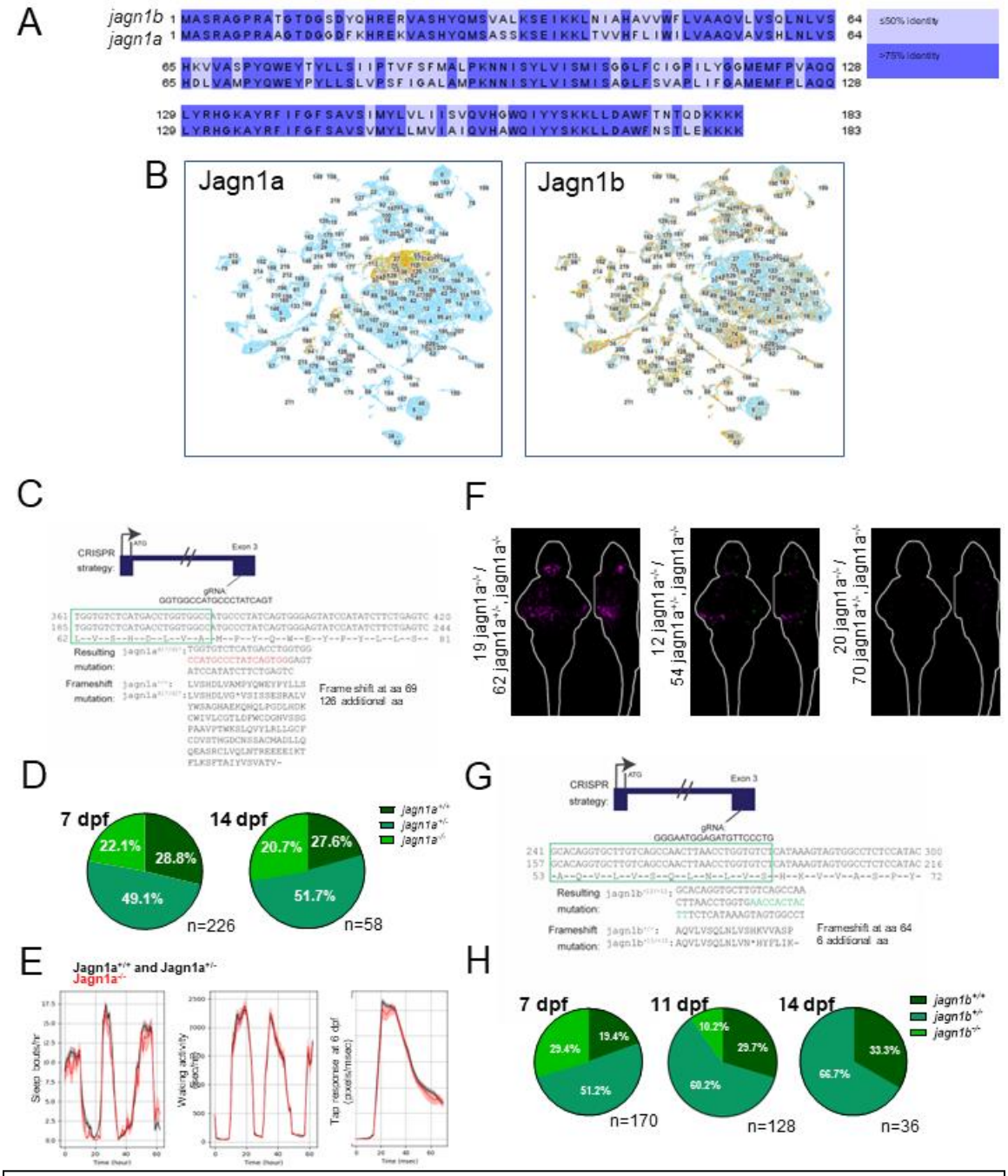

Figure 2. Jagn1a and Jagn1b have conserved sequences but distinct expression patterns and phenotypic effects

A) The two *jagn1* genes in zebrafish show extensive conservation of amino acid sequence. Percent identity is represented by blue shading. **B)** Single cell RNASeq of pooled 1, 2, and 5 dpf larvae shows expression of jagn1a predominantly in the brain, while jagn1b is expressed in other tissues. Figure adapted from Farnsworth et. al, 2020 [1]. **C)** Exon 3 was targeted with CRISPR/Cas9 to generate the *jagn1a*$^{\Delta 17/\Delta 17}$ allele. Site of mutation is indicated in green, and the resulting deletion is indicated in red

text. **D)** *jagn1a*$^{+/-}$ animals were crossed and the resulting progeny assessed by genotyping at 7 dpf and at 14 dpf. The *jagn1a*$^{-/-}$ mutant fish were recovered at normal Mendelian ratios. **E)** 7 or 6 dpf larvae were assessed for sleep bouts/hr, waking activity/hr and responses to dark flash stimuli. *Jagn1a*$^{-/-}$ animals show behaviors analogous to those of control AB fish. N=12 homozygous mutants, 61 heterozygotes and wildtype fish. The red curve represents the behavior over time of the *jagn1*$^{-/-}$ larvae, while the black curve represents the behavior over time of both the *jagn1*$^{+/-}$ and *jagn1*$^{+/+}$ larvae, pooled. Deviations within genotypes are indicated by the shading on each line.. **F)** Brain activity of 6 dpf larvae was determined via ratiometric staining of p-ERK/ERK. *Jagn1a*$^{-/-}$ animals show decreased neuronal activity. N values are indicated on left side of each image. **G)** Exon 3 was targeted with CRISPR/Cas9 to recover the *jagn1a*$^{+11/+11}$ allele. Site of mutation is indicated in green box, and the resulting insertion is indicated in green text. **H)** *jagn1b*$^{-/+}$ animals were crossed and the resulting progeny were genotyped at 7, 11, and 14 dpf. *jagn1b*$^{-/-}$ animals were present at roughly Mendelian ratio at 7 dpf, but their number deceased at 11 dpf and no *jagn1b*$^{-/-}$ animals were recovered at 14 dpf. N values are indicated.

3. CRISPR-Cas9-mediated targeting of *Jagn1* gene in mouse embryonic fibroblasts (MEFs)

To analyze the cellular functions of Jagn1, we used two independent guides to target exon 2 of MEF JAGN1 and recovered 3 alleles (Figure 3A). Cell line 2-19 (generated from guide 2) is predicted to make more than half of the Jagn1 protein (97 amino acids total with 94 amino acids encoding the N-terminus of Jagn1), which is predicted to span the membrane twice (Figure 3B). This truncated Jagn1 might be at least partially functional as a patient with a deletion after amino acid Tyr 99 has neutropenia but is alive. Cell line 3-19 (generated from guide 3) is predicted to express a 78 amino acid protein with N-terminal 66 amino acids encoding Jagn1, while cell line 3-20 (also generated from guide 3) is predicted to express a 74 amino acid protein containing the first 64 amino acids of Jagn1 (Figure 3A and B).

To determine whether the mutant mRNAs undergo a nonsense-mediated decay, we performed RT-PCR on wild type and Jagn1 mutant cells. Two sets of primers were

generated as *Jagn1* has three isoforms with different splicing sites that generate different potential proteins (Figure 3C). Isoform 1 generates a 183 amino acid protein that is assumed to be the fully functional isoform. Isoform 2 generates a protein with a shorter N-terminus (encoding amino acids 55 to 183), due to a different 5' untranslated region (UTR) and an alternate start site. Isoform 3 has an alternative splicing that results in a frameshift mutation and a premature stop codon, generating a truncated protein containing only 67 N-terminal amino acids. It is likely that Jagn1 proteins translated from isoform 2 and isoform 3 (assuming that they are stable) are not functional. Primers were designed to assess levels of isoforms 1 and 3 combined, while distinct primers were designed to assess levels of isoform 2.

As shown in Figure 3D, the 2-19 cells have nearly normal levels of isoforms 1 and 3, with decreased isoform 2, likely due to the CRISPR indel occurring further downstream in the genome, causing nonsense-mediated decay only in isoform 2. Thus, 2-19 cells can potentially synthesize Jagn1 mutant protein (STOP at 97) from isoform 1 and/or only synthesize the truncated (67 amino acids) protein encoded by isoform 3. Line 3-19 has significantly reduced levels of all three isoforms, suggesting that it is unlikely to synthesize any Jagn1 protein, including Jagn1 mutant protein. Thus, 3-19 cells are the closest to a deletion phenotype. In contrast, 3-20 cells have decreased (~50%) level of isoform 1 and 3, and even less (~30%) of isoform 2. Hence, these cells can potentially synthesize Jagn1 mutant protein (STOP at 74) from isoform 1 and/or only synthesize the truncated (67 amino acids) protein encoded by isoform 3. We are currently in the process of determining the relative abundance of isoforms 1 and 3. Thus, the 2-19 and 3-20 cells are likely to express truncated Jagn1 protein(s). Such protein(s) may be functionally

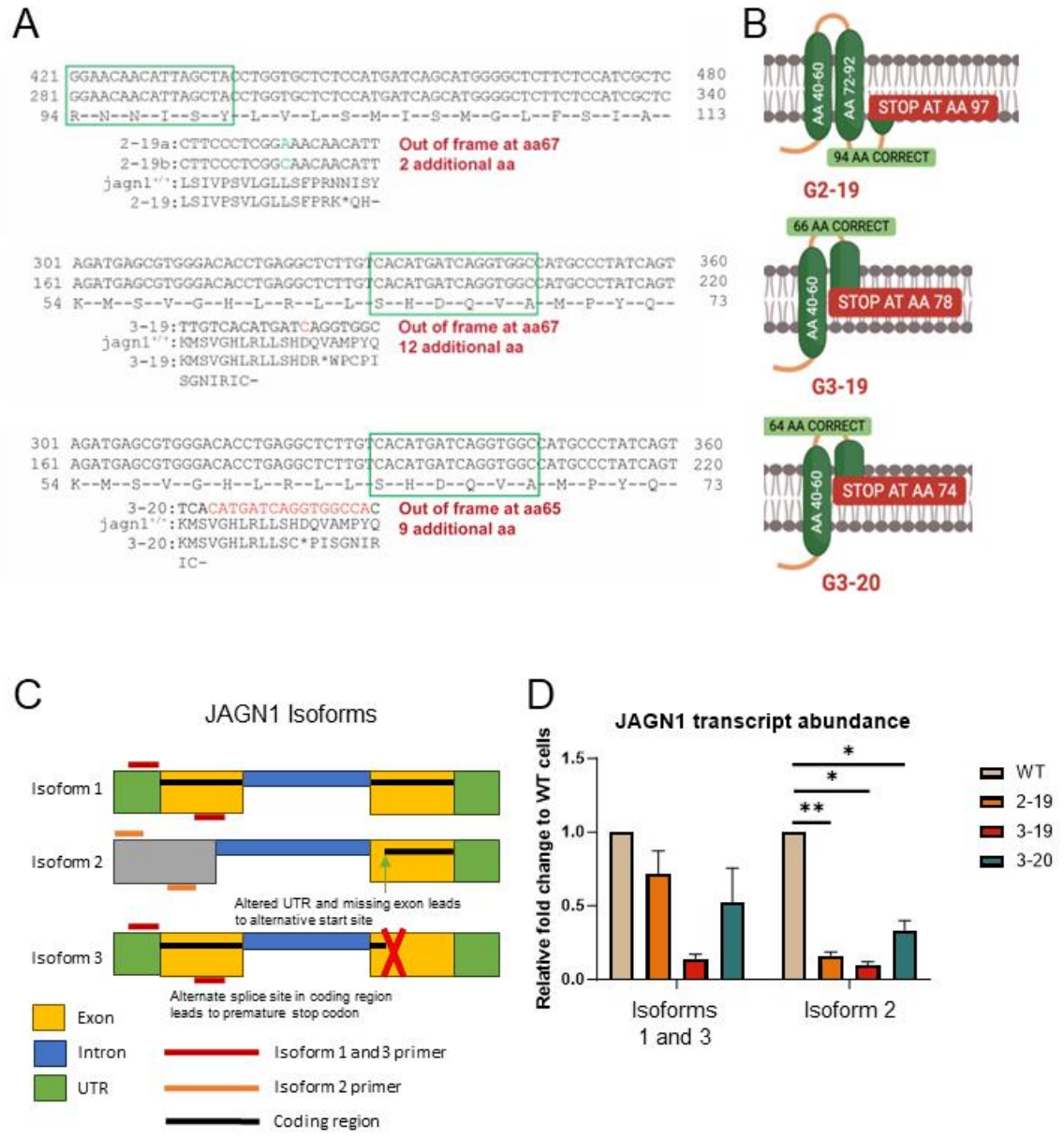

Figure 3. Generating and characterizing *Jagn1* mutant MEFs.

A) Exon 2 of mouse Jagn1 was targeted with CRISPR/Cas9, and three cell lines expressing distinct *Jagn1* alleles were selected. Sites of mutation are indicated by green boxes, and the resulting insertion is indicated in green text, while deletions are represented by red text. **B)** Diagram of wild-type Jagn1 and Jagn1 fragments encoded by each allele. **C**) Schematic of different JAGN1 isoforms assayed via RT-PCR. Primers indicated in red or orange, exons indicated in yellow, introns indicated in blue, UTR indicated in green, and resultant coding region indicated in black. **D)** Transcript levels of Jagn1 in the different cell lines indicate nonsense-mediated decay of all isoforms in line 3-19, but not in lines 2-19 or 3-20. n=3-4.

defective, making these cell lines loss of function alleles. However, if the truncated protein(s) act in a dominant negative manner, lines 2-19 and 3-20 may represent a gain of function alleles. As such, both the significant and less severe decreases in RNA level may result in aberrant cell function.

4. *Jagn1* mutant MEFs have defects in Golgi architecture

Based on JAGN1 being a tetraspanin and containing domains that bind components that mediate ER-Golgi cycling, we previously postulated that JAGN1 may function as a cargo "escort" to transport proteins at the ER-Golgi interface. Defects in protein trafficking to and from the Golgi often result in Golgi fragmentation, and we examined Golgi integrity in Jagn1 mutant cells. Golgi architecture was analyzed by assessing the distribution of the transmembrane GS28 SNARE that continuously cycles at the ER-Golgi interface. As shown in Figure 4A, the Golgi appeared "fluffier" in Jagn1 mutant cells. To provide a quantitative measure of Golgi integrity, the Golgi of an individual cell was selected from each image and the image was thresholded. This selection was then analyzed using the "analyze particles" function of FIJI, and the number and area of particles were recorded. A frequency distribution was generated from these data and pooled into three categories of small particles (from 0-1 μm^2), medium particles (from 1-5 μm^2), and large particles greater than 5 μm^2). As shown in Figure 4B, in wild-type cells ~80 % of all Golgi elements were larger that 1μm, and ~20 % were smaller than 1□m. In contrast, in 2-19 and 3-19 cells, only ~35% of Golgi elements were larger than 1 □m, and ~60% were smaller than 1 □m. Surprisingly, in 3-20 cells, the frequency distribution of Golgi elements was different than in wild-type or the other Jagn1 mutant cells, with ~ 60% of Golgi particles larger than 1 □m. Our results suggest

that any disruption of Jagn1 function affects Golgi integrity, supporting the notion that Jagn1 regulates ER-Golgi trafficking since aberrant vesicle transport in the absence of JAGN1 would cause Golgi disruption.

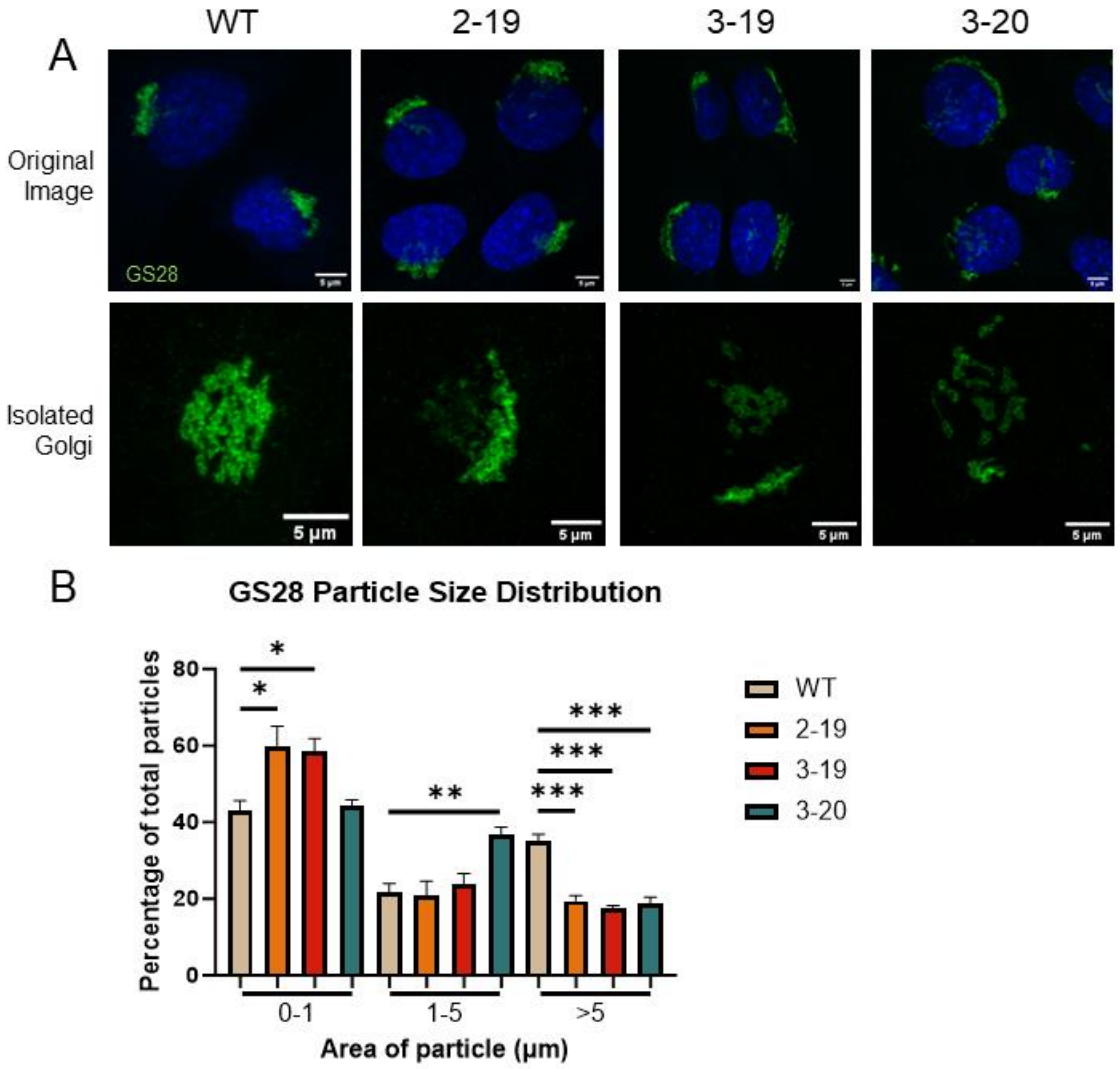

Figure 4. The Golgi is more fragmented in *Jagn1* mutant MEFs.

A) Wild-type and jagn1 mutant cells were stained for immunofluorescence with anti-GS28 and imaged via confocal microscopy, with 1-4 cells in each field of view. Individual Golgi were selected for further analysis. Scale bar = 5µm. **B)** Each Golgi image was thresholded and the number of distinct particles present within each Golgi, and the area of each particle were analyzed. The particles were grouped into 0-1, 1-5, and >5 μm^2 bins and are graphed as % of total particles. *Jagn1* mutant cells 2-19 and 3-19 exhibit a significant increase in small particles 0-1 μm^2. n=3-9 Golgi.

5. *Jagn1* mutant MEFs have defects in cell spreading.

During the selection of the Jagn1 mutant MEFs, we observed a delay in spreading in some of the cells. This was interesting because previous analyses of neutrophils in *Jagn1* KO mice suggested decreased motility, and we examined whether the 2-19, 3-19 and 3-20 mutant MEFs might have spreading defects. To assay this defect, cells were trypsinized, plated on coverslips, and were stained with actin-binding phalloidin at 3 hours after plating. Fluorescent images of the cells were then acquired (Figure 5A). Using the CellProfiler [19] program, these images were processed by generating a mask that included all cellular area containing the actin signal (Figure 5B). From this mask, the cell area, and cell aspect ratio (major axis length divided by minor axis length) were measured. This analysis determined that the area of the Jagn1 mutant cells was significantly decreased (Figure 5C), indicating less extensive spreading of the cells. The deficit in forming stable cellular projections was also evidenced by a significant decrease in the aspect ratio of Jagn1 mutant cells (Figure 5D). While the wild-type MEFs show extensive cell protrusions (white arrowhead in Figure 5A), Jagn1 mutant cells are significantly rounder and lack stable extensions.

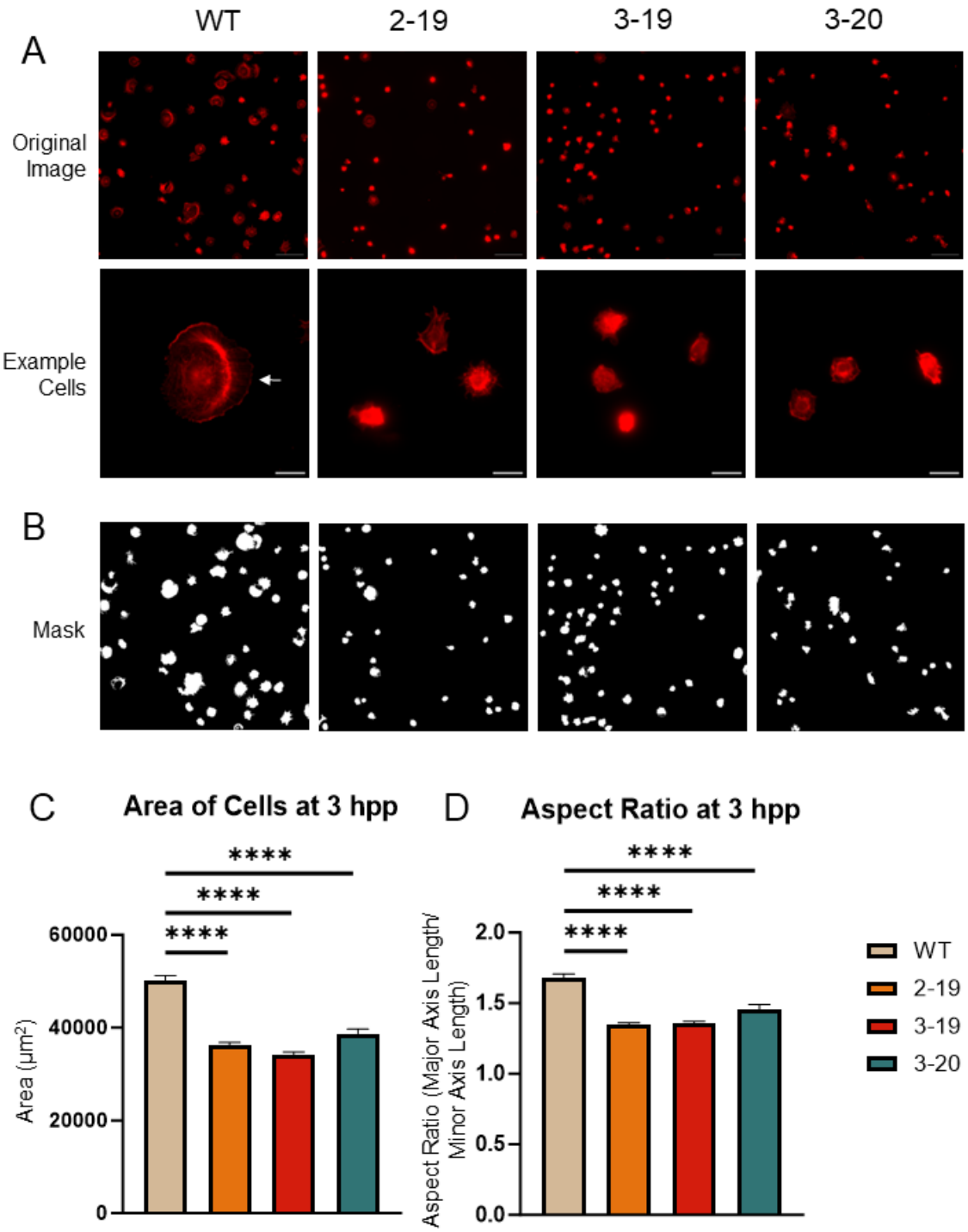

Figure 5. *Jagn1* mutant MEFs exhibit defects in cell spreading and distribution of the actin cytoskeleton.

A) Wild-type and *Jagn1* mutant cells were trypsinized, plated onto coverslips and

fixed at 3 hours post plating. Coverslips were stained with phalloidin and imaged. . Scale bar = 100μm. Example cells demonstrate difference in spreading between WT and *Jagn1* KO lines. White arrowhead indicates cortical actin that outlines a well-spread out wild-type cell. Scale bar = 20μm. Such cortical actin perimeters are not present in the *Jagn1* mutant cells. **B)** Images were processed via CellProfiler to generate masks which represent individual cells. **C)** Areas of individual masks were measured and an average area per cell is graphed. n= 440-808 cells. **D)** Aspect ratio of individual masks were measured and an average ratio per cell is graphed. n= 440-808 cells.

6. *Jagn1* mutant cells exhibit defects in establishment of focal adhesions during spreading

Cell attachment and spreading on a substrate involves the formation of contact sites between the actin cytoskeleton and the extracellular matrix. Such focal adhesion sites are characterized by the presence of integrins, which crosslink the intracellular actin to the extracellular matrix proteins, as well as actin regulatory proteins such as paxillin. To determine whether *Jagn1* might affect the formation of focal adhesions, we examined the distribution of integrin α5, and the focal adhesion protein paxillin in wild-type and *Jagn1* mutant cells at 3 hours post plating. As shown in Figure 6A, all wild-type cells had formed multiple focal adhesions (marked with orange arrowheads) outlining their periphery. In contrast, Jagn1 mutant cells were still mostly round, with significantly fewer focal adhesions, albeit some 3-20 cells had began to spread and to deposit focal adhesions (Figure 6A, orange arrows).

Interestingly, this phenotype appears to be transient, and Jagn1 mutant cells do form apparently normal focal adhesions containing paxillin and integrin □5 when analyzed ~24 hours post plating (white arrowheads in Figure 6B). However, despite establishing focal adhesions, there persists a change in the architecture of the cells. While the wild-type and the 3-20 cells appear fibroblast, spindle like, and are mostly aligned in

parallel “rows”, the 2-19 and 3-19 cells remain more roundish and do not organize into a spindle array.

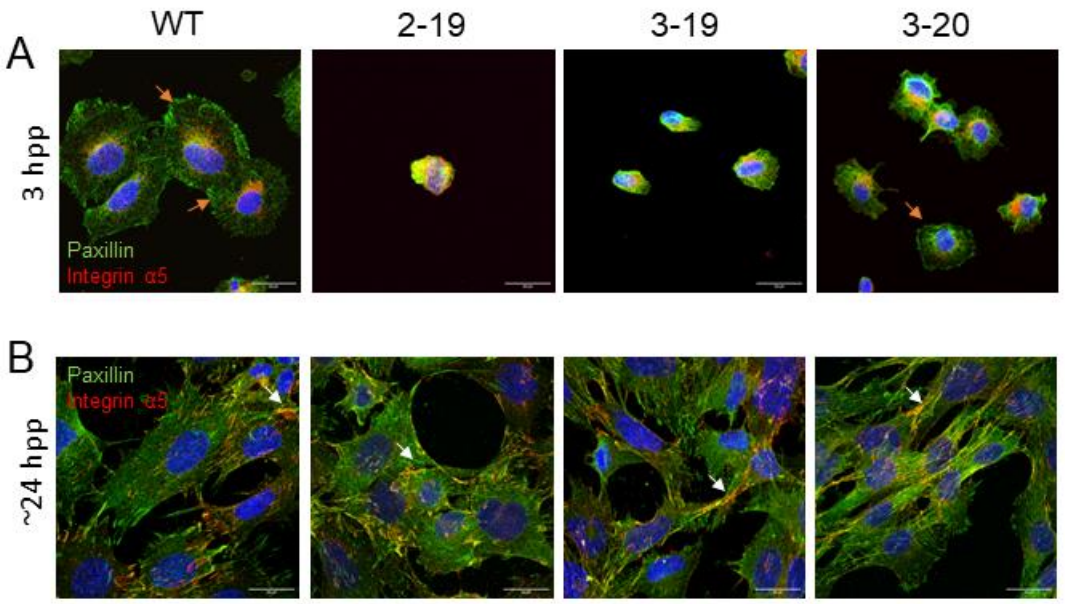

Figure 6: Adhesive molecules have aberrant behavior in *Jagn1* mutant cells.

A) Wild-type and *Jagn1* mutant cells were trypsinized, plated onto coverslips and fixed at 3 hours post plating. Coverslips were stained for Paxillin and Integrin α5 and imaged, and representative images are shown. *Jagn1* mutant cells exhibit significantly less spreading and deposition of adhesive molecules at the cell periphery. Orange arrows indicate focal adhesions. **B)** Cells were fixed ~24 hours after plating. Coverslips were stained for Paxillin and Integrin α5. *Jagn1* mutant cells establish focal adhesions containing colocalized Paxillin and Integrin α5 (white arrows) by ~24 hpp, but do not organize into rows as seen with wild-type cells. n=15 images. Scale bar = 20µm.

7. Proximity-dependent biotinylation by JAGN1 chimera labels proteins involved in ER-Golgi trafficking and that interact with and regulate actin dynamics

The molecular mechanism of JAGN1 action remains to be elucidated, and we used Bio-ID to identify proteins that may interact with Jagn1 to possibly inform on its function. We generated vectors expressing JAGN1 with a promiscuous BirA biotin ligase fused to either the N or the C terminus, transfected them into Human Embryonic Kidney (HEK) cells and allowed the biotin ligase to biotinylate proteins proximal to JAGN1.

Cells were solubilized and the biotinylated proteins were recovered on Streptavidin beads and either analyzed by SDS-PAGE followed by detection with Streptavidin or subjected to mass spectrometry. As shown in Figure 7A, numerous biotinylated proteins were isolated from cells expressing either the N- or the C-terminally tagged JAGN1, but not in non-transfected cells. The major biotinylated protein in each preparation was the JAGN1 construct (marked with an arrow in Figure 7A), consistent with high exogenous expression and suggesting possible oligomerization.

Mass spectrometry identified numerous proteins (Table S1), majority of which were biotinylated by both, the N- and the C-terminal constructs. Among the proteins were components of COPII (SEC22B) and COPI (Coatomer subunit γ-2) vesicles that carry proteins at the ER-Golgi interface, supporting the proposed "escort" role for JAGN1 in cargo trafficking. Interestingly, integrin β-1 was also recovered, raising the possibility that JAGN1 may regulate its trafficking. We note that the BirA ligase moiety is located in the cytoplasm, and not the ER lumen (tetraspanins bind their "escort" proteins within the ER lumen [20]), and thus would biotinylate cargo proteins only on readily accessible cytoplasmic residues. Moreover, a number of actin-binding proteins, as well as regulators of actin dynamics were recovered (Figure 7B). Of special interest are Filamin A, which binds to actin and connects it to the endoplasmic reticulum [21], and Coronin 1b, a cytoplasmic actin scaffolding protein [22] that regulates actin dynamics through Arp2/3 and cofilin mediated pathways. These results demonstrate that multiple proteins responsible for either scaffolding or directly regulating actin polymerization are within a ~20-30 nm radius of JAGN1, suggesting a possible role for JAGN1 in modulating actin dynamics. Such a function could explain the spreading defects in Jagn1 mutant cells.

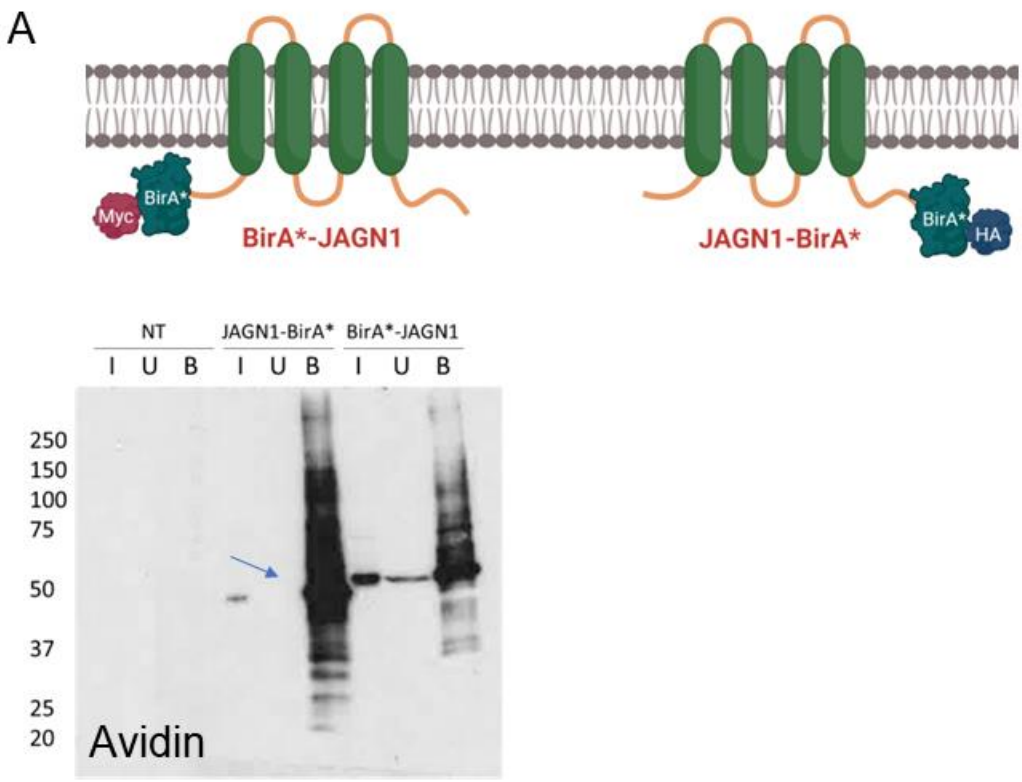
A
Myc
BirA*
BirA*-JAGN1
JAGN1-BirA*
BirA*
HA
NT
JAGN1-BirA*
BirA*-JAGN1
I U B I U B I U B
250
150
100
75
50
37
25
20
Avidin

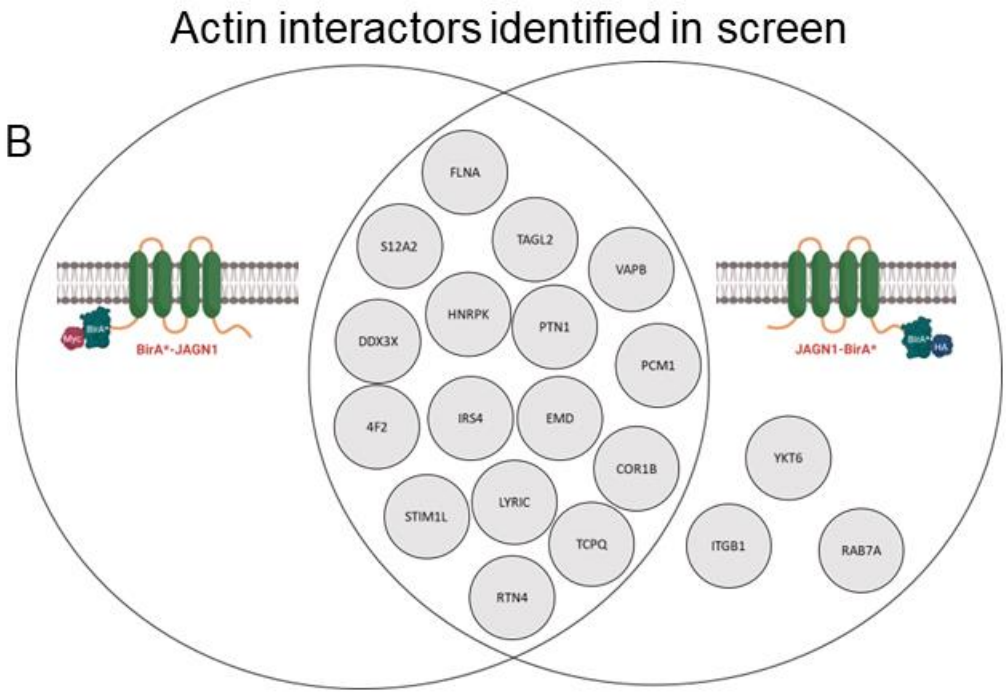
Actin interactors identified in screen
B
BirA*-JAGN1
JAGN1-BirA*
FLNA
S12A2
TAGL2
VAPB
HNRPK
PTN1
DDX3X
PCM1
4F2
IRS4
EMD
COR1B
YKT6
STIM1L
LYRIC
TCPQ
ITGB1
RAB7A
RTN4

Figure 7: JAGN1 has proximity to proteins interacting with actin.

A) HEK cells were transfected with both BirA*-JAGN1 and JAGN1-BirA* constructs and lysed after 24 hrs. Lysates were analyzed via western blot with HRP-conjugated avidin to visualize biotinylated proteins. **B)** Biotinylated proteins were isolated on streptavidin-conjugated agarose and identified by mass spectroscopy. JAGN1-BirA* and BirA*-JAGN1 label several actin-interacting proteins, with some proteins selectively biotinylated by JAGN1-BirA*. n=1.

DISCUSSION

We propose two potential models for JAGN1 mechanism of action. First, we continue to posit that JAGN1 acts as a cargo "escort" protein (Figure 8A). JAGN1 makes a good candidate for a putative cargo "escort" protein as it contains both COPI and COPII sorting motifs in its C-terminus, theoretically allowing it to traffic cargo between the ER and the Golgi. Such a function is supported by previous work showing Jagn1 to be required for Yolkless receptor trafficking in the fly oocyte [2]. Herein, two findings further support this role of JAGN1: 1) the recovery of components of COPI and COPII vesicles as proteins biotinylated by JAGN1-BirA constructs, placing them within ~20 mm of JAGN1; and 2) a more fragmented, "fluffy" Golgi apparatus in Jagn1 cells, indicating a perturbation in membrane trafficking at the ER-Golgi interface. Altered COPI recycling from the Golgi to the ER due to inability of COPI to bind JAGN1 in mutant cells would result in perturbation of Golgi architecture. Previous work has documented that perturbation in COPI function causes Golgi fragmentation [23].

Second, we propose that JAGN1 may play a role in actin dynamics (Figure 8B). A robust phenotype in the *Jagn1* KO cells was a defect in spreading behavior after trypsinization and plating. When analyzed via staining the actin cytoskeleton, Jagn1 mutant cells had less area and a lower aspect ratio than wild-type cells, indicating that they had spread less and had fewer stable projections. The defect in spreading was also reflected in a significant delay in the formation of focal adhesions. Further, Bio-ID demonstrated that JAGN1 interacts with components involved in modulating the actin cytoskeleton. Together, this suggests that JAGN1, may play a role in both, the trafficking

of cargo vesicles, as well as binding to actin-regulating proteins and regulating actin dynamics.

Importantly, other tetraspanin molecules have been shown to oligomerize to form enriched microdomains on the membrane that allows for scaffolding of protein interactions [24, 25]. For example, tetraspanins have been shown to interact directly with ERMs and Rac GTPases, and thereby affect the actin cytoskeleton [25]. It is possible that JAGN1 serves the same function, forming oligomers, partially evidenced by the fact that JAGN1-BirA biotinylates JAGN1 more than any other molecule within the biotinylation screen. It is possible that such JAGN1 microdomains facilitate interactions with actin scaffolders, such as Filamin A or Coronin 1B, both of which were detected in the biotinylation screen. Based on these findings, it is important to consider that similarly to tetraspanins [20, 25, 26], JAGN1 may serve roles in both, regulation of cargo trafficking, and actin scaffolding.

The findings reported herein increase the knowledge of JAGN1 function by both, recapitulating and expanding upon the established role of JAGN1 in motility, and introducing new potential functions such as actin scaffolding. Further, JAGN1 impact on molecules and complexes such as integrins and focal adhesions provides a more specific role for JAGN1 in neutrophil motility defects, potentially allowing for therapeutic advances in SCN. Future work is needed to validate JAGN1 interactions, and to elucidate if JAGN1 acts as a cargo “escort” to traffic integrin to allow the formation of focal adhesions during spreading, or if JAGN1 forms microdomains that facilitate actin scaffolding necessary for normal cytoskeletal function. It is also possible that, much like the multifunctional tetraspanins that have been our model for JAGN1 function, JAGN1

exhibits both of these activities, making it a molecule with diverse utility. This may explain why JAGN1 is so conserved across species, including plants, as both actin mechanics and vesicular transport are broadly required for life, across phyla and kingdoms.

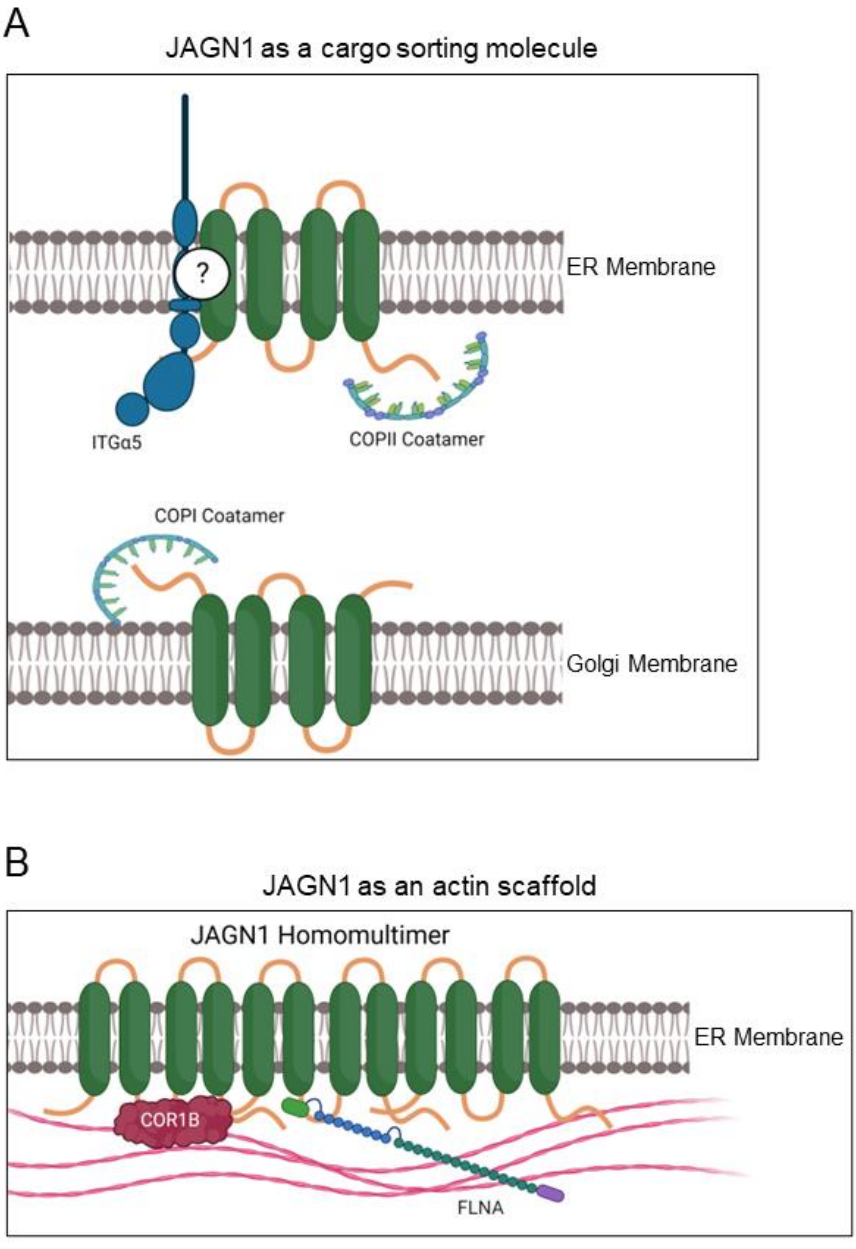

Figure 8: Proposed models for JAGN1 as a cargo chaperone or a component of actin-scaffolding microdomains.

A) Proposed model for JAGN1 as a cargo chaperone. In this model, JAGN1 facilitates trafficking of cargoes such as Integrin α5 by linking the cargo to the COPII machinery, allowing for ER exit and transport to the Golgi. JAGN1 is then recycled back to the ER by the COPI machinery. **B)** Proposed model for JAGN1 as an actin scaffold. In this model, JAGN1 oligomerizes and forms enriched microdomains that scaffold actin-interacting proteins such as Coronin 1B and Filamin A.

MATERIALS AND METHODS

Zebrafish husbandry

Zebrafish (*Danio rerio*) were maintained in accordance with the University of Alabama at Birmingham's Institutional Animal Care and Use Committee, according to the Zebrafish Research Facility and the vertebrate animal welfare protocol (APN 21787). Fish were housed on a circulating water system, on a 14:10 light:dark cycle. Fish were fed Gemma Micro 300 twice daily with one live artemia feeding. Fish were bred using the standard system water and two-piece tank system to prevent oophagy. Eggs were harvested, sorted for healthy eggs, and raised in E3 [27] until placed on the system or utilized for experiments.

Generation of jagn1a and jagn1b mutant fish

Alt-R crRNA target sites were designed with Integrated DNA Technologies Alt-R CRISPR HDR Design Tool (https://www.idtdna.com/pages/tools/alt-r-crispr-hdr-design-tool). Alt-R CRISPR-Cas9 crRNA, tracrRNA (IDT #1072532) and Alt-R S.p. Cas9 Nuclease V3 (IDT) was prepared following manufacturer instructions. 3 µM sgRNA (Table 2) were obtained through diluting 100 µM crRNA and 100 µM tracrRNA into Nuclease-Free Duplex Buffer (IDT #11-05-01-03), heating at 98ºC for 5 min, then

cooling to room temperature. 0.5 µL Cas9 protein was diluted with Cas9 working buffer (20 mM HEPES; 150 mM KCl, pH7.5) to yield a working concentration of 0.5 µg/µL. The diluted Cas9 protein working solution was mixed 1:1 with 3 µM sgRNA solution and then incubated at 37 ºC for 10 min to obtain RNP complex. RNP complex was freshly prepared and left on ice until microinjection. Microinjection was performed by injecting ~1 nL of RNP complex into yolk of 1-cell stage wild-type (AB) embryos.

F0 adults generated from this injection were crossed to AB fish to generate heterozygous offspring. Heterozygous offspring were then sequenced via Sanger Sequencing to determine sequences of CRISPR indels. Sequenced heterozygous fish were crossed to generate homozygous offspring. These offspring were sequenced once more to verify homozygosity for the mutant allele.

Allele	Guide
jagn1a$^{-/-}$	GGTGGCCATGCCCTATCAGT
Sequencing primers:	F: GGATATTGGCAATGGCATCT R: CATCACAGAAACAGCCGAGA
Genotyping primers:	F: TCAATTTGGTGTCTCATGACCTGGT R: GACTCAGAAGATATGGATACTC
jagn1b$^{-/-}$	GGGAATGGAGATGTTCCCTG
Sequencing primers:	F: TCCTTCTGCATTCACACAGC R: TTCCCCCGTAAAGAATAGGG
Genotyping primers:	F: GTCAGCCAACTTAACCTGGTG R: GGTATGGAGAGGCCACTACTTTAT

Table 1: gRNA and primers utilized to generate and characterize *jagn1a* and *jagn1b* mutants.

Genotyping by High Resolution Melt Analysis in Zebrafish

To isolate genomic DNA, adult fish were anaesthetized in 250mg/L Tricaine until opercular motion stopped. Tail clippings were collected from fish and incubated at 98°C for 20 min in 40 µl 25 mM NaOH in a 96-well plate; then neutralized with 40 µl of 40 mM Tris-HCl. For genotyping of whole embryos or larvae, the incubation time at 98°C was shortened to 10 minutes. PCR reactions contained 1 µl of LC Green Plus Melting Dye (Biofire Defense, BCHM-ASY-0005), 1 µl of 10x enzyme buffer, 0.2 µl of dNTP Mixture (10 mM each), 0.3 µl of $MgCl_2$, 0.3 µl of each primer (listed in Table 1) (10 µM), 1 µl of genomic DNA, 0.05 µl of Taq (Genscript #E00101), and water up to 10 µl. Primers are detailed in Table 1. The PCR reaction protocol was 98ºC for 30 sec, then 45 cycles of 98ºC for 10 sec, 59ºC for 20 sec, and 72ºC for 15 sec, followed by 95ºC for 30 sec and then rapid cooling to 4ºC. Following PCR, melting curves were generated and analyzed using the LightScanner instrument (Idaho Technology) over a 65-95°C range.

Analysis of behavior in *jagn1a* mutant larvae

Behavior was analyzed through a 14 time window protocol as previously described [18]Briefly, Fish were transferred to 96-well square 0.7 mL plates on the afternoon of 4 dpf. Plates were filled with standard fish water containing methylene blue, transferred to ice until movement stopped, and sealed with optical adhesive films (ThermoFisher Scientific). Experiments were conducted at approximately 28°C. Larval locations were monitored at using a Grasshopper3 camera (FLIR). The fish were monitored as detailed [18] until 7dpf when they were removed from analysis and genotyped via the previously described genotyping procedures.

Analysis of brain activity in *jagn1a* mutant larvae

Phosphorylated-ERK antibody staining was conducted as previously described [18, 28] Briefly, On 6 dpf fed larvae were maintained in a quiet environment and fixed in the mid-afternoon in 4% paraformaldehyde (PFA). diluted in 1× Phosphate Buffered Saline with 0.25% Triton (PBST). After overnight fixation, larvae were washed and bleached Larvae were then incubated at 70°C for 20 minutes in 150 mM TrisHCl pH 9.0, to retrieve antigens, followed by washes in PBST. Permeabilization of tissue was conducted by incubation in 0.05% Trypsin-EDTA on ice for 45 minutes. After three 15-minute washes and blocking for one hour (PBST with 2% normal goat serum , 1% bovine serum albumin , and 1% dimethyl sulfoxide), primary antibodies were diluted in blocking solution and incubated overnight. The phosphorylated ERK antibody (Cell Signaling, #4370) and total ERK antibody (Cell Signaling, #4696) were diluted both 1:500. The following day larvae were rinsed with PBST, and alexa-fluorophore conjugated secondary antibodies (Life Technologies) were diluted 1:500 in blocking solution for a second overnight incubation. Following three 15-minute PBST washes, larvae were mounted in 2% low-melting agarose in 1× PBS. Images were collected using either Zeiss LSM 780 or 880 upright confocal microscopes with a 20×/1.0 NA water-dipping objective. Larvae were removed from the agarose and genotyped as described above after imaging. Images were registered to a standard zebrafish reference brain using Computational Morphometry Toolkit (CMTK) [29, 30]. All phosphorylated-ERK images were normalized with a total-ERK stain. Similarity was calculated as described [18], with representative images depicting reduced activity as purple pseudocoloring, and increased activity as green pseudocoloring.

Generation and maintenance of *Jagn1* Knockout Cells

The mouse *Jagn1* gene (NCBI gene ID: 67767) is located on chromosome 6, with two exons that are predicted to encode three transcripts. All differences between these three transcripts are found within exon 1. We therefore designed 20 nt guides (Guide 2: AGGTAGCTAATGTTGTTCCG, Guide 3: GCTCTTGTCACATGATCAGG) to target exon 2, biased towards the 5' end, using a combination of the Benchling (https://www.benchling.com/academic/) and Broad Institute (https://portals.broadinstitute.org/gpp/public/analysis-tools/sgrna-design) online algorithms. Guides were cloned into the pSpCas9(BB)-2A-Puro (PX459) V2.0 vector (obtained from Addgene #62988) using the BbsI sites, as previously described (Ran, et al (2013) Nat Protoc, 8: 2281-2308; Turn, et al MBoC (2020)). The targeting strategy is outlined in Figure 1.

Low passage, wild type (WT; ATCC CRL-2991) immortalized mouse embryonic fibroblasts (MEFs) were grown at 37°C, in a humidified atmosphere with 5% CO_2 in DMEM medium (Corning), supplemented with 10% fetal bovine serum (FBS, Atlanta Biologicals; S11150) and 2 mM glutamine. Antibiotics were not used in routine cell culture, and cells are regularly checked for mycoplasma contamination. WT MEFs were grown to ~90% confluence in 6-well dishes, transfected with 4 µg DNA (each guide plasmid) in 5 µl JetOptimus DNA transfection reagent (Polyplus). After overnight incubation cells were then re-plated onto 10 cm plates for growth overnight. Puromycin (3 µg/ml, Sigma) was added the next day and maintained for three days, to enrich for transfected cells. Cells were then plated on 10 cm plates and grown in DMEM supplemented with 10% FBS until confluent. Cell line cloning was performed by seeding wells of 3x96-well plates at a density of ~3 cells/well. Visual inspection was performed

regularly to eliminate wells containing evidence of more than one colony emerging. This approach typically generated ~20 clones per plate. Clones from each of two guides were selected for analysis of genomic DNA sequences.

Primers were designed by visual inspection to allow the PCR amplification of genomic DNA (F: 5'-GTTGCTTCTCCCTTTGCTCTG-3', R: 5'-CTGCTCAATGGGAGACCTAGG-3'). Each primer (forward and reverse) was situated ~200-300 bp outside the targeted region, avoiding homopolymeric or high GC content regions. Primers were first tested on WT genomic DNA to ensure the generation of single bands of the appropriate size. A typical PCR reaction used for analyses used OneTaq (New England Biolabs) polymerase in the supplied buffer, with 40 cycles and using annealing temperatures of at least 55°C, depending on the primers used. PCR products were purified on columns and sent for sequencing using one of the same primers used in the PCR reaction.

Sequence analyses involved the use of simple BLAST to identify indels when both alleles were the same, and differed from wild-type. DNA sequencing data containing high background or the presence of multiple triple peaks were not used. Clones containing indels that resulted in frame-shifting mutations in both alleles were amplified to allow cryopreservation and storage of multiple vials. Cells continued to be maintained in DMEM with 10% FBS and 1% antibiotic/antimycotic (Gibco) at 37°C in 5% CO_2 for all described experiments.

RT-PCR

6cm dishes of cells were lysed in Trizol via cell scraping. This lysate was purified using a Direct-zol RNA Microprep Kit from Zymo Research, including gDNA removal. The concentration of the RNA was measured using a NanoDrop ND-1000. RNA with a 260/280 of ~2.0 was used for further analyses. Up to 2µg of RNA was utilized to synthesize cDNA in the High-Capacity cDNA Reverse Transcription Kit (Applied Biosystems) with RNaseOUT™ Recombinant Ribonuclease Inhibitor (Invitrogen). Prepared cDNA was used for RT-PCR, using a SYBR Green Power UP (Applied Biosystems) master mix, with 0.8 mM Primer concentration (all primers are listed in Table 2). A 10 µL final volume reaction was prepared, with 1 µL of cDNA. This was run using the standard cycling time/temperatures for SYBR Green Power UP with 0.8 mM Primer concentration. Primers for isoforms 1 and 3 are as follows: F: 5'-cgttaggggccttagttctg-3', R: 5'- atgcacgtagatcagcttct- 3'. Primers for isoform 2 are as follows: F: 5'-catgcgcgaagaaggaac-3', R: 5'- tcgtacttgagggtcacactc- 3'. Fold change was calculated via the $2^{-\Delta\Delta Ct}$ method [31]. ΔCt values were utilized for statistics and were compared via t-test or Mann-Whitney test, as described below.

Immunofluorescence

Cells were processed as in [32]. Cells were fixed in 3% paraformaldehyde in PBS for 15 min, and quenched with 10 mM ammonium chloride in PBS for another 10 min. Subsequently, cells were permeabilized in 0.1% Triton X-100 in PBS for 10 min. Coverslips were then washed in PBS, blocked in PBS containing 2.5% goat serum and 0.2% Tween 20 for 5 min, and in PBS, 0.4% fish skin gelatin and 0.2% Tween-20 for another 5 min. Cells stained with antibodies were incubated with primary antibody (GS28- StressGen, 1:300, Paxillin- Invitrogen, 1:300, Integrin α5- Abcam, 1:300) diluted

in 0.4% fish skin gelatin for 1 h at room temperature. Coverslips stained with antibodies were washed in PBS–0.2% Tween 20 and blocked as described above. These steps were skipped for coverslips only stained with phalloidin. Cells were then incubated with secondary antibodies (1:600, Invitrogen) and/or phalloidin (1:1000, Invitrogen) diluted in 2.5% goat serum for 1 hour at room temperature. Nuclei were stained using DAPI (Thermo Scientific) for 3 minutes. Coverslips were washed with PBS–0.2% Tween 20 and mounted on slides in ProLong Gold antifade reagent (Invitrogen) and sealed using nail polish. Cells were visualized with a Nikon A1R-HD25 Confocal microscope or Nikon Eclipse Ti2. Images were processed utilizing the Nikon Acquisition software and FIJI [33]

Golgi morphology

Cells were stained for GS28 and images were acquired as described above. Specifically, z-stack images were taken of 1-2 cells at 90x zoom, with a 0.2 μm z step. Z-stacks were used to generate maximum intensity projections, and these maximum intensity projections were utilized to analyze the Golgi for number of particles and particle size. In order to do this, the Golgi of an individual cell was selected and the image was thresholded. This selection was then analyzed using the "analyze particles" function of FIJI, and the number and size of particles was recorded. A frequency distribution was generated from this data and pooled into three categories- particles from 0-1 μm^2, particles from 1-5 μm^2, and particles greater than 5 μm^2. These values were used for statistical analysis (described below).

Collection of cells 3 hours post plating

Confluent cells in 3cm plates were treated with 500ul of trypsin for 3mins and neutralized with 1ml of media. 10% of this mixture was plated into a 6-well plate with gelatin coated coverslips. After 3h of incubation the cells were fixed with 3% PFA and used for further analyses.

CellProfiler

Cells were plated for 3 hours as described above, and stained with phalloidin (Invitrogen) as previously described. Pictures were taken with Nikon eclipse Ti2 using large picture mode of 3x3mm area with 20% overlap and Optimal path stitching. The pictures were then split into 16 images which were utilized for analysis with CellProfiler. In brief, this pipeline generated masks of all cells in a field of view, and measured the area and aspect ratio of those masks. Pipeline can be provided upon request. From the resulting data, the top 5% of the largest area results were discarded to remove doublet cells from the analysis.

Plasmids

Full length human JAGN1 from was cloned from a JAGN1-Myc-DDK vector (Origene) into vectors containing either an n-terminal myc tagged BirA* or a c-terminal HA-Tagged BirA* (vectors pcDNA3.1 mycBioID and pcDNA3.1 MCS-BirA(R118G)-HA, respectively). The following primers were utilized:

N-myc BirA*-JAGN1:

F:5’-GATCGAATTCATGGCGTCTCGAGCAG-3’

R:5’-GACGGTACCGCTTTATGCTTCTTCTCCT-3’.

JAGN1-BirA*-C-HA:

F: 5’-GATATGCTAGCATGGCGTCTCGAGCAG-3’

R:. 5’-GCGCGCGAATTCTTTATGCTTCTTCTCCTG-3’

These plasmids were subsequently used for transfection.

Streptavidin blot

HEK cells were plated in 10 cm plates, and transfected 3 ug of the appropriate BirA construct, using Lipofectamine 3000 (Thermo Fisher) according to the manufacturer’s protocol. These cells were allowed to transfect overnight, and the next day were treated with biotin at a final concentration of 100 uM in normal media. These cells were incubated again overnight to allow for biotinylation of proteins. These proteins were then harvested in Bio-ID buffer (50 mM Tris, pH 7.4, 500 mM NaCl, 0.4% SDS, 5 mM EDTA, 1 mM DTT, and protease inhibitor) using a cell scraper, as well as sonication for 10 seconds. 1 volume of 50 mM Tris (pH 7.4) was added to the sonicated lysate. This lysate was centrifuged to remove cellular debris and the resulting supernatant was utilized for western blot. The samples were diluted in Lammeli buffer (Bio-Rad) and boiled for 5 minutes. These samples were then loaded on a Novex Tris-Glycine Gel (Invitrogen) with the Precision Plus Duo Color Ladder (Bio-Rad) and ran using a Novex mini gel tank (Thermo Fisher). The gels were then blotted on nitrocellulose membranes and blocked using 5% dry powdered milk. Blocked membranes were stained with Streptavidin HRP (Invitrogen) for one hour at RT. Membranes were washed 3x in TBST before imaging with SuperSignal^{TM} Chemiluminescent substrate (Thermo Fisher) on an Bio-Rad ChemiDoc^{TM} MP Imaging System. Resultant images were processed in FIJI [33]

Proximity Dependent Biotinylation (Bio-ID)

HEK lysates were generated as described above were incubated on washed streptavidin-conjugated agarose beads (Pierce) overnight at 4°C. The unbound fraction

was removed and saved for later analysis. The beads were washed in a series of buffers for 8 minutes per wash to prepare for mass spectroscopy: 2x wash buffer 1 (2% SDS in dH_2O), 2x wash buffer 2 (0.1% deoxycholate, 1% Triton X-100, 500 mM NaCl, 1 mM EDTA, and 50 mM Hepes, pH 7.5), 2x wash buffer 3 (250 mM LiCl, 0.5% NP-40, 0.5% deoxycholate, 1 mM EDTA, and 10 mM Tris, pH 8.1) and 4x wash buffer 4 (PBS, pH 7.4, and 50 mM NaCl). The washed beads were subsequently used for proteomics analysis.

Proteomics Analysis

(Carried out in full detail as previously reported in Ludwig, et. al, under section 2.5 nLC-ESI-MS2 and Protein IDs for GeLC) [34]**:**. IP products were eluted in 30uL of NuPAGE LDS sample buffer (1x final conc., Invitrogen) at 96°C for 10min with gentle shaking, prior to loading onto 10% Bis-Tris Protein gels and separated. The gels were be stained overnight with colloidal coomassie for visualization purposes, the entire gel lane was be cut into 3-8 MW fractions as is determined to be experimentally optimal, and each plug was l be equilibrated in 100 mM ammonium bicarbonate (AmBc), and digested overnight with Trypsin Gold, Mass Spectrometry Grade (Promega, Cat.# V5280) following manufacturer's instruction. Peptide extracts were be reconstituted in 0.1% Formic Acid/ ddH_2O at 0.1µg/µL. Mass spectrometry was carried out, and the data was processed, searched, filtered, grouped, and quantified, as previously reported in detail (Ludwig).

Statistical analyses

All experiments were performed in duplicate or greater. Data were collected and analyzed with Graphpad Prism - Version 10. Mendelian ratio data (Figure 2) was

analyzed using a chi-square analysis of observed vs. expected values. All other data were first analyzed for normality of the data and descriptive statistics. Based on these analyses, the appropriate analyses of non-paired data were chosen; for normal data, unpaired t-tests were utilized, with or without Welch's correction for differences in standard deviation. For data that was not normally distributed, the non-parametric Mann-Whitney test was utilized. Significance was determined as a $p<0.05$ threshold. (* $p\leq0.05$; ** $p\leq0.01$; *** $p\leq0.001$, **** ≤0.0001).

REFERENCES

1. Farnsworth, D.R., L.M. Saunders, and A.C. Miller, *A single-cell transcriptome atlas for zebrafish development.* Dev Biol, 2020. **459**(2): p. 100-108.
2. Lee, S. and L. Cooley, *Jagunal is required for reorganizing the endoplasmic reticulum during Drosophila oogenesis.* The Journal of Cell Biology, 2007. **176**(7): p. 941-952.
3. Cipe, F.E., et al., *A rare case of syndromic severe congenital neutropenia: JAGN1 mutation.* Turk J Pediatr, 2020. **62**(2): p. 326-331.
4. Cifaldi, C., et al., *Next-Generation Sequencing Reveals A JAGN1 Mutation in a Syndromic Child With Intermittent Neutropenia.* J Pediatr Hematol Oncol, 2019. **41**(4): p. e266-e269.
5. Khandagale, A., et al., *JAGN1 is required for fungal killing in neutrophil extracellular traps: Implications for severe congenital neutropenia.* J Leukoc Biol, 2018. **104**(6): p. 1199-1213.
6. Wirnsberger, G., et al., *Jagunal homolog 1 is a critical regulator of neutrophil function in fungal host defense.* Nat Genet, 2014. **46**(9): p. 1028-33.
7. Boztug, K., et al., *JAGN1 deficiency causes aberrant myeloid cell homeostasis and congenital neutropenia.* Nat Genet, 2014. **46**(9): p. 1021-7.
8. Hojabri, M., et al., *JAGN1 mutation with distinct clinical features; two case reports and literature review.* BMC Pediatr, 2023. **23**(1): p. 206.
9. Thomas, S., et al., *Severe congenital neutropenia due to jagunal homolog 1 (JAGN1) mutation: a case report and literature review.* Front Pediatr, 2023. **11**: p. 1223191.
10. Boztug, K., et al., *JAGN1 deficiency causes aberrant myeloid cell homeostasis and congenital neutropenia.* Nature genetics, 2014. **46**(9): p. 1021-1027.
11. Nosak, C., et al., *Jagn1 Is Induced in Response to ER Stress and Regulates Proinsulin Biosynthesis.* PloS one, 2016. **11**(2): p. e0149177-e0149177.
12. Khandagale, A., et al., *Severe congenital neutropenia-associated JAGN1 mutations unleash a calpain-dependent cell death programme in myeloid cells.* Br J Haematol, 2021. **192**(1): p. 200-211.
13. Wirnsberger, G., et al., *Jagunal homolog 1 is a critical regulator of neutrophil function in fungal host defense.* Nature genetics, 2014. **46**(9): p. 1028-1033.
14. Ruhnke, M. and G. Maschmeyer, *Management of mycoses in patients with hematologic disease and cancer -- review of the literature.* Eur J Med Res, 2002. **7**(5): p. 227-35.
15. Garcia-Vidal, C., D. Viasus, and J. Carratala, *Pathogenesis of invasive fungal infections.* Curr Opin Infect Dis, 2013. **26**(3): p. 270-6.
16. Hagelkruys, A., et al., *A crucial role for Jagunal homolog 1 in humoral immunity and antibody glycosylation in mice and humans.* J Exp Med, 2021. **218**(1).

17. VanWinkle, P.E., et al., *JAGN1, tetraspanins and Erv proteins: is common topology indicative of common function in cargo sorting?* American Journal of Physiology-Cell Physiology, 2020.

18. Thyme, S.B., et al., *Phenotypic Landscape of Schizophrenia-Associated Genes Defines Candidates and Their Shared Functions.* Cell, 2019. **177**(2): p. 478-491.e20.

19. Stirling, D.R., et al., *CellProfiler 4: improvements in speed, utility and usability.* BMC Bioinformatics, 2021. **22**(1): p. 433.

20. Berditchevski, F. and E. Odintsova, *Tetraspanins as regulators of protein trafficking.* Traffic (Copenhagen, Denmark), 2007. **8**(2): p. 89-96.

21. Lynch, C.D., et al., *Filamin depletion blocks endoplasmic spreading and destabilizes force-bearing adhesions.* Molecular Biology of the Cell, 2011. **22**(8): p. 1263-1273.

22. Werner, A.C., et al., *Coronin 1B Controls Endothelial Actin Dynamics at Cell-Cell Junctions and Is Required for Endothelial Network Assembly.* Front Cell Dev Biol, 2020. **8**: p. 708.

23. Szul, T. and E. Sztul, *COPII and COPI traffic at the ER-Golgi interface.* Physiology (Bethesda), 2011. **26**(5): p. 348-364.

24. Sala-Valdés, M., et al., *EWI-2 and EWI-F Link the Tetraspanin Web to the Actin Cytoskeleton through Their Direct Association with Ezrin-Radixin-Moesin Proteins *.* Journal of Biological Chemistry, 2006. **281**(28): p. 19665-19675.

25. Toribio, V. and M. Yáñez-Mó, *Tetraspanins interweave EV secretion, endosomal network dynamics and cellular metabolism.* European Journal of Cell Biology, 2022. **101**(3): p. 151229.

26. Källquist, L., et al., *The tetraspanin CD63 is involved in granule targeting of neutrophil elastase.* Blood, 2008. **112**(8): p. 3444-3454.

27. Westerfield, M., *The Zebrafish Book: A Guide for the Laboratory Use of Zebrafish (Danio Rerio)*. 2007: University of Oregon Press.

28. Randlett, O., et al., *Whole-brain activity mapping onto a zebrafish brain atlas.* Nat Methods, 2015. **12**(11): p. 1039-46.

29. Jefferis, G.S., et al., *Comprehensive maps of Drosophila higher olfactory centers: spatially segregated fruit and pheromone representation.* Cell, 2007. **128**(6): p. 1187-203.

30. Rohlfing, T. and C.R. Maurer, Jr., *Nonrigid image registration in shared-memory multiprocessor environments with application to brains, breasts, and bees.* IEEE Trans Inf Technol Biomed, 2003. **7**(1): p. 16-25.

31. Livak, K.J. and T.D. Schmittgen, *Analysis of Relative Gene Expression Data Using Real-Time Quantitative PCR and the 2−ΔΔCT Method.* Methods, 2001. **25**(4): p. 402-408.

32. Bhatt, J.M., et al., *Promiscuity of the catalytic Sec7 domain within the guanine nucleotide exchange factor GBF1 in ARF activation, Golgi homeostasis, and effector recruitment.* Mol Biol Cell, 2019. **30**(12): p. 1523-1535.

33. Schindelin, J., et al., *Fiji: an open-source platform for biological-image analysis.* Nature Methods, 2012. **9**(7): p. 676-682.

34. Ludwig, M.R., et al., *Surveying the serologic proteome in a tissue-specific kras(G12D) knockin mouse model of pancreatic cancer.* Proteomics, 2016. **16**(3): p. 516-31.

Identified Proteins	RepID	NT Control	Jagn1-BirA*	BirA*-Jagn1
Lamina-associated polypeptide 2, isoforms beta/gamma	LAP2B_HUMAN	0	224	153
Protein jagunal homolog 1	JAGN1_HUMAN	0	194	233
Lamin-B receptor	LBR_HUMAN	0	50	58
Torsin-1A-interacting protein 1	TOIP1_HUMAN	0	34	31
Protein ERGIC-53	LMAN1_HUMAN	0	32	15
Extended synaptotagmin-1	ESYT1_HUMAN	0	32	32
Fatty acid synthase	FAS_HUMAN	0	30	41
4F2 cell-surface antigen heavy chain	4F2_HUMAN	0	29	9
Filamin-A	FLNA_HUMAN	0	28	53
Membrane-associated progesterone receptor component 2	PGRC2_HUMAN	0	20	14
Zinc finger CCCH-type antiviral protein 1	ZCCHV_HUMAN	0	20	21
Emerin	EMD_HUMAN	0	18	18
UBX domain-containing protein 4	UBXN4_HUMAN	0	17	16
Coiled-coil domain-containing protein 47	CCD47_HUMAN	0	17	28
T-complex protein 1 subunit theta	TCPQ_HUMAN	0	15	67
Tyrosine-protein phosphatase non-receptor type 1	PTN1_HUMAN	0	14	10
RuvB-like 1	RUVB1_HUMAN	0	13	9
Cytoskeleton-associated protein 4	CKAP4_HUMAN	0	11	4
Fatty aldehyde dehydrogenase	AL3A2_HUMAN	0	10	14
Golgi reassembly-stacking protein 2	GORS2_HUMAN	0	10	14
Long-chain-fatty-acid--CoA ligase 3	ACSL3_HUMAN	0	9	2
Dolichyl-diphosphooligosaccharide--protein glycosyltransferase subunit STT3B	STT3B_HUMAN	0	9	2
Torsin-1A-interacting protein 2	TOIP2_HUMAN	0	9	2
Inner nuclear membrane protein Man1	MAN1_HUMAN	0	9	9
Protein LYRIC	LYRIC_HUMAN	0	9	10
Synaptobrevin homolog YKT6	YKT6_HUMAN	0	8	0
Vesicle-associated membrane protein-associated protein B/C	VAPB_HUMAN	0	8	1
Chloride channel CLIC-like protein 1	CLCC1_HUMAN	0	8	16
Tubulin alpha-1C chain	TBA1C_HUMAN	0	8	17

Neurogenic locus notch homolog protein 2	NOTC2_HUMAN	0	7	2
p180/ribosome receptor	A7BI36_HUMAN	0	7	3
Double-strand break repair protein MRE11A	MRE11_HUMAN	0	7	8
Synapse-associated protein 1	SYAP1_HUMAN	0	7	9
Heat shock protein HSP 90-beta	HS90B_HUMAN	0	7	10
PERQ amino acid-rich with GYF domain-containing protein 2	PERQ2_HUMAN	0	6	2
Renin receptor	RENR_HUMAN	0	6	2
Solute carrier family 12 member 2	S12A2_HUMAN	0	6	3
Signal recognition particle receptor subunit alpha	SRPR_HUMAN	0	6	4
Eukaryotic translation initiation factor 5	IF5_HUMAN	0	6	9
Manganese-transporting ATPase 13A1	AT131_HUMAN	0	5	0
NADPH--cytochrome P450 reductase	NCPR_HUMAN	0	5	1
Sphingomyelin phosphodiesterase 4	NSMA3_HUMAN	0	5	1
Thioredoxin-related transmembrane protein 1	TMX1_HUMAN	0	5	1
Neutral amino acid transporter B(0)	AAAT_HUMAN	0	5	2
ATP-binding cassette sub-family D member 3	ABCD3_HUMAN	0	5	2
Synaptosomal-associated protein 29	SNP29_HUMAN	0	5	2
ATP-dependent RNA helicase DDX3X	DDX3X_HUMAN	0	5	3
Protein lunapark	LNP_HUMAN	0	5	3
Serine/threonine-protein kinase VRK2	VRK2_HUMAN	0	5	4
Importin subunit beta-1	IMB1_HUMAN	0	4	0
Ras-related protein Rab-7a	RAB7A_HUMAN	0	4	0
Vesicle-trafficking protein SEC22b	SC22B_HUMAN	0	4	0
Peptidyl-prolyl cis-trans isomerase FKBP8	FKBP8_HUMAN	0	4	1
Transgelin-2	TAGL2_HUMAN	0	4	1
Ubiquitin-associated protein 2-like	UBP2L_HUMAN	0	4	1
DnaJ homolog subfamily C member 1	DNJC1_HUMAN	0	4	2
Kinectin	KTN1_HUMAN	0	4	3
Insulin receptor substrate 4	IRS4_HUMAN	0	4	8
Reticulon-4	RTN4_HUMAN	0	4	13
Dehydrogenase/reductase SDR family member 7	DHRS7_HUMAN	0	3	0

Integrin beta-1	ITB1_HUMAN	0	3	0
Ran GTPase-activating protein 1	RAGP1_HUMAN	0	3	1
Transmembrane protein 209	TM209_HUMAN	0	3	1
Coronin-1B	COR1B_HUMAN	0	3	11
Golgi resident protein GCP60	GCP60_HUMAN	0	3	14
Coatomer subunit gamma-2	COPG2_HUMAN	0	3	16
Centrosomal protein of 170 kDa	CE170_HUMAN	0	2	0
Leucine-rich repeat-containing protein 59	LRC59_HUMAN	0	2	0
E3 ubiquitin-protein ligase RNF213	RN213_HUMAN	0	2	0
Fibronectin type-III domain-containing protein 3A	FND3A_HUMAN	0	2	1
Signal recognition particle subunit SRP68	SRP68_HUMAN	0	2	1
Ancient ubiquitous protein 1	AUP1_HUMAN	0	2	2
PCM1 protein	B9EIS5_HUMAN	0	2	2
Threonylcarbamoyladenosine tRNA methylthiotransferase	CDKAL_HUMAN	0	2	2
STIM1L	G0XQ39_HUMAN	0	2	2
WW domain-containing oxidoreductase	WWOX_HUMAN	0	2	3
Plasminogen activator inhibitor 1 RNA-binding protein	PAIRB_HUMAN	0	2	4
Protein transport protein Sec16A	SC16A_HUMAN	0	2	9
Elongation factor 2	EF2_HUMAN	0	1	2
POTE ankyrin domain family member E	POTEE_HUMAN	0	1	2
BRD1 protein	Q86X06_HUMAN	0	1	2
FAS-associated factor 2	FAF2_HUMAN	0	1	3
Microtubule-associated protein 4	MAP4_HUMAN	0	1	3
Nuclear pore complex protein Nup155	NU155_HUMAN	0	1	3
Eukaryotic initiation factor 4A-I	IF4A1_HUMAN	0	1	4
Heterogeneous nuclear ribonucleoprotein K	HNRPK_HUMAN	0	1	8

Table S1: Proteins labelled by proximity-dependent biotinylation using a BirA*-tagged JAGN1 in HEK cells. Proteins are listed in descending order of mass spectroscopy hits.

CONCLUSIONS, SUMMARY, AND FUTURE DIRECTIONS

Transcriptional regulation of bone development and regeneration

This body of work demonstrates the systemic effects of perturbing CREB3L1-mediated transcriptional regulation on bone development and regeneration. This transcription factor has been best characterized as a regulator of bone health, with documented roles in regulating collagen transcription and in facilitating the expression of secretory pathway components required for its subsequent deposition via the secretory pathway [1-3]. CREB3L1 also has a role in secretion in other tissues, such as the thyroid, where it regulates both, the expression of thyrocyte-specific Sodium-Iodide Symporter (NIS) and of the secretory machinery needed to traffic thyroglobulin in stimulated thyrocytes [4,5]. Both of these roles demonstrate the bipartite function of CREB3L1 in regulating the transcription of tissue specific genes (*Col1a1* and *Slc5a5* in bones and thyrocytes, respectively [2,4]) and of the more ubiquitous cellular machinery required for functional secretory pathway (*SEC24D* and *Golga2* [5,6]).

CREB3L1

The first focus of this dissertation is CREB3L1 (Chapter 1). We utilized the zebrafish model system to probe the organismal effects of CREB3L1 dysfunction. Although the zebrafish model does not recapitulate the adult skeletal defects present in patients with *CREB3L1* mutations, our results are consistent with the normal skeletal development observed in CREB3L1 KO mice. This suggests that the severe bone abnormalities seen in human patients might be due to additional undetected genetic lesions, as only CREB3L1

genes have been sequenced in many patients. Moreover, there are other possible reasons for the difference in phenotypes. Primarily, zebrafish exhibit different bone physiology than humans, with a higher percentage of intramembranous bone as opposed to the largely endochondral human skeleton. Also, there may be some compensation from the fellow Creb3l1 family member, Creb3l2. While CREB3L2 largely plays a role in chondrogenesis in mammalian systems, it is expressed in overlapping cell clusters with *creb3l1* when analyzed by single-cell sequencing of zebrafish embryos [(7)].

Because of the lack of skeletal defects in CREB3L1 mutant zebrafish, we chose to probe another process regulated by CREB3L1 in mammals; bone regeneration. Indeed, in our model of CREB3L1 dysfunction in zebrafish, we demonstrated that *creb3l1*$^{\Delta bZIP/\Delta bZIP}$ animals exhibit changes in *col1a1a* transcription during regeneration of the caudal fin, mirroring defects in collagen transcription seen in murine fracture healing [(3)]. The effect of CREB3L1 KO in murine fracture healing is further recapitulated in our zebrafish model by both, a decrease in the regenerate length during early regeneration, and a decrease in $Sp7^{+}$ (osteoblastic) area throughout regeneration.

Our findings are important in that they recapitulate the effects of dysfunctional CREB3L1 observed in mammalian fracture healing [(3)]. However, the benefit of the zebrafish model is that it is a facile system through which to visualize the entirety of the regenerative processes within an in vivo environment. In this system, we analyzed an entire regenerating tail from a single animal, at successive time points, by tracking fluorescently labeled osteoblasts (other cells can also be tracked in compound transgenic animals). Additionally, approaches such as in situ hybridization and immunofluorescent staining were used to reveal two distinct attributes of the *creb3l1*$^{\Delta bZIP/\Delta bZIP}$ regenerate

environment; a phenomenon of cell-cycle perturbation and the misregulation of the Sonic Hedgehog pathway.

A disruption of the cell cycle was detected when we analyzed the number of proliferative ($PH3^{+}$) and apoptotic (Cleaved Caspase 3^{+}) cells in a *creb3l1*$^{\Delta bZIP\Delta dbZIP}$ regenerate, followed by probing the mitotic state of the proliferating cells. Surprisingly, this analysis revealed that the *creb3l1* mutant regenerates have fewer cells in mitosis and anaphase, indicating that there is a change to the cell cycle. The mechanisms of this arrest remain to be explored, but may be a result of endoplasmic reticulum stress. CREB3L1 and endoplasmic reticulum stress have been previously associated with perturbations in the cell cycle, which has implications for future study of CREB3L1 function in regeneration.

One of the key novel findings of this work is the demonstration that the regenerating tails of *creb3l1* mutant fish showed defects in bone patterning, with more shallow bifurcations and fewer secondary bifurcations of the bony lepidotrichia. This phenotype prompted the analysis of the Sonic Hedgehog pathway, shown to be essential for appropriate bifurcation of the regenerating tail. Our studies revealed a mislocalization of Sonic Hedgehog during regeneration. Further, the Shh effector Ptch2 also was mislocalized, indicating a defect in Sonic Hedgehog pathway transduction. These findings showcase, for the first time, an intersection of Creb3l1 with the Sonic Hedgehog signaling pathway, as CREB3L1 has never before been reported to regulate patterning.

The molecular mechanism(s) through which Creb3l1 impacts Sonic Hedgehog signaling within the regenerating tail remains to be determined, but may occur through an indirect pathway. Specifically, the patterning defect may be indicative of a Creb3l1-Hedgehog axis that is influenced by Creb3l1 function in the thyroid. In mammalian thyrocytes,

Creb3l1 regulates the transcription of NIS, a transporter required for the production of thyroid hormone [4]. Misregulation of thyroid hormone levels in zebrafish has been shown to alter Sonic Hedgehog signaling and bone patterning during regeneration. Thus, the defect observed in our CREB3L1 mutant fish may result from remote effects of *creb3l1* mutation in the thyroid combined with a more direct effect in the tail, demonstrated by the changes in *col1a1a* expression.

The strength of the phenotypes observed in our *creb3l1*$^{\Delta bZIP\Delta dbZIP}$ fish was further confirmed through the characterization of a second Creb3l1 functionally null allele, described in Chapter 2. This allele, *creb3l1*$^{TA+/TA+}$, was originally intended to represent a constitutively transcriptionally active "TA" form of Creb3l1. However, the CRISPR-Cas9 strategy utilized to generate this model resulted in a frameshift mutation that added ~50 erroneous amino acids to the C-terminus of the TA portion of the Creb3l1 protein. As demonstrated in Chapter 2, this led to the "TA" protein aggregating in the cytosol, which likely inhibits its nuclear import and subsequent transcription factor activity. Importantly, the *creb3l1*$^{TA+/TA+}$ fish also had defects in regeneration, *shha* localization, and bony ray patterning, thereby recapitulating through an alternative allele that Creb3l1 is essential for normal caudal fin regeneration and pattern formation.

Towards Understanding JAGN1 Function – Possible Function In Cargo Transport Within The Secretory Pathway And/Or Cell Adhesion

A group of cargo-sorting molecules is characterized by a tetrspanning topology [8], and shared functionality of binding cargo proteins to "escort" them between compartments. Because JAGN1 has a tetraspanning topology and contains binding sequences for COPI and COPII (components of the trafficking machinery that transports proteins between the ER and the Golgi), we proposed that JAGN1 may be a cargo sorter [8]. In this thesis, we

explored the organismal function of JAGN1 by generating and characterizing two zebrafish models of jagn1 dysfunction. Moreover, using CRISPR/Cas9-modified cells, we explored the cellular consequences of inactivating JAGN1.

JAGN1

A part of this thesis was focused on the as-yet functionally un-characterized protein JAGN1. JAGN1 is highly conserved from the single-cellular amoeba to *H.* sapiens [8] and is also found in plants. However, the primary cell type affected by JAGN1 mutations in humans is the highly specialized neutrophil. JAGN1 mutations have been associated with Severe Congenital Neutropenia 6, which has provided context for most JAGN1 research. Primarily, *JAGN1* mutations have been associated with endoplasmic reticulum stress and poorer neutrophil cytotoxicity, as well as defects in glycosylation [9-12]. However, mice deleted of *Jagn1* die early in embryonic development [9] prior to development of the innate immune system, potentially due to the total knockout of the gene, implying a more essential role for JAGN1 than just neutrophil function. Moreover, *JAGN1* is ubiquitously expressed in numerous tissues, and it is important to search for a more ubiquitous molecular role of JAGN1. This led us to use both, the zebrafish and mouse embryonic fibroblast (MEF) models to probe a more general role of JAGN1 that may apply widely in all cells and also have especially dramatic effects in specialized tissues.

We generated a zebrafish model to determine if *jagn1* dysfunction was as severely deleterious in fish as the embryonic lethality seen in JAGN1 KO mice. Zebrafish have two Jagn1 genes with *jagn1a* expressed almost exclusively in brain tissues in embryonic fish brain and *jagn1b* expressed ubiquitously, with *jagn1b* expression more closely mirroring human expression[13]. Our zebrafish mutants were deleted of only one homolog

of *jagn1* thereby allowing for the exploration of Jagn1function in distinct tissues. Knocking out *jagn1a* is not lethal, but does lead to a slight decrease in brain activity. This is of relevance to studying JAGN1 patient syndromes, as patients with *JAGN1* mutations have been reported to have neurological dysfunction [12,14,15]. The normal life span of *jagn1a*$^{-/-}$ fish is in stark contrast to the phenotype observed in *jagn1b* fish, which all die between 10 and 14 days post fertilization. This lethality recapitulates the essential nature of murine Jagn1, since JAGN1 KO mice die at embryonic E 8.5. Thus, both the *jagn1a*$^{-/-}$ and *jagn1b*$^{-/-}$ fish recapitulate patient phenotypes and previous work on JAGN1 in animal models, making them a unique and valuable system in which to explore tissue-specific functions of JAGN1.

To gain insight into the cellular mechanisms of JAGN1 function, we generated CRISPR/Cas9-modified mouse embryonic fibroblasts (MEFs) expressing truncated forms of Jagn1. These cells allowed us to uncover an uncharacterized function for JAGN1 in cell spreading, as our mutant cell lines took longer to spread and adhere to the substrate. By analyzing the morphology of the cells (via actin cytoskeleton staining) at different times after plating, we obtained quantitative data that the JAGN1 mutant cells had a smaller overall area and were more compact. Cell spreading is dependent on the establishment of contact sites between cells and the substrate, and we analyzed the deposition of focal adhesion protein paxillin and integrin α5 at different times after plating. Our results show a significant delay in the formation of focal adhesions, demonstrating a role for JAGN1 in establishing cell-surface contacts.

To provide insight into the molecular underpinnings of this phenotype, we utilized a Bio-ID approach, in which promiscuous biotin ligase fused to either the N- or the C-terminus

of JAGN1 was expressed in MEFs and allowed to biotinylate its neighboring proteins. The identified biotinylated proteins (those within proximity or possibly interacting with JAGN1) included proteins known to mediate ER to Golgi trafficking, supporting a possible role of JAGN1 as a cargo "escort" protein. This function could explain the phenotype of JAGN1 mutant cells if JAGN1 was needed to "escort" integrins or other cell adhesion proteins between the ER and the Golgi. However, we also identified a number of tubulin- and actin-binding proteins and proteins involved in regulating actin dynamics, raising the possibility that JAGN1 may directly regulate cytoskeletal architecture. Such a role also would explain the observed defects in cell spreading and adhesion to substrate.

Together, our work in fish and in MEF cell culture provides novel data supporting a potential role of JAGN1 in vesicular transport, while also suggesting a novel function in regulating cellular adhesion. While the exact mechanism of Jagn1 action remains to be elucidated, our findings suggest a ubiquitous role in all cells, thus explaining both, JAGN1 heavy evolutionary conservation as well as its universal expression.

FUTURE DIRECTIONS

CREB3L1

Based on the findings presented here, there are several promising avenues to further elucidate the role of CREB3L1 in bone regeneration. Of high interest is CREB3L1 impact on Sonic Hedgehog signaling, as recent work established that Shh is essential for bone regeneration specifically after large injury [16]. The modulation of large injury regeneration is a point of much research in the field of bone research, and the potential functionality of CREB3L1 in this pathway should be explored in mammalian models. Specifically, it would be important to determine if *Creb3l1* expression is upregulated in a

mammalian model of large-scale bone injury, and whether the CREB3L1-SHH axis is also perturbed in a mammalian model with increased similarity to human skeleton structure. These experiments would shed light on the mechanistic role of Creb3l1 in modulating Shh signaling, and broaden the limited understanding of molecules that regulate Shh activity. As such, this novel role for Creb3l1 deserves further investigation to determine its exact mechanism of action.

To probe the Creb3l1-Shh axis in zebrafish, we propose a number of experiments. The first would be to determine if the aberrant tail ray bifurcation of the *creb3l1* mutant is linked to decreased levels of thyroid hormone. We would assay total thyroid hormone levels in the *creb3l1*$^{+/+}$ fish and *creb3l1*$^{dbZIP/dbZIP}$ fish during regeneration and probe NIS transcript levels within the thyroid. Conversely, to assay the more direct effects in the tail due to *col1a1a* misexpression, we would like to generate a zebrafish lacking the Creb3l1 binding motif in the *col1a1a* promoter and determine if this generates a similar phenotype during regeneration.

It would also be interesting to analyze the effect of *creb3l1* mutation on endochondral bone such as the craniofacial bones of the zebrafish. This would be especially relevant to the mammalian skeletal system, which is largely comprised of endochondral bone.

Finally, while the duplication of the null phenotypes in the *creb3l1*$^{dbZIP/dbZIP}$ and the *creb3l1*$^{TA+/TA}$ fish is important because it reinforces our data, it would be extremely interesting to generate zebrafish expressing the constitutively transcriptionally active TA CREB3L1 fragment. It would be extremely pertinent to utilize both, the already available *creb3l1*$^{dbZIP/dbZIP}$ model and the “TA” model for comparative RNA-Seq studies to gain understanding of the cellular pathways affected by *creb3l1* mutation.

JAGN1

While the novel role for JAGN1 in cell spreading discussed in this thesis is a useful discovery, it remains to be determined what molecular interactors are responsible for JAGN1 modulation of adhesion. Further, it remains to be elucidated what molecular changes are responsible for the phenotypes seen in neutropenia patients with point mutations in JAGN1 [12]. This is of special interest as these patients must have at least partial JAGN1 activity since they develop beyond embryogenesis, while JAGN1 knockout mice die at an early embryonic stage [9]. This introduces an important question: which parts of JAGN1 are essential and which are dispensable? Further inquiry could probe structure-function relationships within JAGN1, and the roles of distinct domains (as well as patient mutations) could be probed after transfecting mutant JAGN1 into the JAGN1 knockout MEFs and assessing their phenotypes. The transfected cells would be used to evaluate the rescue of cell spreading activity, and thereby identify the portions of JAGN1 most likely to interact with the cell-spreading machinery. Moreover, it would be important to identify JAGN1 interactors. Once these interactors have been established, the functional significance of those interactors could be assessed in our JAGN1 knockout cells.

CONCLUSIONS

The work presented in this thesis provides new understanding of transcriptional regulation of bone formation and bone regeneration after injury. Using two newly-developed zebrafish models, we determined that functional disruption of the CREB3L1 transcriptional factor impairs bone regeneration in zebrafish. Importantly, our work uncovered a previously unknown role of CREB3L1 in the appropriate bone patterning

during regeneration and revealed that CREB3L1 intersects with the Sonic Hedgehog signaling pathway. Our findings are extremely relevant to regeneration of large-scale tissue injury in mammals [16], which recently has been shown to involve Sonic Hedgehog signaling. Thus, our results and our zebrafish models provide novel information and tools to probe this important field of study.

This thesis also describes the results of an inquiry into the organismal and cellular functions of JAGN1, which up to now, has been studied almost exclusively within the context of human neutropenia. Our zebrafish models of JAGN1 dysfunction provided novel information on the importance of JAGN1 in brain function, and established a novel system in which to probe tissue-specific functions of JAGN1. This is possible because zebrafish have two JAGN1 genes, and our models are especially relevant because a mammalian model of JAGN1 dysfunction dies at an early embryonic stage that precludes such analyses. Moreover, our generation and characterization of MEFs expressing different dysfunctional alleles of JAGN1 showed it as a key regulator of cell spreading. This defect was reflected in the perturbed establishment of focal adhesions. These findings suggest a role for JAGN1 in a cell-spreading activity that is not restricted to migrating neutrophils, and potentially explains why the molecule is so ubiquitously expressed and highly conserved. Importantly, our cellular models provide a unique and optimal system in which to probe the molecular mechanisms of JAGN1 action.

REFERENCES

1. Nikaido T, Yokoya S, Mori T, Hagino S, Iseki K, Zhang Y, et al. Expression of the novel transcription factor OASIS, which belongs to the CREB/ATF family, in mouse embryo with special reference to bone development. Histochemistry and Cell Biology. 2001/08/01 2001;116(2):141-8.
2. Murakami T, Saito A, Hino S, Kondo S, Kanemoto S, Chihara K, et al. Signalling mediated by the endoplasmic reticulum stress transducer OASIS is involved in bone formation. Nat Cell Biol. Oct 2009;11(10):1205-11. Epub 2009/09/22.
3. Funamoto T, Sekimoto T, Murakami T, Kurogi S, Imaizumi K, Chosa E. Roles of the endoplasmic reticulum stress transducer OASIS in fracture healing. Bone. Oct 2011;49(4):724-32. Epub 2011/06/29.
4. Di Giusto P, Martín M, Funes Chabán M, Sampieri L, Nicola JP, Alvarez C. Transcription Factor CREB3L1 Regulates the Expression of the Sodium/Iodide Symporter (NIS) in Rat Thyroid Follicular Cells. Cells. Apr 13 2022;11(8). Epub 2022/04/24.
5. García IA, Torres Demichelis V, Viale DL, Di Giusto P, Ezhova Y, Polishchuk RS, et al. CREB3L1-mediated functional and structural adaptation of the secretory pathway in hormone-stimulated thyroid cells. J Cell Sci. Dec 15 2017;130(24):4155-67. Epub 2017/11/03.
6. Keller RB, Tran TT, Pyott SM, Pepin MG, Savarirayan R, McGillivray G, et al. Monoallelic and biallelic CREB3L1 variant causes mild and severe osteogenesis imperfecta, respectively. Genet Med. Apr 2018;20(4):411-9. Epub 2017/08/18.
7. Farnsworth DR, Saunders LM, Miller AC. A single-cell transcriptome atlas for zebrafish development. Developmental Biology. 2020/03/15/ 2020;459(2):100-8.
8. VanWinkle PE, Parish F, Edwards YJK, Sztul E. JAGN1, tetraspanins and Erv proteins: is common topology indicative of common function in cargo sorting? American Journal of Physiology-Cell Physiology. 2020.
9. Wirnsberger G, Zwolanek F, Stadlmann J, Tortola L, Liu SW, Perlot T, et al. Jagunal homolog 1 is a critical regulator of neutrophil function in fungal host defense. Nat Genet. 2014;46(9):1028-33. Epub 08/17.
10. Khandagale A, Lazzaretto B, Carlsson G, Sundin M, Shafeeq S, Römling U, et al. JAGN1 is required for fungal killing in neutrophil extracellular traps: Implications for severe congenital neutropenia. J Leukoc Biol. 2018;104(6):1199-213. Epub 08/14.
11. Hagelkruys A, Wirnsberger G, Stadlmann J, Wöhner M, Horrer M, Vilagos B, et al. A crucial role for Jagunal homolog 1 in humoral immunity and antibody glycosylation in mice and humans. J Exp Med. Jan 4 2021;218(1).
12. Boztug K, Järvinen PM, Salzer E, Racek T, Mönch S, Garncarz W, et al. JAGN1 deficiency causes aberrant myeloid cell homeostasis and congenital neutropenia. Nat Genet. 2014;46(9):1021-7. Epub 08/17.

13. Farnsworth DR, Saunders LM, Miller AC. A single-cell transcriptome atlas for zebrafish development. Dev Biol. Mar 15 2020;459(2):100-8. Epub 2019/11/30.

14. Cifaldi C, Serafinelli J, Petricone D, Brigida I, Di Cesare S, Di Matteo G, et al. Next-Generation Sequencing Reveals A JAGN1 Mutation in a Syndromic Child With Intermittent Neutropenia. J Pediatr Hematol Oncol. 2019;41(4):e266-e9.

15. Hojabri M, Farsi Y, Jamee M, Abolhassani H, Khani HHK, Karimi A, et al. JAGN1 mutation with distinct clinical features; two case reports and literature review. BMC Pediatr. Apr 29 2023;23(1):206. Epub 20230429.

16. Serowoky MA, Kuwahara ST, Liu S, Vakhshori V, Lieberman JR, Mariani FV. A murine model of large-scale bone regeneration reveals a selective requirement for Sonic Hedgehog. npj Regenerative Medicine. 2022/05/17 2022;7(1):30.

GENERAL REFERENCES

1. Murakami, T., et al., *Signalling mediated by the endoplasmic reticulum stress transducer OASIS is involved in bone formation.* Nat Cell Biol, 2009. **11**(10): p. 1205-11.
2. Funamoto, T., et al., *Roles of the endoplasmic reticulum stress transducer OASIS in fracture healing.* Bone, 2011. **49**(4): p. 724-32.
3. Symoens, S., et al., *Deficiency for the ER-stress transducer OASIS causes severe recessive osteogenesis imperfecta in humans.* Orphanet J Rare Dis, 2013. **8**: p. 154.
4. Lindahl, K., et al., *Homozygosity for CREB3L1 premature stop codon in first case of recessive osteogenesis imperfecta associated with OASIS-deficiency to survive infancy.* Bone, 2018. **114**: p. 268-277.
5. Boztug, K., et al., *JAGN1 deficiency causes aberrant myeloid cell homeostasis and congenital neutropenia.* Nature genetics, 2014. **46**(9): p. 1021-1027.
6. Wirnsberger, G., et al., *Jagunal homolog 1 is a critical regulator of neutrophil function in fungal host defense.* Nature genetics, 2014. **46**(9): p. 1028-1033.
7. Sehring, I.M. and G. Weidinger, *Recent advancements in understanding fin regeneration in zebrafish.* WIREs Developmental Biology, 2020. **9**(1): p. e367.
8. Harper, M., et al., *Thyroid hormone regulates proximodistal patterning in fin rays.* Proceedings of the National Academy of Sciences, 2023. **120**(21): p. e2219770120.
9. García, I.A., et al., *CREB3L1-mediated functional and structural adaptation of the secretory pathway in hormone-stimulated thyroid cells.* Journal of cell science, 2017. **130**(24): p. 4155-4167.
10. Kondo, S., et al., *OASIS, a CREB/ATF-family member, modulates UPR signalling in astrocytes.* Nat Cell Biol, 2005. **7**(2): p. 186-94.
11. Armstrong, B.E., et al., *Shh promotes direct interactions between epidermal cells and osteoblast progenitors to shape regenerated zebrafish bone.* Development, 2017. **144**(7): p. 1165-1176.
12. Omori, Y., et al., *OASIS is a transcriptional activator of CREB/ATF family with a transmembrane domain.* Biochem Biophys Res Commun, 2002. **293**(1): p. 470-7.
13. Laforest, L., et al., *Involvement of the sonic hedgehog, patched 1 and bmp2 genes in patterning of the zebrafish dermal fin rays.* Development, 1998. **125**(21): p. 4175-84.

14. Fox, R.M. and D.J. Andrew, *Transcriptional regulation of secretory capacity by bZip transcription factors.* Front Biol (Beijing), 2015. **10**(1): p. 28-51.

15. Keller, R.B., et al., *Monoallelic and biallelic CREB3L1 variant causes mild and severe osteogenesis imperfecta, respectively.* Genetics in medicine : official journal of the American College of Medical Genetics, 2018. **20**(4): p. 411-419.

16. Braunstein, J.A., et al., *Basal epidermis collective migration and local Sonic hedgehog signaling promote skeletal branching morphogenesis in zebrafish fins.* Developmental Biology, 2021. **477**: p. 177-190.

17. Nachtrab, G., et al., *Transcriptional components of anteroposterior positional information during zebrafish fin regeneration.* Development, 2013. **140**(18): p. 3754-64.

18. Rabinowitz, J.S., et al., *Transcriptomic, proteomic, and metabolomic landscape of positional memory in the caudal fin of zebrafish.* Proc Natl Acad Sci U S A, 2017. **114**(5): p. E717-e726.

19. Barlowe, C.K. and E.A. Miller, *Secretory protein biogenesis and traffic in the early secretory pathway.* Genetics, 2013. **193**(2): p. 383-410.

20. Dancourt, J. and C. Barlowe, *Protein sorting receptors in the early secretory pathway.* Annual review of biochemistry, 2010. **79**: p. 777-802.

21. Guillemyn, B., et al., *A homozygous pathogenic missense variant broadens the phenotypic and mutational spectrum of CREB3L1-related osteogenesis imperfecta.* Hum Mol Genet, 2019. **28**(11): p. 1801-1809.

22. Schindelin, J., et al., *Fiji: an open-source platform for biological-image analysis.* Nature Methods, 2012. **9**(7): p. 676-682.

23. Nikaido, T., et al., *Expression of the novel transcription factor OASIS, which belongs to the CREB/ATF family, in mouse embryo with special reference to bone development.* Histochem Cell Biol, 2001. **116**(2): p. 141-8.

24. Knopf, F., et al., *Bone Regenerates via Dedifferentiation of Osteoblasts in the Zebrafish Fin.* Developmental Cell, 2011. **20**(5): p. 713-724.

25. Blum, N. and G. Begemann, *Retinoic acid signaling spatially restricts osteoblasts and controls ray-interray organization during zebrafish fin regeneration.* Development, 2015. **142**(17): p. 2888-2893.

26. Zhang, J., et al., *Laser ablation of the sonic hedgehog-a-expressing cells during fin regeneration affects ray branching morphogenesis.* Developmental Biology, 2012. **365**(2): p. 424-433.

27. Murakami, T., et al., *Cleavage of the membrane-bound transcription factor OASIS in response to endoplasmic reticulum stress.* Journal of Neurochemistry, 2006. **96**(4): p. 1090-1100.

28. Serowoky, M.A., et al., *A murine model of large-scale bone regeneration reveals a selective requirement for Sonic Hedgehog.* npj Regenerative Medicine, 2022. **7**(1): p. 30.

29. Hojabri, M., et al., *JAGN1 mutation with distinct clinical features; two case reports and literature review.* BMC Pediatr, 2023. **23**(1): p. 206.

30. Donaldson, J.G., *Endocytosis*, in *Encyclopedia of Biological Chemistry (Second Edition)*, W.J. Lennarz and M.D. Lane, Editors. 2013, Academic Press: Waltham. p. 197-199.

31. Feizi, A., et al., *Human protein secretory pathway genes are expressed in a tissue-specific pattern to match processing demands of the secretome.* npj Systems Biology and Applications, 2017. **3**(1): p. 22.

32. Asada, R., et al., *The signalling from endoplasmic reticulum-resident bZIP transcription factors involved in diverse cellular physiology.* J Biochem, 2011. **149**(5): p. 507-18.

33. Almanza, A., et al., *Endoplasmic reticulum stress signalling – from basic mechanisms to clinical applications.* The FEBS Journal, 2019. **286**(2): p. 241-278.

34. Iseki, K., et al., *Gliosis-specific transcription factor OASIS coincides with proteoglycan core protein genes in the glial scar and inhibits neurite outgrowth.* Biomed Res, 2012. **33**(6): p. 345-53.

35. Lee, S. and L. Cooley, *Jagunal is required for reorganizing the endoplasmic reticulum during Drosophila oogenesis.* The Journal of cell biology, 2007. **176**(7): p. 941-952.

36. Bue, C.A., C.M. Bentivoglio, and C. Barlowe, *Erv26p directs pro-alkaline phosphatase into endoplasmic reticulum-derived coat protein complex II transport vesicles.* Molecular biology of the cell, 2006. **17**(11): p. 4780-4789.

37. Yin, Y., et al., *Surf4 (Erv29p) binds amino-terminal tripeptide motifs of soluble cargo proteins with different affinities, enabling prioritization of their exit from the endoplasmic reticulum.* PLoS biology, 2018. **16**(8): p. e2005140-e2005140.

APPENDIX

IACUC APPROVAL FORM

THE UNIVERSITY OF ALABAMA AT BIRMINGHAM

MEMORANDUM

DATE: 28-Jun-2022

TO: Sztul, Elizabeth S

FROM: Robert A. Kesterson, Ph.D., Chair

Institutional Animal Care and Use Committee (IACUC)

SUBJECT: NOTICE OF APPROVAL

The following application was approved by the University of Alabama at Birmingham Institutional Animal Care and Use Committee (IACUC) on 28-Jun-2022.

Protocol PI:	Sztul, Elizabeth S
Title:	Sztul Lab Zebrafish Protocol
Sponsor:	UAB DEPARTMENT
Animal Project Number (APN):	IACUC-21787

This institution has an Animal Welfare Assurance on file with the Office of Laboratory Animal Welfare (OLAW), is registered as a Research Facility with the USDA, and is accredited by the Association for Assessment and Accreditation of Laboratory Animal Care International (AAALAC).

This protocol is due for full review by 27-Jun-2025.

Institutional Animal Care and Use Committee (IACUC)

403 Community Health on 19th | 933 19th Street South

Mailing Address:

CH19 403 | 1720 2nd Ave South | Birmingham AL 35294-2041